NOISE PRODUCED BY THE INTERACTION OF ACOUSTIC WAVES AND ENTROPY WAVES WITH HIGH-SPEED NOZZLE FLOWS

Thesis by

Mark Stephen Bohn

In Partial Fulfillment of the Requirements

for the Degree of

Doctor of Philosophy

California Institute of Technology

Pasadena, California

1976

(Submitted 12 April 1976)

ACKNOWLEDGMENTS

The writer wishes to express his deepest gratitude to Prof. Edward E. Zukoski for the many patient discussions regarding the experimental aspects of this thesis, for allowing the work to be carried out in the most educational manner, and for the careful review of this thesis.

Deepest appreciation is extended to Prof. Frank E. Marble for the valuable advice and stimulating discussions which led to the material presented in Chapters II and III. My appreciation also goes to Dr. Nicholas Cumpsty of Cambridge University for his helpful discussions of the material in Chapter II, and to Professor W. D. Rannie for his involvement in the research since its inception.

Financial assistance, provided by the California Institute of Technology in the form of an Earle C. Anthony fellowship, research assistantships, and teaching assistantships, as well as funding of the research by the Department of Transportation made this thesis possible.

The assistance with the experimental aspects of the research by Dr. Jerome Auerbach and Dr. Haskel Shapiro is greatly appreciated, as is the technical assistance and graphic work of Mr. F. T. Linton. My sincere thanks go to Mrs. Roberta Duffy and Mrs. Virginia Conner for the excellent typing of the manuscript.

ABSTRACT

Some aspects of the noise generated internally by a turbojet engine are considered analytically and experimentally. The emphasis is placed on the interaction of pressure fluctuations and entropy fluctuations, produced by the combustion process in the engine, with gradients in the mean flow through the turbine blades or the exhaust nozzle.

The one-dimensional interaction of pressure fluctuations and entropy fluctuations with a subsonic nozzle is solved analytically. The acoustic waves produced by each of three independent disturbances are investigated. It is seen that results for a large number of physically interesting nozzles may be presented in a concise manner.

Some of the second-order effects which result from the area variations in a nozzle are investigated analytically. The interaction of an entropy wave with a small area variation is investigated and the two-dimensional duct modes, which propagate away from the nozzle, are calculated.

An experiment is described in which one-dimensional acoustic waves and entropy waves are made to interact with a subsonic nozzle. The response of the nozzle to these disturbances is measured and compared with the response as calculated by the analytical model.

The interaction of two-dimensional entropy waves with a subsonic nozzle and with a supersonic nozzle is investigated experimentally. The results are explained in terms of an analysis of the acoustic waves and entropy waves produced by a region of arbitrary heat addition in a duct with flow.

TABLE OF CONTENTS

I. INTRODUCTION TO THE JET NOISE PROBLEM

Well before the first commercial turbojet-powered flight in 1958, the problem of noise from aircraft was recognized. Stevens[1] surveyed the noise in communities near major airports in several cities in 1954. During the same period the popularity of jet-powered military aircraft was rising steadily; in 1953 Boeing delivered its last propeller-powered bomber to the Air Force. Residential areas near military bases were the first to be subjected to noise from jet-powered aircraft, and work[2, 3] similar to the Stevens survey investigated aircraft (primarily jet-powered) noise near several Air Force bases.

Tyler[4] has reported on some noise measurements of turbojet-powered airplanes made near Kennedy International Airport in New York. It is interesting to compare the results of the Stevens survey with those of Tyler. The Stevens survey included such aircraft as the DC-3, DC-6, and the Super Constellation; the latter two were typical of the large commercial transports of that time. Peak sound pressure level was recorded in various frequency bands for positions below the takeoff path. The Tyler survey was a similar measurement for the Boeing 707 turbojet, the first commercial jet-powered airplane used in this country. For a position three miles from the airport, the turbojet gave a noise level of 115 PNdb. The units are perceived noise in decibels and take into account the variation in sensitivity of the ear to sounds of different frequency. The perceived noise level for the propeller-powered airplanes may be calculated from the S. P. L. spectra given by Stevens. At a point below the

takeoff path and three miles away (using the peak sound pressure level in each 1/3 octave band) the results for 90 per cent of the aircraft observed give a noise level of 88 PNdb.

It is reasonable to say that the Boeing 707 was the turbojet replacement for the DC-6 and similar large propeller-driven commercial aircraft. Then we see that the change to jet airplanes in the early 1960's brought an order-of-magnitude increase in the noise near airports. Aircraft noise became more than an interesting technical problem; it became a social problem.

For the turbojet (no bypass), the majority of the noise originates from two sources. Towards the rear portion of the engine the noise from the jet exhaust mixing with the atmosphere predominates. The second source of noise is primarily from the compressor which radiates in a broad angle towards the front of the engine. We will next discuss these two sources of noise and describe some of the related work.

The largest contribution to the understanding of the jet mixing noise came with Lighthill's[5] work on the aerodynamic generation of sound. He found that the acoustic power output of a subsonic mixing region was proportional to the eighth power of the relative velocities. The validity of this result has been verified experimentally. Gerrard[6] used a one-inch diameter air pipe with Mach numbers at the exit ranging from 0.3 to 1.0. In addition to verifying the eighth power variation, he showed that the frequency content of the noise was essentially uniform, implying a random noise source.

Similar experiments were performed by Lush[7] in which the directivity of the noise emission was measured and was seen to compare well with a theory based on Lighthill's work. For the high jet velocities, Lush found a weak peak in the intensity at an angle of about 30^{o} to the jet axis.

The effect of nozzle shape was shown to be small (up to sonic jet velocities) by Callaghan[8]. Coles[9] compared noise generated by air jets and turbojet engines by making a sound survey in a horizontal plane up to 120^{o} from the jet exit. The engine produced a more pronounced peak in sound pressure level at angles between 30^{o} and 40^{o} from the jet exit. The sound power for both the air jet and the engine compared well with Lighthill's theory for jet velocities up to slightly supersonic. The conclusion was that the principal noise-producing mechanism in the turbojet engine (in the rear portion) was the jet mixing.

For flows above sonic velocity the general observation is a distinct increase in sound output with increasing jet velocity, and is attributed to the formation of shock waves. To verify this, Callaghan[8] compared a convergent nozzle with a convergent-divergent plug nozzle designed for shock-free flow at given design pressure ratio. As the pressure ratio was increased from a low subsonic flow, both nozzles gave similar sound power output, which was proportional to the eighth power of the jet velocity, until choking was reached. Beyond this point, both nozzles gave more sound power than would be expected from the eight-power variation, and behaved similarly until the plug nozzle approached the design pressure ratio. At this point

the plug nozzle emitted about one third the sound power of the convergent nozzle (for the same exit velocity) but about twice that predicted by the eighth-power variation.

In a study specifically on supersonic nozzles Louis, et al.[10] also found that the presence of shock waves in the jet was an important factor in the noise emitted from the jet. An additional source of noise was found to be Mach waves apparently emitted from the shear layer near the nozzle exit. Tam[11] considers shear layer instability to be the source of these waves. Ribner[12] models the shear layer as a layer of eddies convecting at some velocity intermediate to the jet and ambient velocity which give rise to the Mach waves by causing pressure perturbations along the shear layer.

It is interesting to note that the pressure fluctuations emitted from a jet engine can cause problems not usually associated with noise. Howes and Mull[13] measured pressure fluctuations in the near field of an exhaust of a turbojet engine with thrust of about 10,000 pounds and exit velocity of 1900 feet per second. Typical values were judged large enough (160 db) to cause structural damage to nearby surfaces.

The compressor noise spectrum is composed of two distinct parts. The first part is a broad-band white noise and may be attributed[14, 15] to the random shedding of vorticity at the trailing edge of the compressor blades and to random fluctuations in the turbulent flow approaching the blades. The second part is discrete frequency components corresponding to blade passage frequency and harmonics. This is caused by periodic disturbances in a blade flow field as it

passes through the wake of an upstream blade.

Both components are usually seen[15, 16] to vary as the sixth power of the relative flow velocity over the blade. This corresponds to noise radiation from a fluctuating force (dipole) field imposed on the gas by solid boundaries.

Sharland[17] has shown, using experiments with a flat plate immersed in an air jet, that upstream turbulence can produce much larger sound intensities than random vortex shedding. The air jet velocities covered a range of velocities from 200 to 700 feet per second. The vortex shedding noise was studied by placing the plate in the potential core of the jet. By moving the plate into the mixing region of the jet, the flow over the plate became more turbulent. For the same values of flow velocity at the center of the plate the radiated noise (on a line 90^{o} to jet axis and about 30 jet diameters away) was seen to increase 15 db for the turbulent flow.

Thus, the main source of compressor noise is upstream turbulence giving broad band noise and wake/blade interactions giving discrete frequency noise. Typical sound pressure level spectra[14-17] show the discrete components protruding about 15 db above the broad band noise.

The relative importance of the compressor and jet noise depends strongly upon the operating condition of the engine. During high thrust operation, such as takeoff, the jet noise dominates and may actually "spill over" to the front portion of the engine and mask out the compressor noise. This is to be expected from the strong dependence of the jet noise power on the jet velocity (high thrust

corresponds to high jet velocity). In low thrust situations, such as landing, the jet noise is likely to become small compared to compressor noise. The turbine noise, which is usually masked out by the jet noise, may become more evident in the rear of the engine under these circumstances.

One of the earlier noise suppression techniques was the multi-tube exhaust nozzle. Keeping in mind the eighth-power variation again, these devices were intended to reduce the total shear of the jet as it enters the atmosphere, effectively reducing the jet velocity and hence the noise power output. Additionally, interference between the noise field of each tube tended to reduce some of the strong directional characteristics associated with jet noise.

As is easily imagined, such devices also cause a loss of performance of the engine. The bypass engine gives the same thrust from a higher mass flow, but lower jet velocity. Hence, jet noise is reduced, but additionally, specific fuel consumption is decreased. The penalty paid is that fan noise increases with increasing bypass ratios because increasing fan tip speed is usually the method for increasing bypass ratio. Also, the flow which is bypassed around the engine convects fan noise into the rear of the engine.

The trend towards higher bypass ratio has reduced significantly the jet mixing noise and has focussed most attention to compressor and fan noise. Some of the techniques considered[18] for compressor and fan noise reduction (principally the discrete component noise) include using resonators and acoustical lining in the fan inlet and exit ducts, choking the engine inlet and adjusting the number and

axial spacing of fan blades.

The method which is most economically feasible for existing engines is the acoustical lining of fan inlet and exit ducts. Mangiarotty[19] gives the results of such treatments in an actual engine. For landing approach conditions for a Boeing 707 powered by a Pratt and Whitney JT3D engine, a reduction of 16 PNdb was achieved. We should note that the sound pressure level of the first harmonic of the discrete fan noise was reduced by 25 db. This is significant because the discrete tones, especially those of the first harmonic, occur in a frequency band (~ 3 kHz) to which our hearing is most sensitive and hence are most irritating.

Measurements on actual engines[20,21] indicate that for low primary jet velocities (< 1000 feet per second) more sound power (in low-frequency bands) is emitted than would be predicted by an eighth-power variation with velocity. The experiments were designed to minimize the influence of rearward-propagated fan noise. The increased noise is usually called excess or core noise since it must come from the core of the engine upstream of the nozzle exit. With the trend toward lower jet velocities this core noise is expected to control the lower limit of sound power generated by turbojet engines. The low-frequency noise is difficult to treat with techniques such as resonators or acoustical lining since the long wavelengths would require physically large treatments. Hence, an understanding of the source of core noise will be a necessity.

The core noise has been attributed to a wide variety of sources such as combustion, flow incidence upon supporting struc-

tures in the engine, turbulent flow in the turbine and nozzle, and others. With the majority of the recent work being done on fan/compressor noise, very little has been done to determine the relative importance of these sources. It is generally agreed, however, that the role of combustion in producing core noise is a major one.

It is clear that neither the flow through the combustor nor the combustion process will be steady. Even with no combustion the presence of the combustor in the flow will create turbulence which will reach the turbine. This situation is somewhat similar to the effect of upstream turbulence on compressor blades discussed previously. The level of turbulence will probably increase significantly when combustion occurs, but two additional effects will be seen. The (unsteady) process of adding heat to the flow causes acoustic (isentropic) disturbances and entropy disturbances to be generated. The acoustic disturbances represent noise in themselves in that a microphone situated downstream of the combustor could detect their presence. The entropy disturbances are unique in that they do not, in themselves, represent noise. They represent "hot spots" or the temperature disturbances which are not associated with the isentropic acoustic disturbances. The convection of these entropy disturbances through mean velocity gradients (such as in turbine flow passages and the primary exhaust nozzle) produces isentropic acoustic waves which are perceivable as noise (see Chapter II).

This thesis will be concerned with the acoustic and entropy disturbance aspect of core engine noise. The acoustic disturbances will be modified in the flow passages, and the noise from the entropy

disturbance relies wholly upon mean velocity gradients in such passages. Hence, the emphasis will be on the interaction of these disturbances with such flow fields as may be found downstream of the combustor.

In Chapter II we develop an analytical model for the interaction of one-dimensional pressure and entropy waves with a one-dimensional subsonic flow with strong mean gradients. This model will be used to explain and to complement the results for the experiments presented in Chapter IV. The analysis will be extended in such a way that results for a wide range of parameters may be presented concisely. In Chapter III we present an analytical investigation of some of the two-dimensional effects neglected by the analysis in Chapter II. In Chapter V we present some experimental results performed with two-dimensional entropy disturbances.

REFERENCES FOR CHAPTER I

1. Stevens, K. "A Survey of Background and Aircraft Noise in Communities near Airports," NACA TN 3379 (1954).

2. Pietrasonta, A. "Field Measurements of Community Noise Exposure near Hanscom AFB, Mass.," WADC TN 58-163 (1958).

3. Clark, W. "Reaction to Aircraft Noise," AF 33 (616) 5629 (1961).

4. Tyler, J. "A New Look at the Aircraft Noise Problem," SAE Paper 911B (1964); Trans. 1965, p. 621 .

5. Lighthill, M. "On Sound Generated Aerodynamically, I. General Theory," Proc. Roy. Soc. A 211 (1951), 564-587.

6. Gerrard, J. "An Investigation of the Noise Produced by a Subsonic Jet," J. Aero. Sci. , V. 23, 9 (1956), 855-866

7. Lush, P. "Measurements of Subsonic Jet Noise and Comparison with Theory," J. Fluid Mech., V. 46, 3 (1971), 477-500.

8. Callaghan, E. and Coles, W. "Investigation of Far Noise Field of Jets, I. Effect of Nozzle Shape," NACA TN 3590 (1956).

9. Coles, W. and Callaghan, E. "Investigation of Far Noise Field of Jets, II. Comparison of Air Jets and Jet Engines," NACA TN 3591 (1956).

10. Louis, J., Letty, R. and Patel, J. "A Systematic Study of Supersonic Jet Noise," AIAA Paper 72-641 (1972).

11. Tam, C. "Directional Acoustic Radiation from a Supersonic Jet Generated by Shear Layer Instability," J. Fluid Mech., V. 46, 4 (1971), 757-768.

12. Ribner, H. "Eddy - Mach Wave Noise from a Simplified Model of a Supersonic Mixing Layer," NASA SP 207 (1969), p. 53.

13. Howes, W. and Mull, H. "Near Noise Field of a Jet Engine Exhaust, I. Sound Pressures," NACA TN 3763 (1956).

14. Smith, M. and House, M. "Internally Generated Noise from Gas Turbine Engines, Measurement and Prediction," ASME Transactions, V. 89 (April 1967), ASME Paper 66-GT/N-43.

15. Bragg, S., and Bridge, R. "Noise from Turbojet Compressors," J. Roy. Aero. Soc., V. 68 (1964), 1-10.

16. Greatrex, F. and Bridge, R. "The Evolution of the Engine Noise Problem," Aircraft Engineering, V. 39 (February 1967), 6-10.

17. Sharland, I. "Sources of Noise in Axial Flow Fans," J. Sound Vib., V. 1, 3 (1964), 302-322.

18. Marsh, A., Elias, I., Hoene, J. and Frasca, R. "A Study of Turbofan Engine Compressor Noise Suppression Techniques," NASA CR 1056 (1968).

19. Mangiarotty, R. "A Reduction of Aircraft Engine Fan/Compressor Noise Using Acoustic Linings," J. Sound Vib., V. 18, 4 (1971), 565-576.

20. Grande, E. "Exhaust Noise Field Generated by the JT8D Core Engine - Noise Floor Presented by Internal Sources," J. Acous. Soc. Am., V. 55, 1 (1974), 30-34.

21. Gerend, R. "Core Engine Noise," AIAA Paper 73-1027, presented at AeroAcoustics Conference, Seattle, Wash. (1973).

II. THE INTERACTION OF ACOUSTIC WAVES AND ENTROPY WAVES WITH A SUBSONIC NOZZLE -- THE ONE-DIMENSIONAL MODEL

2.1 Introduction

In this chapter we investigate the effect of acoustic waves and entropy waves propagating through a nozzle with a subsonic mean flow. The problem of pressure disturbances in ducts with mean flow and area change has been studied by many, ref. 1-5 for example, but the effects caused by entropy disturbances have not been as widely studied.

Candel[6] solved the problem of acoustic and entropy waves convected into a choked nozzle. He used a formulation which was originally developed by Tsien[7] to study the oscillations in a rocket engine. This formulation is the basis of the model developed in this chapter. Auerbach[8] and Zukoski[9] showed the validity of the Candel model experimentally. The (choked) mean flow in a rectangular (cross-section) blowdown tunnel was perturbed with entropy waves. The entropy waves were created by electrically pulsing a resistance heater located upstream of the nozzle, and then, using a periodic mass bleed system (also upstream of the nozzle), the pressure wave component of the disturbance was cancelled. The production of acoustic waves by the entropy disturbance was then verified by the detection of pressure disturbances throughout the nozzle.

The solution for low-frequency disturbances was investigated by Marble[10]. For disturbances with wavelengths which are long compared to the nozzle length, the resulting solution will give disturb-

ances with constant phase throughout the nozzle. This solution is called the compact or quasi-steady solution, and may be solved by considering only matching conditions at the nozzle inlet and exit. The details of the mean flow in the nozzle may be neglected.

Cumpsty and Marble[11] have investigated the interaction of pressure and entropy disturbances with one or more turbine blade rows. Large deflections and accelerations in the mean flow were considered; however, the disturbances were assumed to be quasi-steady so that precise details of the mean flow in the blade passages could be neglected.

Our aim here is to examine these effects of mean flow variations that occur in the flow through such blade passages and, equivalently, exhaust nozzles. We consider only one-dimensional, subsonic flow with small disturbances. In the choked nozzle, the throat essentially decouples the supersonic portion from the rest of the nozzle. Two independent solutions result. The first solution represents the effects of an entropy wave convected into the nozzle, when no acoustic wave is incident upon the nozzle entrance. The second solution represents the results of an acoustic wave incident upon the nozzle entrance when no entropy wave convects into the nozzle.

In the subsonic nozzle, every portion of the nozzle can communicate with every other portion. The result is that we must admit a third independent solution which represents the effects of an acoustic wave propagating upstream and impinging upon the nozzle exit.

In the following sections we develop the equations which will serve as the analytical model. Next, we discuss a method of nu-

merical solution. The emphasis here will be on choosing the appropriate boundary conditions to give the three independent solutions. The solution for high-frequency disturbances is then discussed. The results of this solution are then used to normalize some numerical calculations so that a concise presentation of the results may be made. Finally, the results are discussed and several examples of the use of these results are presented. (See Appendix G for notation.)

2.2 Development of the Analytical Model

We are given a duct of constant cross-sectional area with a mean flow of Mach number M_1. The cross-sectional area then changes in such a way that after an axial distance ℓ, the Mach number is M_2. The flow then continues through a constant cross-sectional area duct. If we let the cross-sectional area (of the axial region in which the mean flow is changing) be called A(x), we have the following diagram describing the duct.

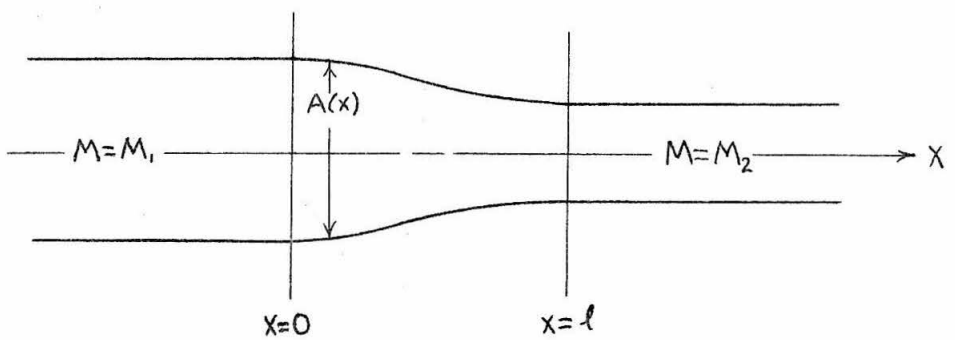

Diagram for the Analytical Model

We assume that the gas flowing in the duct is ideal and inviscid, and that the mean flow is isentropic and wholly subsonic. We will neglect

two-dimensional effects, and simply use the area variations to give mean flow variations. These assumptions allow us to describe the flow with the equations of momentum, continuity, entropy conservation, and the equation of state as follows:

$$\frac{\partial u}{\partial t} + u\frac{\partial u}{\partial x} + \frac{1}{\rho}\frac{\partial P}{\partial x} = 0 \tag{2.1}$$

$$\frac{\partial \rho}{\partial t} + \frac{1}{A}\frac{\partial(\rho u A)}{\partial x} = 0 \tag{2.2}$$

$$\frac{\partial s}{\partial t} + u\frac{\partial s}{\partial x} = 0 \tag{2.3}$$

$$s = c_v \ln\left(\frac{P}{\rho^{\gamma}}\right) \tag{2.4}$$

We will linearize these equations by assuming that a solution exists which is the sum of a known function of axial position only, plus a small periodic function which also varies with axial position. For example, the velocity will be expressed as

$$u(x,t) = \bar{u}(x) + u'(x)\, e^{-i\omega t}$$

where ω is the radial frequency. The primed quantity is, in general, complex, but we let

$$|u'| << \bar{u}$$

We assume a similar form for the remaining dependent quantities in (2.1) - (2.4) and define the following dimensionless quantities:

$$Z_1(x) \equiv \frac{u'}{\bar{u}} \qquad Z_2(x) \equiv \frac{P'}{\gamma \bar{P}} \qquad Z_3(x) \equiv \frac{s'}{c_p} \tag{2.5a}$$

$$U(x) \equiv \frac{\bar{u}}{a^*} = M\frac{a}{a^*} \qquad \beta \equiv \frac{\omega \ell}{a^*} \tag{2.5b}$$

where $M = M(x)$ = mean local Mach number

$\gamma = \frac{C_p}{C_v}$

a = local mean sound speed

a^* = speed of sound at a throat (if mean flow were isentropically choked)

Note that the reduced frequency β relates the wavelength of the disturbance to the nozzle length. For a disturbance with wavelength approximately one nozzle length, the reduced frequency is about 6.

We normalize the axial distance by nozzle length ℓ. After inserting the assumed form of the solution, we retain only terms linear in the perturbation quantities. This process leads to:

$$\frac{dZ_3}{dx} = \frac{i\beta}{U} Z_3 \tag{2.6}$$

$$\frac{dZ_2}{dx} = \frac{i\beta}{U} Z_2 - \frac{dZ_1}{dx} \tag{2.7}$$

and

$$\frac{dZ_1}{dx} = \frac{-i\beta(M^2 Z_1 - Z_2) + M^2 \frac{dU}{dx}(2Z_1 - (\gamma-1)Z_2 - Z_3)}{U(1-M^2)} \tag{2.8}$$

We note that for a constant area channel, $\frac{dU}{dx} \equiv 0$, the entropy component Z_3 does not contribute to the interaction, and thus we may write down the well-known solution:

$$Z_2(x) = P^+ e^{iC_+ x} + P^- e^{iC_- x}$$

$$Z_1(x) = (P^+ e^{iC_+ x} - P^- e^{iC_- x})/M \tag{2.9}$$

where C_+, C_- are the dimensionless wave numbers of the waves propagating downstream and upstream, respectively:

$$C_\pm \equiv \frac{\omega \ell}{\bar{u} \pm a} = \frac{\beta M}{U(M \pm 1)} \tag{2.10}$$

Here, M, U are to be evaluated in the constant-area section in question and P^+ and P^- are the complex magnitudes of the wave propagating downstream and upstream, respectively, in that constant-area section.

If the pressure and velocity disturbances are specified at the nozzle inlet, $x = 0$, and the nozzle exit, $x = l$, it is clear that we can calculate the complex magnitude of the waves entering and leaving the nozzle. Using subscripts 1 and 2 to denote conditions upstream or downstream of the nozzle, respectively, we see from (2.9) that:

$$P_1^+ = \frac{1}{2}\left[Z_2(0) + M_1 Z_1(0)\right]$$

$$P_1^- = \frac{1}{2}\left[Z_2(0) - M_1 Z_1(0)\right] \tag{2.11}$$

for the waves propagating in the upstream constant-area duct, and

$$P_2^+ = \frac{1}{2} e^{-iC_{2+}}\left[Z_2(1) + M_2 Z_1(1)\right]$$

$$P_2^- = \frac{1}{2} e^{-iC_{2-}}\left[Z_2(1) - M_2 Z_1(1)\right] \tag{2.12}$$

for the waves propagating in the downstream constant-area duct.

Consider for a moment that the upstream constant-area duct extends to minus infinity and the downstream constant-area duct extends to plus infinity in the axial dimension. A disturbance upstream (or downstream) of the nozzle will propagate to the nozzle and interact with it. The interaction will cause a pressure wave P_1^- (or P_2^+) to be created, which will propagate upstream (or downstream) from the nozzle to infinity. Also, a wave P_2^+ (or P_1^-) will be created which will propagate downstream (or upstream) from the nozzle to infinity. Since an entropy wave convects with the mean flow, it cannot disturb the nozzle if created downstream of it. Hence, we have just described the three independent disturbances to which the nozzle can be subjected. These are: an entropy wave convecting into the nozzle from upstream, a pressure wave propagating into the nozzle from upstream, or from downstream. In a practical situation, the downstream constant-area duct may be terminated. Some impedance condition will exist there such that a P_2^+ wave reflects from the termination and creates a P_2^- wave. This point is discussed further in an example at the end of this chapter. We consider the three effects to be independent; since the problem is linear, the independent solutions will allow any general solution to be constructed.

In the discussions which follow we will call the first independent solution (in which the entropy wave is convecting into the nozzle) the "entropy solution" and will use a subscript "e" to signify it. The solution corresponding to a pressure disturbance upstream of the nozzle will be called the "plus solution" and will be signified by a "p"

subscript. The solution corresponding to the pressure disturbance downstream of the nozzle will be called the "minus solution" and will be denoted by the subscript "m". The following summarizes the notation:

Disturbance	Name/Subscript	Result
$\sigma \equiv \frac{s'}{c_p}_{x=0}$	entropy/e	$Z_{1e}(x)$, $Z_{2e}(x)$, $Z_{3e}(x)$, P_{1e}^-, P_{2e}^+
P_1^+	plus/p	$Z_{1p}(x)$, $Z_{2p}(x)$, , P_{1p}^-, P_{2p}^+
P_2^-	minus/m	$Z_{1m}(x)$, $Z_{2m}(x)$, , P_{1m}^-, P_{2m}^+

2.3 Numerical Solution

Given $M(x)$ and the reduced frequency β, we would like to solve the system of equations (2.6) - (2.8) for each of the three independent solutions. The "plus" and "minus" solutions have no entropy disturbance; hence, the system reduces to a pair of homogeneous, linear, simultaneous differential equations. We need only to specify the boundary conditions, and use a suitable numerical technique to integrate (2.7) and (2.8). The entropy solution requires that $Z_3(x) \not\equiv 0$. We must specify σ (the entropy disturbance at the inlet), but we see that having done so, (2.6) may be integrated immediately. We are left with a pair of inhomogeneous, linear, simultaneous differential equations. The inhomogeneous term is simply $Z_3(x)$. We now discuss the boundary conditions, used in the numerical integration, for each solution.

For the plus solution, we begin the integration at the exit such that $P_{2p}^- = 0$. For example,

$M_2 Z_{1P}(1) = 1 \qquad Z_{2P}(1) = 1 \qquad Z_{3P}(x) = 0$

We integrate to the inlet, $x = 0$, where we may calculate

$$P_{1P}^{+} = \frac{1}{2}\left[Z_{2P}(0) + M_1 Z_{1P}(0)\right]$$

$$P_{1P}^{-} = \frac{1}{2}\left[Z_{2P}(0) - M_1 Z_{1P}(0)\right]$$

$$P_{2P}^{+} = \frac{1}{2} e^{-iC_2 x}\left[Z_{2P}(1) + M_2 Z_{1P}(1)\right]$$

We will normalize the solution with P_{1P}^{+} , i.e.,

$$\frac{P_{2P}^{+}}{P_{1P}^{+}} \equiv T_P \qquad \text{"transmitted wave, plus solution"} \qquad (2.13)$$

$$\frac{P_{1P}^{-}}{P_{1P}^{+}} \equiv R_P \qquad \text{"reflected wave, plus solution"}$$

For the minus solution, we ensure that $P_{1m}^{+} = 0$. Let

$$M_1 Z_{1m}(0) = -1 \qquad Z_{2m}(0) = 1 \qquad Z_{3m}(x) \equiv 0$$

and we integrate to the exit, where

$$P_{2m}^{+} = \frac{1}{2} e^{-iC_2 x}\left[Z_{2m}(1) + M_2 Z_{1m}(1)\right]$$

$$P_{2m}^{-} = \frac{1}{2} e^{-iC_2}\left[Z_{2m}(1) - M_2 Z_{1m}(1)\right]$$

$$P_{1m}^{-} = \frac{1}{2}\left[Z_{2m}(0) - M_1 Z_{1m}(0)\right]$$

Now define

$$\frac{P_{1m}^{-}}{P_{2m}^{-}} \equiv T_m \qquad \text{"transmitted wave, minus solution"} \qquad (2.14)$$

$$\frac{P_{2m}^{+}}{P_{2m}^{-}} \equiv R_m \qquad \text{"reflected wave, minus solution"}$$

For the entropy solution, we begin the integration at the inlet with

$$Z_{1e}(0) = 0 \qquad Z_{2e}(0) = 0 \qquad Z_{3e}(0) = \sigma$$

This ensures that $P_{1e}^{+} = 0$, but upon reaching the exit we can see that

$$P_{2e}^{-} = \tfrac{1}{2} e^{-iC_2-}\left[Z_{2e}(1) - M_2 Z_{1e}(1)\right] \neq 0$$

in general. This is easily corrected by simply subtracting from this entropy solution "enough" of the previously calculated minus solution (a homogeneous solution) to cancel the P_{2e}^{-}. Let

$$\tilde{Z}_{1e}(x) \equiv Z_{1e}(x) - Z_{1m}(x)\,\frac{P_{2e}^{-}}{P_{2m}^{-}}$$

and

$$\tilde{Z}_{2e}(x) \equiv Z_{2e}(x) - Z_{2m}(x)\,\frac{P_{2e}^{-}}{P_{2m}^{-}}$$

Now we will have

$$\tilde{P}_{1e}^{+} = \tfrac{1}{2}\left[\tilde{Z}_{2e}(0) + M_1 \tilde{Z}_{1e}(0)\right] = 0$$

$$\tilde{P}_{2e}^{-} = \tfrac{1}{2} e^{-iC_2-}\left[\tilde{Z}_{2e}(1) - M_2 \tilde{Z}_{1e}(1)\right] = 0$$

Now define

$$T_e \equiv \frac{1}{2\sigma}\, e^{-iC_2+}\left[\tilde{Z}_{2e}(1) + M_2 \tilde{Z}_{1e}(1)\right] \qquad (2.15a)$$

as the "transmitted wave - entropy solution" and

$$R_e \equiv \frac{1}{2\sigma}\left[\tilde{Z}_{2e}(0) - M_1 \tilde{Z}_{1e}(0)\right] \qquad (2.15b)$$

as the "reflected wave - entropy solution." The actual numerical scheme used in solving these equations was a fourth-order Runge-Kutta method with automatic error control.

Now, any general solution may be calculated from these normalized solutions. For example, if we specify the disturbances P_1^{+},

P_2^- , and σ , then the resultant waves will be

$$P_1^- = P_1^+ R_p + P_2^- T_m + \sigma R_e$$

$$P_2^+ = P_2^- R_m + P_1^+ T_p + \sigma T_e \qquad (2.16)$$

We would like to investigate the behavior of the six solutions for various Mach number distributions and reduced frequencies. The only restriction on the Mach number distribution is that it be wholly subsonic. We will be interested here in Mach number distributions one might find in the passage through turbine blades or in an unchoked exhaust nozzle. The numerical solution only requires that a mean Mach number distribution and reduced frequency be specified; then the independent solutions may be calculated. Even if we restrict the calculations to physically interesting cases, it is clear that some systematic way of presenting the results must be employed. In order to present a large number of results in a concise manner, the calculations have been normalized by using the compact solution as discussed previously and the solution for high-frequency disturbances. In the following section we consider first the high-frequency solution and then discuss the normalization procedure.

2.4 High-Frequency Asymptotic Solution and Normalization

We will assume a linear mean velocity profile for this asymptotic analysis (and for the remainder of this chapter). This allows us to integrate eq. (2.6) immediately, and is a reasonable approximation to the profile one might find in a physical application.

We move the inlet of the nozzle from the origin of our coordinate system so that we may write for the dimensionless axial

distance

$$X = \frac{\bar{u}}{a^*} \qquad X_i \le X \le X_e$$

In all the discussions that follow we use the length scale $\ell a^*/(\bar{u}_2 - \bar{u}_1)$ for normalization purposes. The reduced frequency is now

$$\beta = \frac{\omega}{a^*} \frac{\ell a^*}{\bar{u}_2 - \bar{u}_1}$$

which relates the wavelength of the disturbance to the mean dimensionless velocity gradient. In addition, the dimensionless wave numbers involve this new length scale:

$$C_{\pm} = \frac{\omega}{\bar{u} \pm a} \frac{\ell a^*}{\bar{u}_2 - \bar{u}_1} = \frac{\beta M}{\frac{\bar{u}}{a^*}(M \pm 1)}$$

Now define

$$\mathcal{Z} = X^2 = \frac{\frac{\gamma+1}{2} M^2}{1 + \frac{\gamma-1}{2} M^2} \qquad \mathcal{Z}_i = X_i^2 \qquad \mathcal{Z}_e = X_e^2$$

Equation (2.6) becomes

$$\frac{dZ_3}{Z_3} = \frac{i\beta}{2} \frac{d\mathcal{Z}}{\mathcal{Z}}$$

which gives

$$Z_3(X) = Z_{3i} \left(\frac{\mathcal{Z}}{\mathcal{Z}_i} \right)^{\frac{i\beta}{2}} \qquad Z_{3i} \equiv Z_3(\mathcal{Z}_i)$$

We will specify Z_{3i} .

The two simultaneous, linear, inhomogeneous, first-order equations for pressure and velocity perturbation may be combined to give one second-order, linear equation for the pressure perturbation. To distinguish the high-frequency solution from the numerical analysis, we will use

$$P(\zeta) \equiv \frac{P'}{\gamma \bar{P}} \qquad U(\zeta) \equiv \frac{u'}{\bar{u}} \qquad \eta \equiv i\beta$$

Then we find:

$$\zeta(1-\zeta)\frac{d^2P}{d\zeta^2} - 2\left(1-\frac{\eta}{\gamma+1}\right)\zeta\frac{dP}{d\zeta} + \frac{\eta}{2}\frac{2-\eta}{\gamma+1}P = \frac{\eta}{2(\gamma+1)}Z_{3i}\left(\frac{\zeta}{\zeta_i}\right)^{\eta/2} \tag{2.17}$$

We may get the velocity from

$$(2-\eta)U = \frac{dP}{d\zeta}(\gamma+1)(\zeta-1) + P(\gamma-1-\eta) + Z_{3i}\left(\frac{\zeta}{\zeta_i}\right)^{\eta/2} \tag{2.18}$$

The equation (2.17) is a hypergeometric equation with no singularities in our region of interest:

$$0 < \zeta_i \le \zeta \le \zeta_e < 1$$

For the inhomogeneous solution, we try

$$P(\zeta) = \tilde{P}(\zeta)\left(\frac{\zeta}{\zeta_i}\right)^{\eta/2}$$

where $\tilde{P}(\zeta)$ is an expansion in inverse powers of η :

$$\tilde{P}(\zeta) = \sum_{n=0} \hat{P}_n(\zeta)\,\eta^{-n}$$

By isolating powers of η , we get equations in $\hat{P}_n(\zeta)$.

This yields eventually

$$P(\zeta) = \frac{Z_{3i}}{\eta}M^2\left(\frac{\zeta}{\zeta_i}\right)^{\eta/2} + \mathcal{O}\left(\frac{1}{\eta^2}\right)$$

$$U(\zeta) = \qquad\qquad \mathcal{O}\left(\frac{1}{\eta^2}\right) \tag{2.19}$$

Upon calculating

$$P_1^+ = \frac{1}{2}\left[P(\zeta_i) + M_1 U(\zeta_i)\right] = \frac{1}{2}Z_{3i}\frac{M_1^2}{\eta} + \mathcal{O}\left(\frac{1}{\eta^2}\right)$$

$$P_2^- = \frac{1}{2}e^{-iC_2-(X_e-X_i)}\left[P(\zeta_e) - M_2 U(\zeta_e)\right] = \frac{1}{2}e^{-iC_2-(X_e-X_i)}Z_{3i}\frac{M_2^2}{\eta}\left(\frac{\zeta_e}{\zeta_i}\right)^{\eta/2} \tag{2.20}$$

we realize that we have a situation similar to the numerical entropy solution. We must use the homogeneous solution to eliminate the incident waves if we are to find the three solutions independently.

To solve the homogeneous equation:

$$\zeta(1-\zeta)\frac{d^2P}{d\zeta^2} - 2\left(1-\frac{\eta}{\gamma+1}\right)\zeta\frac{dP}{d\zeta} + \frac{\eta}{2}\frac{2-\eta}{\gamma+1}P = 0 \tag{2.21}$$

We try an expansion of the form

$$P(\zeta) \sim \exp\left\{\sum_{n=0} K_n(\zeta)\eta^{1-n}\right\} \tag{2.22}$$

We will have two independent solutions, so we let

$$P(\zeta) = A\exp\left\{K_{0+}(\zeta)\eta + K_{1+}(\zeta) + \cdots\right\} + B\exp\left\{K_{0-}(\zeta)\eta + K_{1-}(\zeta) + \cdots\right\} \tag{2.23}$$

where A and B are constants to be determined from boundary conditions; hence, we may let

$$K_{n\pm}(\zeta_i) = 0 \qquad n = 0, 1, \cdots$$

The procedure for finding K_n, A, B is straightforward. Substituting of (2.23) into (2.21) and isolating powers of η we get differential equations for $K_n(\zeta)$ of the form

$$\frac{dK_n}{d\zeta} = f_n(\zeta, K_{n-1}(\zeta)) \qquad n = 0, 1, \cdots$$

where f_n is a known function, and K_{-1} is a constant. In order to solve for the $K_n(\zeta)$ we expand $f_n(\zeta, K_{n-1}(\zeta))$ in a power series about the origin: $\zeta = 0$. If we calculate $K_0(\zeta)$ and $K_1(\zeta)$ we will have the magnitude to $\mathcal{O}\left(\frac{1}{\eta^2}\right)$ and the phase to $\mathcal{O}\left(\frac{1}{\eta}\right)$. This power series solution gives

$$K_{0\pm}(\zeta) = \frac{1}{\gamma+1}\ln\frac{1-\zeta}{1-\zeta_i} \pm Z_0(\zeta) \tag{2.24}$$

$$K_{1\pm}(\zeta) = \frac{1}{2}\ln\left(\frac{M_1}{M}\,\frac{1-\zeta}{1-\zeta_i}\right) \mp Z_1(\zeta) \tag{2.25}$$

where

$$Z_0(\zeta)=\frac{1}{\sqrt{2(\gamma+1)}}\left\{\left[\ln\left(\frac{1+\zeta^{1/2}}{1-\zeta^{1/2}}\,\frac{1-\zeta_i^{1/2}}{1+\zeta_i^{1/2}}\right)\right]\left[1+\frac{1}{2}\frac{1-\gamma}{1+\gamma}-\frac{1}{8}\frac{(1-\gamma)^2}{(1+\gamma)^2}+\cdots\right]\right.$$

$$-2\left(\zeta^{1/2}-\zeta_i^{1/2}\right)\left[\frac{1}{2}\frac{1-\gamma}{1+\gamma}-\frac{1}{8}\frac{(1-\gamma)^2}{(1+\gamma)^2}+\cdots\right]$$

$$\left.-\frac{2}{3}\left(\zeta^{3/2}-\zeta_i^{3/2}\right)\left[-\frac{1}{8}\frac{(1-\gamma)^2}{(1+\gamma)^2}+\cdots\right]\right.$$

$$\left.\vdots\qquad\qquad\right\} \tag{2.26}$$

$$Z_1(\zeta)=\frac{1}{\sqrt{2(\gamma+1)}}\left\{\left[\ln\left(\frac{1+\zeta^{1/2}}{1-\zeta^{1/2}}\,\frac{1-\zeta_i^{1/2}}{1+\zeta_i^{1/2}}\right)\right]\left[1+\frac{1}{2}\frac{\gamma-1}{\gamma+1}+\frac{3}{8}\frac{(\gamma-1)^2}{(\gamma+1)^2}+\cdots\right]\right.$$

$$-2\left(\zeta^{1/2}-\zeta_i^{1/2}\right)\left[\frac{1}{2}\frac{\gamma-1}{\gamma+1}+\frac{3}{8}\frac{(\gamma-1)^2}{(\gamma+1)^2}+\cdots\right]$$

$$\left.-\frac{2}{3}\left(\zeta^{3/2}-\zeta_i^{3/2}\right)\left[\frac{3}{8}\frac{(\gamma-1)^2}{(\gamma+1)^2}+\cdots\right]\right.$$

$$\left.\vdots\qquad\qquad\right\} \tag{2.27}$$

To find A , B we use the same procedure as we used in the numerical solution. For the plus solution we specify that

$$P(z_i)+M_1U(z_i)=2P_1^+\neq 0$$

$$P(z_e)-M_2U(z_e)=0$$

Inserting (2.23) into these relations we can solve for A , B in terms of $Z_1(z_e)$ and $Z_0(z_e)$ which we will call Z_{1e} and Z_{oe} for short:

$$Z_{oe}\equiv Z_0(z_e) \qquad\qquad Z_{1e}\equiv Z_1(z_e)$$

In solving for A , B we retain only terms to $\mathcal{O}\left(\frac{1}{\eta}\right)$.

For the minus solution we specify

$$P(z_i)+M_1U(z_i)=0$$

$$P(z_e)-M_2U(z_e)=2P_2^-e^{iC_{2-}(x_e-x_i)}\neq 0$$

The calculation of A , B for both solutions now allows us to calculate T_p , T_m , R_p , R_m . Since this is the high-frequency solution, we use the subscript:

$$T_{p\infty}\equiv T_p\big|_{\beta\to\infty}$$
$$T_{m\infty}\equiv T_m\big|_{\beta\to\infty}$$
$$R_{p\infty}\equiv R_p\big|_{\beta\to\infty}$$
$$R_{m\infty}\equiv R_m\big|_{\beta\to\infty}$$

where T_p, T_m, R_p, R_m are defined in (2.13), (2.14). We find

$$T_{p\infty}=\exp\left\{-\tfrac{1}{2}\ln\frac{M_1}{M_2}\frac{1-z_e}{1-z_i}-Z_{1e}\right\} \qquad (2.28)$$

$$\exp\left[i\beta\left\{\frac{1}{\gamma+1}\ln\frac{1-z_e}{1-z_i}+Z_{oe}-\frac{C_{2+}}{\beta}(x_e-x_i)\right\}\right]+\mathcal{O}\left(\frac{1}{\beta}\right)$$

$$T_{m\infty} = \exp\left\{\frac{1}{2}\ln\frac{M_1}{M_2}\frac{1-\mathfrak{z}_e}{1-\mathfrak{z}_i} - Z_{1e}\right\}$$

$$\exp\left[i\beta\left\{\frac{-1}{\gamma+1}\ln\frac{1-\mathfrak{z}_e}{1-\mathfrak{z}_i} + Z_{oe} + \frac{C_2}{\beta}(X_e - X_i)\right\}\right] + \mathcal{O}\left(\frac{1}{\beta}\right) \qquad (2.29)$$

We mentioned previously that the compact solutions discussed by Marble[10] would be used to help us find a concise representation of the results. We list these solutions here for convenience.

$$T_{po} = \frac{2M_2}{1+M_2}\,\frac{1+M_1}{M_2+M_1}\,\frac{1+\frac{\gamma-1}{2}M_2^2}{1+\frac{\gamma-1}{2}M_1M_2} \qquad (2.30)$$

$$T_{mo} = \frac{2M_1}{M_1+M_2}\,\frac{1-M_2}{1-M_1}\,\frac{1+\frac{\gamma-1}{2}M_1^2}{1+\frac{\gamma-1}{2}M_1M_2} \qquad (2.31)$$

$$R_{po} = \frac{M_2-M_1}{1-M_1}\,\frac{1+M_1}{M_2+M_1}\,\frac{1-\frac{\gamma-1}{2}M_1M_2}{1+\frac{\gamma-1}{2}M_1M_2} \qquad (2.32)$$

$$R_{mo} = \frac{M_2-M_1}{1+M_2}\,\frac{M_2-1}{M_2+M_1}\,\frac{1-\frac{\gamma-1}{2}M_1M_2}{1+\frac{\gamma-1}{2}M_1M_2} \qquad (2.33)$$

$$T_{eo} = \frac{M_2-M_1}{1+M_2}\,\frac{M_2/2}{1+\frac{\gamma-1}{2}M_1M_2} \qquad (2.34)$$

$$R_{eo} = \frac{M_1-M_2}{1-M_1}\,\frac{M_1/2}{1+\frac{\gamma-1}{2}M_1M_2} \qquad (2.35)$$

where the additional subscript (o) refers to the compact ($\beta = 0$) solution.

We define

$$\Delta\phi_{\pm} \equiv \frac{C_{2\pm}}{\beta}(X_e - X_i) = \frac{M_2}{M_2 \pm 1}\left[1 - \left(\frac{\mathfrak{z}_i}{\mathfrak{z}_e}\right)^{1/2}\right]$$

This is simply the phase shift in a downstream (+) or upstream (-) propagating wave caused by using $X = X_i$ as the reference from which all phase angles are measured.

Examining (2.28) and (2.29) in the light of (2.30) and (2.31), we find that

$$\left|T_{p\infty}\right| = \left(\frac{T_{po}}{T_{mo}}\right)^{1/2} \exp(-Z_{ie})$$

$$\frac{\operatorname{Arg} T_{p\infty}}{\beta} = \frac{1}{\gamma+1}\ln\frac{1-\mathfrak{z}_e}{1-\mathfrak{z}_i} + Z_{oe} - \Delta\phi_+ \qquad (2.36)$$

$$\left|T_{m\infty}\right| = \left(\frac{T_{mo}}{T_{po}}\right)^{1/2} \exp(-Z_{ie})$$

$$\frac{\operatorname{Arg} T_{m\infty}}{\beta} = \frac{-1}{\gamma+1}\ln\frac{1-\mathfrak{z}_e}{1-\mathfrak{z}_i} + Z_{oe} + \Delta\phi_- \qquad (2.37)$$

These are functions only of inlet and exit Mach number. For convenience these have been plotted in Figures 2-1 and 2-2 for a wide range of inlet and exit Mach numbers. Note that using eq. (2.36) and Figure 2-2 we may easily calculate Z_{oe} or Z_{ie}.

Normalizing the magnitude of the transmitted waves by their compact value we see that

$$\frac{\left|T_{p\infty}\right|}{T_{po}} = \frac{\exp(-Z_{ie})}{(T_{mo}T_{po})^{1/2}} = \frac{\left|T_{m\infty}\right|}{T_{mo}}$$

which tells us that if we normalize our transmitted waves (for any frequency β) by the compact solution, the magnitude tends to the same value (as $\beta \to \infty$) whether the transmitted wave was created by a P_1^+ disturbance or a P_2^- disturbance. Since this is obviously true for $\beta = 0$, we might expect it for all frequencies. All numerical calculations performed verified this was the case. In addition, it was found that the phase, for any frequency, could be calculated with very good accuracy from the high-frequency solution. That is,

$$\text{Arg } T_p \approx \beta\left\{\frac{1}{\gamma+1}\ln\frac{1-\mathfrak{z}_e}{1-\mathfrak{z}_i} + Z_{oe} - \Delta\phi_+\right\}$$

$$\text{Arg } T_m \approx \beta\left\{\frac{-1}{\gamma+1}\ln\frac{1-\mathfrak{z}_e}{1-\mathfrak{z}_i} + Z_{oe} + \Delta\phi_-\right\}$$

The numerical calculations showed that the errors were small and were equal for plus or minus solutions. Hence, the asymptotic solution tells us that normalization with the compact solution will allow the two isentropic transmitted waves to be considered the same function of β .

We now consider the reflected waves for plus and minus solution. It is well known that the reflected waves will be inversely proportional to the frequency, for high frequency, but we can extract some useful information by calculating the $\mathcal{O}(\frac{1}{\beta})$ terms. Following the usual procedure to find the A and B in eq. (2.23), we get:

$$2i\beta R_{P\infty} =$$

$$\frac{(1+M_1)^2}{2M_1}\left(1-\frac{\gamma-1}{2}M_1^2\right)\left\{e^{-2\left[Z_{1e}-i\beta Z_{oe}\right]}\left(\frac{1+M_2}{1+M_1}\right)^2\frac{M_1}{M_2}\,\frac{1-\frac{\gamma-1}{2}M_2^2}{1-\frac{\gamma-1}{2}M_1^2}-1\right\}+\mathcal{O}\left(\frac{1}{\beta}\right) \qquad (2.38)$$

$$2i\beta R_{m\infty} = \frac{(1-M_1)^2}{2M_1}\left(1-\frac{\gamma-1}{2}M_1^2\right)e^{-2Z_{1e}}e^{i\beta[\Delta\phi_- - \Delta\phi_+]}$$

$$\left\{\frac{(1-M_2)^2}{(1-M_1)^2}\frac{M_1}{M_2}\frac{1-\frac{\gamma-1}{2}M_2^2}{1-\frac{\gamma-1}{2}M_1^2}e^{2Z_{1e}} - e^{2i\beta Z_{oe}}\right\} + \mathcal{O}\left(\frac{1}{\beta}\right) \qquad (2.39)$$

It is instructive to imagine the functions in braces plotted in the phase plane as $\beta \to \infty$. We see that if the terms inside the braces in eq. (2.38) or (2.39) are the same order of magnitude, the high-frequency solutions will be very sensitive to M_1 , M_2 , and normalization will not be possible. However, under the conditions

$$M_1 \to 0 \qquad M_2 \to 1$$

the first terms inside the braces in (2.38) and (2.39) are negligible. In this case,

$$|R_{p\infty}| = \frac{1}{2\beta}\frac{(1+M_1)^2}{2M_1}\left(1-\frac{\gamma-1}{2}M_1^2\right) \qquad (2.40)$$

$$\text{Arg}\, R_{p\infty} = \frac{\pi}{2}$$

$$|R_{m\infty}| = \frac{1}{2\beta}\frac{1-M_1^2}{2M_1}\frac{1-M_2}{1+M_2}\left(1-\frac{\gamma-1}{2}M_1^2\right) \qquad (2.41)$$

$$\text{Arg}\, R_{m\infty} = \frac{\pi}{2} + \beta\left[\Delta\phi_- - \Delta\phi_+ + 2Z_{oe}\right]$$

Using (2.32) and (2.33) with the above restrictions on the Mach number we can show

$$\left|\frac{R_{m\infty}}{R_{mo}}\right| = \left|\frac{R_{p\infty}}{R_{po}}\right|$$

Then we might expect that normalization of the magnitude of the reflected waves by the compact solution would be advantageous just as in the case of the transmitted waves. Numerical calculations verified that the reflected waves, when normalized by the compact solution, respond to frequency in the same manner whether created by P_{1+} disturbance or P_{2-} disturbance. This was true even when the restrictions on the Mach number were not strictly met.

Using the results for the phase of the reflected waves, we plot $\text{Arg } R_p$ directly, and we normalize $\text{Arg } R_m$ by plotting

$$\text{Arg } R_m - \beta\left[\Delta\phi_- - \Delta\phi_+ + 2Z_{oe}\right]$$

We expect both of the functions to tend toward $\pi/2$ for high frequency.

Finally, we consider the entropy solution. Using the inhomogeneous solution (2.19), we saw that it included some extraneous pressure waves, eq. (2.20). We may now use (2.36), (2.37) to remove these solutions and produce the independent entropy solution for high frequency to $\mathcal{O}\left(\frac{1}{\beta}\right)$. The results are

$$2i\beta T_{e\infty} = e^{-i\beta\Delta\phi_+}\left\{M_2^2 \exp\left[\frac{i\beta}{2}\ln\frac{\mathfrak{Z}e}{\mathfrak{Z}i}\right]\right.$$
$$\left. -M_1^2 \exp\left[i\beta\left(\frac{1}{\gamma+1}\ln\frac{1-\mathfrak{Z}e}{1-\mathfrak{Z}i} + Z_{oe}\right) - \frac{1}{2}\ln\left(\frac{M_1}{M_2}\frac{1-\mathfrak{Z}e}{1-\mathfrak{Z}i}\right) - Z_{1e}\right]\right\} + \mathcal{O}\left(\frac{1}{\beta}\right) \qquad (2.42)$$

and

$$2i\beta R_{e\infty} =$$
$$M_1^2 - M_2^2 \exp\left[\frac{i\beta}{2}\ln\frac{\mathfrak{Z}e}{\mathfrak{Z}i}\right]\exp\left[i\beta\left(\frac{-1}{\gamma+1}\ln\frac{1-\mathfrak{Z}e}{1-\mathfrak{Z}i} + Z_{oe}\right) + \frac{1}{2}\ln\left(\frac{M_1}{M_2}\frac{1-\mathfrak{Z}e}{1-\mathfrak{Z}i}\right) - Z_{1e}\right] \qquad (2.43)$$
$$+\mathcal{O}\left(\frac{1}{\beta}\right)$$

If we use the same assumptions on M_1 , M_2 as we used when discussing the isentropic reflected waves, it is possible to show that

$$T_{e\infty} = \frac{1}{2i\beta}\, e^{-i\beta\Delta\phi_+} M_2^2 \exp\left(\frac{i\beta}{2} \ln \frac{\beta_e}{\beta_i}\right) \tag{2.44}$$

Note that this solution is not related to the compact solution, T_{eo} .

Since this solution tends to zero for high frequency, we will normalize the magnitude of T_e by its compact solution. In addition, we might expect

$$-\left(\text{Arg } T_e + \beta\Delta\phi_+ - \frac{\beta}{2} \ln \frac{\beta_e}{\beta_i}\right) \to \frac{\pi}{2}$$

We will plot this function as the normalized phase. For the same restrictions on M_1 and M_2 it is possible to show that the two terms in (2.43) are of comparable magnitude. Hence, $R_{e\infty}$ will be very sensitive to M_1 and M_2 and normalization of the phase will not be possible. To be consistent, we will normalize the magnitude of by the compact value, R_{eo} .

2.5 Numerical Results

The numerical calculations were normalized using the previously discussed methods. These are presented in Figures 2-3 through 2-9. The inlet Mach numbers 0.2, 0.3, and 0.4 with exit Mach number 0.9 were chosen to represent the flow in an exhaust nozzle. The inlet Mach numbers 0.5 and 0.6 with exit Mach number 0.9 were chosen to represent the flow through turbine blades. The remaining case M_1 = 0.3, and M_2 = 0.4, was chosen to show the effect of large M_1 and small M_2 on the normalization. In all the plots, it is clear that this last case does not normalize with the

other cases.

The magnitude of the transmitted wave (plus and minus solution) is plotted in Figure 2-3. These functions do not tend to zero for high frequency. The asymptotic values, which may be taken from Figures 2-1 and 2-2, are also used in the normalization. We have plotted

$$\frac{|T/T_o| - 1}{|T_\infty/T_o| - 1}$$

where we recall that T_o is the compact solution and T_∞ is the high-frequency solution. Normalizing in this manner, however, causes the differences (for a given frequency) in results for each Mach number to be greatly exaggerated. We could use one curve to represent these results with very good accuracy. The insensitivity to Mach numbers is to be expected, since the asymptotic solution is so closely related to the compact solution, and since both values were used to normalize the numerical results. From the plot we see that for reduced frequencies above 5, the results are within 10 per cent of the high-frequency limit. For reduced frequencies below one, the results are within 10 per cent of the compact solution.

In Figure 2-4 we have the phase of the transmitted wave (plus and minus solution). Recall that this value was closely related to the high-frequency solution. We have plotted

$$-\text{Arg}\, T_m + \beta\left\{\frac{1}{\gamma+1}\ln\frac{1-\beta_e}{1-\beta_i} + Z_{oe} - \Delta\phi_+\right\} = -\text{Arg}\, T_m + \beta\left[\frac{\text{Arg}\, T_m}{\beta}\bigg|_{\beta\to\infty}\right]$$

and

$$-\text{Arg}\, T_p + \beta\left\{\frac{-1}{\gamma+1}\ln\frac{1-\beta_e}{1-\beta_i} + Z_{oe} + \Delta\phi_-\right\} = -\text{Arg}\, T_p + \beta\left[\frac{\text{Arg}\, T_p}{\beta}\bigg|_{\beta\to\infty}\right]$$

We may use Figures 2-1, 2-2, and 2-4 to calculate $Arg\ T$. Doing so, we see that the corrections given by Figure 2-4 are small compared to the actual values, $Arg\ T$, and could be neglected. To good accuracy, then, we could simply use the high-frequency solution for all values of reduced frequency. By definition, the asymptotic solution must predict that the phase will be proportional to the frequency. This graph tell us that the constant of proportionality

$$\left.\frac{Arg\ T}{\beta}\right|_{\beta\to\infty}$$

holds quite accurately for all frequencies. The constant of proportionality may be taken from Figures 2-1 and 2-2.

In Figure 2-5 we have the magnitude of the reflected waves (plus and minus solution) plotted. We see that the normalization is somewhat less satisfactory. Recall that we restricted the exit Mach number to a value close to unity and the entrance Mach number to small values. This graph verifies that as the inlet Mach number increases, the normalization becomes less effective. We could, with reasonably good accuracy, represent these data with one curve.

The phase of the reflected wave, plus solution, is plotted directly in Figure 2-6. The phase of the reflected waves, minus solution, was normalized. We have plotted

$$Arg\ R_p$$

and

$$Arg\ R_m - \beta\left[2\bar{z}_{oe} + \Delta\phi_- - \Delta\phi_+\right]$$

Both of these functions tend to 90°, as expected, and the same difficulties occur for large entrance Mach numbers as occurred in the

magnitude (Figure 2-5). We could represent these data with one curve for the plus solution and one curve for the minus solution quite accurately. Considering Figures 2-5 and 2-6, we essentially have the compact solutions for reduced frequency below 1/2, and the high-frequency solution for reduced frequency above 10. The normalization factor used when plotting $\text{Arg } R$ may easily be calculated using eq. (2.36) and Figure 2-2.

In Figures 2-7 and 2-8 we have the magnitude and phase, respectively, of the transmitted wave, entropy solution. The normalization is clearly unsatisfactory, as could be expected from eq. (2.44). The high-frequency solution is not related to the compact solution, even with the restrictions we made on M_1 and M_2. It is clear, however, that the compact solution may be used quite satisfactorily for reduced frequencies below one.

The magnitude of the reflected wave, entropy solution, is plotted in Figure 2-9. The normalization is equally ineffective in this case. The high-frequency value (zero) is effectively attained for reduced frequency greater than 10.

The results given in Figures 2-3 through 2-9 were intended primarily to represent inlet and exit Mach numbers characteristic of turbine blade rows and exhaust nozzles. For other applications the exit Mach number might be lower. Calculations were performed for exit Mach numbers 0.8 and 0.7 also. The normalization described previously was used on these results and are given in Figures 2-10 through 2-23.

Comparing Figures 2-3, 2-10, and 2-17 for the magnitude of the isentropic transmitted waves, we see that the normalization becomes less effective as the exit Mach number becomes small. From Figures 2-4, 2-11, and 2-19 it seems that the phase of the isentropic transmitted wave is more accurately represented by the high-frequency solution as the nozzle exit Mach number decreases. However, from Figures 2-1, 2-2 we see that the actual phase also decreases.

The normalization for the magnitude of the isentropic reflected waves becomes less effective as exit Mach number decreases (see Figures 2-5, 2-14, and 2-19). The same is seen to be true for the phase of these waves by comparing Figures 2-6, 2-15, and 2-20.

It is reasonable to expect that for exit Mach numbers approaching unity the normalization will improve (although for values very close to unity special care will be needed in the numerical integration). In conclusion then, it seems that while the normalization scheme is limited, it appears to be quite useful for practical Mach number nozzles.

2.6 Examples of the One-Dimensional Model

Example 1. We would like to use these solutions to solve a practical problem and to see how the graphs are implemented. Suppose we are given a nozzle which accelerates a flow from M_1 to M_2 in a length X_1. The flow continues through a constant-area duct and after a length $X_e - X_1$ is terminated with a known impedance ζ_e. The impedance is defined as

$$\zeta \equiv \frac{p'}{u'} \frac{a}{\gamma \bar{p}}$$

Given that a P_1^+ disturbance exists, and also that an entropy wave $\sigma = s'/c_p$ is convected into the nozzle, we would like to be able to calculate the resulting waves in the downstream duct (see accompanying diagram).

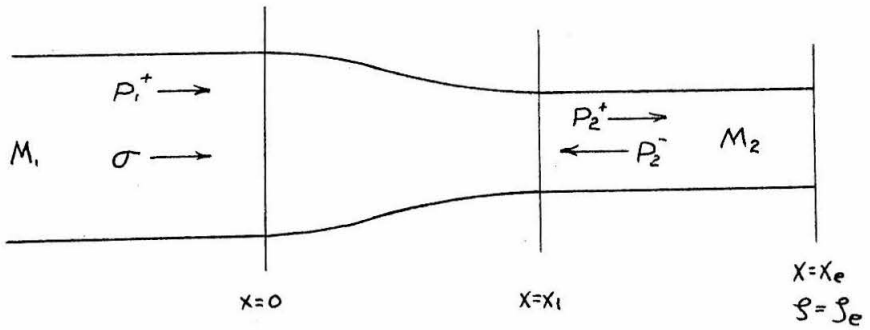

Consistent with our analysis, we use the length scale $x_1 a^*/(\bar{u}_2 - \bar{u}_1) \equiv \ell$ to make the problem dimensionless. We may write

$$Z_2(\xi) = P_2^+ e^{iC_{2+}\xi} + P_2^- e^{iC_{2-}\xi}$$
$$MZ_1(\xi) = P_2^+ e^{iC_{2+}\xi} - P_2^- e^{iC_{2-}\xi} \qquad \xi > \xi_1$$

where

$$\xi \equiv \frac{x}{\ell} \qquad \xi_1 \equiv \frac{x_1}{\ell} \qquad \xi_e \equiv \frac{x_e}{\ell}$$

The impedance may be written as

$$\zeta_e = \frac{Z_2(\xi_e)}{M_2 Z_1(\xi_e)}$$

and from eq. (2.16)

$$P_2^+ = P_1^+ T_p + P_2^- R_m + \sigma T_e$$

By using ζ_e, we may eliminate P_2^-:

$$P_2^- = P_2^+ \frac{\zeta_e - 1}{\zeta_e + 1} e^{i\xi_e (C_{2+} - C_{2-})}$$

and solve for P_2^+ explicitly

$$P_2^+ = \frac{P_1^+ T_P + \sigma T_e}{1 - R_m \frac{\gamma_e - 1}{\gamma_e + 1} e^{i \gamma_e (C_{2+} - C_{2-})}}$$

It only remains that T_P , T_e , R_m be calculated. Let

$$M_1 = 0.3 \Rightarrow \gamma_i = 0.106 \qquad M_2 = 0.9 \Rightarrow \gamma_e = 0.837$$

and suppose

$$\beta = \frac{\omega X_1}{\bar{u}_2 - \bar{u}_1} = 1.0$$

This gives

$$\Delta\phi_+ = \frac{M_2}{M_2 + 1}\left[1 - \left(\frac{\gamma_i}{\gamma_e}\right)^{1/2}\right] = 17.5^\circ$$

$$\Delta\phi_- = \frac{M_2}{M_2 - 1}\left[1 - \left(\frac{\gamma_i}{\gamma_e}\right)^{1/2}\right] = 28.0^\circ$$

The compact solutions (2.30), (2.33), (2.34) give

$$T_{po} = 1.132$$

$$R_{mo} = -0.024$$

$$T_{eo} = 0.135$$

Then Figure 2-2 gives

$$T_{p\infty} = 1.265 \qquad \left.\frac{\text{Arg } T_P}{\beta}\right|_{\beta \to \infty} + \Delta\phi_+ = 20.3^\circ$$

Figure 2-3 gives

$$\frac{\left|\frac{T}{T_o}\right| - 1}{\left|\frac{T_\infty}{T_o}\right| - 1} = 0.210 \Rightarrow |T_P| = 1.160$$

Figure 2-4 gives

$$-\text{Arg}\,T + \left(\frac{\text{Arg}\,T}{\beta}\bigg|_{\beta\to\infty}\right)\beta = 3^\circ$$

$$\therefore \qquad T_p = 1.16\,\angle 0^\circ$$

Figure 2-5

$$\left|\frac{R}{R_0}\right| = 0.90 \quad \Rightarrow \quad |R_m| = 0.021$$

Figure 2-6 gives

$$\text{Arg}\,R_m = 142^\circ + \beta\left[2\mathcal{Z}_{oe} + \Delta\phi_- - \Delta\phi_+\right]$$

To get $\mathcal{Z}_{oe}$ we need eq. (2.36) and Figure 2-2, which give

$$\frac{1}{\gamma+1}\ln\frac{1-\mathcal{J}_e}{1-\mathcal{J}_i} + \mathcal{Z}_{oe} = 20.3^\circ \quad \Rightarrow \quad \mathcal{Z}_{oe} = 60.8^\circ$$

Hence,

$$\text{Arg}\,R_m = -85.9^\circ \qquad \therefore \quad R_m = 0.021\,\angle -86.^\circ$$

Figure 2-7 gives

$$\left|\frac{T_e}{T_{eo}}\right| = 0.92 \quad \Rightarrow \quad |T_e| = .124$$

Figure 2-8 gives

$$-\text{Arg}\,T_e + \frac{\beta}{2}\ln\frac{\mathcal{J}_e}{\mathcal{J}_i} - \beta\Delta\phi_+ = 7^\circ \Rightarrow \text{Arg}\,T_e = 35^\circ$$

$$\therefore\ T_e = 0.124\,\angle 35^\circ$$

which completes the solution.

As an example, suppose the nozzle continues to infinity (i.e., the end impedance is somehow matched). Let us perturb only the entropy upstream of the nozzle. A typical static temperature fluctuation one might find downstream of a turbojet burner is

$$|T'/T| \approx .05$$

Since there is no pressure disturbance, this gives

$$|S'/C_p| = .05$$

and our analysis gives an acoustic wave propagating downstream of the contraction

$$|P'/\gamma\bar{P}| = (.05)(.124) = .0062$$

or

$$|P'| = 150\,db \text{ re } .0002\ dyne/cm^2$$

if the mean pressure in the exit section is 1 atmosphere.

Example 2.[13] As a final example we would like to discuss a rather unusual application of the quasi-steady analysis.[10] We consider the inlet of a duct with a mean flow Mach number $M < 1$. Suppose that somewhere downstream of the inlet we create an acoustic disturbance, P^-, which will propagate upstream. The wave, upon reaching the inlet, will reflect, and a wave RP^- will be created which will propagate downstream of the inlet. The quantity R is

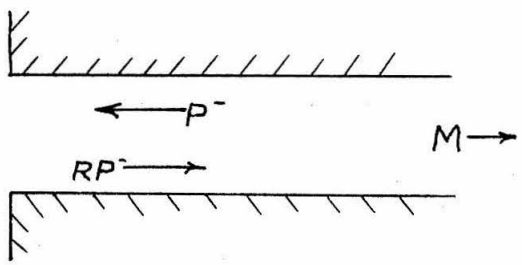

Reflection of an Acoustic Wave P^- at a Duct Inlet.

complex in general and is known as the reflection coefficient of the inlet. The problem is to determine the value of R given the duct

Mach number M , i.e., $R(M)$.

We model the inlet of the duct as a region of zero axial length over which the mean flow is accelerated from rest ($M=0$) to the duct Mach number M . A disturbance of finite wave length will appear as quasi-steady, and hence this region appears as a compact nozzle with inlet Mach number zero and exit Mach number M . For a disturbance downstream of this "nozzle" equation (2.33) reduces to

$$R_{mo} = \frac{M-1}{M+1}$$

where the inlet reflection coefficient $R \equiv R_{mo}$. Hence,

$$R(M) = \frac{M-1}{M+1} \tag{2.46}$$

Some recent measurements by Ingard and Singhal[1] of this reflection coefficient $R(M)$ were seen to be accurately represented by

$$|R| = .95\left(\frac{1-M}{1+M}\right)^{1.33} \tag{2.47}$$

These experiments were performed in a duct 3/4" × 3/4" in cross section for disturbances of frequency $\approx$ 1 kHz and Mach number from zero to 0.4. The following graph shows the magnitude of R from eq. (2.46) (dashed line) and that from eq. (2.47) (solid line).

The similarity is obvious, but the experimental results (solid line) are consistently low. This discrepancy is discussed in ref. 13 in terms of three-dimensional losses at the inlet (which our simple model cannot consider) and in terms of some possible problems with the methods used to measure the values of R (and M) leading to (2.47). It seems clear, however, that the reflection coefficient R is most strongly influenced by the acceleration of mean flow from ambi-

ent conditions to the duct Mach number M in the inlet region.

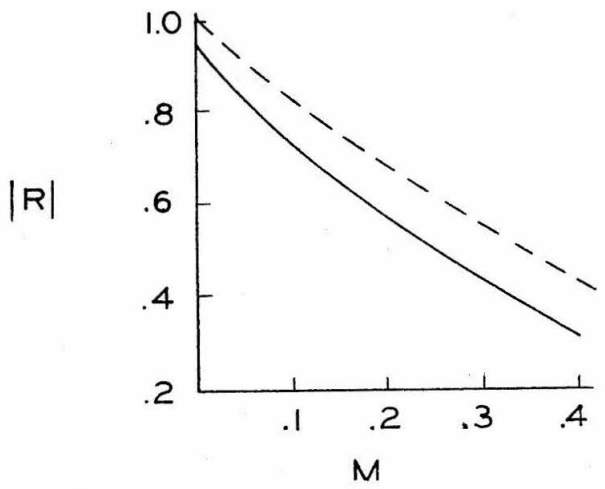

Acoustic Reflection Coefficient at a Duct Inlet Versus Duct Mach Number. Solid Line Represents Eq. (2.47). Dashed Line Represents Magnitude of Eq. (2.46).

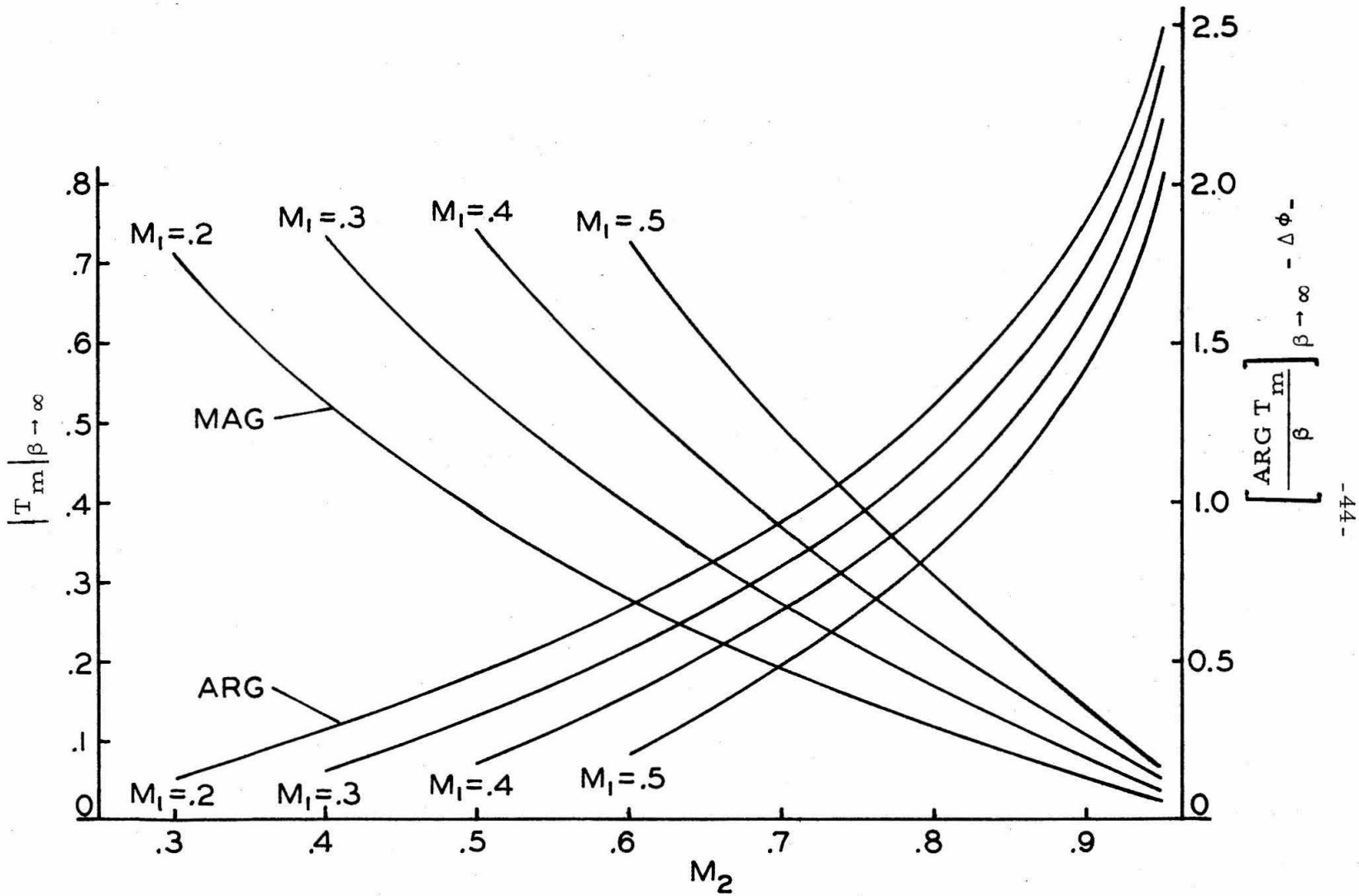

Fig. 2-1 Transmitted Wave (Minus Solution) for High Frequency vs. Inlet and Exit Mach Number

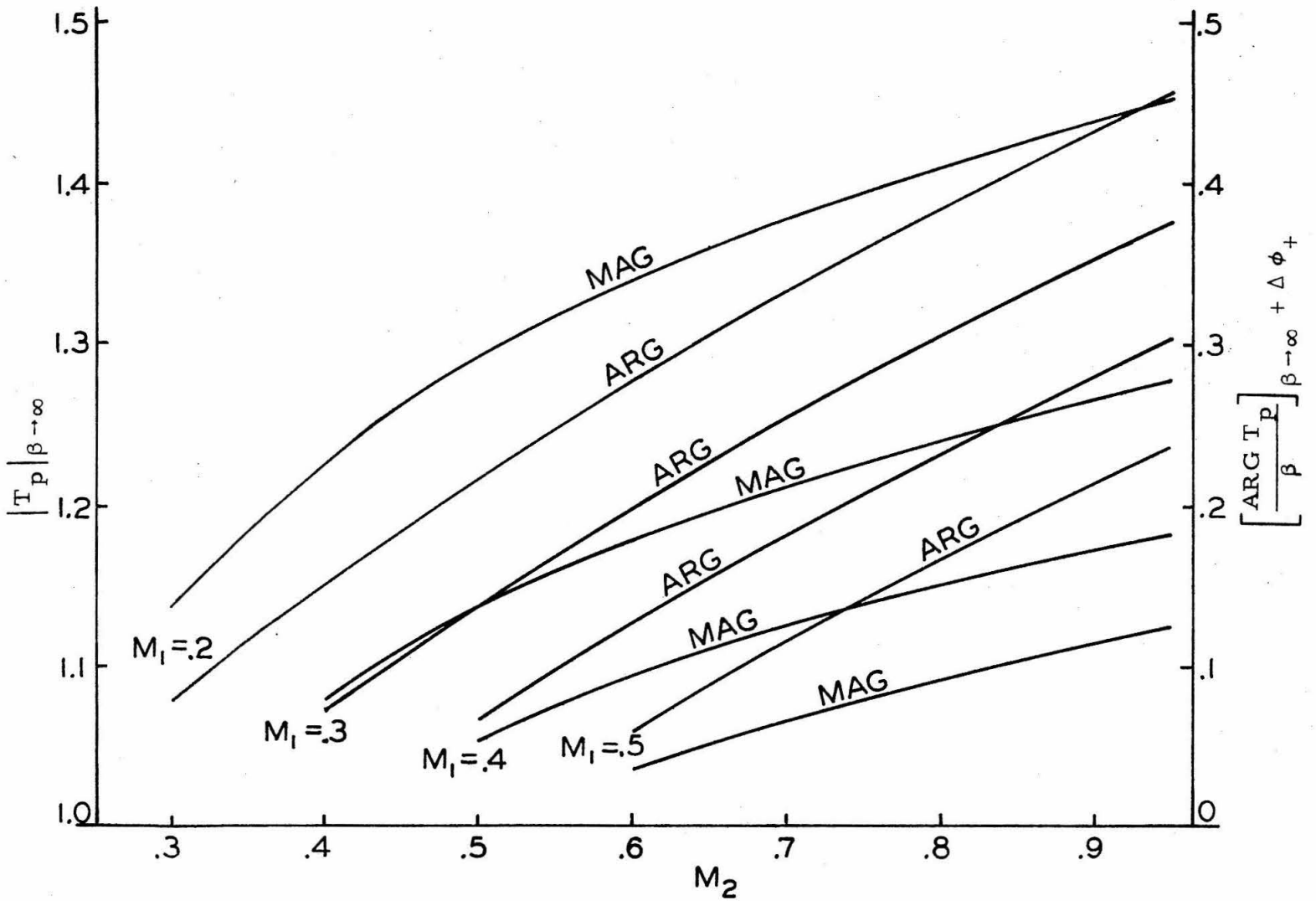

Fig. 2-2 Transmitted Wave (Plus Solution) for High Frequency vs. Inlet and Exit Mach Number

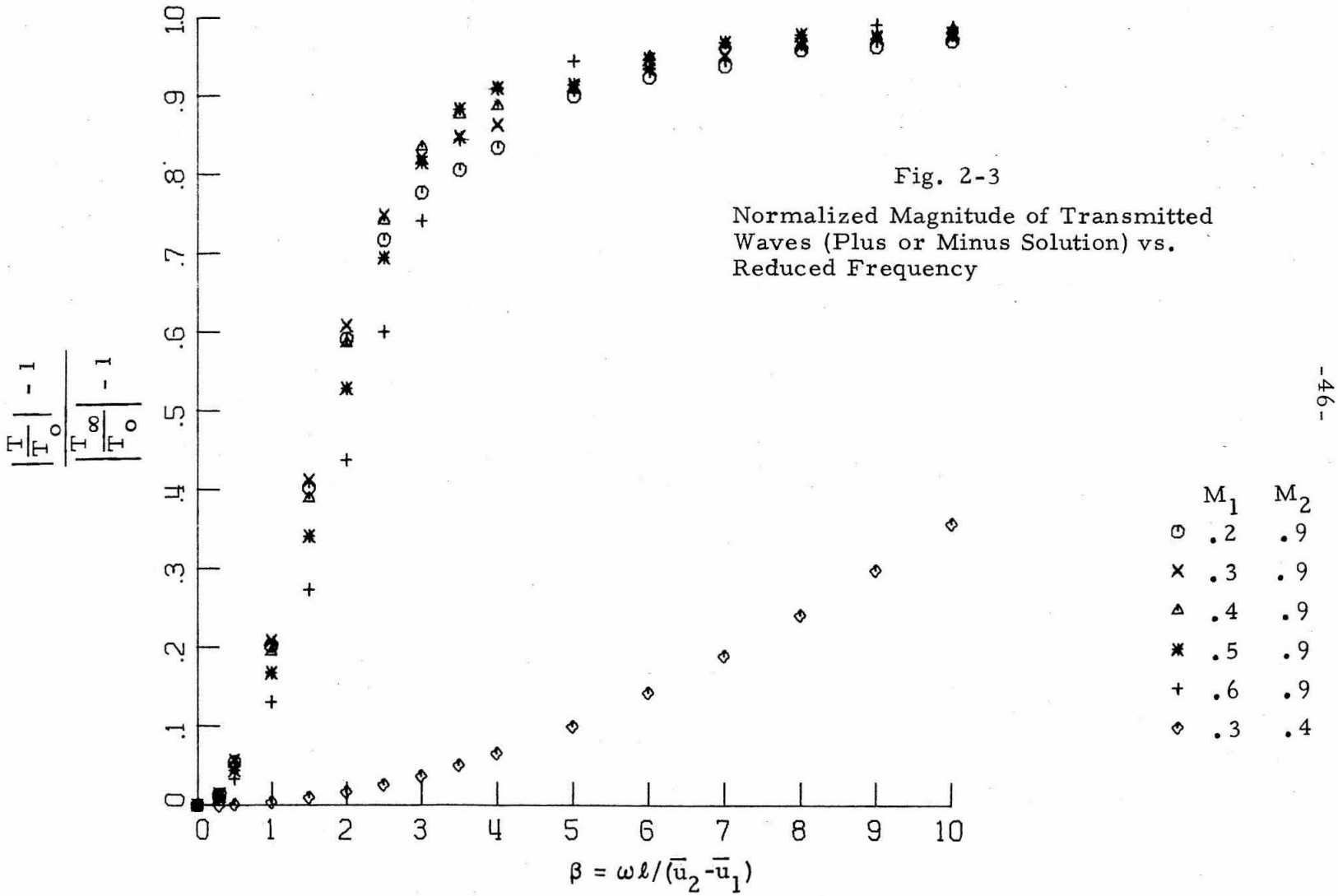

Fig. 2-3

Normalized Magnitude of Transmitted Waves (Plus or Minus Solution) vs. Reduced Frequency

Fig. 2-4

Error in Using High Frequency Solution for Phase of Transmitted Waves (Plus or Minus Solution) vs. Reduced Frequency

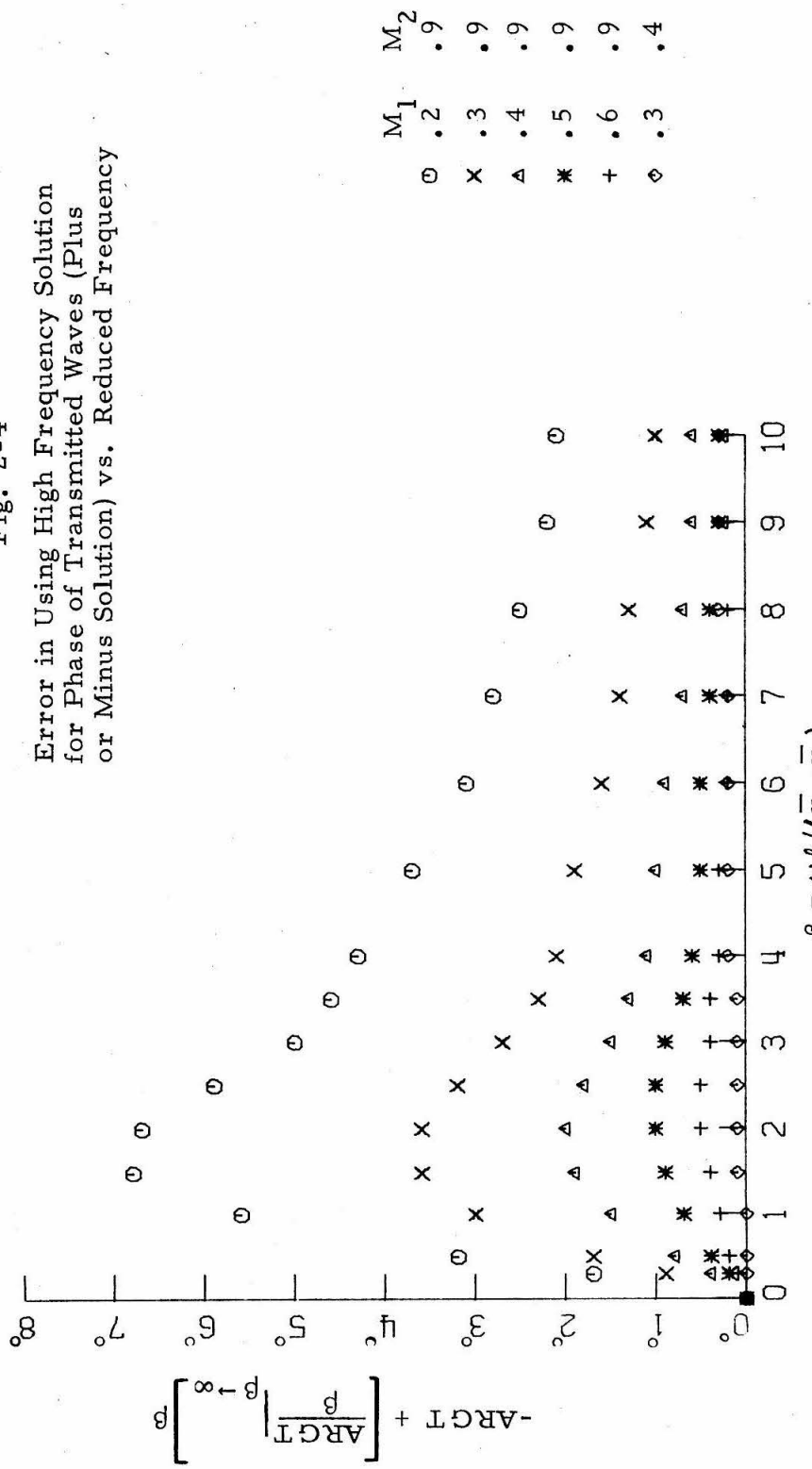

Fig. 2-5

Normalized Magnitude of Reflected Waves (Plus or Minus Solution) vs. Reduced Frequency

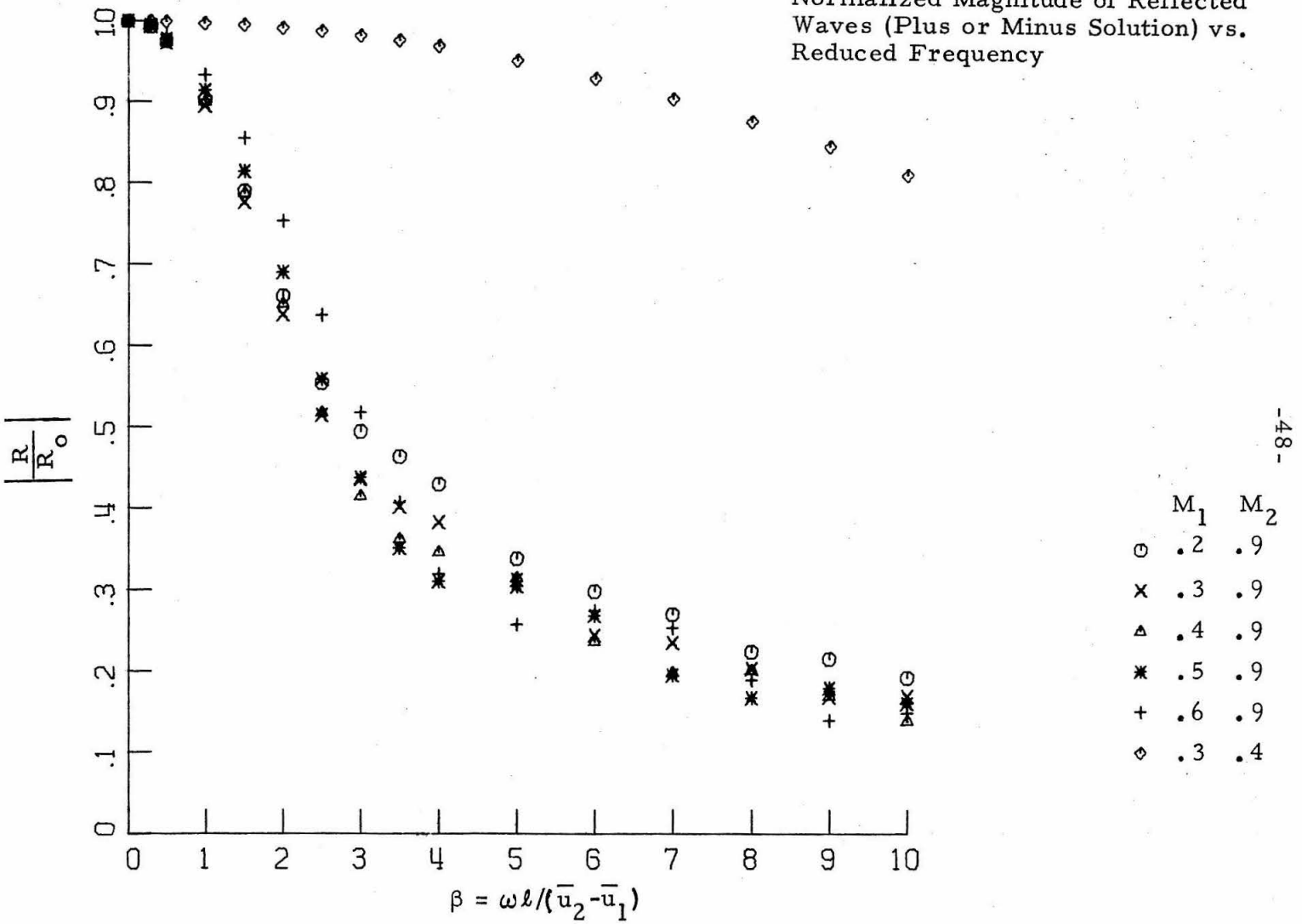

Fig. 2-6

Phase of Reflected Waves (Plus or Minus Solution) vs. Reduced Frequency

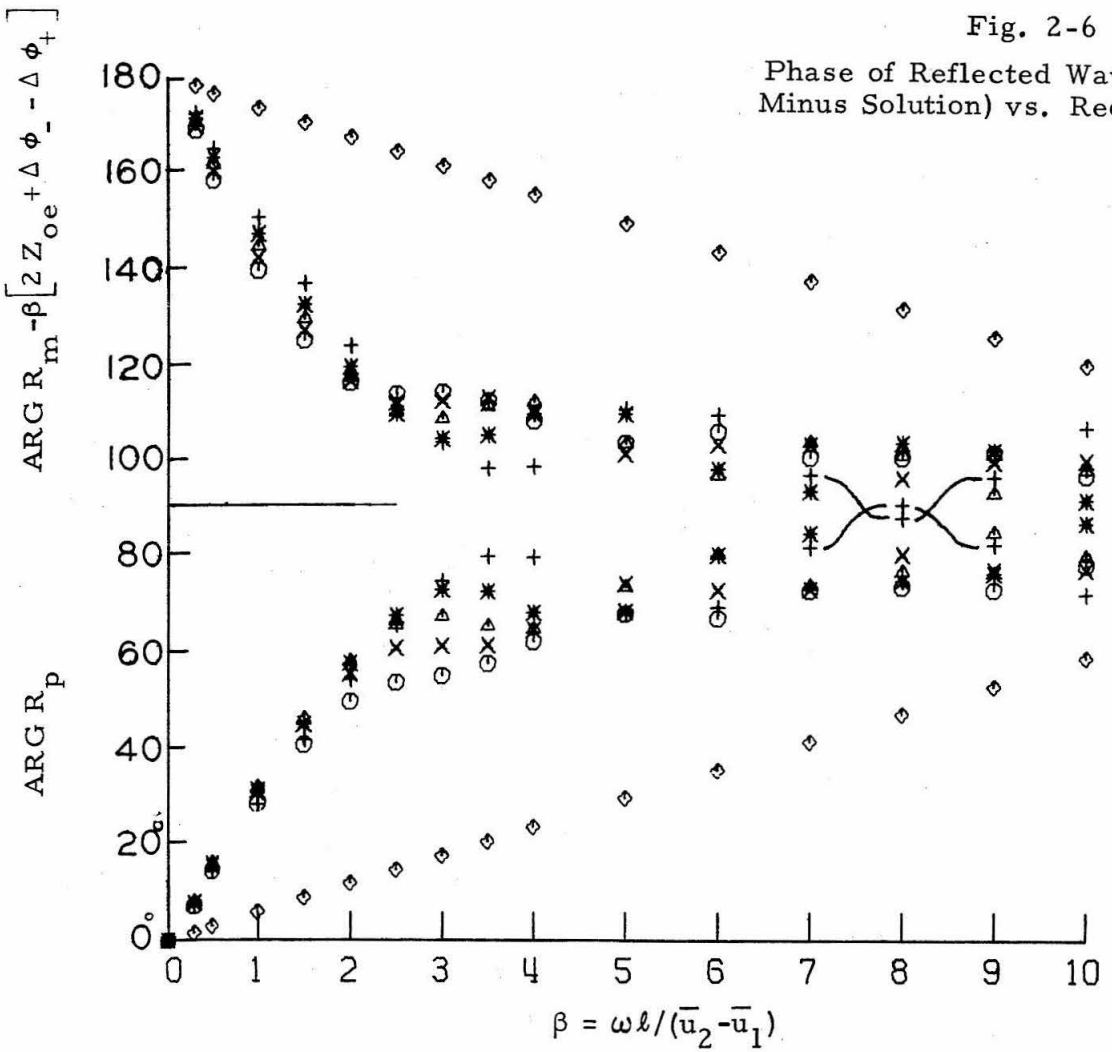

	M_1	M_2
⊙	.2	.9
×	.3	.9
△	.4	.9
✱	.5	.9
+	.6	.9
◇	.3	.4

Fig. 2-7

Normalized Magnitude of Transmitted Wave (Entropy Solution) vs. Reduced Frequency

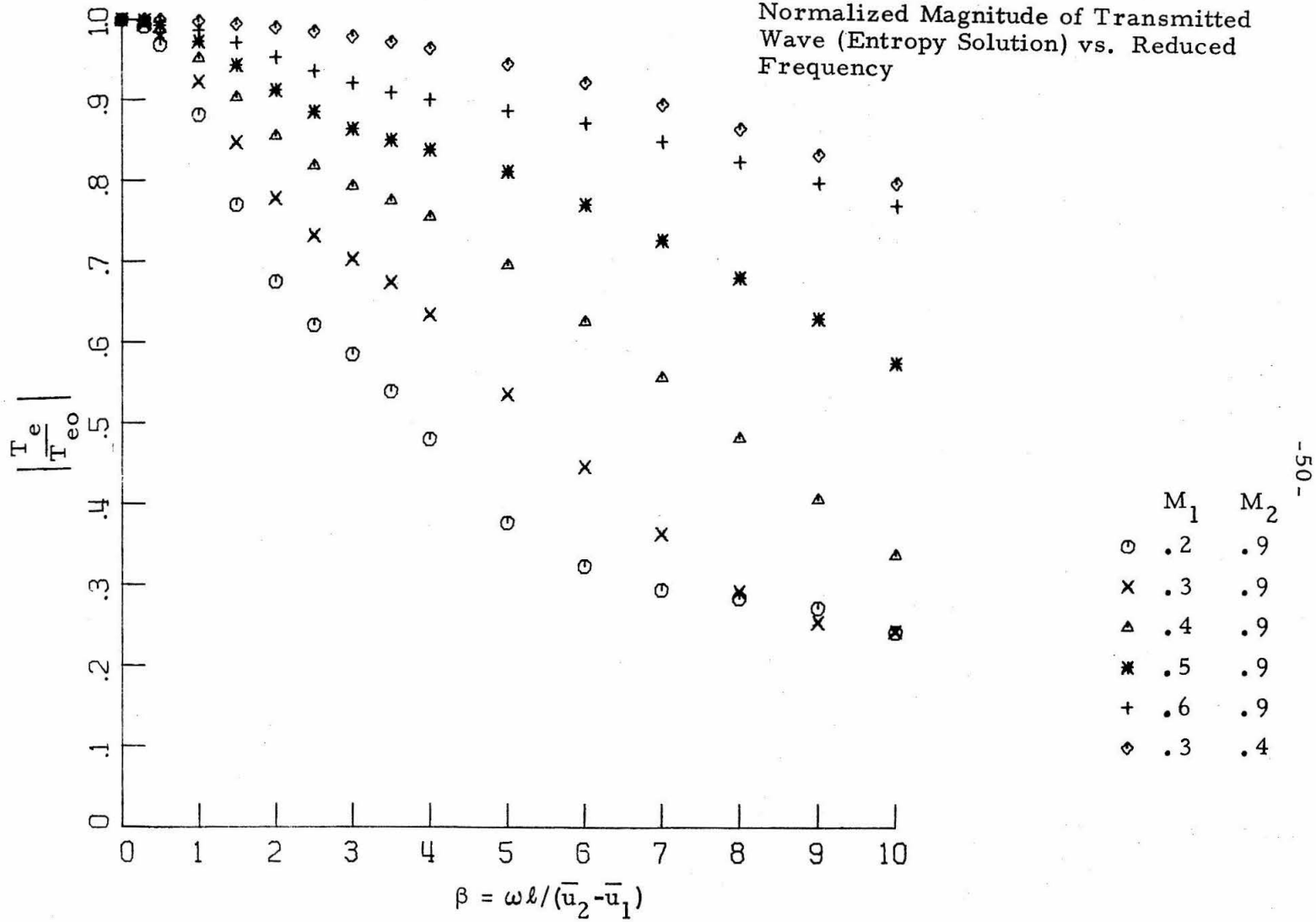

Fig. 2-8

Phase of Transmitted Wave (Entropy Solution) vs. Reduced Frequency

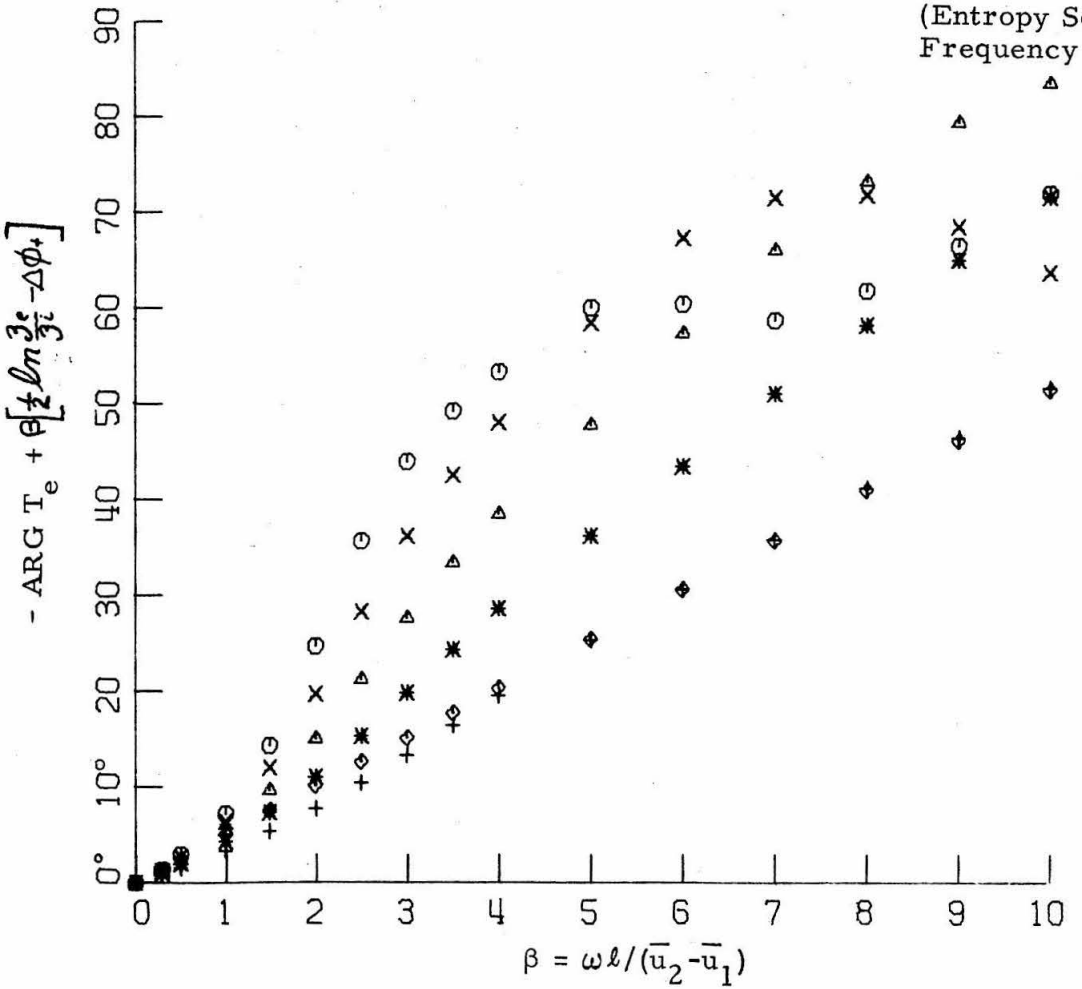

	M_1	M_2
⊙	.2	.9
×	.3	.9
△	.4	.9
✱	.5	.9
+	.6	.9
◇	.3	.4

Fig. 2-9
Normalized Magnitude of Reflected Waves
(Entropy Solution) vs. Reduced Frequency

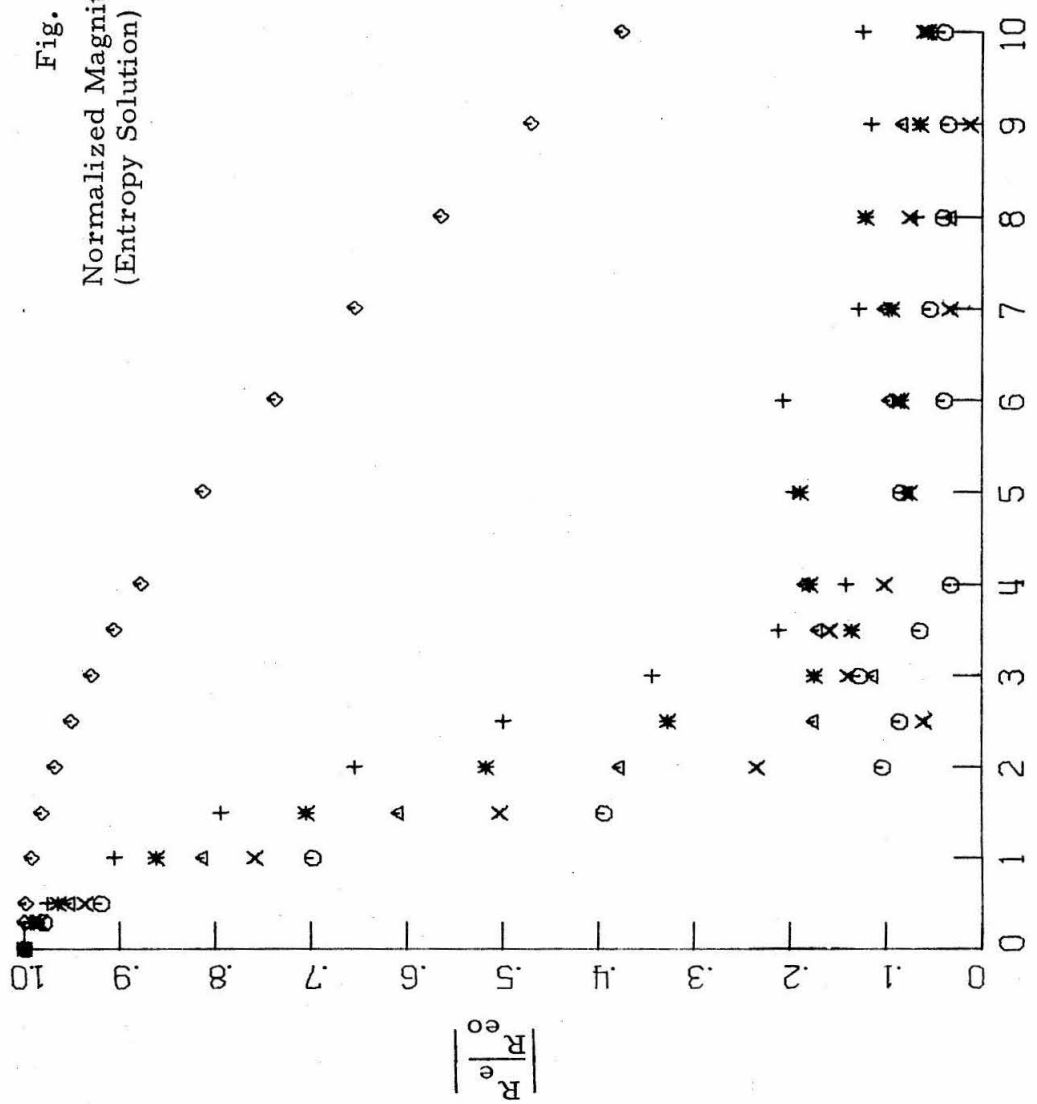

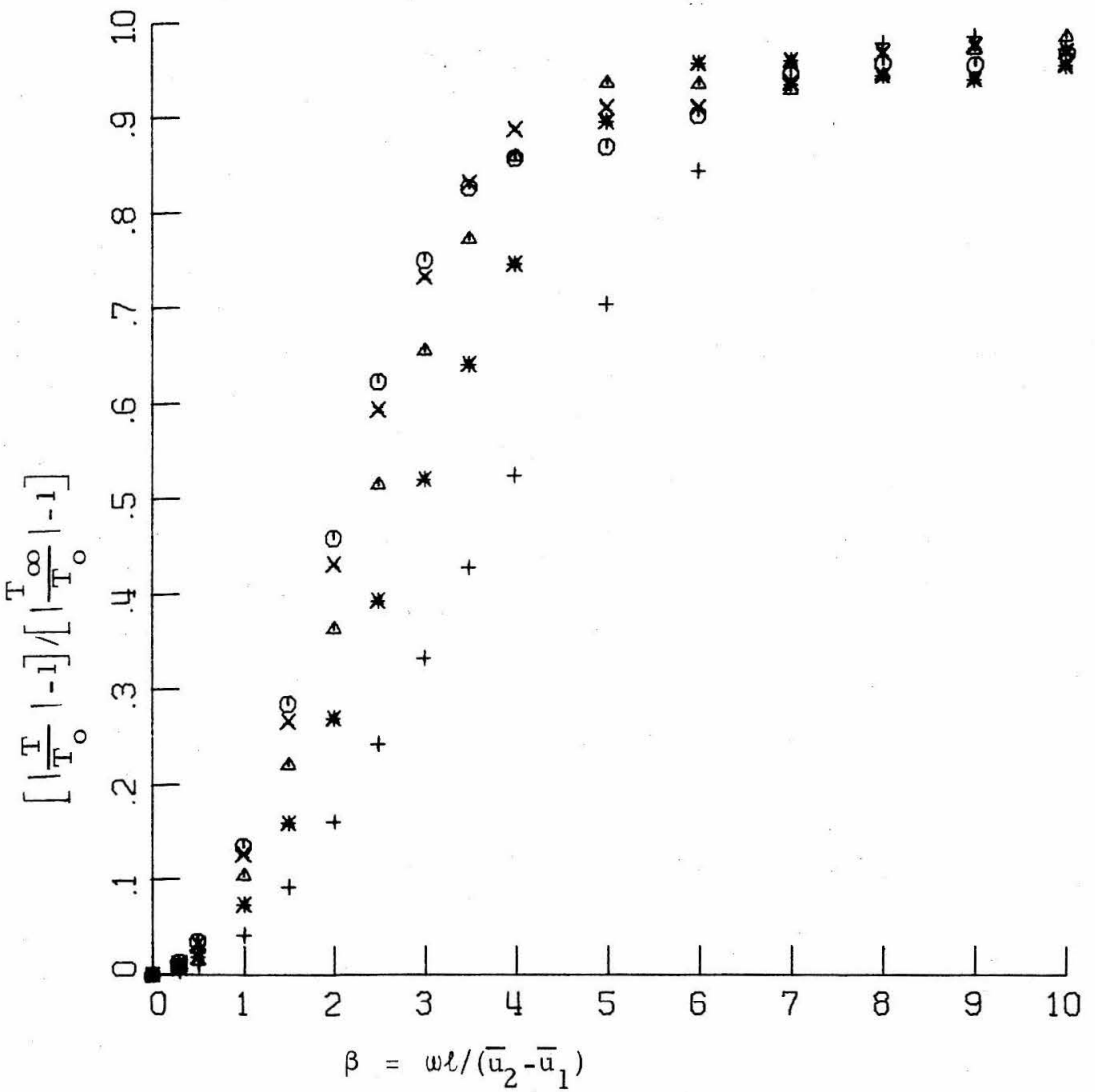

Fig. 2-10

Normalized Magnitude of Transmitted Waves (Plus or Minus Solution) Versus Reduced Frequency

M_1	M_2
⊙ .2	.8
× .3	.8
△ .4	.8
✱ .5	.8
+ .6	.8

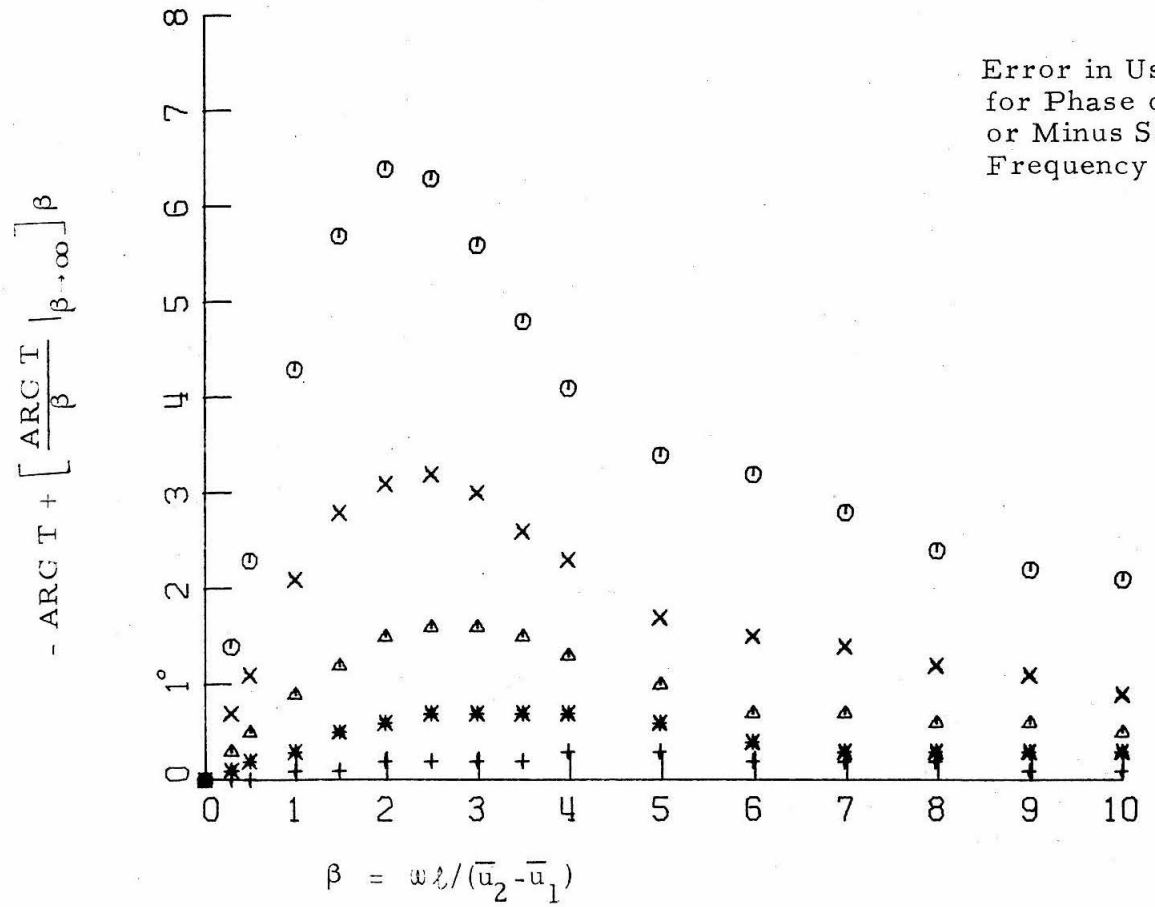

Fig. 2-11

Error in Using High Frequency Solution for Phase of Transmitted Waves (Plus or Minus Solution) Versus Reduced Frequency

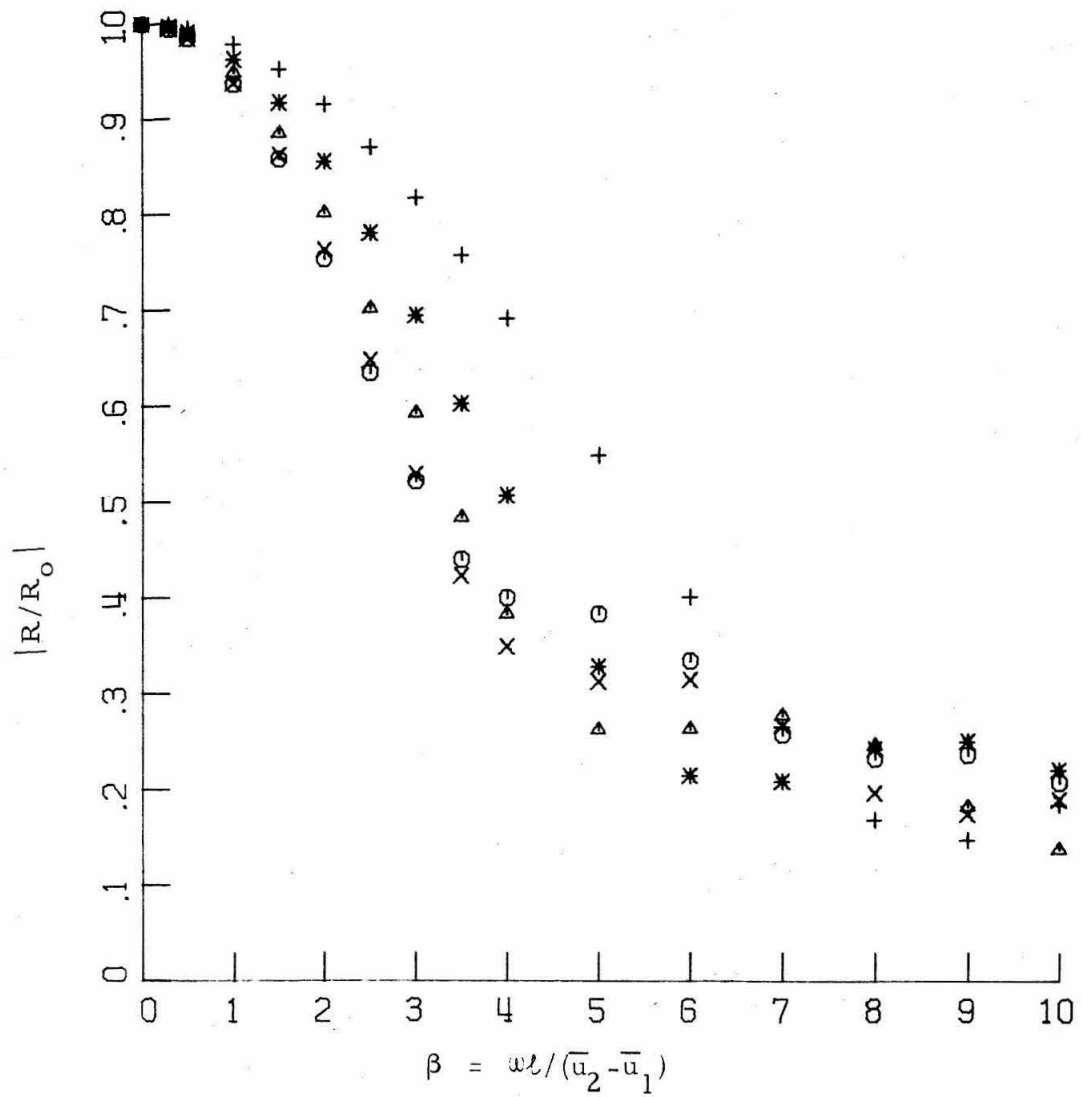

Fig. 2-12

Normalized Magnitude of Reflected Waves (Plus or Minus Solution) Versus Reduced Frequency

	M_1	M_2
⊙	.2	.8
×	.3	.8
△	.4	.8
✱	.5	.8
+	.6	.8

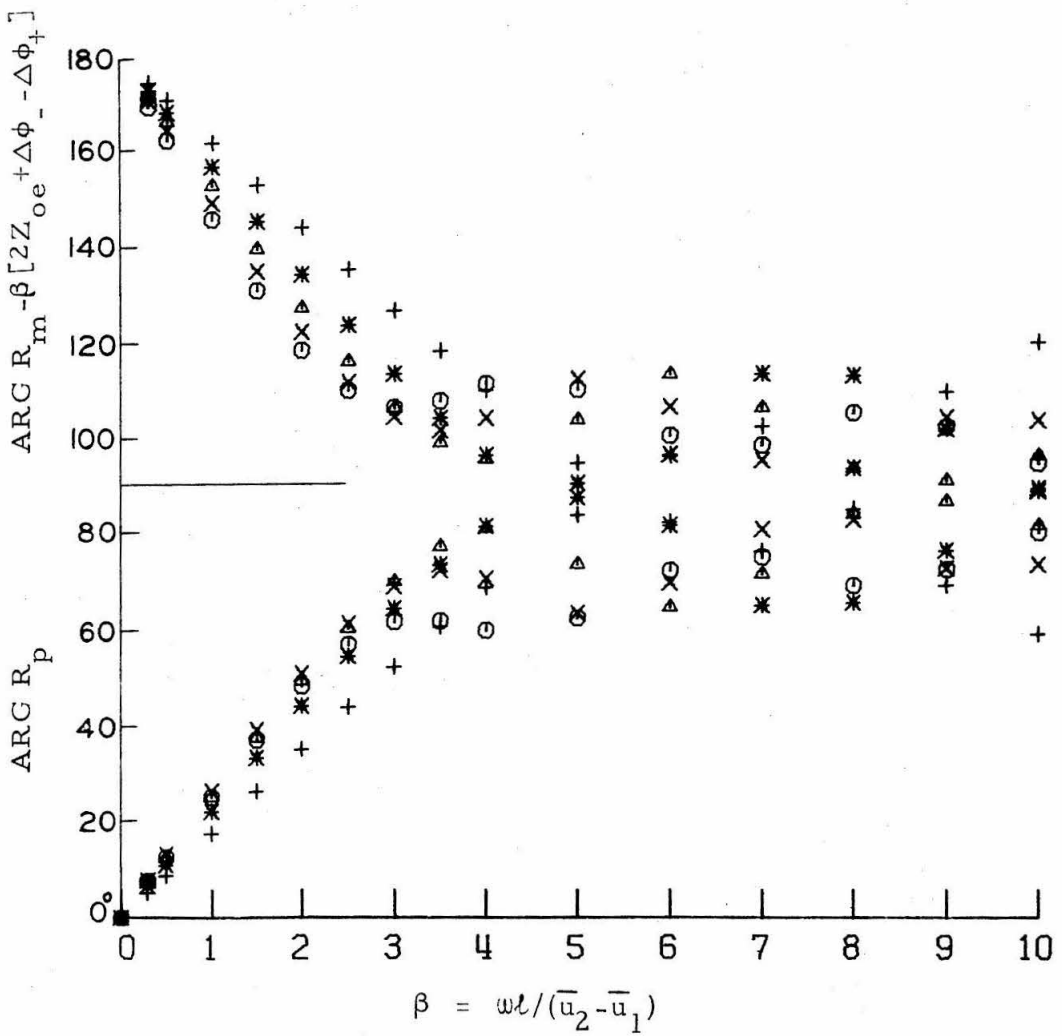

Fig. 2-13
Phase of Reflected Waves
(Plus or Minus Solution)
Versus Reduced Frequency

	M_1	M_2
⊙	.2	.8
×	.3	.8
△	.4	.8
✱	.5	.8
+	.6	.8

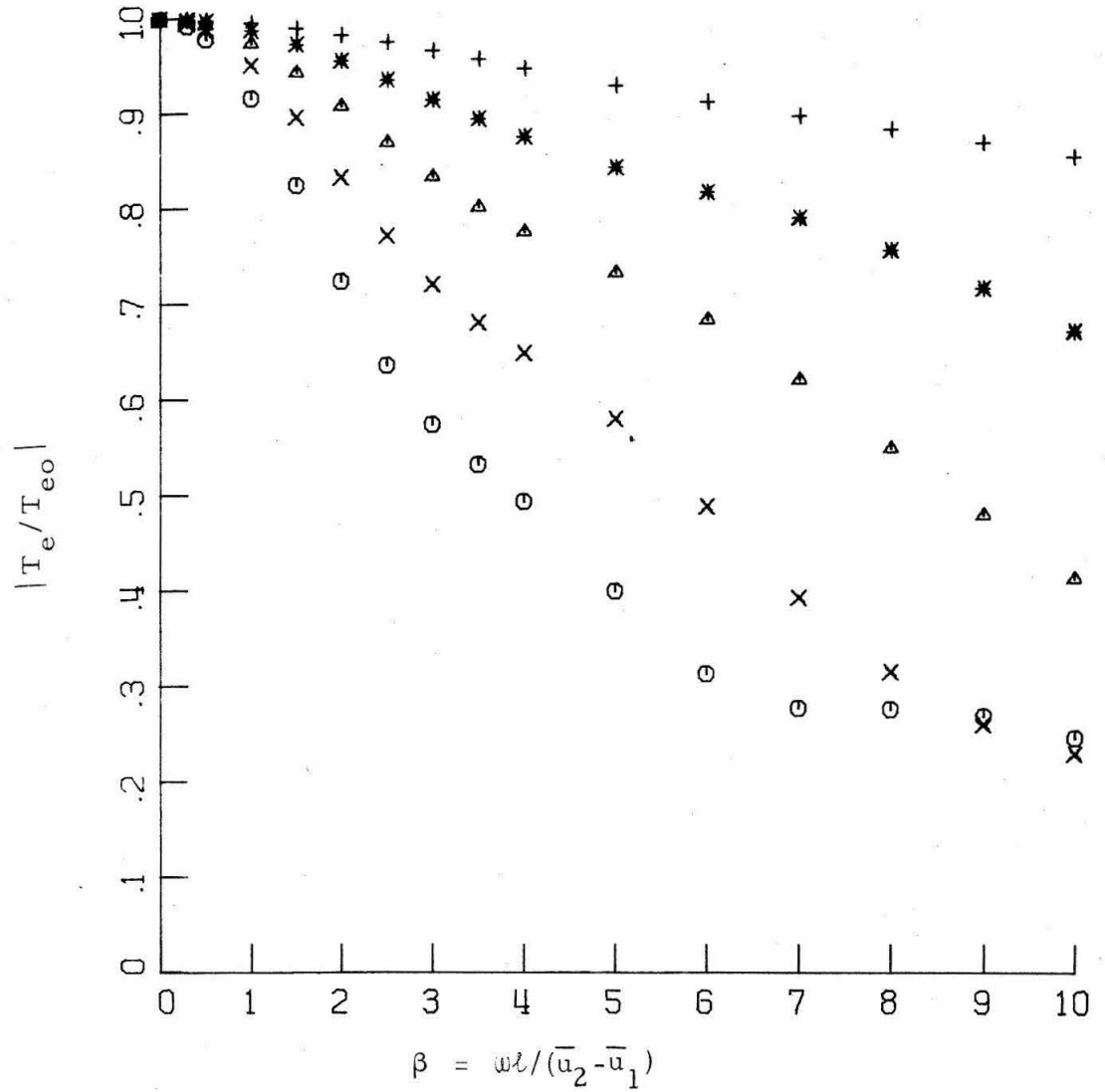

Fig. 2-14

Normalized Magnitude of Transmitted Wave (Entropy Solution) Versus Reduced Frequency

	M_1	M_2
⊖	.2	.8
×	.3	.8
△	.4	.8
✱	.5	.8
+	.6	.8

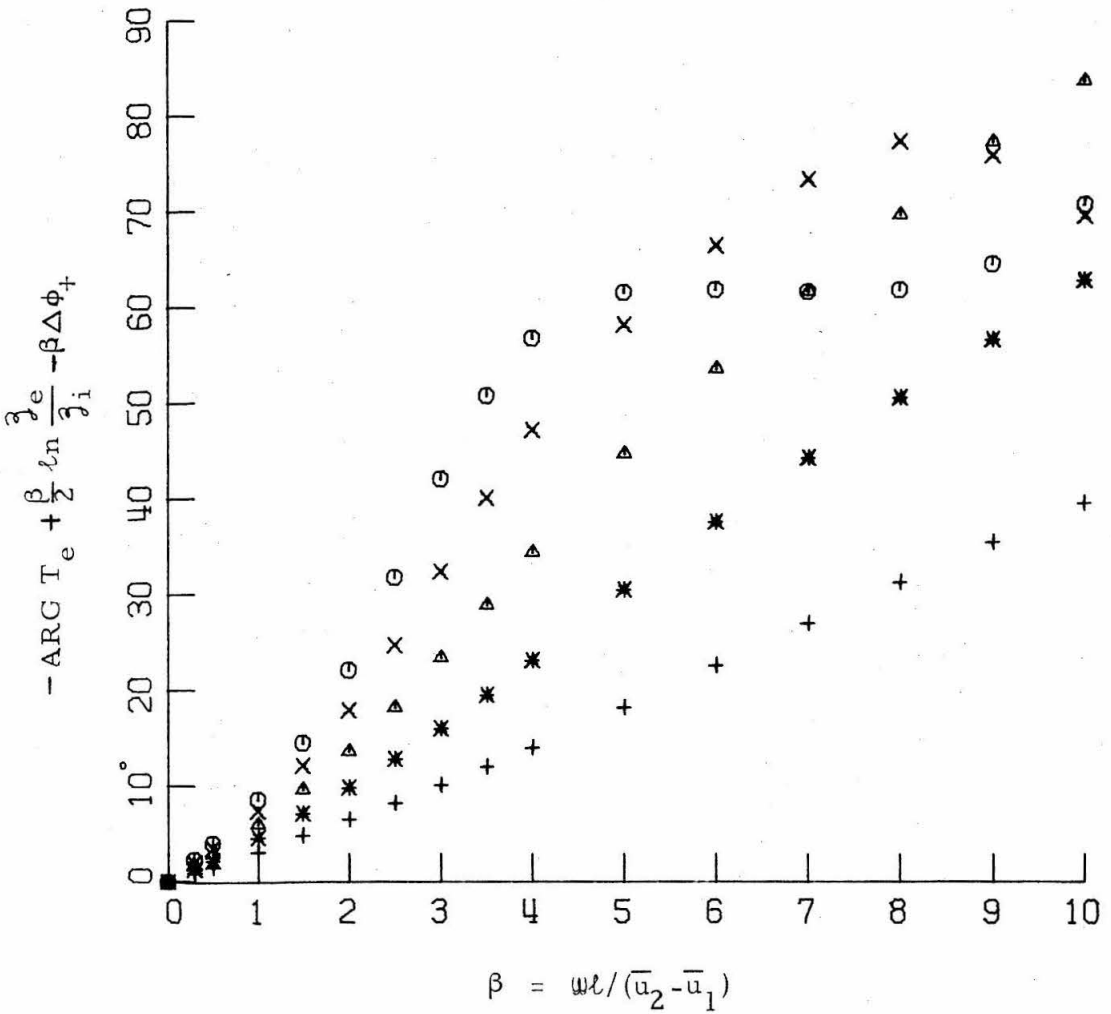

Fig. 2-15

Phase of Transmitted Wave (Entropy Solution) Versus Reduced Frequency

	M_1	M_2
⊙	.2	.8
×	.3	.8
△	.4	.8
✱	.5	.8
+	.6	.8

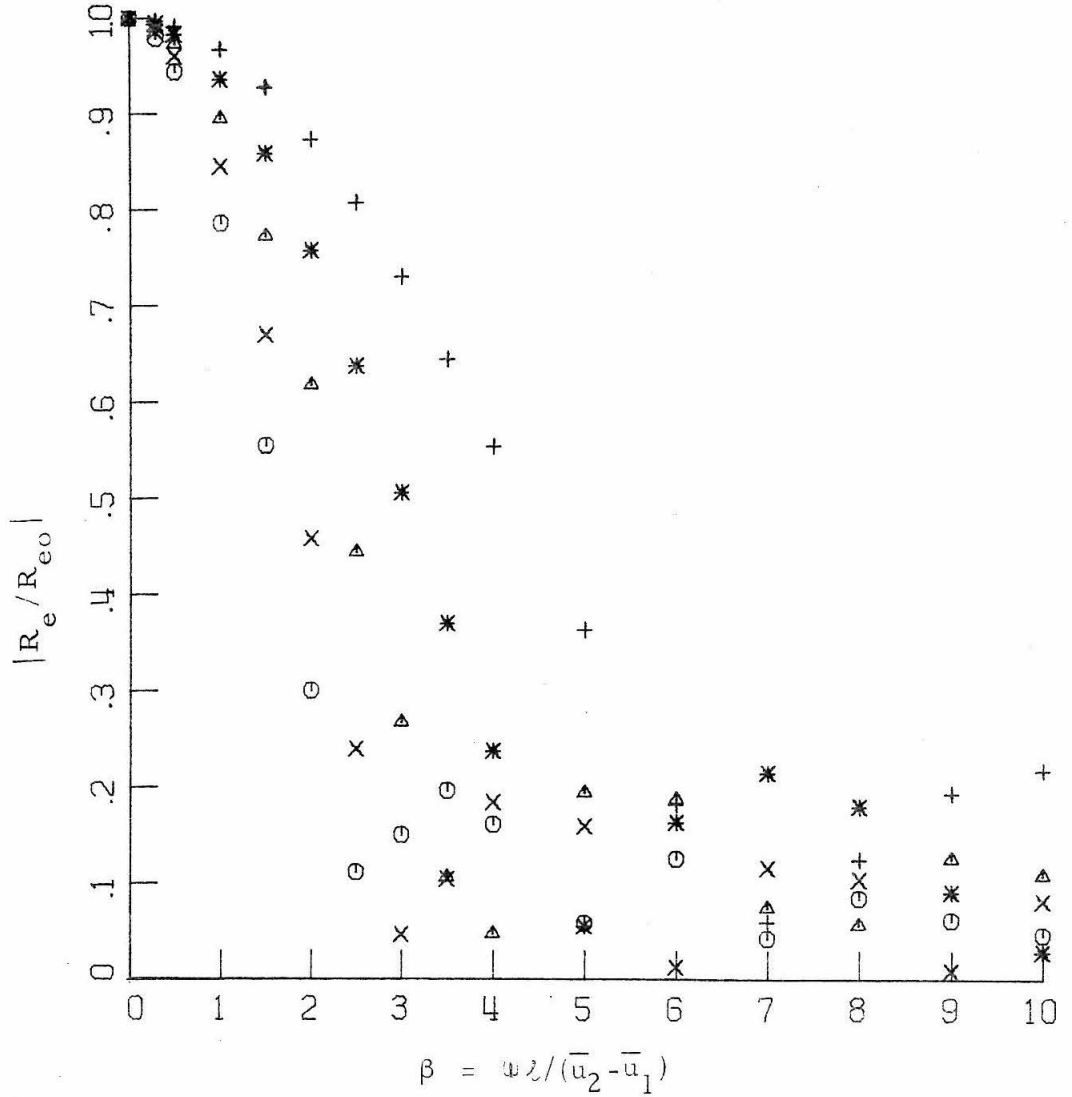

Fig. 2-16

Normalized Magnitude of Reflected Waves (Entropy Solution) Versus Reduced Frequency

	M_1	M_2
⊖	.2	.8
×	.3	.8
△	.4	.8
✳	.5	.8
+	.6	.8

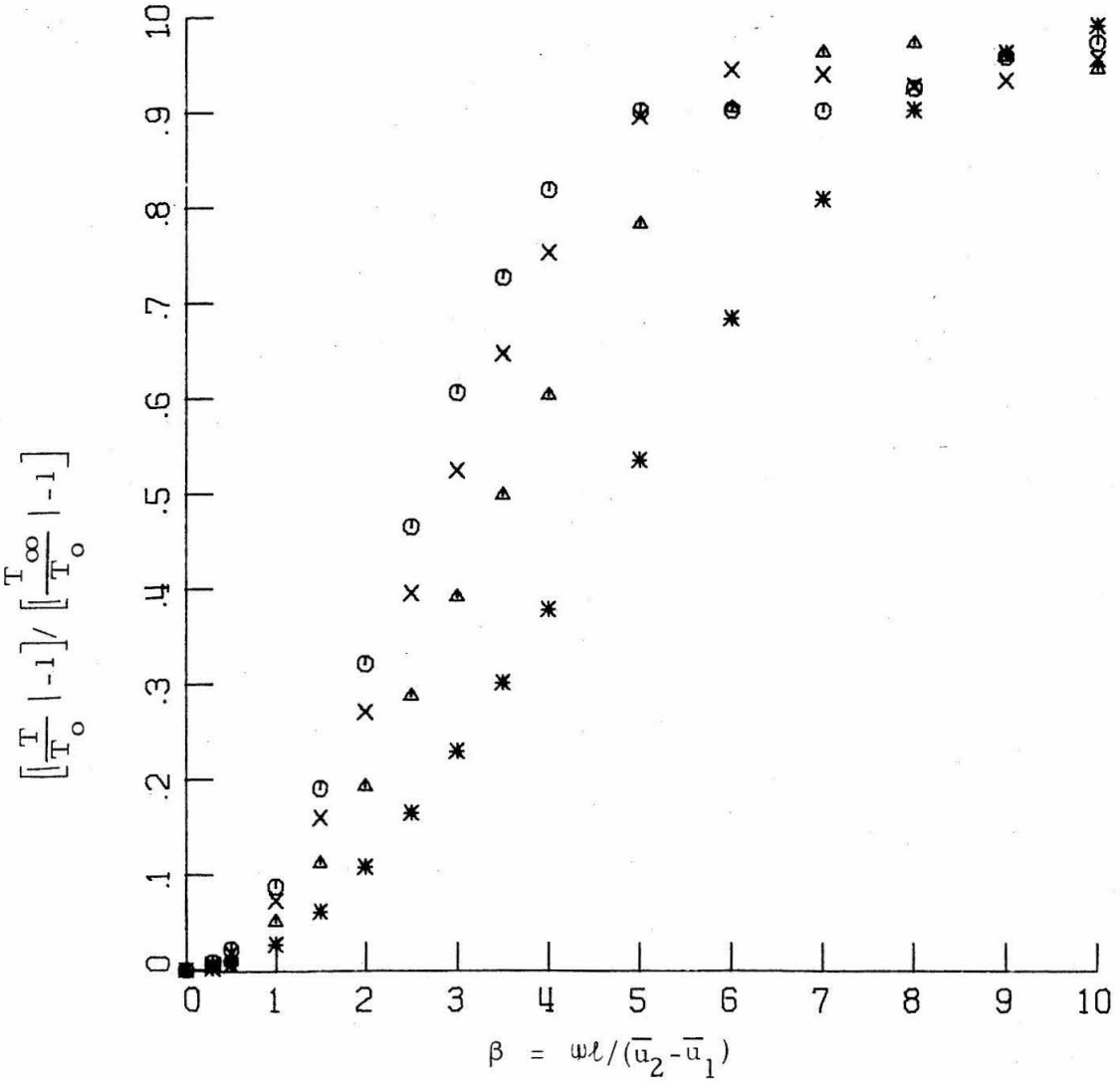

Fig. 2-17

Normalized Magnitude of Transmitted Waves (Plus or Minus Solution) Versus Reduced Frequency

	M_1	M_2
⊙	.2	.7
×	.3	.7
△	.4	.7
✱	.5	.7

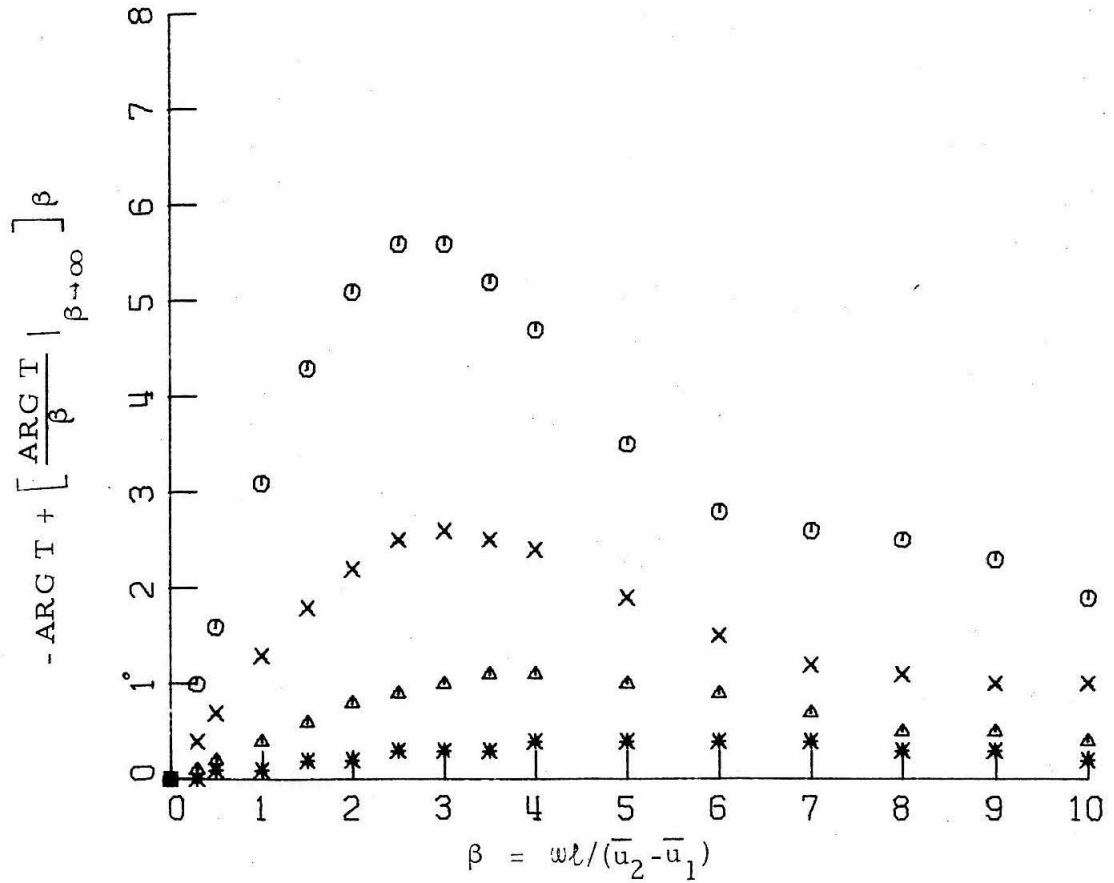

Fig. 2-18

Error in Using High Frequency Solution for Phase of Transmitted Waves (Plus or Minus Solution) Versus Reduced Frequency

	M_1	M_2
⊙	.2	.7
×	.3	.7
△	.4	.7
✱	.5	.7

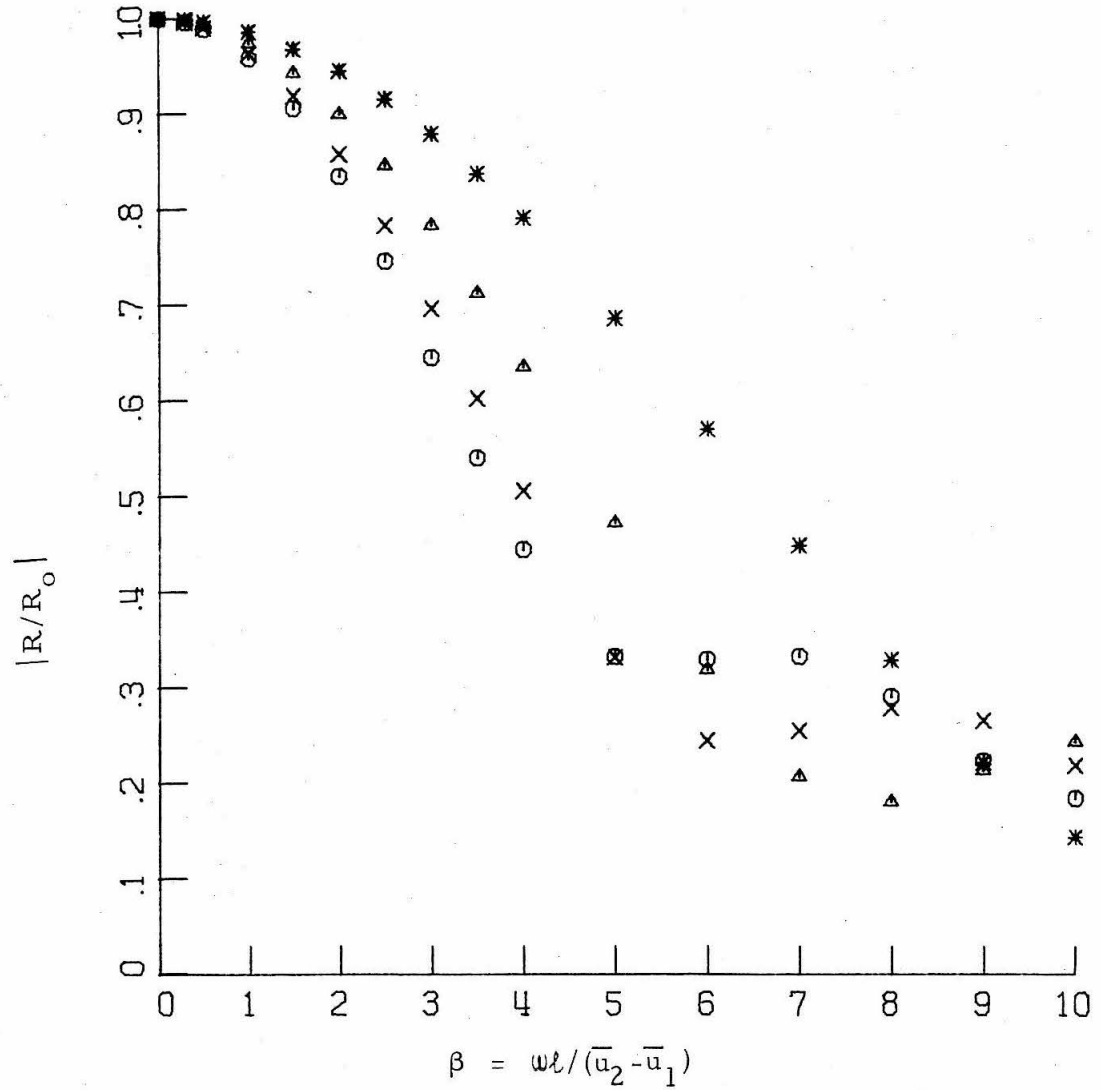

Fig. 2-19
Normalized Magnitude of Reflected Waves (Plus or Minus Solution) Versus Reduced Frequency

	M_1	M_2
⊙	.2	.7
×	.3	.7
△	.4	.7
✳	.5	.7

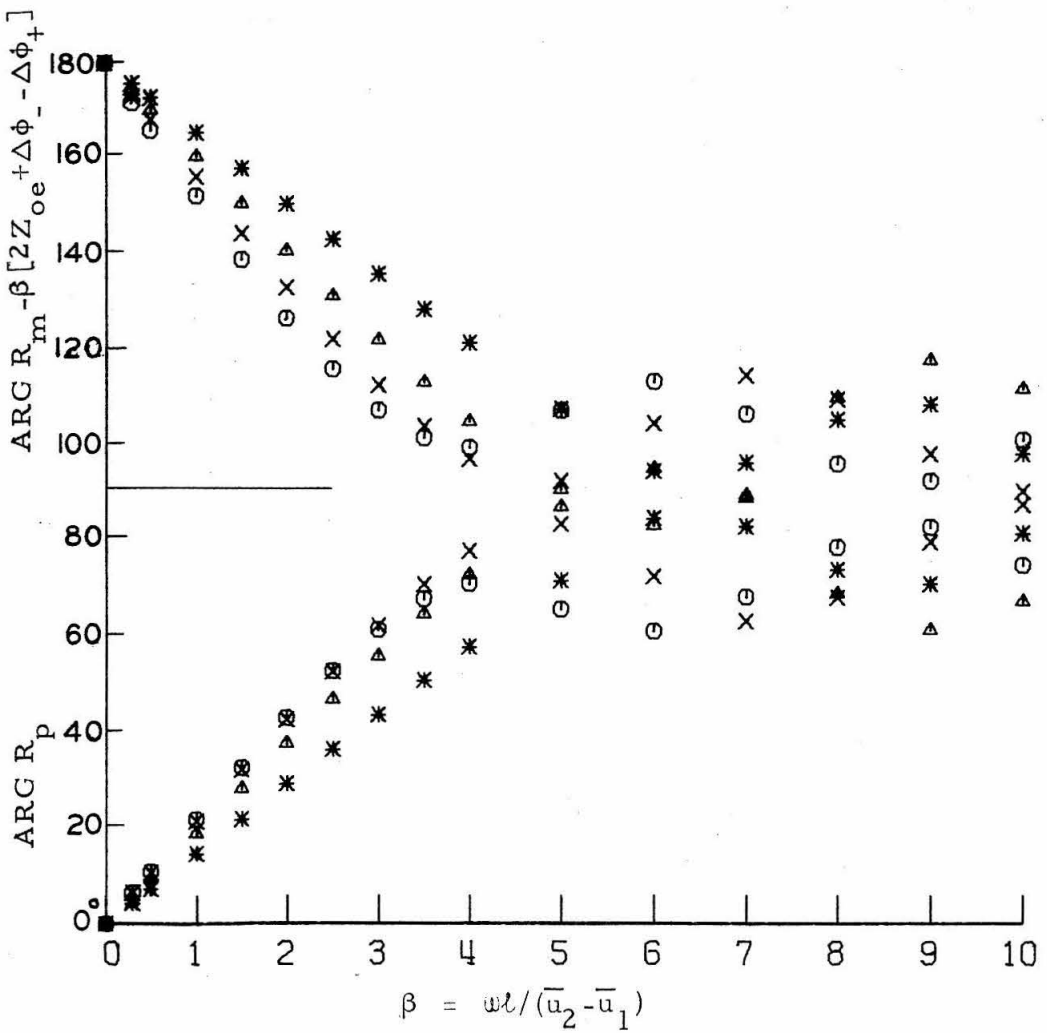

Fig. 2-20

Phase of Reflected Waves
(Plus or Minus Solution)
Versus Reduced Frequency

	M_1	M_2
⊙	.2	.7
×	.3	.7
△	.4	.7
*	.5	.7

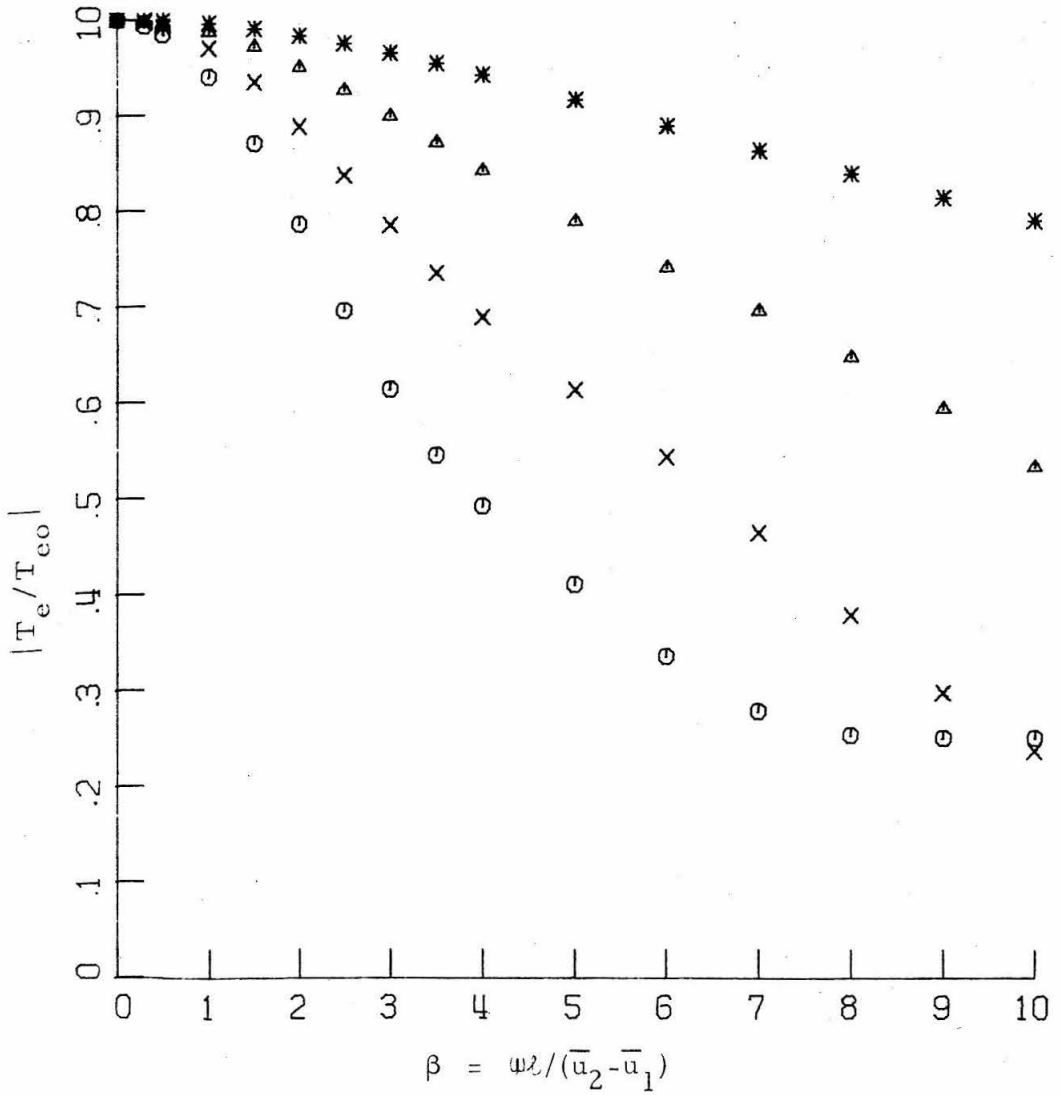

Fig. 2-21

Normalized Magnitude of Transmitted Wave (Entropy Solution) Versus Reduced Frequency

	M_1	M_2
⊙	.2	.7
×	.3	.7
△	.4	.7
✳	.5	.7

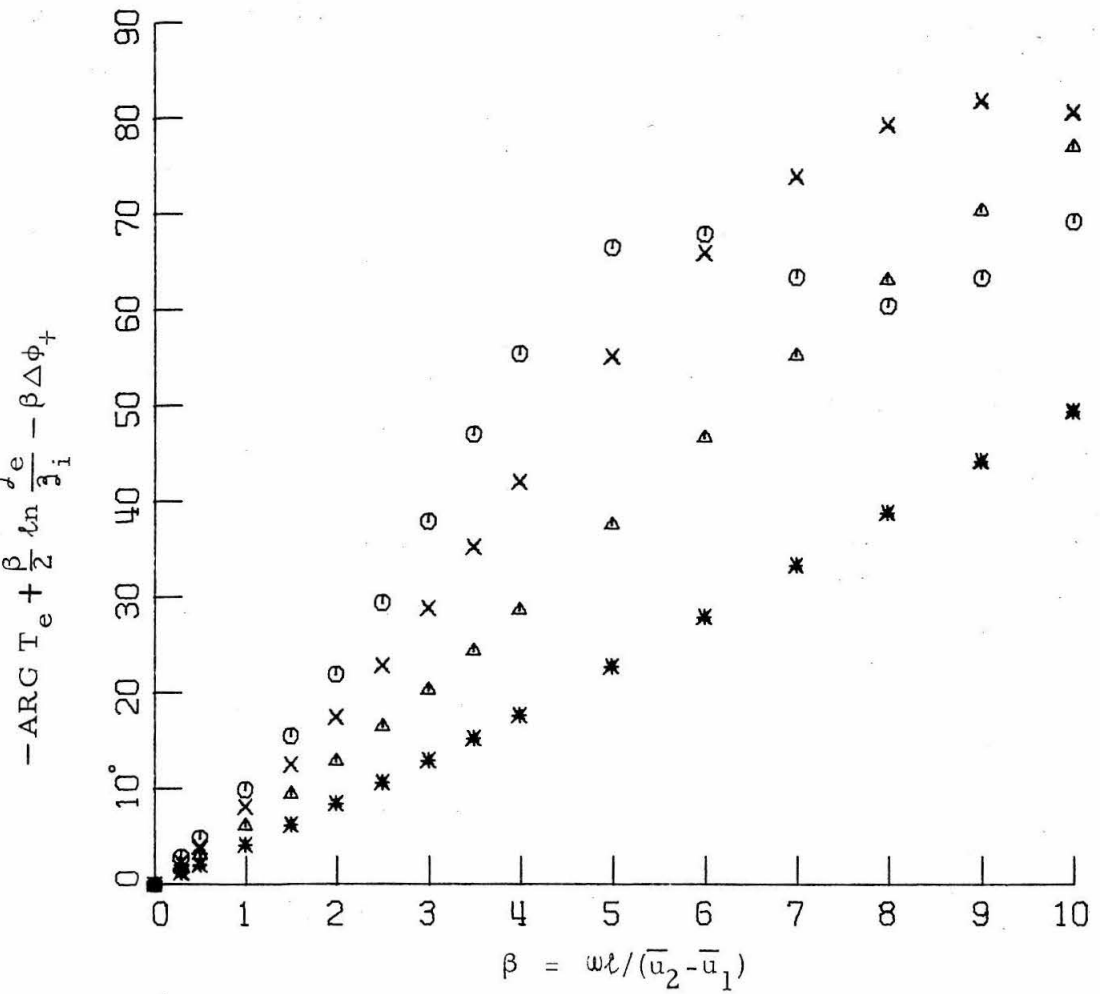

Fig. 2-22

Phase of Transmitted Wave (Entropy Solution) Versus Reduced Frequency

	M_1	M_2
⊙	.2	.7
×	.3	.7
△	.4	.7
✱	.5	.7

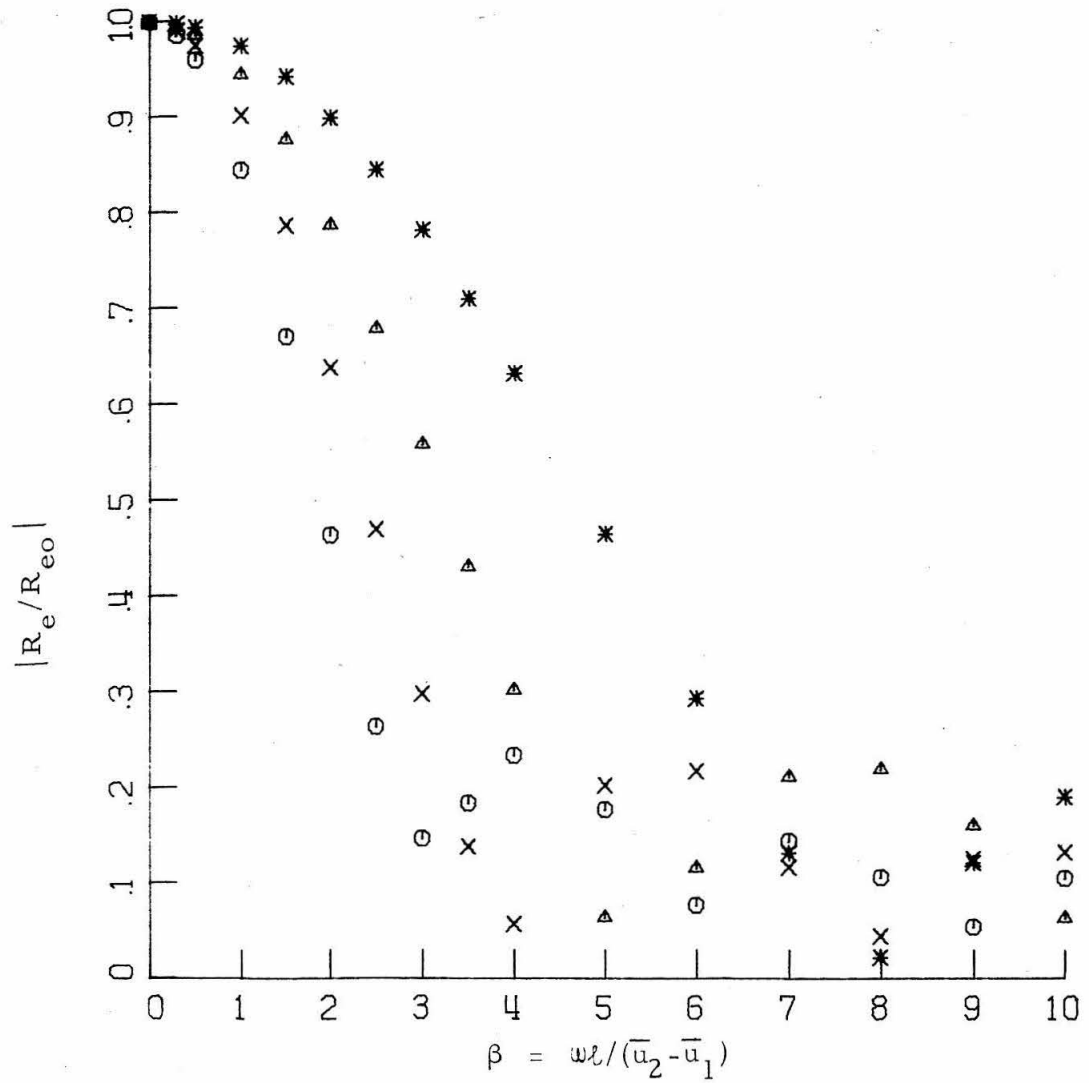

Fig. 2-23

Normalized Magnitude of Reflected Waves (Entropy Solution) Versus Reduced Frequency

	M_1	M_2
⊙	.2	.7
×	.3	.7
△	.4	.7
✳	.5	.7

REFERENCES FOR CHAPTER II

1. Ingard, U. and Singhal, V. K. "Effect of Flow on the Acoustic Resonances of an Open Ended Duct," J. Ac. Soc. Am., V. 58, 4 (1975), 1343, 1346.

2. Mason, V. "Some Experiments on the Propagation of Sound Along a Cylindrical Duct with Air Flow," J. Sound Vib., V. 10, 2 (1969), 208-226.

3. Nayfeh, A. "Effect of Mean Velocity Profile Shapes on Sound Transmission through Two-Dimensional Ducts," J. Sound Vib., Vol. 34, 3 (1974), 413-433.

4. Powell, A. "Theory of Sound Propagation Through a Duct with High Speed Flows," J. Ac. Soc. Am., V. 32, 12 (1960), 1640

5. Yurkovich, R. "Attenuation of Acoustic Modes in Circular and Annular Ducts in the Presence of Sheared Flow," presented at the AIAA 13th Aerospace Sciences Meeting, Pasadena, Calif., 1975; AIAA Paper 75-131.

6. Candel, S. "Analytical Studies of Some Acoustical Problems of Jet Engines," Ph. D. Thesis (1972), California Institute of Technology, Pasadena, California.

7. Tsien, H. "The Transfer Functions of Rocket Nozzles," J. Am. Rocket Soc., V. 22, 3 (1952), 139-143.

8. Auerbach, J. "Experimental Studies of the Noise Produced in a Supersonic Nozzle by Upstream Acoustic and Thermal Disturbances," Ph. D. Thesis (1975), California Institute of Technology, Pasadena, California.

9. Zukoski, E. "Experiments Concerning the Response of Supersonic Nozzles to Fluctuating Inlet Conditions," presented at the Gas Turbine Conference, Houston, Texas (1975); ASME Paper 75-GT-40.

10. Marble, F. "Acoustic Disturbances from Gas Nonuniformities Convected through a Nozzle," presented at the Interagency Symposium on University Research in Transportation Noise, Stanford University, Calif. (1973); Proceedings, V. 3.

11. Cumpsty, N. and Marble, F. "Generation of Noise by the Fluctuations in Gas Temperature into a Turbine," Cambridge University, Engineering Dept. Report TR57 (1974), Cambridge, England.

12. Shapiro, A.H. The Dynamics and Thermodynamics of Compressible Fluid Flow, The Ronald Press, New York (1953).

13. Bohn, M. and Zukoski, E. "Effect of Flow on the Acoustic Reflection Coefficient at a Duct Inlet," submitted for publication in the Journal of the Acoustical Society of America, February 1976.

III. SECOND-ORDER DUCT ACOUSTICS

3.1 Introduction

In the previous chapter we found that a mean flow with strong gradients could interact with first-order pressure and entropy waves and give resulting pressure waves of the same order. In that case we wrote the governing equations (2.1) - (2.4) by considering an average of the flow variables over a cross section of the duct in the same spirit as the equations of one-dimensional gas dynamics for variable-area channel flow are derived. To consider the variation of the flow variables across the duct we would need to calculate the full two-dimensional solution. This calculation is difficult because the two-dimensional disturbance and the resulting two-dimensional waves are of the same order.

Much of the recent work [1-3] on such two-dimensional effects has been concerned with the effect of a sheared mean flow on the duct modes; area variations were not considered. Small area variations, as well as mean velocity shear, mean temperature shear, and acoustical duct linings were considered simultaneously by Nayfeh and Kaiser[4].

If the variations in area of the duct are small (such that the steady disturbance to the mean flow is small), then first-order periodic disturbances give resulting two-dimensional waves which may be calculated by a second-order expansion. In general, we may consider three kinds of disturbances: entropy waves, acoustic waves, and vorticity waves. In this chapter we will seek the second-order solution which results from the interaction of a two-dimensional entropy

wave and the small area variation.

The solution will be found in the following manner. The equations of motion (two-dimensional) are expanded to second order. The zero-order solution is just the constant-area channel flow. The first-order solution has a steady part which corresponds to the disturbance to the steady channel flow imposed by the area contraction. The non-steady portion of the first-order solution corresponds to the periodic disturbances due to the entropy wave.

Having solved for the first-order solutions, we may write the second-order equations with inhomogeneous terms involving products of first-order terms. We will retain only the periodic inhomogeneous terms of interest, i.e., those involving the interaction of the entropy disturbance and the steady flow disturbance caused by the wall deflection. We solve for an inhomogeneous solution with homogeneous boundary conditions (no wall deflection) via the Green's function method. A homogeneous solution satisfying the boundary condition (wall deflection) expanded to second order is found via the Fourier transform method. The final solution is expressed in terms of complex amplitudes of propagating duct modes (the waves which propagate far upstream and far downstream of the contraction).

We will express the solution in terms of a general entropy wave disturbance and show how this leads to some simplifications of the calculations of the acoustic mode amplitudes. Some general observations will be made about the behavior of the duct modes and some calculations for particular examples will be presented and discussed.

3.2 The Expansion to Second Order

We have a duct of height $2b$, with a (subsonic) axial mean flow velocity U . Over a portion of the axial distance x $(-a<x<a)$, the area of the channel varies slightly. The area variation is expressed as a small deflection in the wall, $f(x)$, away from $y=0$ or $y=2b$, see accompanying diagram.

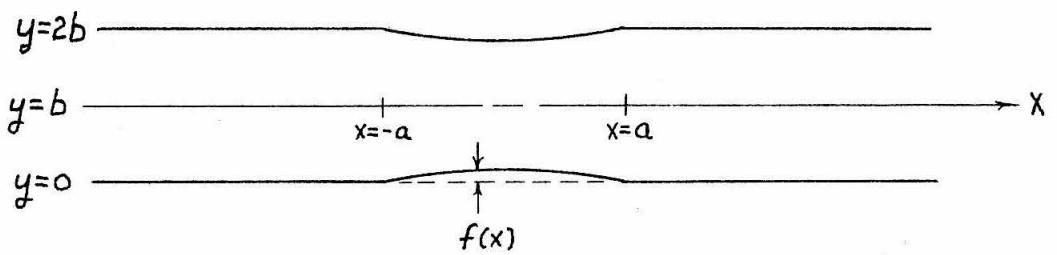

The equations of continuity, axial momentum, vertical momentum, and entropy conservation are

$$\left(\frac{\partial}{\partial t}+u\frac{\partial}{\partial x}+v\frac{\partial}{\partial y}\right)\rho+\rho\left(\frac{\partial u}{\partial x}+\frac{\partial v}{\partial y}\right)=0 \qquad (3.1)$$

$$\left(\frac{\partial}{\partial t}+u\frac{\partial}{\partial x}+v\frac{\partial}{\partial y}\right)u+\frac{1}{\rho}\frac{\partial P}{\partial x}=0 \qquad (3.2)$$

$$\left(\frac{\partial}{\partial t}+u\frac{\partial}{\partial x}+v\frac{\partial}{\partial y}\right)v+\frac{1}{\rho}\frac{\partial P}{\partial y}=0 \qquad (3.3)$$

$$\left(\frac{\partial}{\partial t} + u\frac{\partial}{\partial x} + v\frac{\partial}{\partial y}\right) S = 0 \tag{3.4}$$

Assuming a second-order expansion for the solution:

$$\begin{aligned} &\rho + \rho^{(1)} + \rho^{(2)} \\ &u + u^{(1)} + u^{(2)} \\ &\quad v^{(1)} + v^{(2)} \\ &p + p^{(1)} + p^{(2)} \\ &\quad S^{(1)} + S^{(2)} \end{aligned} \tag{3.5}$$

The zero-order quantities are constants; the first- and second-order quantities depend on x, y, t in general. Inserting (3.5) into (3.1)-(3.4), we get the first-order equations

$$\left(\frac{\partial}{\partial t} + U\frac{\partial}{\partial x}\right)\frac{\rho^{(1)}}{\rho} + \frac{\partial u^{(1)}}{\partial x} + \frac{\partial v^{(1)}}{\partial y} = 0 \tag{3.6}$$

$$\rho\left(\frac{\partial}{\partial t} + U\frac{\partial}{\partial x}\right)u^{(1)} + \frac{\partial p^{(1)}}{\partial x} = 0 \tag{3.7}$$

$$\rho\left(\frac{\partial}{\partial t} + U\frac{\partial}{\partial x}\right)v^{(1)} + \frac{\partial p^{(1)}}{\partial y} = 0 \tag{3.8}$$

$$\left(\frac{\partial}{\partial t} + U\frac{\partial}{\partial x}\right)\frac{S^{(1)}}{c_p} = \left(\frac{\partial}{\partial t} + U\frac{\partial}{\partial x}\right)\left(\frac{p^{(1)}}{\gamma p} - \frac{\rho^{(1)}}{\rho}\right) = 0 \tag{3.9}$$

and the corresponding second-order equations:

$$\begin{aligned} &\left(\frac{\partial}{\partial t} + U\frac{\partial}{\partial x}\right)\rho^{(2)} + u^{(1)}\frac{\partial \rho^{(1)}}{\partial x} + v^{(1)}\frac{\partial \rho^{(1)}}{\partial y} + \rho\left(\frac{\partial u^{(2)}}{\partial x} + \frac{\partial v^{(2)}}{\partial y}\right) \\ &\quad + \rho^{(1)}\left(\frac{\partial u^{(1)}}{\partial x} + \frac{\partial v^{(1)}}{\partial y}\right) = 0 \end{aligned} \tag{3.10}$$

$$\rho\left(\frac{\partial}{\partial t}+U\frac{\partial}{\partial x}\right)v^{(2)}+\rho^{(1)}\left(\frac{\partial}{\partial t}+U\frac{\partial}{\partial x}\right)v^{(1)}$$
$$+\rho\left(u^{(1)}\frac{\partial}{\partial x}+v^{(1)}\frac{\partial}{\partial y}\right)v^{(1)}+\frac{\partial p^{(2)}}{\partial y}=0 \qquad (3.11)$$

$$\rho\left(\frac{\partial}{\partial t}+U\frac{\partial}{\partial x}\right)v^{(2)}+\rho^{(1)}\left(\frac{\partial}{\partial t}+U\frac{\partial}{\partial x}\right)v^{(1)}$$
$$+\rho\left(u^{(1)}\frac{\partial}{\partial x}+v^{(1)}\frac{\partial}{\partial y}\right)v^{(1)}+\frac{\partial p^{(2)}}{\partial y}=0 \qquad (3.12)$$

$$\frac{1}{\gamma}\left(\frac{\partial}{\partial t}+U\frac{\partial}{\partial x}\right)\left(\frac{p^{(2)}}{p}-\frac{1}{2}\left(\frac{p^{(1)}}{p}\right)^2\right)-\left(\frac{\partial}{\partial t}+U\frac{\partial}{\partial x}\right)\left(\frac{\rho^{(2)}}{\rho}-\frac{1}{2}\left(\frac{\rho^{(1)}}{\rho}\right)^2\right)$$
$$+\frac{1}{\gamma}\left(u^{(1)}\frac{\partial}{\partial x}+v^{(1)}\frac{\partial}{\partial y}\right)\frac{p^{(1)}}{p}-\left(u^{(1)}\frac{\partial}{\partial x}+v^{(1)}\frac{\partial}{\partial y}\right)\frac{\rho^{(1)}}{\rho}=0 \qquad (3.13)$$

3.3 First-Order Solutions

Non-Steady Solution. The non-steady, first-order disturbances that may exist are, in general, entropy waves, vorticity waves, and acoustic waves. We will be interested here in the entropy waves (for which there are no associated pressure fluctuations) and hence (3.9) becomes

$$-\left(\frac{\partial}{\partial t}+U\frac{\partial}{\partial x}\right)\frac{\rho^{(1)}}{\rho}=\left(\frac{\partial}{\partial t}+U\frac{\partial}{\partial x}\right)\frac{S^{(1)}}{C_p}=0$$

Suppose we consider entropy waves with lines of constant phase with normal at angle ν_s to the channel axis, radial frequency ω_s, and convecting through the channel with the mean flow. In this case we get

$$\frac{\rho_s^{(1)}}{\rho} = \sigma e^{i\omega_s t} \exp\{-i k_s (x\cos\nu_s + y\sin\nu_s)\} \tag{3.14}$$

$$P_s^{(1)} \equiv 0$$

$$u_s^{(1)} \equiv 0$$

$$v_s^{(1)} \equiv 0$$

and $k_s = \omega_s/(U\cos\nu_s)$

σ = (first order) complex amplitude $= -S^{(1)}/C_P$

S = subscript referring to quantities associated with the entropy wave

Steady Solution. Here, we seek the first-order, steady perturbation to the channel flow, U, ρ, and P caused by the contraction in the channel. Recall that the height is given by $f(x)$ (see diagram).

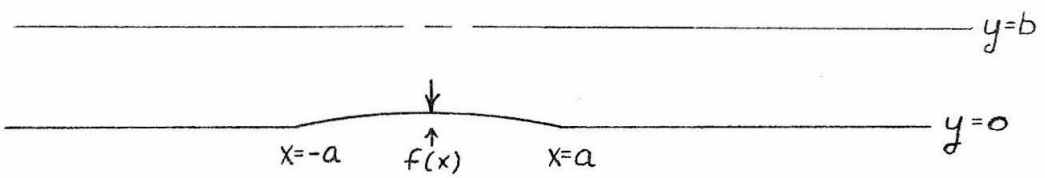

For the sake of simplicity, we assume the same deflection for the top of the duct, $y=2b$. The duct is symmetric about $y=b$. The equations (3.6) - (3.9) give

$$U\frac{\partial}{\partial x}\frac{\rho^{(1)}}{\rho} + \frac{\partial u^{(1)}}{\partial x} + \frac{\partial v^{(1)}}{\partial y} = 0 \tag{3.15}$$

$$\rho U\frac{\partial u^{(1)}}{\partial x} + \frac{\partial P^{(1)}}{\partial x} = 0 \tag{3.16}$$

$$\rho U \frac{\partial v^{(1)}}{\partial x} + \frac{\partial p^{(1)}}{\partial y} = 0 \tag{3.17}$$

$$\frac{\rho^{(1)}}{\rho} = \frac{p^{(1)}}{\gamma p} \tag{3.18}$$

Equations (3.16) and (3.17) may be used to show that a potential-type solution is appropriate:

$$u^{(1)} = \frac{\partial \varphi}{\partial x} \tag{3.19}$$

$$v^{(1)} = \frac{\partial \varphi}{\partial y} \tag{3.20}$$

Then we find

$$p^{(1)} = -\rho U \frac{\partial \varphi}{\partial x} \tag{3.21}$$

Using (3.21) and (3.18) in (3.15) we get

$$(1-M^2)\varphi_{xx} + \varphi_{yy} = 0 \tag{3.22}$$

where $M^2 = U^2\rho/\gamma p = U^2/c^2$, mean Mach number. We define the Fourier transform Φ of φ :

$$\Phi(\xi, y) = \frac{1}{(2\pi)^{1/2}} \int_{-\infty}^{\infty} \varphi(x, y) e^{-ix\xi} dx$$

Assuming this integral converges, this gives for (3.22)

$$\Phi_{yy} - \xi^2(1-M^2)\Phi = 0 \tag{3.23}$$

To insure rapid convergence of $\varphi(x,y)$ we pick the area change to be:

$$f(x) = \frac{\epsilon}{8}\left(3 + 4\cos\pi\frac{x}{a} + \cos 2\pi\frac{x}{a}\right) \qquad |x| \le a \tag{3.24}$$

$$f(x) = 0 \qquad |x| > a$$

Then $f(x)$ has first, second, and third derivatives which are continuous.

The boundary condition on $v^{(1)}$ (velocity is tangent to the wall) gives

$$\frac{\partial \varphi}{\partial y} = \begin{cases} 0 & y=b \\ U\frac{df}{dx} & y=0 \end{cases}$$

and therefore

$$\frac{\partial \Phi}{\partial y}(\xi,0) = \frac{1}{(2\pi)^{1/2}}\int_{-\infty}^{\infty} \frac{\partial \varphi}{\partial y}(x,0)e^{-ix\xi}dx \tag{3.25}$$

$$\frac{\partial \Phi}{\partial y}(\xi,b) = 0$$

The solution for $\Phi(\xi,y)$ takes the form

$$\Phi(\xi,y) = a(\xi)e^{\xi\sqrt{1-M^2}y} + b(\xi)e^{-\xi\sqrt{1-M^2}y} \tag{3.26}$$

where $a(\xi)$ and $b(\xi)$ will be determined upon applying (3.25). The potential φ is then found by the Fourier inversion of Φ :

$$\varphi(x,y) = \frac{1}{(2\pi)^{1/2}}\int_{-\infty}^{\infty} \Phi(\xi,y)e^{i\xi x}d\xi \tag{3.27}$$

Some of the details of the calculation may be found in Appendix A. We present here only the results for the steady pressure disturbance.

$$|x|>a \qquad \frac{p^{(1)}}{\gamma P} = \frac{M^2\pi^2\epsilon}{(1-M^2)ba^2}$$

$$\sum_{n=1}^{\infty} P_n \sinh\left[\frac{n\pi a}{b(1-M^2)^{1/2}}\right]\cos\left(n\pi\frac{y}{b}\right)\exp\left[\frac{-n\pi|x|}{b(1-M^2)^{1/2}}\right]$$

$$|X|<a \qquad \frac{p^{(1)}}{\gamma P} = \frac{-M^2\pi\epsilon}{4a^2(1-M^2)^{1/2}}$$

$$\left\{ \frac{3\pi}{2b(1-M^2)^{1/2}}\left(\frac{a}{\pi}\right)^2 \right.$$

$$+2a\left[\frac{\cos(\pi\frac{x}{a})\cosh\left[\frac{\pi}{a}(1-M^2)^{1/2}(b-y)\right]}{\sinh\left[\pi\frac{b(1-M^2)^{1/2}}{a}\right]} + \frac{\cos(2\pi\frac{x}{a})\cosh\left[\frac{2\pi}{a}(1-M^2)^{1/2}(b-y)\right]}{2\sinh\left[2\pi\frac{b(1-M^2)^{1/2}}{a}\right]}\right]$$

$$\left. +\frac{4\pi}{(1-M^2)^{1/2}b}\sum_{n=1}^{\infty} P_n \cosh\left[\frac{n\pi x}{(1-M^2)^{1/2}b}\right]\cos\left(n\pi\frac{y}{b}\right)\exp\left[\frac{-n\pi a}{(1-M^2)^{1/2}b}\right] \right\}$$

$$P_n \equiv \frac{1}{\left(\frac{\pi}{a}\right)^2+\left(\frac{n\pi}{(1-M^2)^{1/2}b}\right)^2} - \frac{1}{\left(\frac{2\pi}{a}\right)^2+\left(\frac{n\pi}{(1-M^2)^{1/2}b}\right)^2} \qquad (3.28)$$

3.4 Second-Order Solutions

Inhomogeneous Equation, Homogeneous Boundary Conditions.

The second-order equations (3.10) - (3.13) may be rearranged to give

$$\left(\frac{\partial}{\partial t}+U\frac{\partial}{\partial x}\right)^2\left(\frac{p^{(2)}}{\gamma P}\right) - c^2\left(\frac{\partial^2}{\partial x^2}+\frac{\partial^2}{\partial y^2}\right)\left(\frac{p^{(2)}}{\gamma P}\right) =$$

$$-\left(\frac{\partial}{\partial t}+U\frac{\partial}{\partial x}\right)\left(u^{(1)}\frac{\partial}{\partial x}+v^{(1)}\frac{\partial}{\partial y}\right)\left(\frac{p^{(1)}}{\gamma P}\right)$$

$$+\frac{\gamma}{2}\left(\frac{\partial}{\partial t}+U\frac{\partial}{\partial x}\right)^2\left(\frac{p^{(1)}}{\gamma P}\right)^2 + \frac{\partial}{\partial x}\left(u^{(1)}\frac{\partial}{\partial x}+v^{(1)}\frac{\partial}{\partial y}\right)u^{(1)}$$

$$+\frac{\partial}{\partial y}\left(u^{(1)}\frac{\partial}{\partial x}+v^{(1)}\frac{\partial}{\partial y}\right)v^{(1)} - \frac{\rho^{(1)}}{\rho}c^2\left(\frac{\partial^2}{\partial x^2}+\frac{\partial^2}{\partial y^2}\right)\left(\frac{p^{(1)}}{\gamma P}\right)$$

$$-c^2\left\{\left[\frac{\partial}{\partial x}\left(\frac{p^{(1)}}{\gamma P}\right)\right]\left[\frac{\partial}{\partial x}\left(\frac{\rho^{(1)}}{\rho}\right)\right] + \left[\frac{\partial}{\partial y}\left(\frac{p^{(1)}}{\gamma P}\right)\right]\left[\frac{\partial}{\partial y}\left(\frac{\rho^{(1)}}{\rho}\right)\right]\right\} \qquad (3.29)$$

The inhomogeneous term simplifies because we are only considering a first-order entropy wave interacting with the first-order steady disturbance. In this case, the unsteady second-order terms which remain are:

$$-c^2\left[\frac{\partial}{\partial x}\left(\frac{\rho_s^{(1)}}{\rho}\ \frac{\partial}{\partial x}\left(\frac{P^{(1)}}{\gamma P}\right)\right)+\frac{\partial}{\partial y}\left(\frac{\rho_s^{(1)}}{\rho}\ \frac{\partial}{\partial y}\left(\frac{P^{(1)}}{\gamma P}\right)\right)\right]$$

where $P^{(1)}/\gamma P$ is the steady pressure field due to the wall deflection and $\rho_s^{(1)}/\rho$ is due to the entropy disturbance. Then write eq. (3.29) as:

$$\frac{1}{c^2}\left(\frac{\partial}{\partial t}+U\frac{\partial}{\partial x}\right)^2\varphi-\left(\frac{\partial^2}{\partial x^2}+\frac{\partial^2}{\partial y^2}\right)\varphi=F(x,y)e^{i\omega t}\ ;\ \varphi\equiv\frac{P^{(2)}}{\gamma P} \tag{3.30}$$

We will have the boundary conditions

$$\frac{\partial\varphi}{\partial y}(x,0)=\frac{\partial\varphi}{\partial y}(x,2b)=0 \tag{3.31}$$

In addition, we specify that no waves propagate towards the contraction for $|x|\to\infty$. This is the radiation condition.

We will express the solution as:

$$\varphi(x,y)=\int_{-\infty}^{\infty}\int_{0}^{2b}G(x,y;\xi,\eta)F(\xi,\eta)\,d\eta\,d\xi \tag{3.32}$$

where $G(x,y;\xi,\eta)$ is the Green's function. The details of the calculation of the Green's function will be found in Appendix B. We present the results here:

$x < \xi \qquad G(x,y,\xi,\eta) =$

$$e^{i\omega t}\left\{\frac{c}{4ib\omega}\exp\left[\frac{i\omega/c}{1-M}x\right]\right.$$

$$+\sum_{m=1}^{N}\frac{1}{2ib}\frac{\cos\left(m\pi\frac{\eta}{2b}\right)\cos\left(m\pi\frac{y}{2b}\right)}{\left(\left(\frac{\omega}{c}\right)^2-\left(\frac{m\pi}{2b}\right)^2(1-M^2)\right)^{1/2}}\exp\left[i\left(\frac{M}{1-M^2}+\sqrt{\frac{1}{(1-M^2)^2}-\left(\frac{m\pi c}{2b\omega}\right)^2\frac{1}{1-M^2}}\right)\frac{\omega}{c}(x-\xi)\right]$$

$$-\sum_{m=N_1+1}^{N}\frac{1}{2ib}\frac{\cos\left(m\pi\frac{\eta}{2b}\right)\cos\left(m\pi\frac{y}{2b}\right)}{\left(\left(\frac{\omega}{c}\right)^2-\left(\frac{m\pi}{2b}\right)^2(1-M^2)\right)^{1/2}}\exp\left[i\left(\frac{M}{1-M^2}-\sqrt{\frac{1}{(1-M^2)^2}-\left(\frac{m\pi c}{2b\omega}\right)^2\frac{1}{1-M^2}}\right)\frac{\omega}{c}(x-\xi)\right]$$

$$\left.+\sum_{m=N+1}^{\infty}\frac{1}{2b}\frac{\cos\left(m\pi\frac{\eta}{2b}\right)\cos\left(m\pi\frac{y}{2b}\right)}{\left(\left(\frac{m\pi}{2b}\right)^2(1-M^2)-\left(\frac{\omega}{c}\right)^2\right)^{1/2}}\exp\left[i\left(\frac{M}{1-M^2}\frac{\omega}{c}(x-\xi)\right)+\sqrt{\left(\frac{m\pi c}{2b\omega}\right)^2\frac{1}{1-M^2}-\frac{1}{(1-M^2)^2}}\frac{\omega}{c}(x-\xi)\right]\right\}$$

(3.33)

$x > \xi \qquad G(x,y,\xi,\eta) =$

$$e^{i\omega t}\left\{\frac{c}{4ib\omega}\exp\left[\frac{-i\omega/c}{1+M}x\right]\right.$$

$$+\sum_{m=1}^{N_1}\frac{1}{2ib}\frac{\cos\left(m\pi\frac{\eta}{2b}\right)\cos\left(m\pi\frac{y}{2b}\right)}{\left(\left(\frac{\omega}{c}\right)^2-\left(\frac{m\pi}{2b}\right)^2(1-M^2)\right)^{1/2}}\exp\left[i\left(\frac{M}{1-M^2}-\sqrt{\frac{1}{(1-M^2)^2}-\left(\frac{m\pi c}{2b\omega}\right)^2\frac{1}{1-M^2}}\right)\frac{\omega}{c}(x-\xi)\right]$$

$$\left.+\sum_{m=N+1}^{\infty}\frac{1}{2b}\frac{\cos m\pi\frac{\eta}{2b}\cos m\pi\frac{y}{2b}}{\left(\left(\frac{m\pi}{2b}\right)^2(1-M^2)-\left(\frac{\omega}{c}\right)^2\right)^{1/2}}\exp\left[i\left(\frac{M}{1-M^2}\frac{\omega}{c}(x-\xi)\right)-\sqrt{\left(\frac{m\pi c}{2b\omega}\right)^2\frac{1}{1-M^2}-\frac{1}{(1-M^2)^2}}\frac{\omega}{c}(x-\xi)\right]\right\}$$

(3.34)

where we define

$$N = \text{largest integer such that } \frac{N\pi c}{2b\omega} < \frac{1}{(1-M^2)^{1/2}}$$

$$N_1 = \text{largest integer such that } \frac{N_1\pi c}{2b\omega} < 1 \quad , \text{ i.e., } N_1 \leq N$$

In (3.33) the first and second summations represent waves propagating upstream. Note that these represent two unique waves which may exist. The third summation represents waves which propagate upstream but are attenuated as they do so. In (3.34) the first summation represents waves propagating downstream and the second summation represents waves which propagate upstream but attenuate as they do so.

To calculate the forcing function for eq. (3.32) we recall

$$F(x,y) = -\left\{\frac{\partial}{\partial x}\left(\frac{\rho_s''}{\rho}\frac{\partial}{\partial x}\left(\frac{p''}{\gamma p}\right)\right) + \frac{\partial}{\partial y}\left(\frac{\rho_s''}{\rho}\frac{\partial}{\partial y}\left(\frac{p''}{\gamma p}\right)\right)\right\} \qquad (3.35)$$

where $\frac{p''}{\gamma p}$ is given by eq. (3.28) and $\frac{\rho_s''}{\rho}$ is given by eq. (3.14). The results of the calculation of $F(x,y)$ are given in Appendix C. We now define

$$A_m \equiv \begin{cases} \dfrac{c}{4ib\omega} & m=0 \\ \dfrac{1}{2ib\left(\left(\frac{\omega}{c}\right)^2-\left(\frac{m\pi}{2b}\right)^2(1-M^2)\right)^{1/2}} & 0<m\leq N \\ \dfrac{1}{2b\left(\left(\frac{m\pi}{2b}\right)^2(1-M^2)-\left(\frac{\omega}{c}\right)^2\right)^{1/2}} & N<m \end{cases}$$

$$\Omega_n \equiv \left| \frac{1}{(1-M^2)^2} - \frac{n\pi c}{2b\omega} \frac{1}{1-M^2} \right|^{1/2}$$

Then we may write the Green's function

$$x<\xi \quad G(x,y;\xi,\eta) =$$

$$\sum_{m=0}^{N} A_m \cos(m\pi \frac{y}{2b}) \cos(m\pi \frac{\eta}{2b}) \exp\left[i \frac{\omega}{c}(x-\xi)\left(\frac{M}{1-M^2} + \Omega_m\right)\right]$$

$$- \sum_{N_1+1}^{N} A_m \cos(m\pi \frac{y}{2b}) \cos(m\pi \frac{\eta}{2b}) \exp\left[i \frac{\omega}{c}(x-\xi)\left(\frac{M}{1-M^2} - \Omega_m\right)\right]$$

$$+ \sum_{N+1}^{\infty} A_m \cos(m\pi \frac{y}{2b}) \cos(m\pi \frac{\eta}{2b}) \exp\left[i \frac{\omega}{c}(x-\xi)\left(\frac{M}{1-M^2} - i\Omega_m\right)\right] \qquad (3.36)$$

$$x>\xi \quad G(x,y,\xi,\eta) =$$

$$\sum_{m=0}^{N_1} A_m \cos(m\pi \frac{y}{2b}) \cos(m\pi \frac{\eta}{2b}) \exp\left[i \frac{\omega}{c}(x-\xi)\left(\frac{M}{1-M^2} - \Omega_m\right)\right]$$

$$+ \sum_{N+1}^{\infty} A_m \cos(m\pi \frac{y}{2b}) \cos(m\pi \frac{\eta}{2b}) \exp\left[i \frac{\omega}{c}(x-\xi)\left(\frac{M}{1-M^2} + i\Omega_m\right)\right] \qquad (3.37)$$

We must calculate

$$\varphi(x,y) = \int_{-\infty}^{\infty} \int_{0}^{2b} G(x,y;\xi,\eta)\, F(\xi,\eta)\, d\eta\, d\xi$$

If we let

$$G_-(x,y;\xi,\eta) \equiv G(x,y;\xi,\eta) \qquad x>\xi$$

$$G_+(x,y;\xi,\eta) \equiv G(x,y;\xi,\eta) \qquad x<\xi$$

$$F_-(\xi,\eta) \equiv F(\xi,\eta) \qquad \xi<-a$$

$$F_0(\xi,\eta) \equiv F(\xi,\eta) \qquad -a<\xi<a \tag{3.38}$$

$$F_+(\xi,\eta) \equiv F(\xi,\eta) \qquad \xi>a$$

We may now break up (3.32)

$$x<-a \qquad \varphi(x,y) = \int_0^{2b}\left\{\int_{-\infty}^{x} G_-F_-\,d\xi + \int_{x}^{-a} G_+F_-\,d\xi + \int_{-a}^{a} G_+F_0\,d\xi + \int_{a}^{\infty} G_+F_+\,d\xi\right\}d\eta \tag{3.39}$$

$$|x|<a \qquad \varphi(x,y) = \int_0^{2b}\left\{\int_{-\infty}^{-a} G_-F_-\,d\xi + \int_{-a}^{x} G_-F_0\,d\xi + \int_{x}^{a} G_+F_0\,d\xi + \int_{a}^{\infty} G_+F_+\,d\xi\right\}d\eta \tag{3.40}$$

$$x>a \qquad \varphi(x,y) = \int_0^{2b}\left\{\int_{-\infty}^{-a} G_-F_-\,d\xi + \int_{-a}^{a} G_-F_0\,d\xi + \int_{a}^{x} G_-F_+\,d\xi + \int_{x}^{\infty} G_+F_+\,d\xi\right\}d\eta \tag{3.41}$$

and the solution may be found.

Suppose we are interested in waves which propagate far away from the contraction, i.e., as a result of the second order interaction, what disturbances exist for $x\to\pm\infty$.

Consider first $x\to+\infty$; we use (3.41) and neglect the fourth integral since it must converge to zero. In the first through third integrals we use (3.37) for G_- , and we neglect the second summation

as being exponentially small (we neglect the attenuated waves). Then the Green's function for these three integrals becomes

$$G_-(x,y,\xi,\eta) = \sum_{m=0}^{N_1} A_m \cos\left(m\pi\frac{y}{2b}\right)\cos\left(m\pi\frac{\eta}{2b}\right)\exp\left[i\frac{\omega}{c}(x-\xi)\left(\frac{M}{1-M^2}-\Omega_m\right)\right]$$

and F may be had from (C2), (C3), or (C4) according to (3.38). Since this calculation will give the (inhomogeneous) solution for the pressure wave at $x\to+\infty$ we call it

$$P_I^+ \equiv \varphi(x,y)\Big|_{x\to+\infty} \tag{3.42}$$

Next, we consider $x\to-\infty$. We use (3.39), neglect the first integral, and in G_+ in the last three integrals (use eq. (3.36)), we neglect the third summation (attenuated waves). The Green's function simplifies to

$$G_+(x,y;\xi,\eta) = \sum_{m=0}^{N} A_m \cos\left(m\pi\frac{y}{2b}\right)\cos\left(m\pi\frac{\eta}{2b}\right)\exp\left[i\frac{\omega}{c}(x-\xi)\left(\frac{M}{1-M^2}+\Omega_m\right)\right]$$

$$-\sum_{N_1+1}^{N} A_m \cos\left(m\pi\frac{y}{2b}\right)\cos\left(m\pi\frac{\eta}{2b}\right)\exp\left[i\frac{\omega}{c}(x-\xi)\left(\frac{M}{1-M^2}-\Omega_m\right)\right]$$

and F may be had from (C2), (C3), or (C4) according to (3.38). We call this solution

$$P_I^- \equiv \varphi(x,y)\Big|_{x\to-\infty} \tag{3.43}$$

Homogeneous Equation with Boundary Condition. To complete the solution we must solve the following problem:

$$\left(\frac{\partial}{\partial t}+U\frac{\partial}{\partial x}\right)^2\varphi - c^2\left(\frac{\partial^2}{\partial x^2}+\frac{\partial^2}{\partial y^2}\right)\varphi = 0 \tag{3.44a}$$

$$\left.\frac{\partial \varphi}{\partial y}\right|_{y=0} = G(x)\, e^{i\omega t} \tag{3.44b}$$

$$\left.\frac{\partial \varphi}{\partial y}\right|_{y=2b} = F(x)\, e^{i\omega t} \tag{3.44c}$$

where $\varphi(x,y,t) = \frac{p^{(2)}}{\gamma P}(x,y)e^{i\omega t}$ and the functions F, G will be determined from a second-order expansion of the boundary condition on the channel walls. The sum of this solution and the inhomogeneous solution from the last section will give the complete solution. Let $\Phi(x,y) = \frac{p^{(2)}}{\gamma P}(x,y)$ for brevity; then we get

$$\left(-\omega^2 + 2i\omega U \frac{\partial}{\partial x} + U^2 \frac{\partial^2}{\partial x^2}\right)\Phi - c^2\left(\frac{\partial^2}{\partial x^2} + \frac{\partial^2}{\partial y^2}\right)\Phi = 0 \tag{3.45}$$

Let

$$\Phi(x,y) = \frac{1}{(2\pi)^{1/2}} \int_{-\infty}^{\infty} \psi(\xi, y) e^{-ix\xi}\, d\xi \; : \tag{3.46}$$

assuming the integral converges, this gives for (3.45)

$$\psi_{yy} - (g(\xi))^2 \psi = 0 \tag{3.47}$$

where

$$g(\xi) \equiv + \left(\frac{\omega}{c}\left(2\xi M - \frac{\omega}{c}\right) + (1-M^2)\xi^2\right)^{1/2}$$

which gives

$$\psi_y = a(\xi) e^{g(\xi)y} + b(\xi) e^{-g(\xi)y} \tag{3.48}$$

Transforming the boundary conditions, we define

$$\tilde{G}(\xi) \equiv \psi_y(\xi, 0) = \frac{1}{(2\pi)^{1/2}} \int_{-\infty}^{\infty} G(x) e^{i\xi x} dx \tag{3.49a}$$

$$\tilde{F}(\xi) \equiv \Psi_y(\xi, 2b) = \frac{1}{(2\pi)^{1/2}} \int_{-\infty}^{\infty} F(x) e^{i\xi x} dx \tag{3.49b}$$

We now solve for $a(\xi)$ and $b(\xi)$ in (3.48), to find

$$\Psi_y = \tilde{F}(\xi)\tilde{H}(\xi) + \tilde{G}(\xi)\tilde{J}(\xi) \tag{3.50}$$

where

$$\tilde{H}(\xi) = \frac{\sinh[y\, g(\xi)]}{\sinh[2b g(\xi)]} \qquad \tilde{J}(\xi) = \frac{\sinh[g(\xi)(2b-y)]}{\sinh[2b g(\xi)]} \tag{3.51}$$

Using the convolution theorem we may solve:

$$\Phi_y(x,y) = \frac{1}{(2\pi)^{1/2}} \left\{ \int_{-\infty}^{\infty} F(\xi) H(x-\xi)\, d\xi + \int_{-\infty}^{\infty} G(\xi) J(x-\xi)\, d\xi \right\} \tag{3.52}$$

We must find

$$H(x) = \frac{1}{(2\pi)^{1/2}} \int_{-\infty}^{\infty} \tilde{H}(\xi) e^{-i\xi x} d\xi \qquad J(x) = \frac{1}{(2\pi)^{1/2}} \int_{-\infty}^{\infty} \tilde{J}(\xi) e^{-i\xi x} d\xi \tag{3.53}$$

The details of these calculations may be found in Appendix D. We present the results here.

$x \lesseqgtr 0 \quad H(x) =$

$$\mp \left(\frac{\pi}{2}\right)^{1/2} \left(\frac{1}{b}\right) \exp\left[ix \frac{\omega}{c} \frac{M}{1-M^2}\right]$$

$$\sum_{n=1}^{N} \frac{(-)^n \sin\left(n\pi \frac{y}{2b}\right)}{\left(\left(\frac{2b\omega}{n\pi c}\right)^2 - (1-M^2)\right)^{1/2}} \sin\left[\frac{x}{1-M^2}\left(\left(\frac{\omega}{c}\right)^2 - (1-M^2)\left(\frac{n\pi}{2b}\right)^2\right)^{1/2}\right]$$

$$-\left(\frac{\pi}{2}\right)^{1/2}\left(\frac{1}{b}\right)\sum_{N+1}^{\infty}\frac{(-)^n \sin\left(n\pi\frac{y}{2b}\right)}{\left((1-M^2)-\left(\frac{2b\omega}{n\pi c}\right)^2\right)^{1/2}}$$

$$\exp\left[\frac{x}{1-M^2}\left(i\frac{\omega}{c}M \pm\left((1-M^2)\left(\frac{n\pi}{2b}\right)^2-\left(\frac{\omega}{c}\right)^2\right)^{1/2}\right)\right] \tag{3.54}$$

$x \lesseqgtr 0 \quad J(x) =$

$$\pm\left(\frac{\pi}{2}\right)^{1/2}\left(\frac{1}{b}\right)\exp\left[ix\frac{\omega}{c}\frac{M}{1-M^2}\right]$$

$$\sum_{n=1}^{N}\frac{\sin\left(n\pi\frac{y}{2b}\right)}{\left(\left(\frac{2b\omega}{n\pi c}\right)^2-(1-M^2)\right)^{1/2}}\sin\left[\frac{x}{1-M^2}\left(\left(\frac{\omega}{c}\right)^2-(1-M^2)\left(\frac{n\pi}{2b}\right)^2\right)^{1/2}\right]$$

$$+\left(\frac{\pi}{2}\right)^{1/2}\left(\frac{1}{b}\right)\sum_{N+1}^{\infty}\frac{\sin\left(n\pi\frac{y}{2b}\right)}{\left((1-M^2)-\left(\frac{2b\omega}{n\pi c}\right)^2\right)^{1/2}}$$

$$\exp\left[\frac{x}{1-M^2}\left(i\frac{\omega}{c}M \pm\left((1-M^2)\left(\frac{n\pi}{2b}\right)^2-\left(\frac{\omega}{c}\right)^2\right)^{1/2}\right)\right] \tag{3.55}$$

where again N is the largest integer such that

$$\left(\frac{\omega}{c}\right)^2 > (1-M^2)\left(\frac{N\pi}{2b}\right)^2$$

We now calculate $G(x), F(x)$ from (3.44). The boundary condition on $y=0$ is

$$\left.\frac{v^{(1)}+v^{(2)}}{U+u^{(1)}+u^{(2)}}\right|_{y=f(x)} = \frac{df}{dx} \tag{3.56}$$

which insures tangency of velocity at the wall. Expand the velocity terms in a Taylor series about y = 0:

$$u^{(1)}(x,f(x)) = u^{(1)}(x,0) + \left.\frac{\partial u^{(1)}}{\partial y}\right|_{y=0} f(x) + \cdots$$

$$v^{(1)}(x,f(x)) = v^{(1)}(x,0) + \left.\frac{\partial v^{(1)}}{\partial y}\right|_{y=0} f(x) + \cdots$$

We insert this expression into (3.56), and retaining second-order terms

$$\frac{v^{(2)}}{U}(x,0) = \frac{v^{(1)}}{U}(x,0)\ \frac{u^{(1)}}{U}(x,0) - \frac{\partial v^{(1)}}{\partial y}(x,0)\ \frac{f(x)}{U} \tag{3.57}$$

A similar procedure at $y = 2b$ gives

$$\frac{v^{(2)}}{U}(x,2b) = \frac{v^{(1)}}{U}(x,2b)\ \frac{u^{(1)}}{U}(x,2b) - \frac{\partial v^{(1)}}{\partial y}(x,2b)\ \frac{f(x)}{U} \tag{3.58}$$

Using (3.12) we may write

$$\frac{\partial \varphi}{\partial y} = -\frac{1}{c^2}\left[\left(\frac{\partial}{\partial t}+U\frac{\partial}{\partial x}\right)v^{(2)} + \frac{\rho^{(1)}}{\rho}\left(\frac{\partial}{\partial t}+U\frac{\partial}{\partial x}\right)v^{(1)} + \left(u^{(1)}\frac{\partial}{\partial x}+v^{(1)}\frac{\partial}{\partial y}\right)v^{(1)}\right] \tag{3.59}$$

which we evaluate at $y=0$ (or $y = 2b$) and insert (3.58).

Consistent with our previous work we retain only the cross terms of interest, which simplifies (3.59):

$$\frac{\partial \varphi}{\partial y} = -\frac{1}{c^2}\frac{\rho_s^{(1)}}{\rho}U\frac{\partial v^{(1)}}{\partial x} \tag{3.60}$$

where $\frac{\rho_s^{(1)}}{\rho}$ may be had from (3.14) and $v^{(1)}$ from

$$v^{(1)} = \begin{cases} 0 & |x|>a \\ \left.\begin{matrix} \cup \frac{df}{dx} \\ -\cup \frac{df}{dx} \end{matrix}\right\} & |x|<a \end{cases} \qquad \begin{matrix} y=0 \\ y=2b \end{matrix} \tag{3.61}$$

Combining (3.14) and (3.61) into (3.60) and setting $\omega_s = \omega$:

$$G(x) = \tfrac{1}{2} M^2 \sigma \epsilon \left(\frac{\pi}{a}\right)^2 \exp(-ik_s x \cos\nu_s)\left(\cos(\pi\tfrac{x}{a}) + \cos(2\pi\tfrac{x}{a})\right) \quad |x|<a$$

$$= 0 \quad |x|>a$$

$$F(x) = -\tfrac{1}{2} M^2 \sigma \epsilon \left(\frac{\pi}{a}\right)^2 \exp(-ik_s x\cos\nu_s - i2bk_s \sin\nu_s)$$
$$\left(\cos(\pi\tfrac{x}{a}) + \cos(2\pi\tfrac{x}{a})\right) \quad |x|<a$$

$$= 0 \quad |x|>a \tag{3.62}$$

We are now in a position to perform the integration (3.52) using (3.54), (3.55), and (3.62). We substitute ξ for x in (3.62) and $x-\xi$ for x in (3.54) and (3.55). The integration (3.52) may be written

$$(2\pi)^{1/2} \Phi_y(x,y) = \int_{-a}^{a} F(\xi) H(x-\xi)\, d\xi + \int_{-a}^{a} G(\xi) J(x-\xi)\, d\xi \tag{3.63}$$

If we are interested in $x<-a$ (or $x>a$) we have $\xi>x$ (or $\xi<x$) in these expressions, so we use the appropriate form of $H(x-\xi)$ and $J(x-\xi)$ for $x-\xi<0$ (or $x-\xi>0$, see (3.54)). We also must insure that the radiation condition is satisfied. We want no waves propagating upstream for $x>>a$ and no waves propagating downstream for

$x << -a$. This condition is satisfied by limiting the indices on eqs. (3.54), (3.55). If we are interested in $|x| >> a$ we may neglect the attentuated waves, i.e., $n > N$ in any summation.

For $|x| < a$ we must integrate in the following manner:

$$(2\pi)^{1/2}\,\Phi_y(x,y) = \int_{-a}^{x} F(\xi) H_l(x-\xi)\,d\xi + \int_{x}^{a} F(\xi) H_r(x-\xi)\,d\xi$$

$$+ \int_{-\infty}^{x} G(\xi) J_l(x-\xi)\,d\xi + \int_{x}^{a} G(\xi) J_r(x-\xi)\,d\xi \qquad (3.64)$$

where the subscript l (or r) refers to the appropriate form of $H(x-\xi)$ or $J(x-\xi)$ for $x-\xi > 0$ (or $x-\xi < 0$). In this manner we may find

$$\varphi(x,y,t) = \Phi(x,y) e^{i\omega t} = \frac{P^{(2)}}{\gamma P}(x,y) e^{i\omega t}$$

Since this is the homogeneous solution, we define

$$P_H^+ = \varphi(x,y,t)\Big|_{x\to+\infty} \qquad (3.65)$$

$$P_H^- = \varphi(x,y,t)\Big|_{x\to-\infty} \qquad (3.66)$$

which will give the waves propagating at large distances from the contraction and correspond to (3.42) and (3.43) for the inhomogeneous solutions.

3.5 Calculation of the Duct Modes

The acoustic waves which propagate in a (constant-area) channel must satisfy the homogeneous wave equation:

$$\left\{\left(\frac{\partial}{\partial t}+U\frac{\partial}{\partial x}\right)^2-c^2\left(\frac{\partial^2}{\partial x^2}+\frac{\partial^2}{\partial y^2}\right)\right\}\varphi = 0 \qquad (3.67)$$

where $\varphi(x,y,t)$ is the velocity potential associated with the wave. The solutions to (3.67) will be of the form

$$\varphi(x,y,t) \sim \exp\left[i(\omega t - kx\cos\nu - ky\sin\nu)\right] \qquad (3.68)$$

which are waves with constant phase lines with normal at angle ν to X direction. Substitution of (3.68) into (3.67) gives the dispersion relation

$$k = \frac{\omega/c}{M\cos\nu \pm 1} \qquad (3.69)$$

Since the vertical velocity must vanish at the channel top and bottom, say $y=0, 2b$, we have

$$\left.\frac{\partial\varphi}{\partial y}\right|_{y=0} = \left.\frac{\partial\varphi}{\partial y}\right|_{y=2b} = 0$$

and so the vertical velocity will be of the form

$$\sin\left(m\pi\frac{y}{2b}\right)\exp\left[i(\omega t - kx\cos\nu)\right] \qquad m=0,1,\cdots$$

The pressure may be written in the form

$$P(\nu)\cos\left(m\pi\frac{y}{2b}\right)\exp\left[i(\omega t - kx\cos\nu)\right] \qquad (3.70)$$

where $P(\nu)$ is the amplitude of the mode with wave front angle ν, and is complex in general. We would like to express our solutions, P_I^+, P_I^-, P_H^+, P_H^- (3.42), (3.43), (3.65), (3.66) in this form. Then, given the mode number m we should be able to give the angle of the wavefront ν, the amplitude, and the phase of the

mode. First, we define the following dimensionless variables:

$\beta = \frac{\omega a}{c}$ the reduced frequency, which relates the acoustic wavelength to the contraction length

$\xi = \frac{x}{a}$ dimensionless axial length

$\eta = \frac{y}{2b}$ dimensionless vertical length

$\delta = b/a$ height-to-length ratio of contraction

$$R_m = \left(1-(1-M^2)\left(\frac{m\pi}{2\beta\delta}\right)^2\right)^{1/2} \quad m \le N \quad \text{(i.e., } R_m \text{ is real and positive)}$$

For the homogeneous transmitted wave (P_H^+) we have wavefront angle:

$$\cos \nu_m = \frac{M-R_m}{MR_m-1} \tag{3.71}$$

and amplitude P_{Hm}^+ :

$$\frac{P_{Hm}^+}{\frac{3i}{2}\frac{\epsilon\sigma}{a}M^2\pi^3} = \left[2\left(1+\cos\left(2\beta\delta\tan\nu_s+m\pi\right)\right)\right]^{1/2}$$

$$\left\{\frac{\frac{\beta}{1-M^2}\left(\frac{1}{M}-R_m\right)\sin\left[\frac{\beta}{1-M^2}\left(\frac{1}{M}-R_m\right)\right]}{m\left(\left(\frac{2\beta\delta}{m\pi}\right)^2-(1-M^2)\right)^{1/2}\left[\pi^2-\left(\frac{\beta}{1-M^2}\right)^2\left(\frac{1}{M}-R_m\right)^2\right]\left[(2\pi)^2-\left(\frac{\beta}{1-M^2}\right)^2\left(\frac{1}{M}-R_m\right)^2\right]}\right\} \tag{3.72a}$$

and phase ϕ_{Hm}^+ :

$$\tan\phi_{Hm}^+ = \frac{\sin\left(2\beta\delta\tan\nu_s+m\pi\right)}{1+\cos\left(2\beta\delta\tan\nu_s+m\pi\right)} \tag{3.72b}$$

$1 \le m \le N_1$

Just as in the inhomogeneous solution, two unique waves may propagate upstream. For the homogeneous reflected wave P_H^- we have wavefront angles ν_{1m}, ν_{2m} :

$$\cos \nu_{1m} = \frac{M+R_m}{1+MR_m} \qquad 1 \le m \le N \tag{3.73}$$

$$\cos \nu_{2m} = \frac{M-R_m}{1-MR_m} \qquad N_1 < m \le N \tag{3.74}$$

and amplitude P_{H1m}^{-}, P_{H2m}^{-}

$$\frac{P_{H1m}^{-}}{\frac{3i}{2}\frac{\epsilon\sigma}{a}M^2\pi^3} = \left[2\left(1+\cos(2\beta\delta\tan\nu_s+m\pi)\right)\right]^{1/2}$$

$$\left\{\frac{\frac{\beta}{1-M^2}\left(\frac{1}{M}+R_m\right)\sin\left[\frac{\beta}{1-M^2}\left(\frac{1}{M}+R_m\right)\right]}{m\left(\left(\frac{2\beta\delta}{m\pi}\right)^2-(1-M^2)\right)^{1/2}\left[\pi^2-\left(\frac{\beta}{1-M^2}\right)^2\left(\frac{1}{M}+R_m\right)^2\right]\left[(2\pi)^2-\left(\frac{\beta}{1-M^2}\right)^2\left(\frac{1}{M}+R_m\right)^2\right]}\right\} \tag{3.75}$$

$1 \le m \le N$

$$P_{H2m}^{-} = -P_{Hm}^{+} \tag{3.76a}$$

$N_1 < m \le N$

and phase ϕ_{H1m}^{-}, ϕ_{H2m}^{-}

$$\tan\phi_{H1m}^{-} = \tan\phi_{Hm}^{+} \qquad 1 \le m \le N \tag{3.76b}$$

$$\tan\phi_{H2m}^{-} = \tan\phi_{Hm}^{+} \qquad N_1 < m \le N$$

For the inhomogeneous transmitted wave P_{Im}^{+} we have wavefront angle ν_m,

$$\cos\nu_m = \frac{M-R_m}{MR_m-1} \qquad 0 \le m \le N_1 \tag{3.77}$$

The amplitude is best left complex:

$$\frac{P_{Im}^{(+)}}{\frac{\epsilon\sigma}{b}\frac{M^2}{1-M^2}\pi^2 A_m} = \Bigg\{$$

$$-i\beta\delta\frac{(1-M^2)^{1/2}}{M}\Bigg[-\frac{1}{2}\left(\frac{\left(\frac{I_{a1m}}{a}\right)\left(\frac{I_{em1}}{a}\right)}{\sinh(\pi\delta(1-M^2)^{1/2})}+\frac{\left(\frac{I_{a2m}}{a}\right)\left(\frac{I_{em2}}{a}\right)}{\sinh(2\pi\delta(1-M^2)^{1/2})}\right)$$

$$+\sum_{n=1}^{\infty}\exp\left[\frac{-n\pi}{\delta(1-M^2)^{1/2}}\right]\left(\frac{I_{cnm}}{a}\right)\left(\frac{I_{fmn}}{a}\right)\left(\frac{n\pi}{1-M^2}\right)\frac{\Phi_n}{b^2}\Bigg]$$

$$-\frac{\delta\pi}{2}(1-M^2)^{1/2}\left(\frac{\left(\frac{I_{b1m}}{a}\right)\left(\frac{I_{em1}}{a}\right)}{\sinh(\pi\delta(1-M^2)^{1/2})}+2\frac{\left(\frac{I_{b2m}}{a}\right)\left(\frac{I_{em2}}{a}\right)}{\sinh(2\pi\delta(1-M^2)^{1/2})}\right)$$

$$+\sum_{n=1}^{\infty}\exp\left[\frac{-n\pi}{\delta(1-M^2)^{1/2}}\right]\left(\frac{I_{dnm}}{a}\right)\left(\frac{I_{fmn}}{a}\right)\left(\frac{n^2\pi^2}{1-M^2}\right)\frac{\Phi_n}{b^2}$$

$$-i\beta\delta\tan\nu_s\Bigg[-\frac{(1-M^2)}{2}\frac{\left(\frac{I_{b1m}}{a}\right)\left(\frac{I_{hm1}}{a}\right)}{\sinh(\pi\delta(1-M^2)^{1/2})}+\frac{\left(\frac{I_{b2m}}{a}\right)\left(\frac{I_{hm2}}{a}\right)}{\sinh(2\pi\delta(1-M^2)^{1/2})}$$

$$-\sum_{n=1}^{\infty}\exp\left[\frac{-n\pi}{\delta(1-M^2)^{1/2}}\right]\left(\frac{I_{dnm}}{a}\right)\left(\frac{I_{gmn}}{a}\right)(n\pi)\frac{\Phi_n}{b^2}\Bigg]$$

$$+\delta(1-M^2)^{3/2}\frac{\pi}{2}\left(\frac{\left(\frac{I_{b1m}}{a}\right)\left(\frac{I_{em1}}{a}\right)}{\sinh(\pi\delta(1-M^2)^{1/2})}+2\frac{\left(\frac{I_{b2m}}{a}\right)\left(\frac{I_{em2}}{a}\right)}{\sinh(2\pi\delta(1-M^2)^{1/2})}\right)$$

$$-\sum_{n=1}^{\infty}\exp\left[\frac{-n\pi}{\delta(1-M^2)^{1/2}}\right]\left(\frac{I_{dnm}}{a}\right)\left(\frac{I_{fmn}}{a}\right)(n\pi)^2\frac{\Phi_n}{b^2}$$

$$+\sum_{n=1}^{\infty}\left(\frac{\rho_n}{b^2}\right)\sinh\left[\frac{n\pi}{\delta(1-M^2)^{\frac{1}{2}}}\right]$$

$$\left[\left\{\frac{\exp\left[\frac{-n\pi}{\delta(1-M^2)^{1/2}}\right]\exp\left[-i\beta\left(\frac{1}{M(1-M^2)}-\left(\frac{1}{(1-M^2)^2}-\left(\frac{m\pi}{2\beta\delta}\right)^2\frac{1}{1-M^2}\right)^{1/2}\right)\right]}{\frac{n\pi}{\delta(1-M^2)^{1/2}}+i\beta\left(\frac{1}{M(1-M^2)}-\left(\frac{1}{(1-M^2)^2}-\left(\frac{m\pi}{2\beta\delta}\right)^2\frac{1}{1-M^2}\right)^{1/2}\right)}\right\}\right.$$

$$\left\{\left[\frac{-n\pi}{(1-M^2)^{1/2}}\left(\frac{n\pi}{(1-M^2)^{1/2}}+\frac{i\beta\delta}{M}\right)+(n\pi)^2\right]\left(\frac{I_{fmn}}{a}\right)-\frac{in\pi\beta\delta}{M}\tan\nu_s\left(\frac{I_{gmn}}{a}\right)\right\}$$

$$-\left\{\frac{\exp\left[\frac{-n\pi}{\delta(1-M^2)^{1/2}}\right]\exp\left[i\beta\left(\frac{1}{M(1-M^2)}-\left(\frac{1}{(1-M^2)^2}-\left(\frac{m\pi}{2\beta\delta}\right)^2\frac{1}{1-M^2}\right)^{\frac{1}{2}}\right)\right]}{\frac{n\pi}{\delta(1-M^2)^{1/2}}-i\beta\left(\frac{1}{M(1-M^2)}-\left(\frac{1}{(1-M^2)^2}-\left(\frac{m\pi}{2\beta\delta}\right)^2\frac{1}{1-M^2}\right)^{1/2}\right)}\right\}$$

$$\left.\left\{\left[\frac{n\pi}{(1-M^2)^{1/2}}\left(\frac{n\pi}{(1-M^2)^{1/2}}-\frac{i\beta\delta}{M}\right)-(n\pi)^2\right]\left(\frac{I_{fmn}}{a}\right)+\frac{in\pi\beta\delta}{M}\tan\nu_s\left(\frac{I_{gmn}}{a}\right)\right\}\right]$$

$$\Bigg\} = \frac{P_{Im}^{(+)}}{\frac{\epsilon\sigma}{b}\frac{M^2}{1-M^2}\pi^2 A_m}$$

$$0 \le m \le N, \qquad (3.78)$$

For the inhomogeneous reflected wave (P_I^-) we have wave-front angles ν_{1m}, ν_{2m}

$$\cos \nu_{1m} = \frac{M + R_m}{1 + M R_m} \qquad 0 \le m \le N \tag{3.79}$$

$$\cos \nu_{2m} = \frac{M - R_m}{1 - M R_m} \qquad N_1 < m \le N \tag{3.80}$$

and complex amplitudes :

$$\frac{P^{(-)}_{I1m}}{\frac{\epsilon\sigma}{b}\frac{M^2}{1-M^2}\pi^2 A_m} = \Bigg\{$$

$$-i\beta\delta\frac{(1-M^2)^{1/2}}{M}\Bigg[\left(-\frac{1}{2}\frac{\left(\frac{I_{a1m}}{a}\right)\left(\frac{I_{em1}}{a}\right)}{\sinh(\pi\delta(1-M^2)^{1/2})}+\frac{\left(\frac{I'_{a2m}}{a}\right)\left(\frac{I_{em2}}{a}\right)}{\sinh(2\pi\delta(1-M^2)^{1/2})}\right)$$

$$+\sum_{n=1}^{\infty}\exp\left[\frac{-n\pi}{\delta(1-M^2)^{1/2}}\right]\left(\frac{I'_{cnm}}{a}\right)\left(\frac{I_{fmn}}{a}\right)\left(\frac{n\pi}{1-M^2}\right)\frac{\rho_n}{b^2}\Bigg]$$

$$-\frac{\delta}{2}\pi(1-M^2)^{1/2}\left(\frac{\left(\frac{I_{b1m}}{a}\right)\left(\frac{I_{em1}}{a}\right)}{\sinh(\pi\delta(1-M^2)^{1/2})}+2\frac{\left(\frac{I_{b2m}}{a}\right)\left(\frac{I_{em2}}{a}\right)}{\sinh(2\pi\delta(1-M^2)^{1/2})}\right)$$

$$+\sum_{n=1}^{\infty}\exp\left[\frac{-n\pi}{\delta(1-M^2)^{1/2}}\right]\left(\frac{I'_{dnm}}{a}\right)\left(\frac{I_{fmn}}{a}\right)\left(\frac{n^2\pi^2}{1-M^2}\right)\frac{\rho_n}{b^2}$$

$$-\frac{i\beta\delta}{M}\tan\nu_3\Bigg[-\frac{(1-M^2)}{2}\left(\frac{\left(\frac{I_{b1m}}{a}\right)\left(\frac{I_{hm1}}{a}\right)}{\sinh(\pi\delta(1-M^2)^{1/2})}+\frac{\left(\frac{I_{b2m}}{a}\right)\left(\frac{I_{hm2}}{a}\right)}{\sinh(2\pi\delta(1-M^2)^{1/2})}\right)$$

$$-\sum_{n=1}^{\infty}\exp\left[\frac{-n\pi}{\delta(1-M^2)^{1/2}}\right]\left(\frac{I'_{dnm}}{a}\right)\left(\frac{I_{gmn}}{a}\right)(n\pi)\frac{\rho_n}{b^2}\Bigg]$$

$$+\delta(1-M^2)^{3/2}\frac{\pi}{2}\left(\frac{\left(\frac{I_{b1m}}{a}\right)\left(\frac{I_{em1}}{a}\right)}{\sinh(\pi\delta(1-M^2)^{1/2})}+2\frac{\left(\frac{I_{b2m}}{a}\right)\left(\frac{I_{em2}}{a}\right)}{\sinh(2\pi\delta(1-M^2)^{1/2})}\right)$$

$$-\sum_{n=1}^{\infty}\exp\left[\frac{-n\pi}{\delta(1-M^2)^{1/2}}\right]\left(\frac{I'_{dnm}}{a}\right)\left(\frac{I_{fmn}}{a}\right)(n\pi)^2\frac{\rho_n}{b^2}$$

$$+\sum_{n=1}^{\infty}\left(\frac{\rho_n}{b^2}\right)\sinh\left[\frac{n\pi}{\delta(1-M^2)^{1/2}}\right]$$

$$\left[\left\{\frac{\exp\left[\frac{-n\pi}{\delta(1-M^2)^{1/2}}\right]\exp\left[-i\beta\left(\frac{1}{M(1-M^2)}+\left(\frac{1}{(1-M^2)^2}-\left(\frac{m\pi}{2\beta\delta}\right)^2\frac{1}{1-M^2}\right)^{1/2}\right)\right]}{\frac{n\pi}{\delta(1-M^2)^{1/2}}+i\beta\left(\frac{1}{M(1-M^2)}+\left(\frac{1}{(1-M^2)^2}-\left(\frac{m\pi}{2\beta\delta}\right)^2\frac{1}{1-M^2}\right)^{1/2}\right)}\right\}\right.$$

$$\left\{\left[\frac{-n\pi}{(1-M^2)^{1/2}}\left(\frac{n\pi}{(1-M^2)^{1/2}}+\frac{i\beta\delta}{M}\right)+(n\pi)^2\right]\left(\frac{I_{fmn}}{a}\right)-\frac{in\pi\beta\delta}{M}\tan\nu_s\left(\frac{I_{gmn}}{a}\right)\right\}$$

$$-\left\{\frac{\exp\left[\frac{-n\pi}{\delta(1-M^2)^{1/2}}\right]\exp\left[+i\beta\left(\frac{1}{M(1-M^2)}+\left(\frac{1}{(1-M^2)^2}-\left(\frac{m\pi}{2\beta\delta}\right)^2\frac{1}{1-M^2}\right)^{1/2}\right)\right]}{\frac{n\pi}{\delta(1-M^2)^{1/2}}-i\beta\left(\frac{1}{M(1-M^2)}+\left(\frac{1}{(1-M^2)^2}-\left(\frac{m\pi}{2\beta\delta}\right)^2\frac{1}{1-M^2}\right)^{1/2}}\right\}$$

$$\left.\left\{\left[\frac{n\pi}{(1-M^2)^{1/2}}\left(\frac{n\pi}{(1-M^2)^{1/2}}-\frac{i\beta\delta}{M}\right)-(n\pi)^2\right]\left(\frac{I_{fmn}}{a}\right)+\frac{in\pi\beta\delta}{M}\tan\nu_s\left(\frac{I_{gmn}}{a}\right)\right\}\right]$$

$$\left.\right\}=\frac{P_{Im}^{(-)}}{\frac{\epsilon\sigma}{b}\frac{M^2}{1-M^2}\pi^2 A_m}\qquad 0\le m\le N\qquad(3.81)$$

$$P_{I2m}^{(-)}=-P_{Im}^{(+)}\qquad N_1<m\le N\qquad(3.82)$$

The quantity A_m has been defined before. In terms of the dimensionless quantities

$$A_m = \begin{cases} \dfrac{1}{4i\beta\delta} & m = 0 \\ \dfrac{1}{2i}\left((\beta\delta)^2 - \left(\dfrac{m\pi}{2}\right)^2 (1-M^2)\right)^{-1/2} & 0 < m \le N \end{cases} \qquad (3.82a)$$

also

$$\frac{Q_n}{b^2} = \frac{3\delta^2/\pi^2}{\left(\delta^2 + \frac{n^2}{1-M^2}\right)\left((2\delta)^2 + \frac{n^2}{1-M^2}\right)} \qquad (3.82b)$$

The remaining quantities to be defined are:

$I_{alm}, I'_{alm}, I_{blm}, I'_{blm}$ $(l=1,2)$, $I_{cnm}, I'_{cnm}, I_{dnm}, I'_{dnm}$

$I_{eml}, I_{fml}, I_{fmn}, I_{gmn}$ and may be found in Appendix E.

We recall that N and N_1 are the largest integers such that

$$\frac{N\pi}{2\beta\delta} < \frac{1}{(1-M^2)^{1/2}} \qquad \frac{N_1\pi}{2\beta\delta} < 1 \qquad (3.82c)$$

The procedure for calculating the final solution is straightforward. The dimensionless parameters at our disposal are M, δ, β, and ν_s, the entropy wavefront angle. We may then calculate the complex amplitude of each mode by adding the homogeneous solution (eqs. (3.72a), (3.72b) or (3.75), (3.76a), (3.76b)) and the inhomogeneous solution (eq. (3.78) or (3.81), (3.82)).

If we specify M, δ, β we can calculate N, the number of modes which will propagate in the duct, from

$$N = \text{largest integer} < \frac{2\beta\delta}{\pi(1-M^2)^{1/2}}, \qquad (3.83)$$

so a higher frequency disturbance gives more propagating modes.

3.6 Response to a General Two-Dimensional Entropy Wave

We have an entropy wave of general vertical dependence convecting with the mean flow. Then taking the place of (3.14) we assume

$$\frac{\rho_s^{(1)}}{\rho} \equiv \sigma(x,y,t) = e^{i(\omega t - \frac{\omega x}{U})} f(y) \tag{3.84}$$

Expand f as a Fourier series in $(0, 2b)$:

$$f(y) = \frac{a_0}{2} + \sum_{j=1}^{\infty} \left(a_j \cos\left(j\pi \frac{y}{b}\right) + b_j \sin\left(j\pi \frac{y}{b}\right)\right) \tag{3.85}$$

the coefficients of the expansion may be calculated from

$$\begin{aligned} a_j &= \frac{1}{b}\int_0^{2b} f(y)\cos\left(j\pi\frac{y}{b}\right) dy \\ b_j &= \frac{1}{b}\int_0^{2b} f(y)\sin\left(j\pi\frac{y}{b}\right) dy \end{aligned} \tag{3.86}$$

Hence,

$$\sigma(x,y,t) = e^{i\omega t} e^{-i\frac{\omega x}{U}} \left[\frac{a_0}{2} + \sum_{j=1}^{\infty} \left\{ \frac{a_j}{2}\left[e^{ij\pi\frac{y}{b}} + e^{-ij\pi\frac{y}{b}}\right] + \frac{b_j}{2i}\left[e^{ij\pi\frac{y}{b}} - e^{-ij\pi\frac{y}{b}}\right] \right\} \right] \tag{3.87}$$

Since our previous work requires the entropy wavefront angle for calculation of the acoustic mode, we would like to express (3.87) in the form

$$\sigma_\nu e^{i\omega t} e^{-ik_s(x\cos\nu_s + y\sin\nu_s)} \qquad k_s = \omega/U\cos\nu_s \tag{3.88}$$

We therefore re-write (3.87):

$$\sigma(x,y,t) = e^{i\omega t}\left\{ \sigma_o e^{-ik_s(x\cos\nu_o + y\sin\nu_o)} \right.$$

$$\left. + \sum_{j=1}^{\infty}\left[\sigma_j e^{-ik_s(x\cos\nu_j + y\sin\nu_j)} + \tilde{\sigma}_j e^{-ik_s(x\cos\tilde{\nu}_j + y\sin\tilde{\nu}_j)}\right]\right\} \quad (3.89)$$

with

$$\sigma_o = \frac{a_o}{2} \qquad \nu_o = 0 \quad (3.90a)$$

and for the j^{th} entropy mode:

$$\sigma_j = \frac{a_j}{2} + \frac{b_j}{2i} \qquad \nu_j = \tan^{-1} j\frac{\pi M}{\beta\delta}, \quad j>0$$

$$\tilde{\sigma}_j = \frac{a_j}{2} - \frac{b_j}{2i} \qquad \tilde{\nu}_j = -\nu_j \qquad j>0 \quad (3.90b)$$

We have seen, eq. (3.70), that in the m^{th} acoustic mode resulting from a disturbance of the type (3.88) propagating at infinity may be written

$$\frac{P_m^{(2)}}{\gamma P}(x,y,t) = K P_m(\nu_s)\sigma_\nu \cos\left(m\pi\frac{y}{2b}\right) e^{i(\omega t - k\cos\nu_m x)} \quad (3.91)$$

Here, K is a constant depending on M and ϵ/b, σ_ν is the amplitude of the entropy wave with wavefront angle ν_s, and $P_m(\nu_s)$ is the amplitude of the mode. Given the entropy wave $f(y)$ we can use (3.89) to give the general result for the amplitude of the mode m, $\tilde{P}_m$:

$$\tilde{P}_m = \sigma_o P_m(\nu=0) + \sum_{j=1}^{\infty}\left[\sigma_j P_m(\nu_j) + \tilde{\sigma}_j P_m(-\nu_j)\right] \quad (3.92)$$

We would like to relate $P_m(\nu_j)$ to $P_m(-\nu_j)$. Since an entropy wave of the form of (3.88) gives a resulting mode of the form of (3.91), we consider an entropy wave of the form

$$\sigma(x,y,t) = \sigma_\nu e^{i\omega t} e^{-ik_s(x\cos(-\nu_s)+y\sin(-\nu_s))} \tag{3.93}$$

which is identical with (3.88) except we use the negative of the entropy wavefront angle. For non-zero wavefront angles of interest (i.e., $\tan\nu_s = j\pi\frac{M}{\beta\delta}$), (3.93) may be written as

$$\begin{aligned}\sigma(x,y,t) &= \sigma_\nu e^{i\omega t} e^{-ik_s x\cos\nu_s} e^{ij\pi\frac{y}{b}} \\ &= \sigma_\nu e^{i\omega t} e^{-ik_s x\cos\nu_s} e^{-ij\frac{\pi}{b}(2b-y)} \qquad (3.94)\end{aligned}$$

$$k_s\cos\nu_s = \omega/U$$

If we now let $\eta = 2b-y \qquad 0\le\eta\le 2b$ we get

$$\sigma(x,\eta,t) = \sigma_\nu e^{i\omega t} e^{-ik_s x\cos\nu_s} e^{-ij\frac{\pi}{b}\eta} \tag{3.95}$$

but from (3.91) we must get an acoustic mode of the form

$$\frac{p^{(2)}}{\gamma P}(x,\eta,t) = K P_m(\nu_j)\sigma_\nu \cos\left(m\pi\frac{\eta}{2b}\right) e^{i(\omega t - kx\cos\nu_m)}$$

where

$$\nu_j = \tan^{-1}\left(j\pi\frac{M}{\beta\delta}\right)$$

If we now express the mode in terms of y again (we are essentially turning the duct "upside down" from the viewpoint of any pressure measurement but not from the point of view of the entropy wave), we get

$$\begin{aligned}\frac{p_m^{(2)}}{\gamma P} &= K\sigma_\nu P_m(\nu_j)\cos\left(m\pi\left(1-\frac{y}{2b}\right)\right)e^{i(\omega t-kx\cos\nu_m)} \\ &= (-)^m K\sigma_\nu P_m(\nu_j)\cos\left(m\pi\frac{y}{2b}\right)e^{i(\omega t-kx\cos\nu_m)} \qquad (3.96)\end{aligned}$$

which is identical to (3.91) except for the factor $(-)^m$.

We now have the mode amplitude resulting from a negative entropy wavefront angle. Comparing (3.96) with (3.91) we may write

$$P_m(-\nu_s) = (-)^m P_m(\nu_s) \qquad (3.97)$$

$$\text{if} \qquad \nu_s = \tan^{-1}\left(j \frac{M\pi}{\beta\delta}\right) \qquad j = 1,2\cdots$$

We may now write (3.92) as

$$\tilde{P}_m = \sigma_0 A_m(\nu=0) + \sum_{j=1}^{\infty} A_m(\nu_j)\left[\sigma_j + (-)^m \tilde{\sigma}_j\right] \qquad (3.98)$$

We see that given the Fourier coefficients (3.90) of the cross-sectional dependence of the entropy wave we can calculate the amplitude of mode m by considering only non-negative entropy wavefronts. Each wavefront ν_j corresponds to a mode of the Fourier expansion (3.89).

Expressing the wavefront angles as

$$\nu_j = \tan^{-1}\left(j \frac{M\pi}{\beta\delta}\right) \qquad (3.99)$$

we notice from Appendix E, eq. (E7) and eq. (E8), that the integrals I_{fmn} and I_{gmn} must be calculated differently if

$$2n = \pm(m \pm 2j) \qquad (3.100)$$

Otherwise, we may use eq. (E7) or eq. (E8) directly.

In Section 3.3 we solved for the steady pressure disturbance resulting from the wall deflection. The solution (3.28) may be considered a cosine series expansion, $a_n \cos(n2\pi\eta)$, $(\eta = y/2b)$ where

the a_n are functions of X. By writing a general entropy wave in terms of a Fourier series (3.85), (3.86), we found that only certain wavefront angles need be considered, (3.99). Now the first term in the integral for I_{fmn}, i.e., $\cos m\pi\eta$, is the vertical dependence of the duct mode. The second term ($\cos n2\pi\eta$) is from the cosine series expansion (3.28) of the steady wall pressure. The third term ($e^{-i2\frac{\beta\delta}{M}(\tan\nu_s)\eta}$) is the vertical dependence of the entropy wave. The term $(\cos n2\pi\eta)(e^{-2i\frac{\beta\delta}{M}(\tan\nu_s)\eta})$ may be considered to be the vertical dependence of the interaction of the entropy wave and the steady pressure disturbances from the wall deflections. Then the integral I_{fmn} is just a calculation of the m^{th} cosine coefficient of an expansion (from $0 \le \eta \le 1$) of this interaction.

3.7 Response to High-Frequency Disturbances

We would like to investigate the behavior of the mode amplitude for a given entropy mode (j = constant) as the reduced frequency becomes large. Since j = constant, (3.99) gives

$$\frac{\beta\delta}{M}\tan\nu_j = \text{constant} \qquad (3.101)$$

Consider first the homogeneous solution (3.72), (3.75), and (3.76). It is clear that

$$P^{\pm}_{Hm} \sim \beta^{-4} \qquad \beta \to \infty$$

Now consider the inhomogeneous transmitted wave (3.78). By looking at the values of the integrals defined in Appendix E, and keeping in mind (3.101), we find for $\beta \to \infty$

$$I_{alm},\ I'_{alm} \sim \beta^{-2}$$
$$I_{blm}, I'_{blm}, I_{cnm}, I'_{cnm}, I_{dnm}, I'_{dnm} \sim \beta^{-1} \qquad (3.102)$$
$$I_{eml}, I_{hml}, I_{fmn}, I_{gmn} \sim \beta^{0}$$

From the definition of (3.82b)

$$A_m \sim \beta^{-1}$$

By considering (3.78), we see that the dominant terms seem to be the first and the last summations. Considering the factor A_m leading the equation, we see that

$$\frac{P^{+}_{Im}}{\frac{\epsilon}{b}\sigma\frac{M^2}{1-M^2}\pi} = \frac{K}{\beta} + \mathcal{O}(\beta^{-2}) \qquad \beta \to \infty$$

The coefficient K may be easily calculated by expanding I_{cnm} for high frequency and by expanding the coefficient in the fifth summation similarly. Doing so, however, we will find that to $\mathcal{O}(\beta^{-1})$ K is zero, which implies that the first and fifth summations do not dominate.

The inhomogeneous solution for the mode amplitude tends to zero for high frequency like β^{-n} where n is at least 2.

Rather than carry out the expansion to $\mathcal{O}(\beta^{-2})$, the full calculation was carried out for several large values of β. The results, as well as the other parameters, are given below:

$\delta = 1$ (contraction aspect ratio, b/a)

$M = .3$

$m = 2$ (second acoustic mode)

$j = 1$ (first entropy mode)

β	$\beta^4\lvert P_H^+\rvert$	$\beta^4\lvert P_H^-\rvert$	$\beta^4\lvert P_I^+\rvert$	$\beta^4\lvert P_I^-\rvert$
30	.80	.12	2.12	.16
100	.73	.12	1.96	.17
500	.23	.05	3.02	.05

The above amplitudes have been normalized as follows

$$|P| \equiv \frac{\left|\frac{P'}{\gamma P}\right|}{\frac{\epsilon}{b}\sigma \frac{M^2}{1-M^2}\pi^2} \qquad (3.103)$$

The subscripts H and I refer to the homogeneous and inhomogeneous solutions, respectively. The superscripts refer to the downstream wave and the upstream wave.

We noted that the homogeneous solution behaved like β^{-4} for large β and that the inhomogeneous solution behaved like β^{-n} for large β where n is larger than 1. We have normalized both solutions in the preceding table by β^{-4}, which shows that both solutions behave like β^{-4}. It is not unexpected that the inhomogeneous solution should behave as the homogeneous solution.

This behavior is closely related to the wall deflection function $f(x)$, (3.24). Recall that we chose $f(x)$ to have continuous first, second, and third derivatives. This was to facilitate convergence of the series representation of the steady pressure disturbance due to the wall deflection. Equation (3.28) verifies that the convergence is like n^{-4}, where n is the index of the series expansion. If one follows through the details leading to the homogeneous solution, it is possible to see that the β^{-4} high-frequency behavior is a result of

the n^{-4} convergence of the expansion for the steady pressure.

3.8 Calculations and Discussion

For low-frequency entropy disturbances, the duct responds only with plane waves ($m=0$ mode) propagating far away. For high-frequency entropy disturbances, we have shown that the duct response drops off rapidly. If we are to examine the two-dimensional response of the duct, we should calculate for a reduced frequency high enough to give a few propagating modes, but not for such a high frequency that the response is negligible.

For the calculations to be discussed here, we have chosen $M = .3$, the contraction aspect ratio (height-to-length ratio, b/a) $\delta = 1$, and reduced frequency $\beta = \omega a/c = 5.0$. These values represent an entropy wavelength about one third the contraction length, and according to (3.82b) will give four propagating modes (including the plane mode) far away from the contraction. Our high-frequency analysis tells us to expect mode amplitudes of about $5^{-4} \approx 10^{-3}$ (if $\beta = 5.0$ is indeed a "high frequency).

The Fourier decomposition of the vertical dependence of the entropy wave (3.85) will, in general, give an infinite number of terms (entropy wavefront angles) for which we must calculate the duct modes. For a "reasonably smooth" function $f(y)$ we expect the Fourier coefficients (3.86) to decrease at least as fast as j^{-1} where j is the entropy mode under consideration. Hence, we will calculate for only the first ten entropy modes, including the plane mode. These results are presented in Figure 3-1.

The amplitudes have been normalized by $\sigma \frac{\epsilon}{b} \pi r^2 \frac{M^2}{1-M^2}$ and are generally $\sim 10^{-3}$ as per the high-frequency analysis. Each curve is labeled with $P_m^{\pm}$ where the superscript indicates transmitted or reflected wave (+, - respectively), and the subscript m indicates the acoustic mode. The phase is also given for each curve, since the amplitudes are complex, in general. The amplitudes of the modes are not strongly dependent upon the entropy disturbance.

The odd acoustic modes give no contribution for the $j=0$ entropy mode. Then we expect no asymmetric acoustic modes to result from that symmetric entropy disturbance (the symmetry is referred to the duct axis $y=b$). Suppose a general entropy wave exists which has no mean component. Then (3.86) and (3.90) give $\sigma_0=0$ to be used in (3.98), which then simplifies to

$$\tilde{P}_m = \begin{cases} \sum_{j=1}^{\infty} A_m(\nu_j)\, a_j & m \text{ even} \\ \sum_{j=1}^{\infty} A_m(\nu_j)\, b_j & m \text{ odd} \end{cases}$$

If our general entropy wave is symmetric, $b_j=0$, then no asymmetric acoustic modes $\tilde{P}_m$ exist. If the entropy is asymmetric, $a_j=0$, then no symmetric acoustic modes $\tilde{P}_m$ exist. This behavior is not related to the symmetry of the duct deflection. The $A_m(\nu_j)$ may be taken from Figure 3-1, for our particular example, for $j \leq 9$.

In the introduction to this chapter we noted that a one-dimensional analysis, such as used in Chapter II, may be interpreted as an average of the perturbation quantities over the duct cross section.

Since all the acoustic modes have a cross-sectional dependence $\sim \cos\left(m\pi \frac{y}{2b}\right)$ (far from the contraction), it is clear that only the plane mode can contribute to the average. For an asymmetric entropy disturbance, the plane acoustic mode will not be excited, and hence the average of the pressure disturbance across the duct will be zero.

Note that on the duct axis $y=b$, the odd modes give no contribution, while all the even modes do contribute. Hence, any pressure measurement we make on the duct axis will respond to the (complex) sum of the even modes. For example, the results of Figure 3-1 show that the second acoustic mode gives about five times the contribution of the plane acoustic mode.

In conclusion then, the duct responds to symmetric entropy disturbances by producing symmetric acoustic modes, and to asymmetric entropy disturbances by producing asymmetric acoustic modes. The high-frequency response of the duct is governed by the smoothness of the wall deflection. A smooth wall deflection will tend to respond less strongly than a "rough" wall will to high frequencies. The calculations also indicate that the amplitude of the acoustic modes is not overly sensitive to which entropy mode is disturbing the flow.

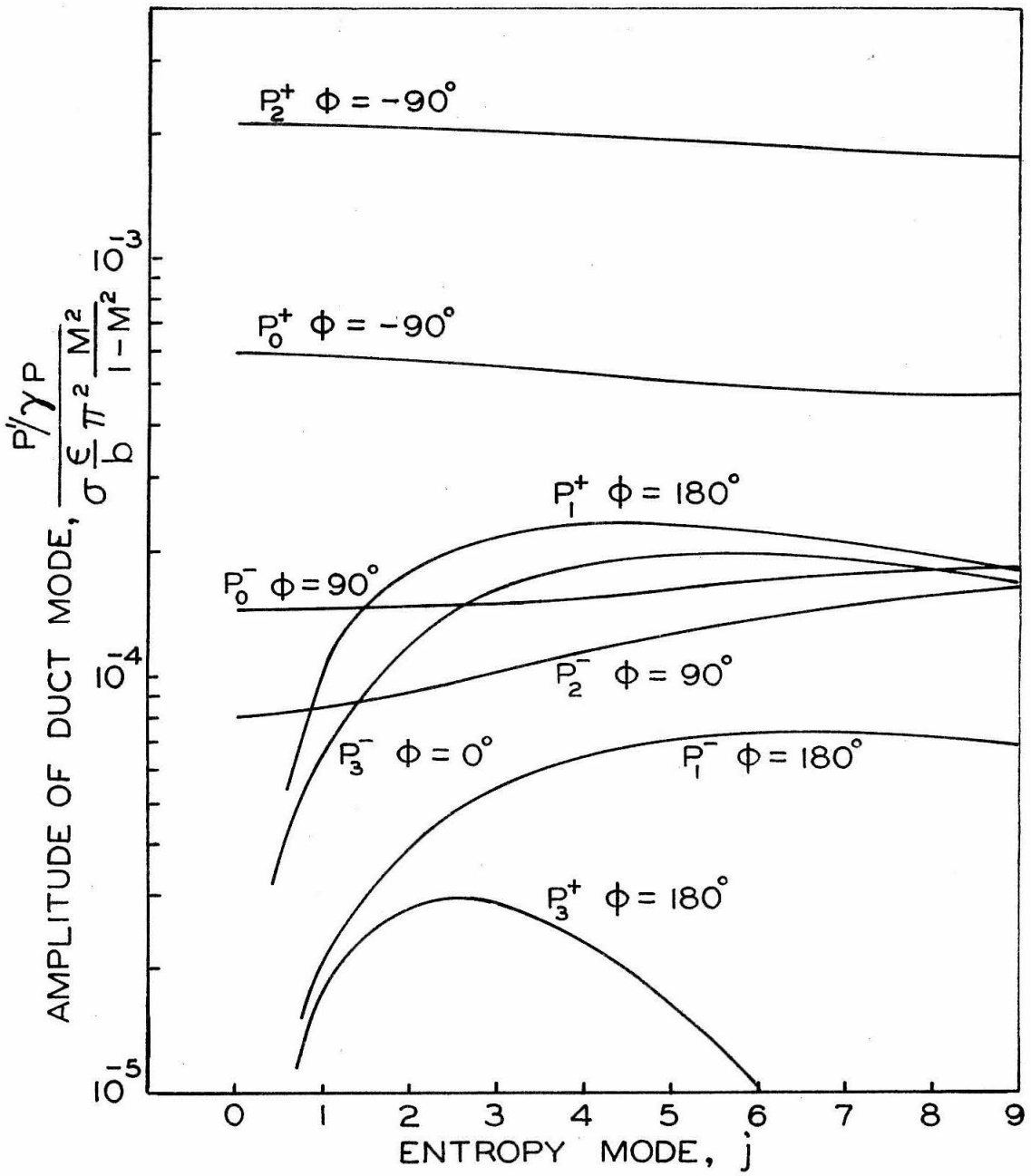

Fig. 3-1 Response for first ten entropy modes. Phase of mode (P^+ downstream propagating, P^- upstream propagating wave) given on each curve. $M = 0.3$, $\beta = \omega a/c = 5.0$, $\delta = b/a = 1.0$.

REFERENCES FOR CHAPTER III

1. Kapur, A. and Mungur, P. "On the Propagation of Sound in a Rectangular Duct with Gradients of Mean Flow and Temperature in Both Transverse Directions," J. Sound Vib. (1972), 23 (1), 401-404.

2. Mason, V. "Some Experiments on the Propagation of Sound Along a Cylindrical Duct Containing Flowing Air," J. Sound Vib. (1969), 10 (2), 208-220.

3. Yurkovich, R. "Attenuation of Acoustic Modes in Circular and Annular Ducts in the Presence of Sheared Flow," AIAA Paper 73-131, presented at AIAA 13th Aerospace Sciences Meeting, Pasadena, California (January 1975).

4. Nayfeh, A. H. and Kaiser, J. E. "Effect of Compressible Sheared Mean Flow on Sound Transmission Through Variable-Area Plane Ducts," AIAA Paper 73-128, presented at AIAA 13th Aerospace Sciences Meeting, Pasadena, California (January 1975).

IV. EXPERIMENTS CONCERNING THE RESPONSE OF A SUBSONIC NOZZLE TO ONE-DIMENSIONAL PRESSURE AND ENTROPY DISTURBANCES

4.1 Introduction

In this chapter we describe an experiment which was intended to test the analysis of Chapter II. In that chapter we found that a one-dimensional nozzle could be subjected to three independent disturbances: an entropy wave convected into the nozzle inlet, a pressure wave impinging upon the nozzle inlet, and a pressure wave impinging upon the nozzle exit. If the distribution of mean properties (Mach number) in the nozzle were known, the response of the nozzle could be calculated for each disturbance of a given frequency. Linearity then allows superposition of the independent solutions to give a general solution.

The results of the calculation give the pressure perturbation field through the nozzle and also the pressure waves which are caused, by the interaction, to be propagated away from the nozzle.

The experiments were carried out in a blowdown tunnel (inlet cross section 1 inch by 3 inches) which accelerates a mean flow of nitrogen from $M \approx .27$ to $M \approx .87$. The mean flow is perturbed by periodic heating of a grid of nichrome wires which are located upstream of the nozzle. By electrically pulsing the wire grid, the stream of nitrogen received a periodic fluctuation in total temperature. This causes an entropy wave and a pressure wave to propagate into the nozzle inlet. The downstream end of the nozzle was open to

the atmosphere, and hence any pressure wave which impinges upon the exit creates a wave (by reflection) which propagates upstream towards the nozzle. Thus, the three disturbances are created. By making measurements of the fluctuating pressure and other quantities, the three disturbances can be determined (the complex magnitude of the quantity is measured). After measuring the mean Mach number distribution through the nozzle, one may use the analysis of Chapter II to calculate the pressure perturbation field in the nozzle on the basis of the measured disturbances. The measured and calculated pressure perturbation field may then be compared. The measurements and calculation both give the resulting waves which propagate away from the nozzle, and these may also be compared.

The description of the experiment includes a brief discussion of the calibration (measurement and adjustment) of the mean flow in the blowdown tunnel. The pulse heater (nichrome wire grid) will be described, as well as the electrical circuitry required to produce the electrical pulse for the heater. We then describe how the three disturbances are measured and include here a discussion of data acquisition and processing. Results of some experiments are then presented so that the data may be compared with the analysis.

4.2 Description of the Experiment: The Blowdown Tunnel and Pulse Heater

The Blowdown Tunnel. A schematic representation of the blowdown tunnel is shown in Figure 4-1. The gas (nitrogen) is supplied from a bank of 20 high-pressure gas cylinders, passes through a

pressure regulation system, a plenum chamber (designed to reduce turbulence levels in the gas flow), and finally enters the blowdown tunnel just to the left of the pulse heater in the diagram. This blowdown system was designed and constructed by Dr. J. Auerbach (see ref. 8, Chapter II) in conjunction with experimental studies with a supersonic nozzle. The blowdown tunnel was re-designed to give the subsonic Mach number distribution required for the present experiments.

At the pulse heater, the tunnel is 3 inches in height and 1 inch in depth. The depth is fixed throughout the tunnel; the cross-sectional area is varied by changes in the height. From x = -8" to x = -1" (see Figure 4-1), the tunnel height increases slightly. This is to compensate for boundary layer growth so as to provide a region of essentially constant Mach number flow. This will be discussed in more detail shortly. In this portion of the tunnel, the Mach number was nominally .27. The tunnel height then decreased to approximately 1.5 inches in an axial distance of $6\frac{3}{4}$ inches. This accelerated the flow to about Mach .87. The tunnel height was again increased slightly from this point ($x = 6\frac{3}{4}$") to the tunnel exit (x = 14") to provide another constant Mach number flow region.

In order to distinguish the three portions of the blowdown tunnel in this chapter, we use "tunnel" to refer to the entire blowdown tunnel. The region over which the flow is accelerated will be called the "nozzle." The two constant-area regions (one upstream of the nozzle and one downstream) will be called the "upstream duct" or "downstream duct."

The upstream and downstream ducts were each about 7 inches in length and their purpose will be discussed next.

Recall from Chapter II that in regions of constant mean flow the equations (2.1) - (2.4) simplified such that the solution (2.9) could be written down:

$$Z_2(x) \equiv \frac{P'(x)}{\gamma \bar{P}} = P^+ e^{iC_+ x} + P^- e^{iC_- x} \tag{4.1}$$

The dimensionless wave numbers $C\pm$ were defined by (2.10). Recall that P^+, P^- are the complex magnitude of the downstream and upstream waves propagating in the constant-area section. If one were to measure Z_2 at two positions, say x_1 and x_2 in the constant-area duct, P^+ and P^- could be calculated from (4.1):

$$P^+ = \left(Z_2(x_1) e^{iC_- x_2} - Z_2(x_2) e^{iC_- x_1} \right) / D$$

$$P^- = \left(Z_2(x_2) e^{iC_+ x_1} - Z_2(x_1) e^{iC_+ x_2} \right) / D \tag{4.2}$$

$$D = e^{iC_+ x_1} e^{iC_- x_2} - e^{iC_+ x_2} e^{iC_- x_1}$$

By applying (4.2) to measurements made at two locations x_1 and x_2 in our "constant area" ducts, we can determine the waves leaving and entering the nozzle. In each of these ducts we see in Figure 4-1 there are four dynamic pressure transducer ports, on the duct axis. The length of the ducts and separation of the ports were chosen to allow adequate resolution in the pressure measurements. Notice that the system (4.2) becomes singular if $x_1 = x_2$. If, in the presence of flow noise, the two points x_1 and x_2 are not separated "enough," large errors will result in the calculation of P^+ and P^-, because the resolution between the two measurements will be poor.

In other words, the two transducers should be far enough apart so that differences in their signals will be much larger than any flow noise. The effects of flow noise will be discussed in more detail in the section on data acquisition and processing, §4.3.

It is necessary to not only determine the distribution of Mach number through the nozzle, but also to determine if the Mach number is constant in the upstream and downstream duct. The total pressure was determined by inserting a pitot probe just downstream of the pulse heater. The static pressure was then measured at four positions in each of the ducts and in seven positions in the nozzle. In this manner, assuming the flow (exclusive of the boundary layers) was isentropic, the Mach number could be determined at each position.

The adjustments to give constant Mach number in the two ducts were essentially a trial and error process. The first estimate (as to the slope of the walls) was made by assuming that the boundary layer was turbulent and incompressible. Schlichting[1] gives a relationship between boundary layer thickness and rate of growth of boundary layer thickness under these conditions. By assuming various initial boundary layer thicknesses (thought to be at least within an order of magnitude correct), a mean rate of boundary layer thickness growth over the duct could be estimated. This mean rate was used as the first guess in determining the wall slope. By alternately adjusting the wall slope and measuring the static pressure distribution through the duct, the best value of wall slope was eventually determined. After the final adjustment, measurements showed that the change in the Mach number in the upstream duct was less than 2 per cent over

its length and less than 1 per cent over the length of the downstream duct. These figures represent approximately the resolution of the static pressure measurement system used.

After having satisfactorily adjusted for boundary layer growth in the upstream and downstream ducts, the Mach number was measured at the seven positions in the nozzle contraction. The numerical solution, as described in Section 2.3, requires the Mach number at any point within the nozzle; hence, it was necessary to interpolate between the seven measured values. A cubic splines method was used to do this interpolation. This method guarantees a continuous first and second derivative throughout the region of interpolation, but does not allow one to specify, for example, the beginning or ending first derivative. Thus, the smoothed Mach number distribution which results from this calculation will not necessarily have a zero first derivative at the inlet and exit of the nozzle as we know must exist. To allow a zero first derivative to be specified at the inlet of the nozzle, the cubic splines curve was not used between the inlet and the first static pressure measurement location ($x \approx 1''$). In its place, a third-order polynomial was used. The four conditions specified for the polynomial were the Mach number at both ends and the first derivative at both ends. This allows one to specify zero first derivative at the inlet. Also, continuity of first derivative is preserved, but continuity of second derivative is not.

A similar method was used at the nozzle exit, but it was found that a slight overshoot in the Mach number resulted just upstream of the nozzle exit. This overshoot was minimized by slightly

moving the point, at which the cubic splines curve and the polynomial were joined, upstream or downstream.

A typical graph of the Mach number and dimensionless velocity gradient, $d(\bar{u}/a^*)/d(x/\ell)$ [see (2.5)] as calculated by this method is shown in Figure 4-2. The upstream point ($x \approx 1''$) where the two curves (cubic splines and polynomial) were joined is clearly evident in the velocity gradient. This discontinuity in the second derivative should cause no problems as far as accuracy of representation of the mean flow. Recall from (2.8) that the gradient only enters as $M^2\, du/dx$ and hence, the contribution is small in the inlet region of the nozzle where the discontinuity occurs.

It was not possible to control the total pressure exactly for each experiment. Since the nozzle is not choked this means that the Mach number distribution could vary from one experiment to another. It was assumed that for these small unavoidable changes in the total pressure the boundary layer thickness, and hence effective flow area, would not change appreciably. Thus, this smoothed Mach distribution was used to generate a normalized area ratio distribution through the nozzle, which was assumed to be independent of nozzle total pressure. The inlet static pressure recorded for a given experiment could be used in conjunction with the area ratio function to calculate a Mach number distribution for that experiment.

The Pulse Heater. We show a more detailed diagram of the pulse heater in Figure 4-3. The heater actually consists of three smaller heaters, each occupying about 1/3 of the upstream duct cross-sectional area. The three heaters could be operated independ-

ently to produce a two-dimensional heat pulse. Experiments concerned with this mode of operation will be discussed in Chapter V. By connecting the heaters together (external to the tunnel) the entire cross section of flow could be heated uniformly, thus creating one-dimensional disturbances. We will be concerned with this mode of operation in this chapter, and we will consider the heater to be simply a grid of wires strung uniformly across the entire cross section of the duct. To produce a periodic disturbance a square wave of voltage was applied across the heater. The square wave was produced by an SCR commutation circuit which is described in more detail in Appendix F. The resistance of the heater was 5.4 ohms and the peak voltage was about 300. Hence, the peak power input to the heater was about 16 kilowatts and this produced a temperature fluctuation in the gas of approximately $0.3^{\circ}C$. This fluctuation is small because of the high frequency (400 Hz) of the pulsing and the finite length of the heater. A higher frequency pulse produces a smaller temperature fluctuation due to the thermal lag of the heater wires. The thermal time constant of the nichrome wires in this flow corresponds to about 4 Hz.

A longer heater will allow more heat to be transferred to a fluid element, but since the heat transfer decreases as the fluid element temperature rises, this benefit has its limit. Also, an element of fluid will lose heat if it must pass through wires which are not conducting current. The present heater represents a compromise between wire diameter and melting temperature, gas flow rate, electrical power available, and frequency of pulses required.

4.3 Data Acquisition and Processing

Dynamic Transducers and Measurement of the Entropy Wave.

The temperature fluctuation was measured at the position x = -0.5" shown on Figure 4-1 with a 1.28 μm platinum/rhodium cold-wire resistance thermometer/amplifier system. The wire carries a constant current of a low value (0.2 ma) so that the velocity fluctuations do not affect the wire temperature. Gas temperature fluctuations are sensed by the wire as resistance fluctuations; the constant current then gives a fluctuating voltage cross the wire proportional to the gas temperature fluctuations. The signal is then amplified.

Pressure fluctuations were detected with piezoelectric transducers and associated charge amplifiers. The transducers were calibrated by inserting a (calibrated) microphone nearly in the tunnel. A loudspeaker was operated near the tunnel exit such that typical signal strengths were detected by the microphone as would be expected in the actual experiments; there was no gas flowing in the blowdown tunnel. Care was taken to insure that the transducers were inserted to the same depth in the tunnel and inserted with the same torque for each experiment, as for the calibration.

By measuring the temperature fluctuation, T', and the pressure fluctuation, P', the complex magnitude of the entropy wave being convected into the nozzle can be calculated. The equation of state (2.4) and the ideal gas law, $P=\rho RT$, may be linearized to give:

$$\frac{s'}{c_p} = \frac{T'}{\bar{T}} - \frac{\gamma-1}{\gamma}\frac{P'}{\bar{P}} \qquad (4.3)$$

Effect of Flow Noise on the Measurements. Since our analysis of Chapter II was a harmonic analysis, we must deal with signals of only a single frequency. If we pulse the heater at a fundamental frequency, say F_o, we expect to find temperature and pressure fluctuations at that frequency and all harmonics. We expect the fundamental component of the signal to be the largest, and hence we will attempt to measure the phase and magnitude of that component.

The determination of phase and magnitude of the fundamental component, by any method, will be affected by the presence of noise. Consider, for example, a signal at the fundamental frequency of magnitude 1.0 and phase 0^o. Suppose we also have present at this frequency another signal of magnitude S and phase ϕ_s where $-\pi \leq \phi_s \leq \pi$. The sum of these two signals can be represented by the vector sum in the phase plane:

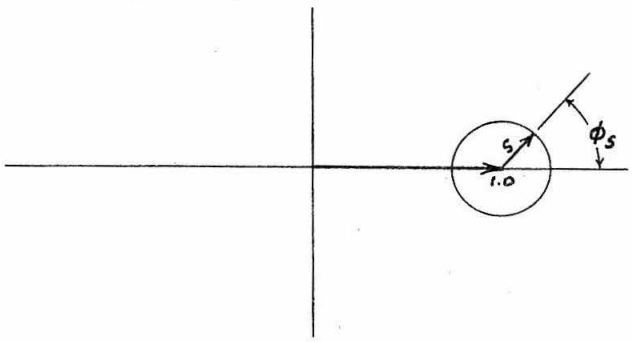

The horizontal axis here represents the real (cosine) component of the signal and the vertical axis represents the imaginary (sine) component. Then the net signal at the fundamental frequency will be represnted as the locus of points given by the circle in the above diagram. We can write the magnitude of the net signal as

$$((1+S\cos\phi_s)^2+(S\sin\phi_s)^2)^{1/2} = (1+2S\cos\phi_s+S^2)^{1/2}$$

and the phase will be

$$\tan^{-1}\left(\frac{S\sin\phi_s}{1+S\cos\phi_s}\right)$$

The presence of the secondary signal will cause a maximum "error" S in the determination of the magnitude and a maximum phase error $= \sin^{-1} S$. If we consider the secondary signal to be noise, then we may call $1/S$ the signal-to-noise ratio since it is the ratio of the amplitude of the signal to that of the noise.

As an example, consider a signal-to-noise ratio of 10. We would expect to determine the magnitude of the signal to ± 10 per cent and the phase to $\pm \sin^{-1}(.1) = \pm 5.7^\circ$.

Since the temperature fluctuation in this experiment is small, one would expect that the pressure signals would be small (in fact, we expect $P'/\bar{P} = \mathcal{O}(T'/\bar{T}) = 10^{-3}$, see Section 5.3). In this case, the flow noise will be expected to be significant compared to these signals. Reference 2 reports on the pressure fluctuation due (primarily) to turbulence in a subsonic boundary layer. The power spectrum of this fluctuating pressure was found to be quite flat for frequencies which cover our range of interest. The reported magnitude of pressure fluctuation was

$$\frac{|P'|}{P_{atm}} = 3\cdot 10^{-4}$$

This does not include any noise such as we may have from the mean flow region, from the plenum chamber, or from the flow passing across the pulse heater wires. It is clear, then, that the flow noise we will encounter will be roughly the same magnitude as the signals we seek to measure. Our previous statements imply that the

resulting errors in any calculation of phase and magnitude will be unacceptable.

The method used to increase the signal-to-noise ratio here will be called ensemble averaging. The method is very straightforward and consists of averaging ensembles of data which, except for the noise, are identical. Suppose that we begin recording the output of one of the pressure transducers, for example, at time t_1 after the pulse heater is turned on at time t_0 . If we stop recording data at some later time t_2 , we call the record of data an ensemble of length $t_2 - t_1$. The next time the heater is turned on, we again wait a period $t_1 - t_0$ and record the output of the same transducer for length of time $t_2 - t_1$. We now have two ensembles of the same length. Since they represent data recorded with the same relative phase with respect to a periodic disturbance, they should be identical except for any contribution not associated with the periodic disturbance.

Suppose we have several such ensembles which were digitally sampled (each ensemble consists of a given number of discrete values). If we look at the same respective value in each ensemble (i. e., the j^{th} value in each ensemble), then this value represents the signal recorded at exactly the same phase (time delay) with respect to the heat pulse. If the noise were small, all the values would be about the same, with some small scatter. Our inclination would be to simply take the mean of these values to get some average representation of the signal (without the noise) which occurred at that time. The ensemble average technique simply performs this averaging for all the

respective points in the ensembles. The resulting averaged ensemble would be expected to represent the signal more closely. We also expect that if the noise is large we will need to average more ensembles to get a close representation of the signal. It is possible to show (see ref. 3) that if the noise has a Gaussian distribution, then averaging in this manner will tend to decrease the noise relative to the signal like $n^{1/2}$ where n is the number of ensembles averaged.

We have shown that the unprocessed signal should have about equal amounts of noise, hence if we average 100 ensembles we should get a final signal-to-noise ratio of about 10.

The circuit required to allow data acquisition in synchronization with the heat pulses is described schematically in Figure 4-4. A detailed description of each circuit may be found in Appendix F. We describe briefly the operation of the system here. The frequency reference consists of a crystal oscillator and provides a fixed (frequency) digital signal to act as a time base for the entire experiment. The pulse generator logic (digitally) divides the reference signal to give five signals, three of which are shown on Figure 4-4 leaving the pulse generator logic and passing through a ground isolation system. These three signals are amplified and ultimately produce the high power pulses required to operate the pulse heaters. When we are producing a one-dimensional heat pulse, all three heaters (Figure 4-3) operate as a single heater. In this case, only two of the three signals leaving the pulse generator are used. The reason that two are required is explained in Appendix F (in the discussion of the SCR commutation circuit). The third signal is required when it is neces-

sary to operate the pulse heaters independently. This mode of operation will be described in more detail in Chapter V.

The production of the high power heat pulses causes a large amount of electrical noise which must not be allowed to interfere with the operation of the logic circuits. The ground isolation circuit allows the logic circuit ground and the high power circuit ground to be independent of each other. Besides the electrical noise in the ground of the high power circuit, a large amount of noise was radiated because the SCR commutation circuit generally switched on 60 amps in about 1 microsecond. This noise is in phase with the temperature and pressure fluctuations to be measured, and thus is not affected by the ensemble averaging process. Hence, it can strongly influence the calculation of the phase and amplitude of the fundamental component of those quantities unless isolated from the instrumentation (resistance wire amplifier and charge amplifiers).

In order to prevent the radiated electrical noise from reaching the instrumentation, all wires carrying a high current with fast transients were heavily shielded. We were able to demonstrate that the electrical noise was not affecting the instrumentation; a typical experiment was performed with two modifications. First, a pressure transducer was isolated from acoustic disturbances in such a way that its sensitivity to electrical noise was not altered. Second, the constant current required to operate the cold-wire resistance thermometer was turned off. The cold wire remained as input to its amplifier, but in this way it would not be sensitive to temperature fluctuations. Any electrical interference could still affect the wire. After the data

were processed, it was seen that the remaining signals (from these two transducers) at the fundamental frequency (which could only be caused by electrical interference) were negligible compared to the pressure and temperature signals recorded during a normal experiment.

Data Acquisition System. In order to allow the acquisition of data ensembles in synchronization with the heat pulses, the pulse generator produces two other signals. These signals ultimately reach a computer/data acquisition system which consists of a computer (Hewlett-Packard model 2100, with 32K integer words of memory) and a 16-channel analog/digital (A/D) conversion system. The "instrumentation" referred to in Figure 4-4 consists of seven (analog) signals from the pressure transducer/charge amplifiers, one (analog) signal from the cold-wire resistance thermometer/amplifier, and two reference signals. One of these reference signals is a constant 1.000 volt d.c. signal which acts as a calibration check on the A/D converter. The second reference signal is a TTL square wave at the fundamental frequency and allows one to easily check whether or not the ensemble averaging was performed correctly. (After any number of ensembles have been averaged, the square wave should be unaltered.) These ten signals are input to the A/D converter.

The "clock" signal, which comes from the pulse generator, is a TTL square wave of a frequency which is some multiple of the fundamental frequency. The frequency of this signal will be discussed shortly. The "beta" signal is also a TTL square wave. If the beta signal is logical true, then the A/D converter samples the analog

channels in order, digitizes the voltage from each channel, and makes the digital number (representing the voltage for that channel) available to the computer. The frequency that the A/D converter samples from one channel to the next is that of the "clock" signal. The data controller (see Figure 4-4) causes the "beta" signal to be logical true for a pre-set number of cycles (of the fundamental frequency) and then become logical false for a pre-set number of cycles. The number of cycles that "beta" is true determines the length of the ensemble. The length of time required by the computer to process the ensemble determines the number of cycles that "beta" is false (which inhibits data acquisition).

The processing of the ensemble was done in one of two ways. For short ensembles (up to about 2 cycles in length), the ensemble averaging could be carried out in (computer) core. The A/D converts the data making up the ensemble to digital form and the computer stores the ensemble in memory. After the next ensemble is sampled, the values are added to the respective values of the previous ensemble which was already in core. For longer ensembles, this adding process requires too much time, and it is more efficient to write each ensemble on the magnetic disk memory. After the experiment is complete, the ensembles are read off the disk and averaged by the computer.

Since the static temperature of the gas falls during the experiment, and since the cost of the gas is appreciable, it is best to waste the least amount of time during the experiment. At least part of the time the ensembles are being processed (either averaged in core or

being written on the disk), no data are being recorded. These two methods of processing the ensemble were used in order to minimize the time during which no data were being recorded.

Calculation of the Fourier Spectrum. After the experiment is complete, the averaged data are written on magnetic tape for further processing. The data in this form are a record (for each channel) consisting of a set number of cycles of a signal with about 10 per cent noise content. We are now ready to determine the phase and magnitude of the fundamental component of each signal recorded.

We denote the values in each record as v_j , $j = 0,1,\ldots N-1$, where we have N equally spaced samples. Each sample v_j represents the voltage (on the particular channel) at a particular time $j\Delta t$ where Δt is the sampling period for each channel. The sampling period is just the period of the "clock" signal multiplied by the number of channels scanned by the A/D converter.

We would like to calculate the Fourier Series representation of the data record. If the record were a continuous function of time $v(t)$, $0 \le t \le T = N\Delta t$, we would represent $v(t)$ as

$$v(t) = \sum_{n=-\infty}^{\infty} C_n \exp(-2\pi i n t/T) \tag{4.4}$$

with

$$C_n = \frac{1}{T} \int_0^T v(t) \exp(2\pi i n t/T) dt \tag{4.5}$$

Since we have sampled $v(t)$ at the discrete times $0, \Delta t, 2\Delta t \cdots N\Delta t$

we approximate the coefficients by

$$C_n \approx \frac{1}{N} \sum_{j=0}^{N-1} v(j\Delta t) \exp(2\pi i n j/N) \tag{4.6}$$

which may be considered as the application of the trapezoidal integration rule to eq. (4.5). Note that since $v(t)$ is real,

$$C_n = \frac{1}{T} \int_0^T v(t) \cos(2\pi n t/T)\, dt + i \frac{1}{T} \int_0^T v(t) \sin(2\pi n t/T)\, dt \tag{4.7}$$

Consequently, the real part of C_n ($n>0$) is just half the cosine coefficient of $v(t)$, and the imaginary part of C_n ($n>0$) is just half the sine coefficient of $v(t)$. This may be verified by changing the variable of summation in the negative portion of the summation in (4.4) and by using (4.7), write that portion as a summation over positive n . This gives

$$v(t) = \sum_{n=1}^{\infty} [2\, Re(C_n) \cos(2\pi n t/T) + 2\, Im(C_n) \sin(2\pi n t/T)] + C_0$$

The question remains as to how accurate a representation of eq. (4.5) is eq. (4.6). Cooley, et al.[4] have shown that for

$$C_{pn} \equiv \frac{1}{N} \sum_{j=0}^{N-1} v(j\Delta t) \exp(2\pi i n j/N) \tag{4.8}$$

we will find

$$C_{pn} = \sum_{\ell=-\infty}^{\infty} C_{(n+N\ell)} \tag{4.9}$$

The equation (4.9) is an expression of the so-called aliasing effect. This says that if we want the C_{pn} to accurately represent the Fourier coefficients C_n, then N must be "large enough" so that the approximation (4.6) is acceptable. Since $N=T/\Delta t$, large N implies that we must sample $v(t)$ at a "high" frequency. If the sampling frequency is $F=1/\Delta t$, then we would like F to be large enough so that $C_n \approx 0$ for frequency f, $|f|>\frac{1}{2}F$ $(n/T=f)$.

We will then have

$$C_{pn} \approx C_n \qquad n=0,1,2\cdots N/2$$

$$C_{pN-n} \approx C_{-n} \qquad n=1,2\cdots N/2$$

In the present work, high-frequency signals were associated with noise, and the largest signals of this type were expected from the pressure transducers. The resistance thermometer had low sensitivity to velocity fluctuations and a signal with high frequency content was not expected. A nominal value for the fundamental frequency was 250 Hz and the data were sampled at 32 times this frequency per channel. The frequency $F/2$ (called the Nyquist frequency) is then 4 kHz. To insure that the frequency content of the pressure signals was very small for frequencies greater than 4 kHz, a low-pass analog filter was inserted between the charge amplifiers and the A/D converter. The filter had -3 db point at 2 kHz with a roll-off of 42 db/octave. Hence, any signal of 4 kHz or greater would be attenuated by about 42 db (reduced to less than 1 per cent).

The coefficients of the expansion C_{pn} may be calculated directly from eq. (4.8) in $\mathcal{O}(N^2)$ operations. This constitutes the classical "discrete Fourier transform method," and is suitable if

only a very few of the frequency components are required. In order to make some estimate of the quality of the signal (i.e., signal-to-noise ratio) and to be able to easily determine if a large amount of electrical interference had occurred, it was desirable to calculate all the coefficients C_{pn} , $n=0,1,2\cdots N/2$. In order to perform this calculation in a reasonable amount of time, the Fast Fourier Transform (FFT) method was used. This method is discussed at length in ref. 5. For our purposes, we need only note that the method requires that N be highly composite such as $N=K^m$, K,m are integers. The computer program we used was given in ref. 5 and requires that $K=2$. In this case, the calculation of the coefficients C_{pn} may be performed in $\mathcal{O}(N \log_2 N)$ operations. Nominal values used for the data acquisition were such that 16 cycles of data, 32 points per cycle, comprised a record for each channel. Thus, approximately one per cent$\left([\log_2 N]/N\right)$ of the operations were required by using the FFT method. An additional savings of a factor of 2 was realized by using the fact that the data $v(j\Delta t)$ were real. The procedure for utilizing this savings is covered in ref. 8.

As previously mentioned, there are two sources of noise which may be present in our signal. The first is random (generally considered Gaussian-white noise) which was caused by flow noise. Our previous discussion showed that a nominal value for this flow noise will be about 10 per cent of the signal. It is clear that the pressure fluctuation field will vary through the duct and indeed, (spatially) local minima, or nodes, in the amplitude may occur.

The flow noise may strongly influence the calculation of the

amplitude and phase of the frequency component "seen" by the transducer located at these nodes (see Effect of Flow Noise on the Measurements, page 120). It is clear, then, that any calculation of the amplitude and phase of a component must be accompanied by a statement giving some indication of how meaningful the calculated amplitude and phase are. The measurement at a "node" may be 50 per cent noise, in which case the amplitude calculation would be in error by as much as ± 50 per cent and the phase calculation would be in error as much as 30^{o}.

It was assumed here that the flow noise was at least "locally white," meaning that the amplitude spectrum, near but excluding the fundamental frequency of interest, was constant. In this way the amplitude of the noise component (at the fundamental frequency) could be estimated as the mean of the noise components near the fundamental component. As an example, consider an experiment performed at 250 Hz with a 16 cycle record. This gives a resolution (in the frequency domain) $\Delta f \simeq$ 16 Hz. The calculated amplitudes for the frequency components $f_n = 250 \pm n\Delta f$, $n = 1, 2 \cdots 10$ were averaged to give the noise component at 250 Hz. In this way, an estimate of the signal-to-noise ratio (as used above) could be made.

The second type of noise is due to electrical interference created by the rapid switching of high currents in the SCR commutation system. This noise generally appeared as sharp transients in the voltage waveform, and since this noise is in phase with the heat pulse, it was not reduced by the ensemble averaging technique. Small amounts of electrical noise were always present in the cold-wire out-

put, probably because the wire acts like a small antenna (located quite close to the pulse heater). Also, the shielding of the high power cables is not perfectly effective. Large amounts of electrical noise were indicative of a shielding problem and could easily be seen from the waveform or the amplitude spectrum. Since this noise appears as very sharp transients in the waveform, the spectrum reveals nearly equal amplitude, evenly spaced components. To check for objectionable amounts of electrical interference, the fundamental component was compared with the harmonic component with largest amplitude. A harmonic of comparable amplitude to the fundamental is indicative of a large contribution by electrical noise to the fundamental component.

The estimation of the two types of noise made possible the elimination of:

(i) entire experiment if excessive electrical interference occurred, indicating a broken wire shield ;

(ii) one data point (pressure fluctuation measurement) if the flow noise were comparable to the amplitude at that point.

Note that in the case of (ii) we will still be able to say that the point was a node, but we must be aware that the values of the phase and magnitude are not reliable.

Typical waveforms and respective amplitude spectra from an experiment with fundamental frequency $\approx$ 250 Hz are shown in Figures 4-5 through 4-10. For this experiment, 100 ensembles were averaged; each ensemble was 16 cycles in length, 32 data points were recorded per cycle. In Figures 4-5 and 4-6 we have the output of the

pressure transducer/charge amplifier located at x = 11.5" (see Figure 4-1). In Figures 4-7 and 4-8 we have the output of the pressure transducer/charge amplifier located at x = 13.5". In Figures 4-9, 4-10, we have the output of the cold-wire resistance thermometer/amplifier which was located just upstream of the nozzle inlet (x = $-\frac{1}{2}$").

The pressure fluctuation recorded from the position x = $11\frac{1}{2}$" (Figures 4-5, 4-6) is a large signal in the sense that the amplitude components other than the fundamental are negligible. The wave form (Figure 4-5) clearly exhibits the 16 cycles of the fundamental frequency. Our scheme for calculating the signal-to-noise ratio gives 32 db for this signal, and the largest harmonic is 19 db below the fundamental. The pressure fluctuation recorded from the position x = $13\frac{1}{2}$" has about one half the amplitude at the fundamental frequency, as does the signal recorded at x = 11.5". Most of the noise seems concentrated around 800 - 1600 Hz, and we expect that the amplitude component of noise at the fundamental will be small. For this signal-to-noise ratio we get 30 db, and the largest harmonic is 8 db below the fundamental.

The figures 4-9, 4-10 demonstrate the electrical interference noise discussed earlier. It was mentioned that the resistance thermometer was more susceptible to this noise and this is evident in these figures. There is obviously very little random (flow) noise remaining. The signal-to-noise ratio here is 48 db; the largest harmonic is 21 db below the fundamental.

The sharp, periodic transients seen in the waveform are due to electrical interference and cause the evenly spaced smaller peaks

in the amplitude spectrum. The effect of the analog filter is clearly evident in Figures 4-6 and 4-8 from the sharp roll-off in response for frequencies above 2 kHz. The filter used for the resistance thermometer had a -3 db point at 5 kHz and a roll-off of 18 db/octave. The electrical interference was evidently not reduced by the filter. It is also possible that the interference actually occurred in the long cables from the thermometer/amplifier output to the computer. In either case, this high-frequency content is not enough to cause significant problems either with aliasing or with determination of phase and amplitude of the fundamental component of the temperature fluctuation.

Finally, it should be noted that the digital sampling causes a phase shift due to the finite sampling frequency. The last channel sampled will be shifted the most (in the time domain) relative to the first channel. This phase shift has been compensated for in reporting the phase of the fundamental component of any signal.

4.4 Results and Discussion

In this section we first discuss the calculations leading to $P_1^{\pm}$, $P_2^{\pm}$ from the experimental data for one experiment. This will lead to a value of P_1^{+} and P_2^{-} used in the numerical calculation. Numerical results will be presented for two experiments performed at different fundamental frequencies.

An experiment was performed with fundamental frequency $F_o \approx$ 250 Hz. One hundred ensembles were averaged, each consisting of 16 cycles, 32 points per cycle of data from a given trans-

ducer. An attempt was made to measure the pressure perturbation in the two constant-area ducts from this one experiment. The pressure perturbations for the remaining positions (in the nozzle) were then measured in another experiment. Due to the difficulty in precisely controlling the mean conditions (total pressure and total temperature) it was felt that this method would be the most self-consistent.

In order to determine the upstream and downstream propagating waves in the upstream duct (P_1^- and P_1^+ respectively), pressure measurements were made at x = - 6.75", -2.75" and -0.75" (see Figure 4-1). This allows three independent calculations of each quantity P_1^- , P_1^+ . The waves in the downstream duct (P_2^- and P_2^+) were determined from pressure measurements at x = 6.75", 9.25", 11.25", and 13.25". This allows six independent calculations of each quantity. The temperature fluctuation was measured at x = -0.75". The following table summarizes the values recorded.

Parameter	Distance from Nozzle Inlet	Magnitude	Phase
T'/T	-0.75"	1.39×10^{-3}	43^{o}
P'/P	-6.75"	$.64\times10^{-4}$	168^{o}
P'/P	-2.75"	1.23×10^{-4}	-99^{o}
P'/P	-0.75"	1.90×10^{-4}	-94^{o}
P'/P	6.75"	1.80×10^{-4}	-126^{o}
P'/P	9.25"	3.59×10^{-4}	-144^{o}
P'/P	11.25"	2.68×10^{-4}	$+178^{o}$
P'/P	13.25"	1.08×10^{-4}	$+149^{o}$

where T is the mean total temperature measured upstream of the pulse heater (compensation was later made for the increase in this

quantity across the pulse heater). The mean pressure P is the static pressure recorded at the position x =-.75" (Figure 4-1).

The results of calculating $P^{\pm}$ (eq. (4.2)) were plotted in the phase plane. For example, a vector was drawn for the value of P_1^+. The length represented the magnitude of the quantity, $((Re\ P_1^+)^2 + (Im\ P_1^+)^2)^{1/2}$, the counter-clockwise angle from the right horizontal axis represented the phase $= \tan^{-1}(Im P_1^+/Re P_1^+)$. Figure 4-11 is such a display of P_1^+ and P_1^- based on the values of $P'/\gamma P_{local}$ recorded in the upstream duct and listed in the preceding table. The vectors terminated with "M" represent the three calculations of P_1^- and those terminated with "P" represent the three calculations of P_1^+. The vector terminated with "-" represents the vector average of the three values of P_1^-. The vector terminated with "+" represents the vector average of the three values of P_1^+. We should note that the "M" vectors were not necessarily drawn to the same scale as the "P" vectors.

There seems to be no particular problem with these results; the scatter is quite small. We use the vector-averaged values:

$$P_1^+ = 1.29 \cdot 10^{-4} \angle -131^\circ \qquad (4.29)$$

$$P_1^- = 0.93 \cdot 10^{-4} \angle -34^\circ \qquad (4.30)$$

The first quantity P_1^+ will be required in the numerical computation, while the second will be compared with the results of that computation.

The results for the downstream duct ($P_2^{\pm}$) are presented in Figure 4-12; the notation "M", "P", "+", "−" is unchanged from Fig-

ure 4-11. Only five vectors are shown; the calculation based on the first and last positions in the duct (6.75" and 13.25") was not plotted. These two positions are very nearly one (upstream propagating) wavelength apart:

$$\lambda_- \equiv \frac{2\pi}{C_{2-}} \ell \approx 6.7"$$

Since the downstream propagating wavelength $\lambda \approx 96"$ is so large, the variation of the pressure perturbation field (in the downstream duct) is primarily due to the short wave λ_-. Hence, the result of using positions 6.75" and 13.25" gives very large errors (because the system (4.2) is "near" singular). There is apparently a large amount of scatter in the measurements presented in Figure 4-12.

The vectors are labeled with two digits which give, from the table on Figure 4-12, the position of the two points used to calculate that vector. For example, the P_2^+ vector in the fourth quadrant with indices (1, 2) was calculated from positions 6.75 and 9.25 inches from the nozzle inlet.

From these indices it is possible to see that the vectors have a monotonically increasing phase (decreasing for the P_2^+ wave) as the measurement position moves downstream in the tunnel. Note that in using (4.2) to calculate $P^{\pm}$ the wave number $C_- = \beta M/(U(1-M))$ is very sensitive to Mach numbers near unity; for our experiment, a 1 per cent error in the Mach number gave a 6 per cent error in the wave number C_{2-}. Such an error in the Mach number could easily result from the manner in which we measured it. Additionally, a weak Mach number gradient can exist in the duct, making an accurate

determination of the Mach number difficult. However, it will be seen shortly that since the flow is nearly sonic in the downstream duct the wave P_2^- has very little influence on the remainder of the duct. Hence, difficulties in accurately determining P_2^- are offset by the relative unimportance of the wave .

If these phase errors had been random in nature, a more fundamental difficulty with the experiment would have been indicated. However, since the consistent increase in phase angle seems to be closely related to the difficulties in determining the duct Mach number, we will use for $P_2^{\pm}$ those values most nearly representative of the duct. Since the most representative value of the Mach number would be the one near the center of the duct we will use the vectors with indices (2, 3). Note that those values are quite nearly the average values indicated by "+" or "-", further indicating that the data are scattered in an ordered manner about the middle, (2, 3), points. The value we use is then

$$P_2^+ = 2.50 \angle 165^\circ \tag{4.31}$$

$$P_2^- = 1.53 \angle 14^\circ \tag{4.32}$$

The value calculated for the entropy using eq. (4.3) and the values given in the table on page 135 is

$$\sigma = \left.\frac{S'}{C_p}\right|_{x=-.75''} = 13.52 \cdot 10^{-4} \angle 45^\circ \tag{4.33}$$

The measured static pressure for the experiment was used, as previously described, to calculate the distribution of mean Mach number in the nozzle such as in Figure 4-2. Having specified the

fundamental frequency of the disturbance, a numerical integration such as described in Section 2.3 was performed. The results of this numerical calculation are:

T_P	transmitted wave, plus solution
R_P	reflected wave, plus solution
$Z_{2P}(X)$	normalized pressure perturbation through the nozzle, plus solution
T_m	transmitted wave, minus solution
R_m	reflected wave, minus solution
$Z_{2m}(X)$	normalized pressure perturbation through the nozzle, minus solution
T_e	transmitted wave, entropy solution
R_e	reflected wave, entropy solution
$\tilde{Z}_{2e}(X)$	normalized pressure perturbation through the nozzle, entropy solution

The results are presented in two ways. First, the calculation (2.16) is carried out graphically. Using the experimental values of P_1^+, P_2^-, σ [eqs. (4.29), (4.32), and (4.33), respectively] and the values of T_P, R_P, T_m, R_m, T_e and R_e from the numerical solution we calculate

$$P_{1*}^- = P_1^+ R_P + P_2^- T_m + \sigma R_e$$

$$P_{2*}^+ = P_1^+ T_P + P_2^- R_m + \sigma T_e$$

The * subscript indicates the wave was calculated, not measured. These four vectors, the three components and the resultant, are drawn (in the usual convention) in Figure 4-13 as solid lines. The

dashed vectors are experimentally determined vectors $P_1^{\pm}$ or $P_2^{\pm}$ [eq. (4.29), (4.30), (4.31), or (4.32)]. The resultant waves P_1^- and P_{1*}^- are to be compared as well as P_2^- and P_{2*}^-. The scales are shown for the upstream duct (coordinate system on left of diagram) and for the downstream duct (coordinate system on right of diagram).

The comparison of P_1^- and P_{1*}^- shows that the magnitude of the experimentally determined wave, P_1^-, is about 30 per cent less than the calculated value. The phase of the two vectors is in good agreement. The magnitude of the calculated resultant wave P_{2*}^+ is about 18 per cent less than the experimentally determined value. The phase difference is about 14°.

That the error in the upstream duct is quite large is believed to be related, at least partly, to inaccuracies in the representation of the mean Mach number distribution. By making slight systematic adjustments to the Mach number distributions (used in the numerical calculations), it was observed that the normalized reflected waves R_p, R_e were about 4 to 8 times more strongly affected than the transmitted waves T_p and T_e. In the upstream duct, R_p, R_e are seen to have the strongest influence; while in the downstream duct, T_p and T_e have the strongest influence. We should note, however, that these slight adjustments in the Mach number distribution did not affect these reflected waves strongly enough so that the discrepancy (between P_1^- and P_{1*}^-) could be entirely related to this problem.

By presenting the results in a manner such as Figure 4-13,

the contributions of each disturbance in each duct can easily be seen. As mentioned before, the P_2^- wave does not contribute significantly, and this is clear from the diagram. Recall that this is because of the high exit Mach number. The entropy and the plus (P_1^+) wave contribute about equally and, due to their phase relationships, tend to slightly complement each other, producing a somewhat larger resultant, P_{1*}^- or P_{2*}^+ .

The second manner of presenting the data is to calculate the pressure perturbation field using the experimentally measured values of P_1^+, P_2^- and σ (as before) with the normalized pressure perturbation functions which we found from the numerical calculation. The general solution may be calculated:

$$\frac{P'}{\gamma \bar{P}}(x) = Z_2(x) = P_1^+ Z_{2p}(x) + P_2^- Z_{2m}(x) + \sigma \tilde{Z}_{2e}(x) \qquad (4.34)$$

where $\bar{P}$ = local mean static pressure. The magnitude of this function $|Z_2(x)|$ is plotted in Figure 4-14 and the phase is plotted in Figure 4-15, both as solid curves. The experimentally measured values are designated on the graphs also and seem to agree quite well with the computed curves.

The phase errors are seen to increase as the magnitude becomes small because the signal-to-noise ratio for these data points was small. The measured phase near the exit has a large error. This seemed to be consistent with all experiments performed, and is probably due to three-dimensional effects near the duct opening (x = 14").

The behavior of the pressure perturbation is easily understood. In the upstream duct the waves propagating upstream and downstream have wavelength

$$\lambda_{\pm} = 2\pi\ell \frac{U(M\pm1)}{\beta M}$$

which are both several nozzle lengths. Hence, the pressure perturbation changes slowly in the upstream duct which is about one nozzle length.

In the downstream duct the situation is different. The downstream propagating wave has a very long wavelength (many nozzle lengths) and the upstream propagating wave has a wavelength roughly one nozzle length. The resulting pressure perturbation field is the vector resulting from the sum of P_2^+ and P_2^- in the right portion of Figure 4-13. Moving through the downstream duct the P_2^+ vector may be considered to rotate very slowly. The P_2^- vector rotates approximately one revolution as we pass down the duct. Since P_2^+ and P_2^- are roughly the same magnitude, the rapid changes in the magnitude of the pressure perturbation result. The $|P_2^+|$ value gives a mean value about which the rotation of the P_2^- vector gives the oscillation seen in Figure 4-14. The peak and two nodes result as P_2^- rotates, in phase or out of phase, respectively, with the vector.

A similar experiment was performed with a fundamental frequency $\approx$ 400 Hz. The resulting waves are drawn in Figure 4-16. The differences between calculated and measured resultant waves

(P_{1*}^{-} and P_1^{-} or P_{2*}^{+} and P_2^{+}) are similar to the previous experiment. We see that in both ducts the pressure wave disturbance gives the largest contribution. The magnitude of the pressure perturbation field is shown in Figure 4-17, while the phase is shown in Figure 4-18. The agreement between the calculated curve (solid line) and measured data points (as indicated) is quite good. The problem with measuring the phase at the position near the end of the duct is obvious in this experiment also. The same rapid oscillation appears in the downstream duct with the slower changes again appearing in the upstream duct.

4.5 Conclusion

The measurement of the incident pressure wave P_1^{+} poses no special difficulty. The measurement of the incident pressure wave P_2^{-} is very (phase) sensitive, apparently because the Mach number is near unity. The normalized solutions show, however, that this wave, P_2^{-}, does not strongly influence any other portion of the nozzle under these conditions. The calculation of the entropy wave, σ, is straightforward.

The normalized solutions can be used with the measured disturbances P_1^{+}, P_2^{-} and σ, to construct the resultant waves P_{1*}^{-}, P_{2*}^{+}, or the complete pressure perturbation field through the nozzle. These constructed quantities show good agreement through the nozzle and in the downstream duct. The agreement in the upstream duct is not quite as good, and this seems to be at least partly due to difficulty in accurately representing the mean Mach number distribution through

the nozzle.

The experiments verify that the analytical model proposed in Chapter II can be used to adequately describe the interaction of pressure and entropy waves with a one-dimensional subsonic nozzle flow. Although the experiments described here tested only two frequencies and one Mach number distribution, there is no reason to expect anomalous behavior at other frequencies or Mach distributions.

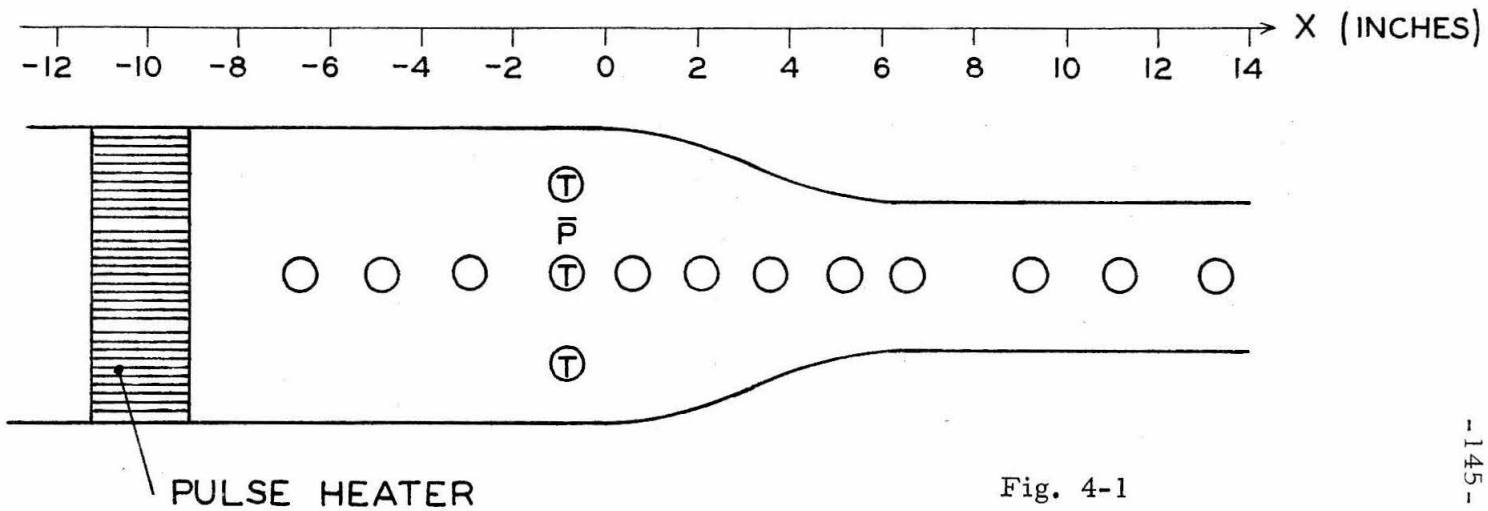

Fig. 4-1

BLOWDOWN TUNNEL

○ = DYNAMIC PRESSURE TRANSDUCER PORT

T = DYNAMIC TEMPERATURE TRANSDUCER PORT

$\bar{P}$ = STATIC PRESSURE PORT

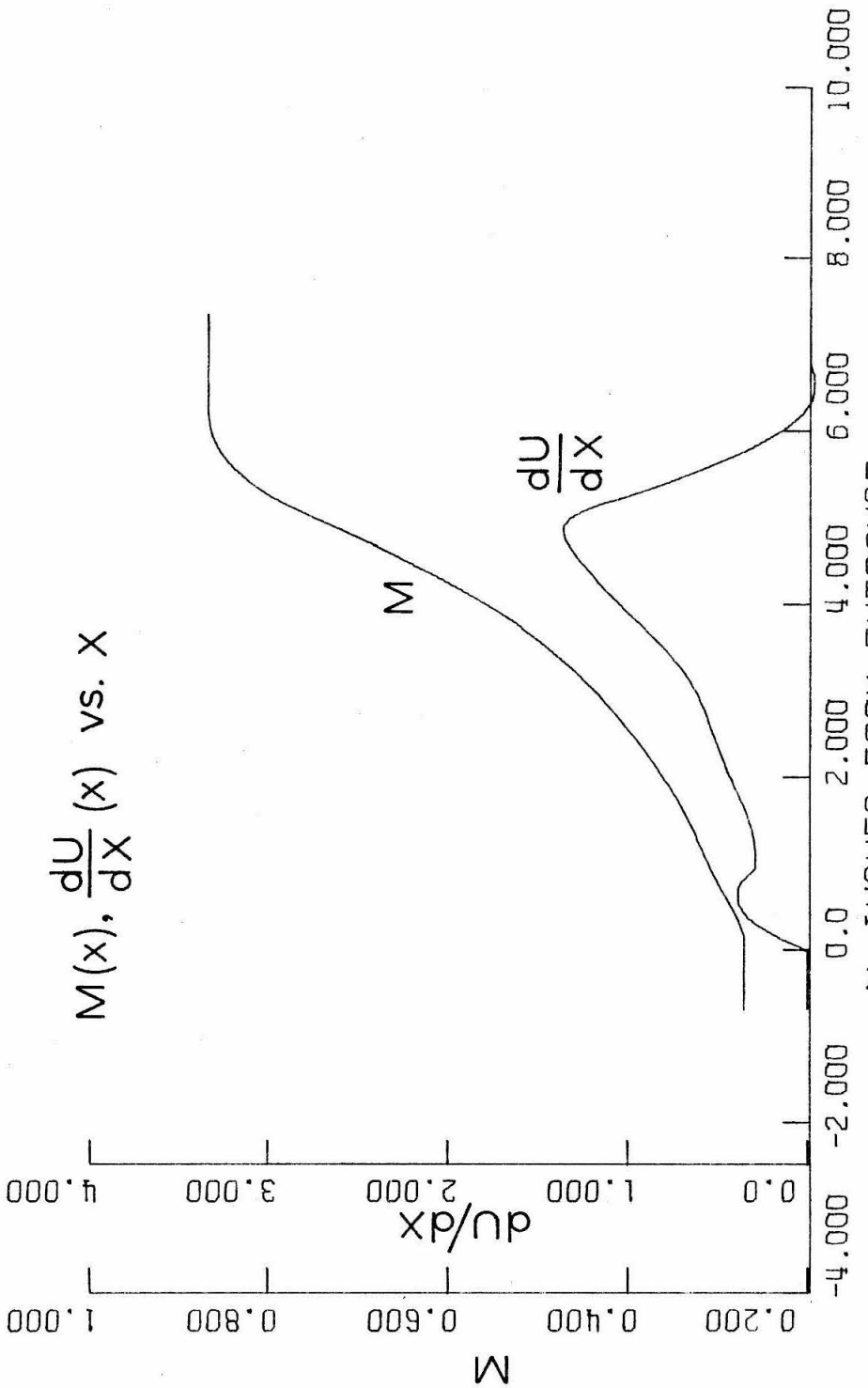

Fig. 4-2 Mach number and mean velocity gradient as used in numerical calculations. The curves represent interpolation between values based on static pressure measurements of several positions in the nozzle.

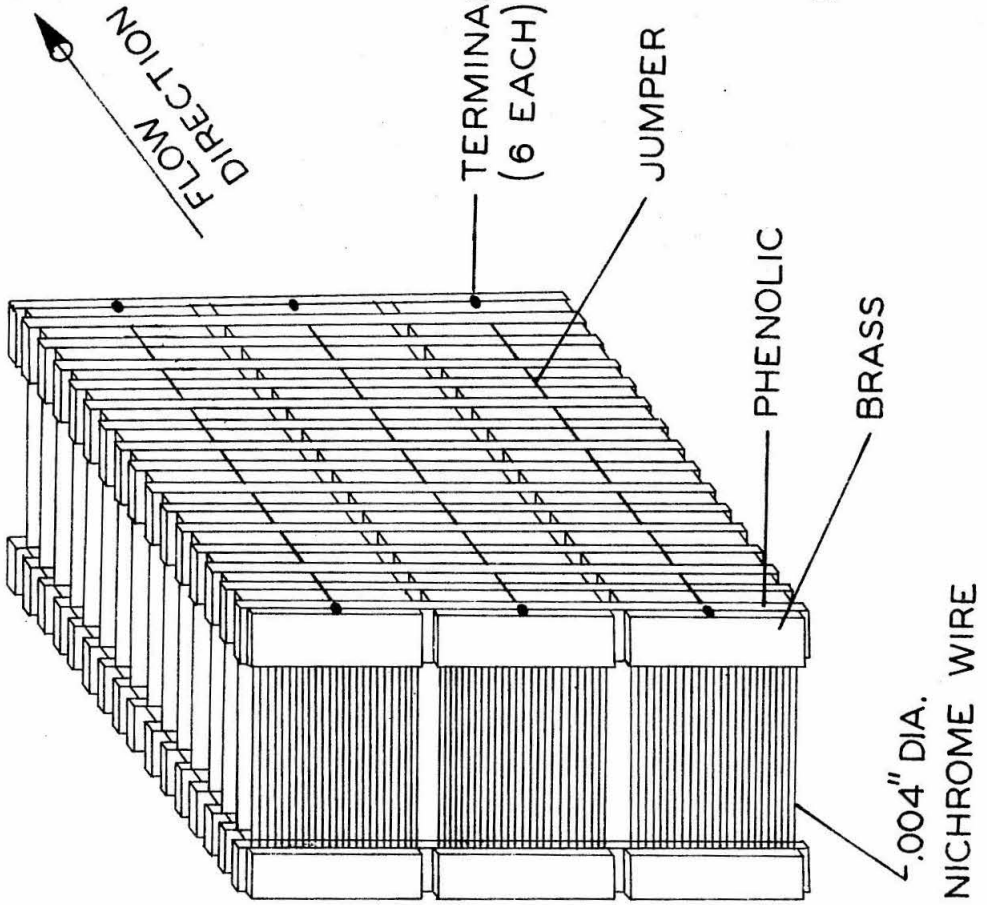

Fig. 4-3 PULSE HEATER

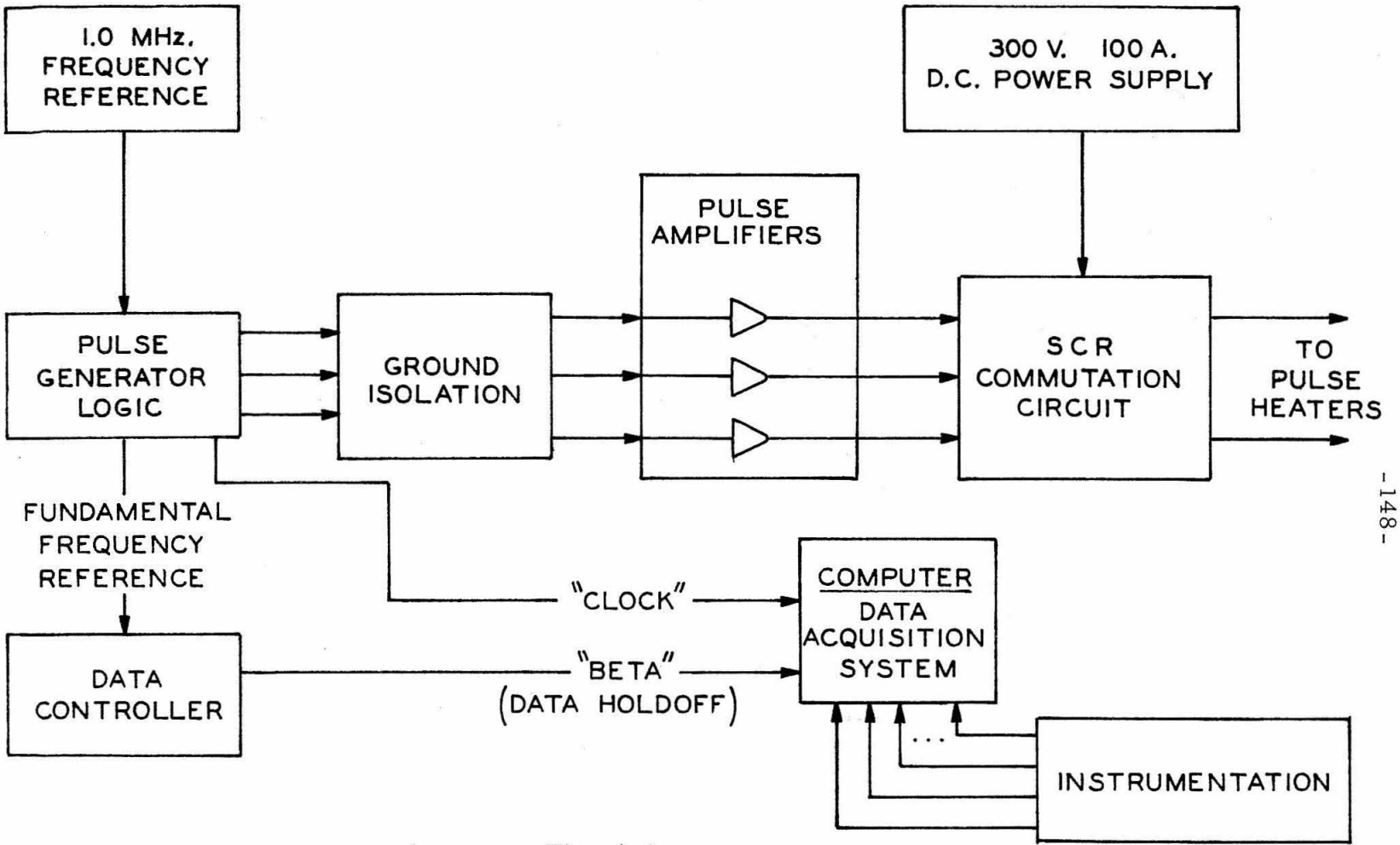

Fig. 4-4

GENERAL SCHEMATIC

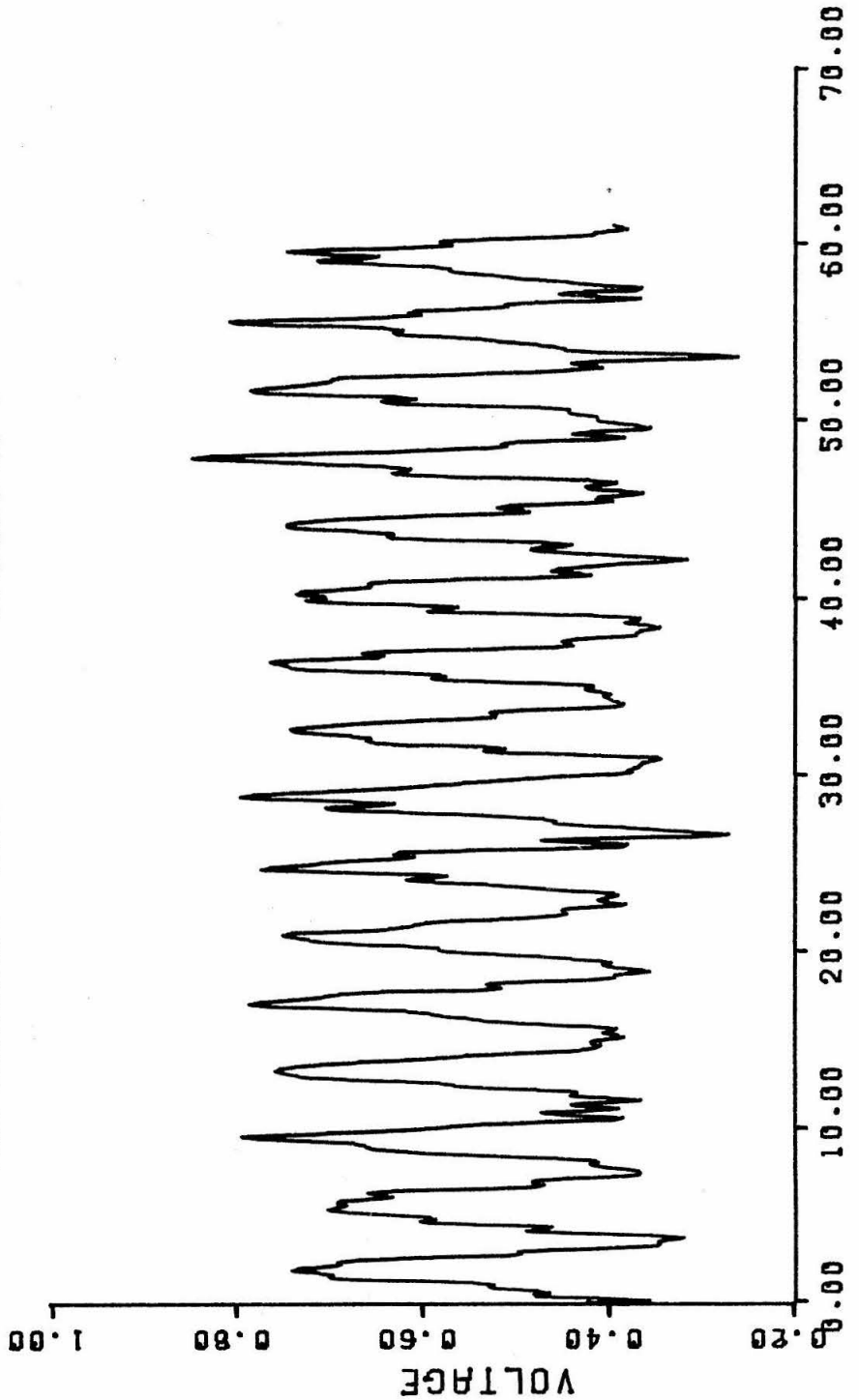

Fig. 4-5. Ensemble averaged waveform for typical pressure fluctuation recorded from position x = 11.5" (See Fig. 4-1). Fundamental frequency is 250 Hz.

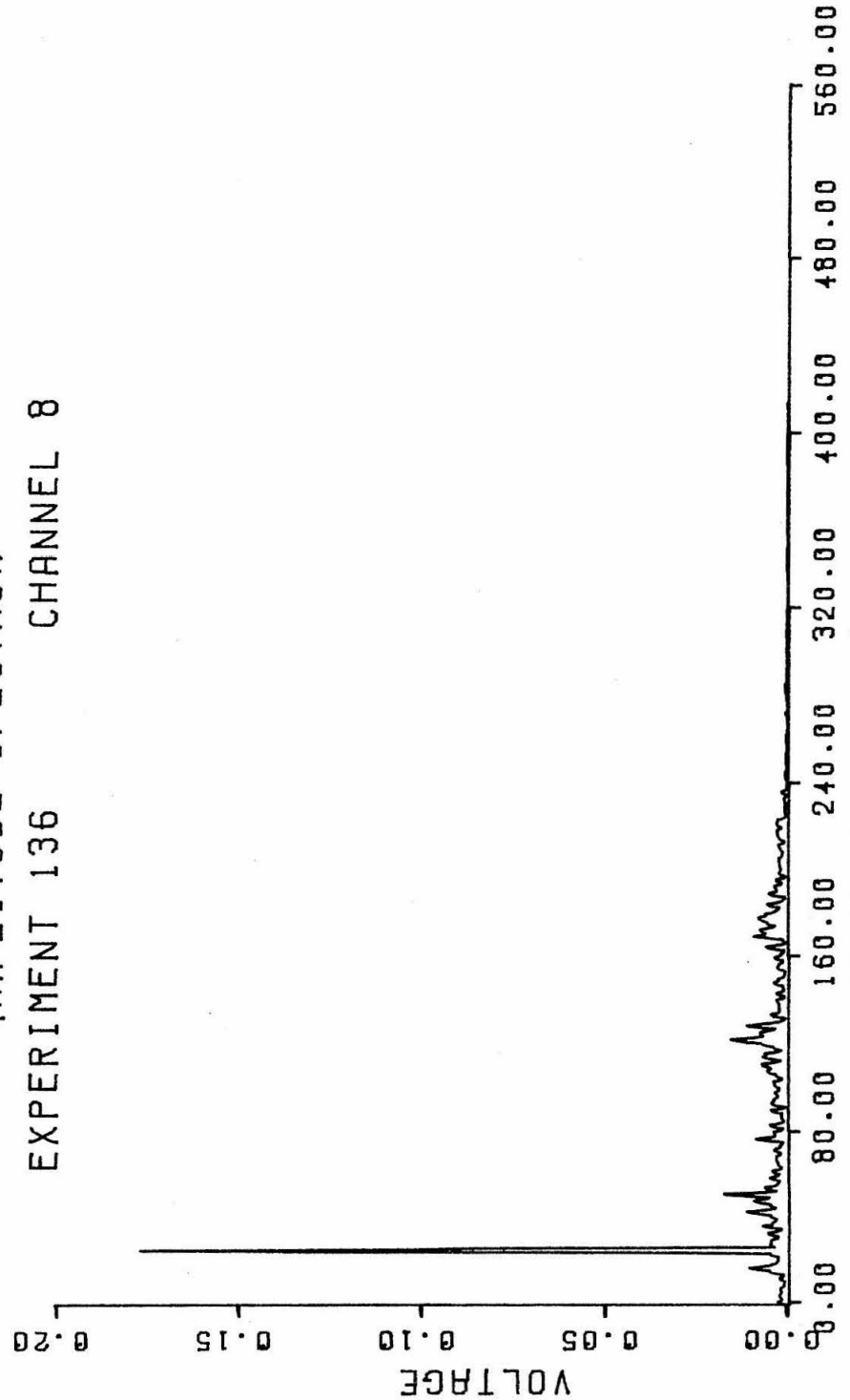

Fig. 4-6 The spectrum of the waveform given in Fig. 4-5. The peak (at 250 Hz) represents a pressure fluctuation of 123 db.

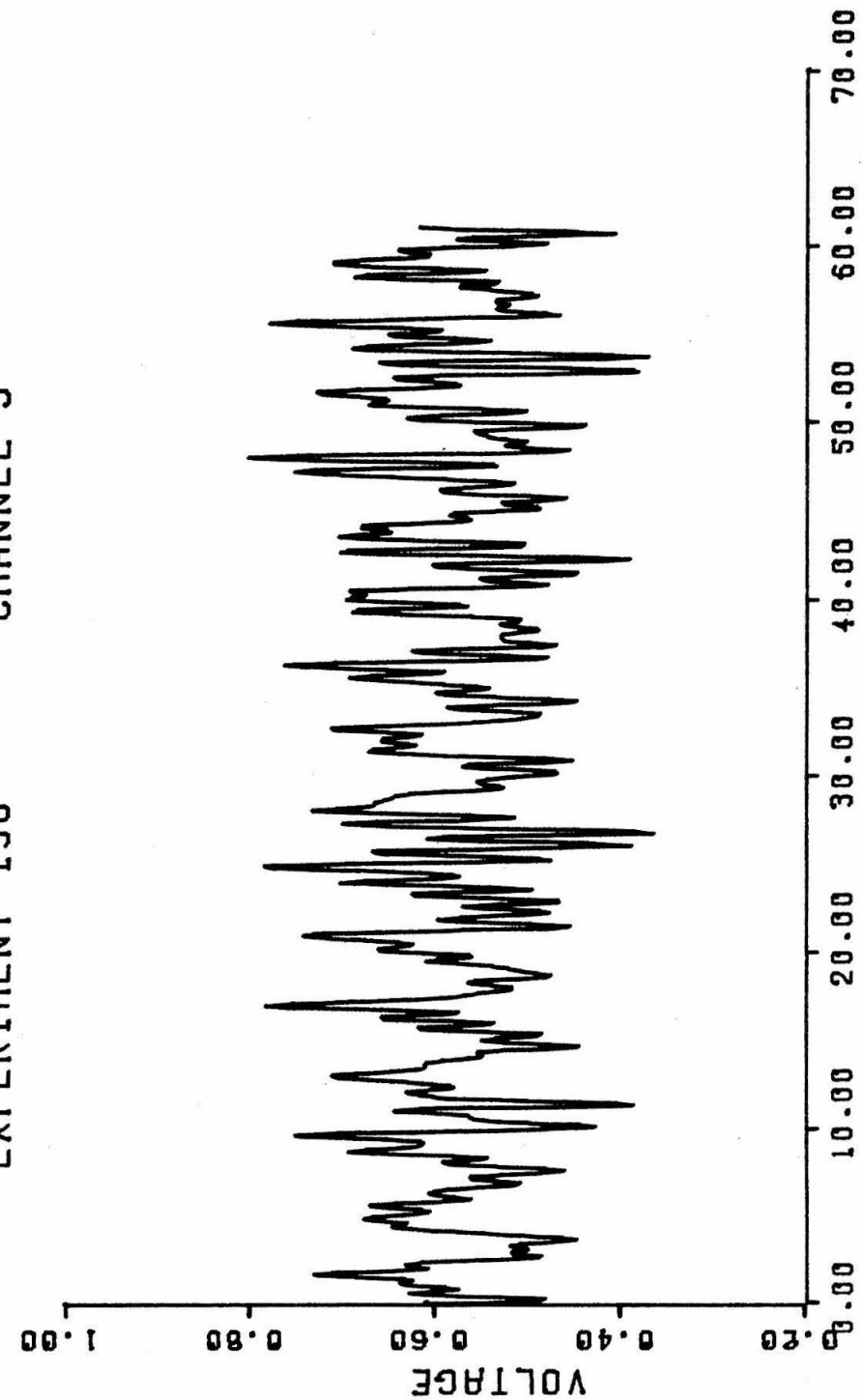

Fig. 4-7 Ensemble averaged waveform for typical pressure fluctuation recorded from position x = 13.5" (See Fig. 4-1). Fundamental frequency is 250 Hz.

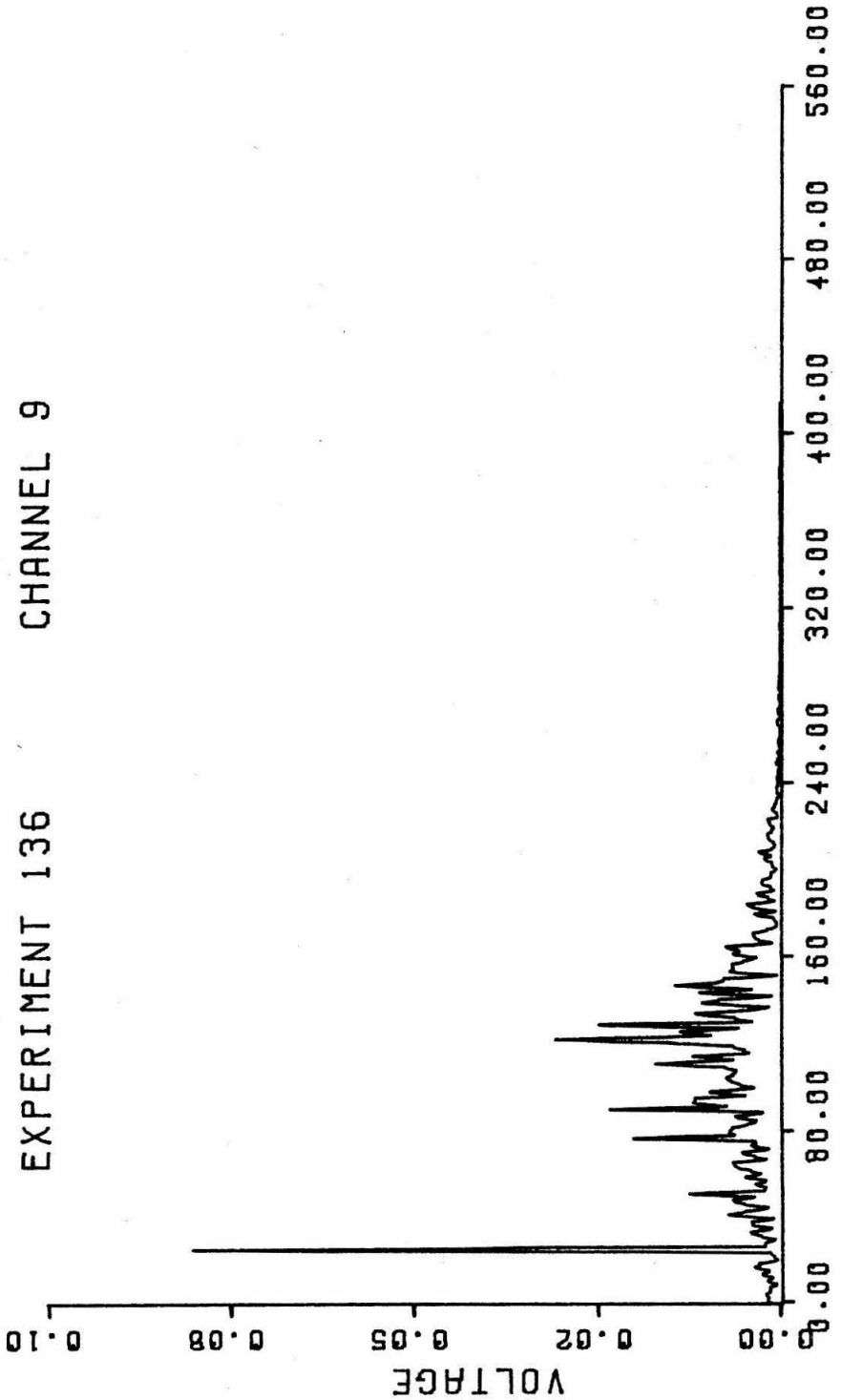

Fig. 4-8 The spectrum of the waveform given in Fig. 4-7. The peak (at 250 Hz) represents a pressure fluctuation of 115 db.

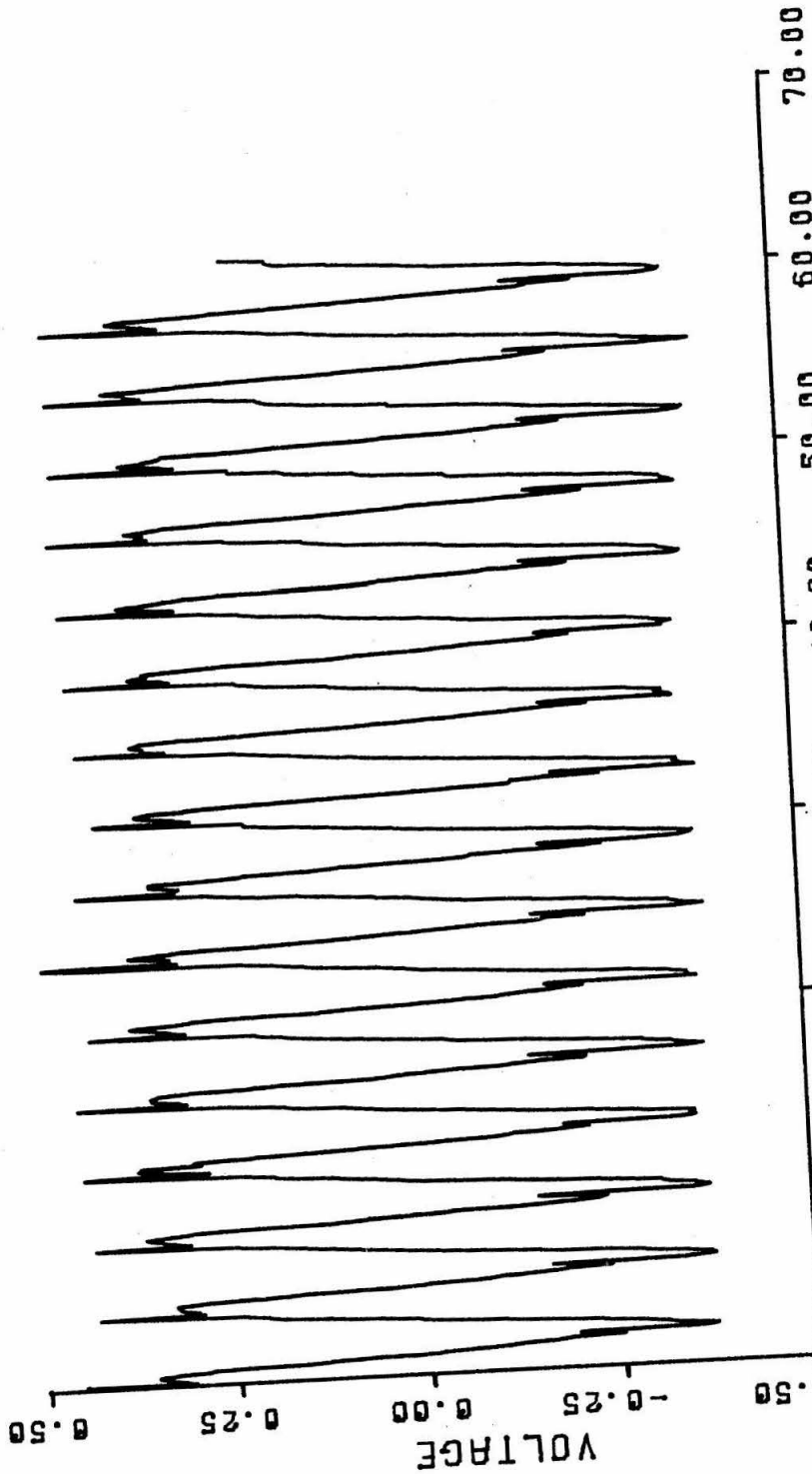

Fig. 4-9 Ensemble averaged waveform for typical temperature fluctuation signal. Fundamental frequency is 250 Hz.

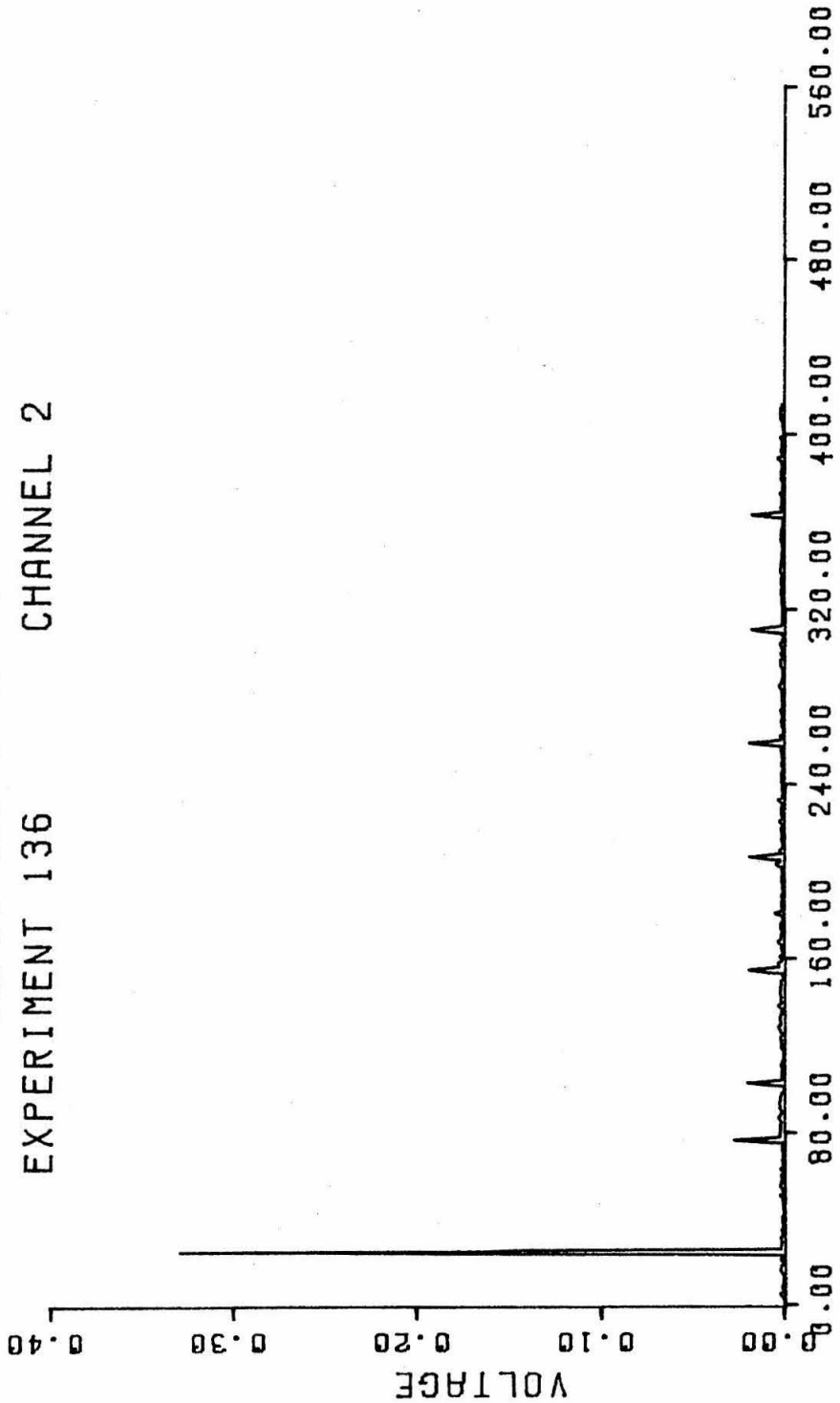

Fig. 4-10 The spectrum of the waveform given in Fig. 4-9. The peak (at 250 Hz) represents a temperature fluctuation of .40°C.

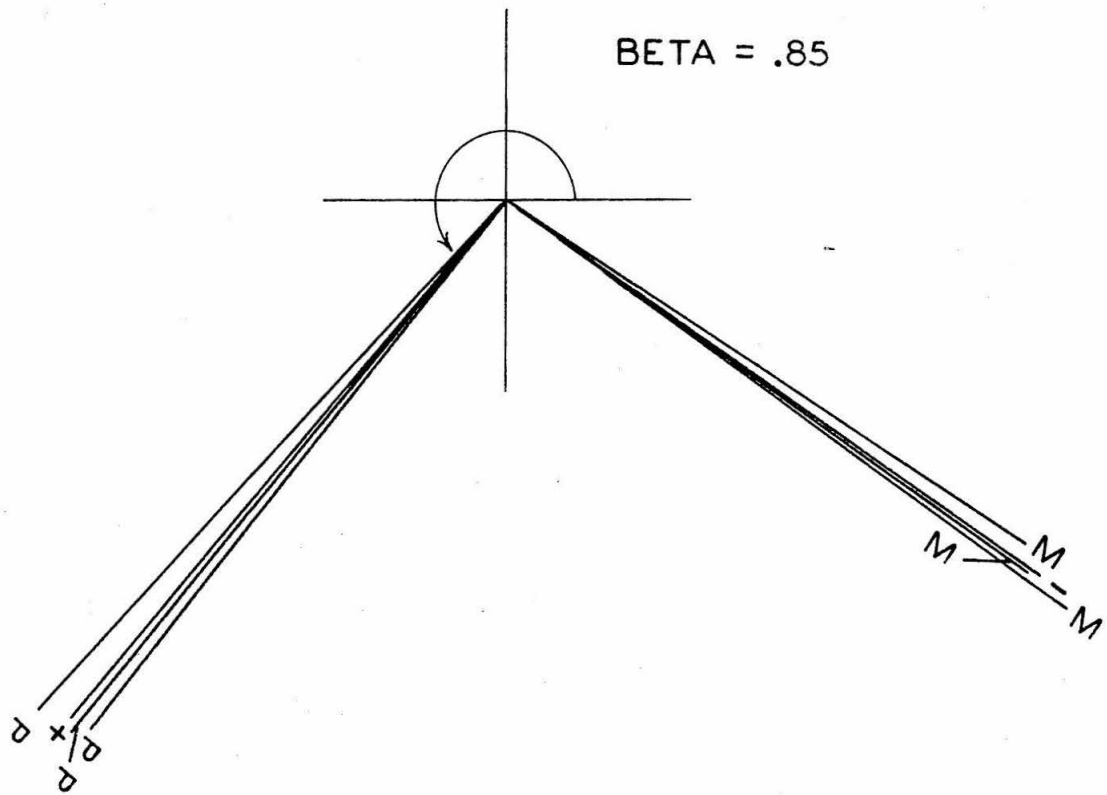

Fig. 4-11 Phase plane representation of P_1^+ (denoted "P") and P_1^- (denoted "M") acoustic waves from several pressure measurements in the upstream duct. The respective vector averages are denoted "+" and "-". Phase angles are measured (positive) counter-clockwise from right horizontal axis. Magnitude scale is arbitrary, but consistent for the same type of wave.

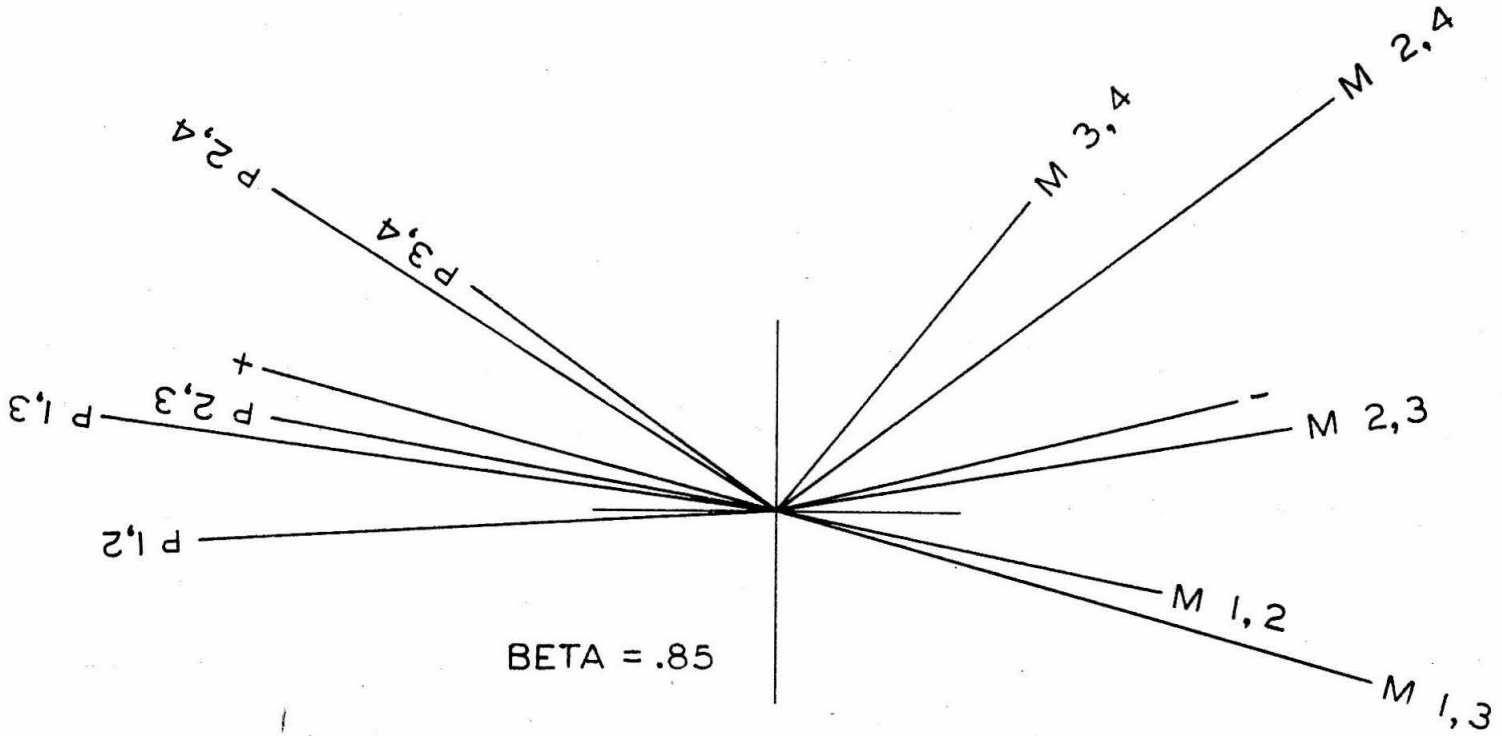

INDEX	POSITION
1	6.75"
2	9.25"
3	11.25"
4	13.25"

Fig. 4-12 Phase plane representation of P_2^+ and P_2^- as calculated from several positions in downstream duct. Notation and convention follows Fig. 4-11. Indices near end of vector can be used with the table to determine location of 2 points in the duct at which the pressure measurements were made which determined that vector.

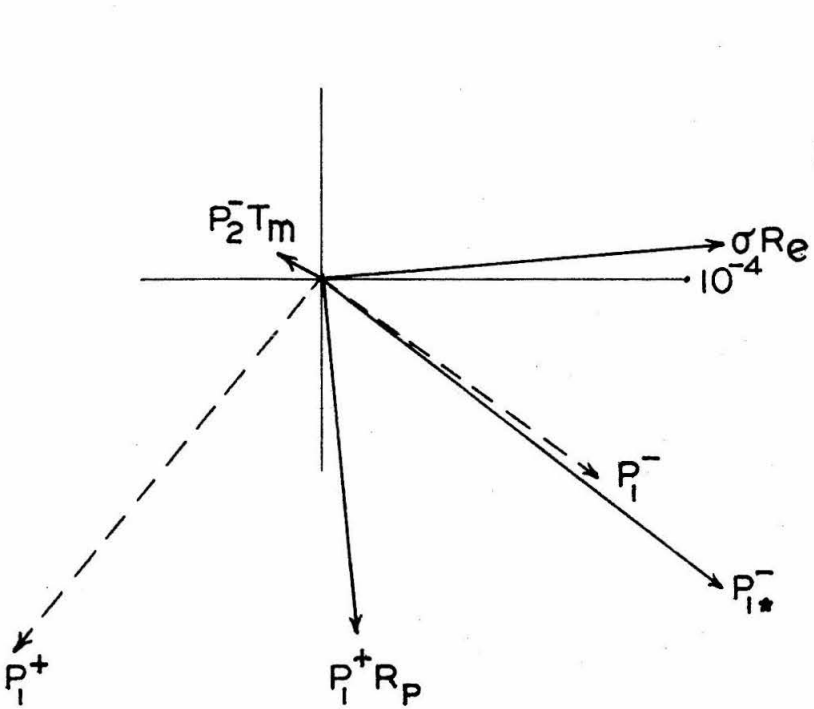

Fig. 4-13a
Phase plane representation of three ($P_1^+ R_p$, σR_e, $P_2^- T_m$) components making up computed vector P_{1*}^-. The measured values, P_1^+ and P_1^- are shown dashed and were taken from Fig. 4-11.

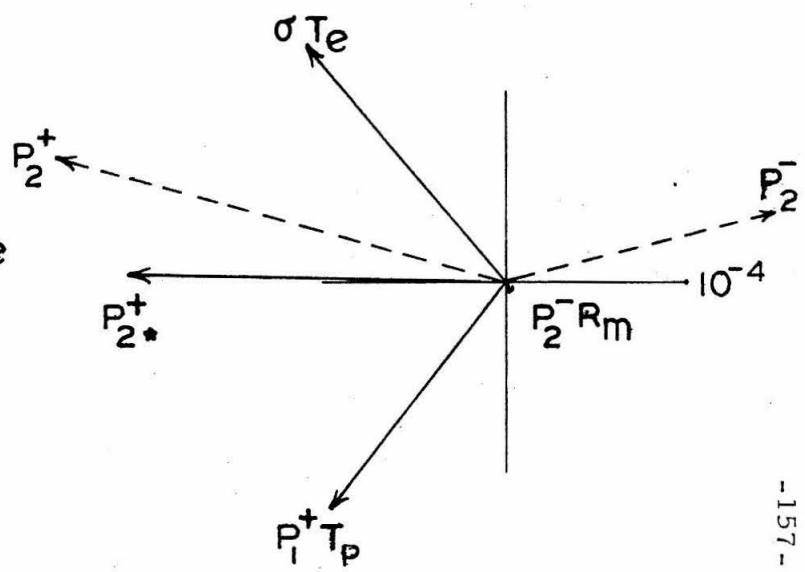

Fig. 4-13b
Phase plane representation of three ($P_1^+ T_p$, σT_e, $P_2^- R_m$) components making up computed vector P_{2*}^+. The measured values P_2^+ and P_2^- are shown dashed and were taken from Fig. 4-12 (see vectors labeled "+" and "-").

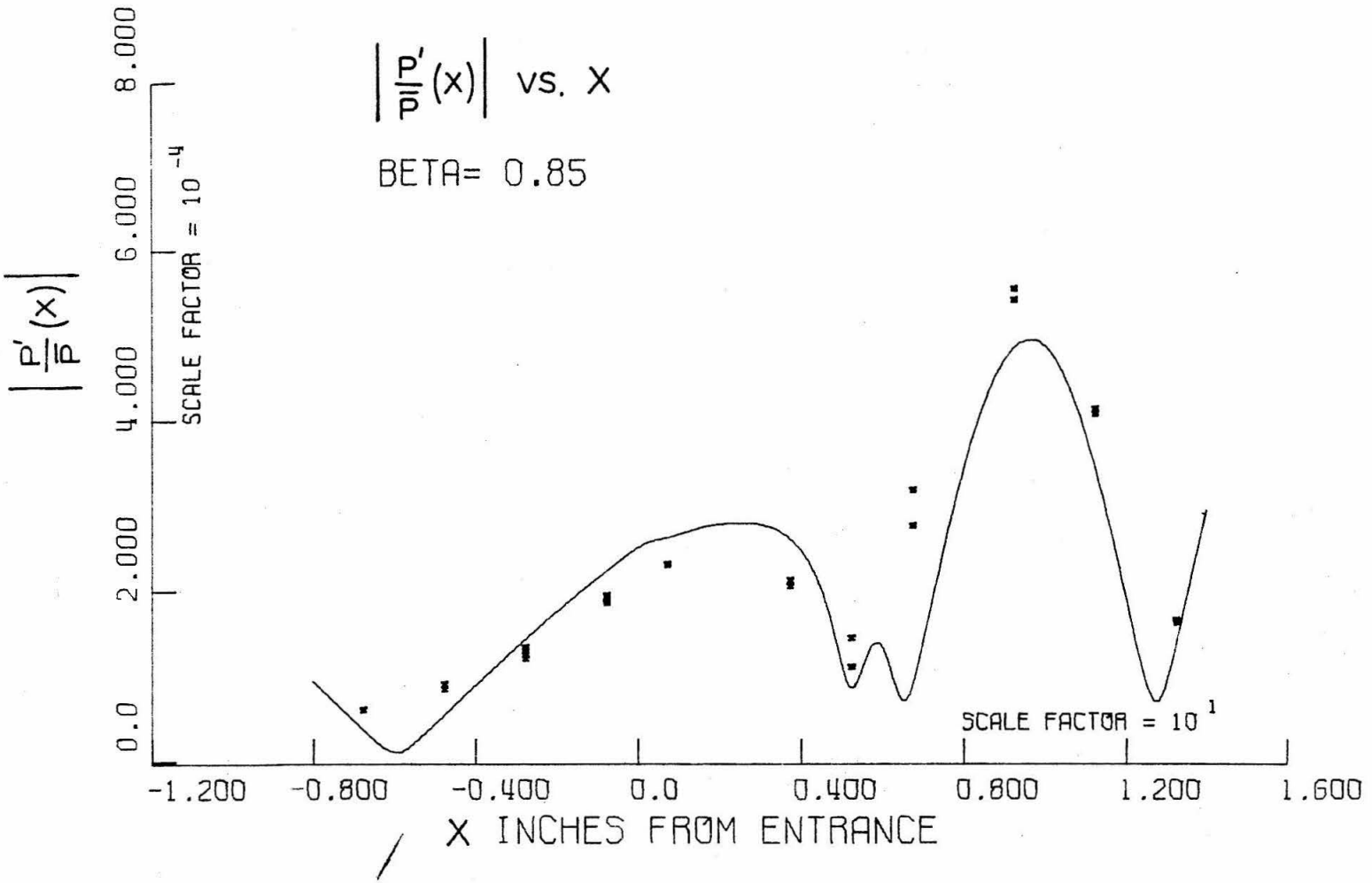

Fig. 4-14 Magnitude of pressure perturbation field in the tunnel as calculated by equation 4.34. Measured data points are indicated with the symbol. (The reduced frequency BETA = $\omega \ell / a^*$)

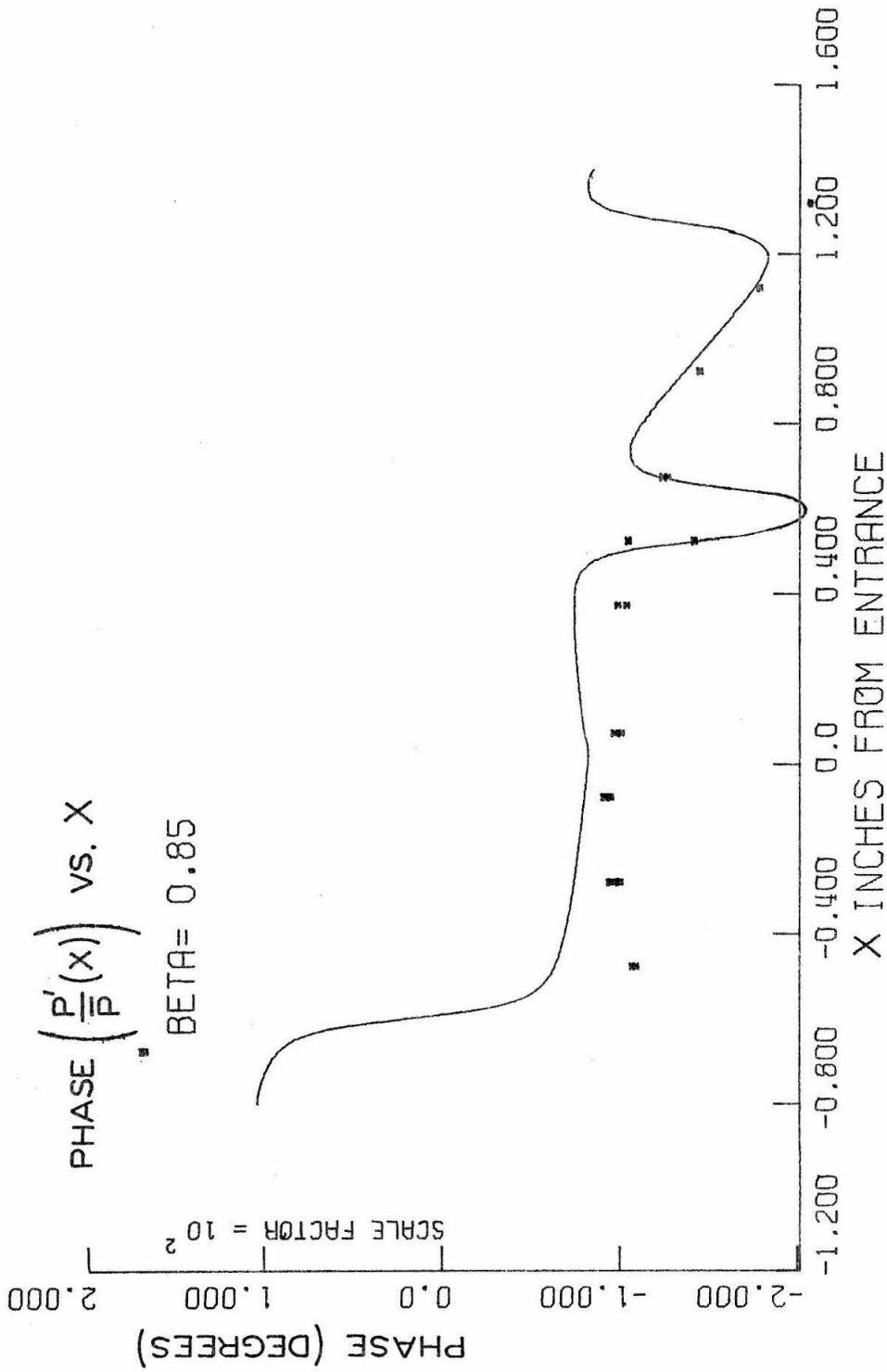

Fig. 4-15 Phase of pressure perturbation(corresponding magnitude is Fig. 4-14) field in the tunnel as calculated by equation 4.34. Measured data points are indicated with the symbol.

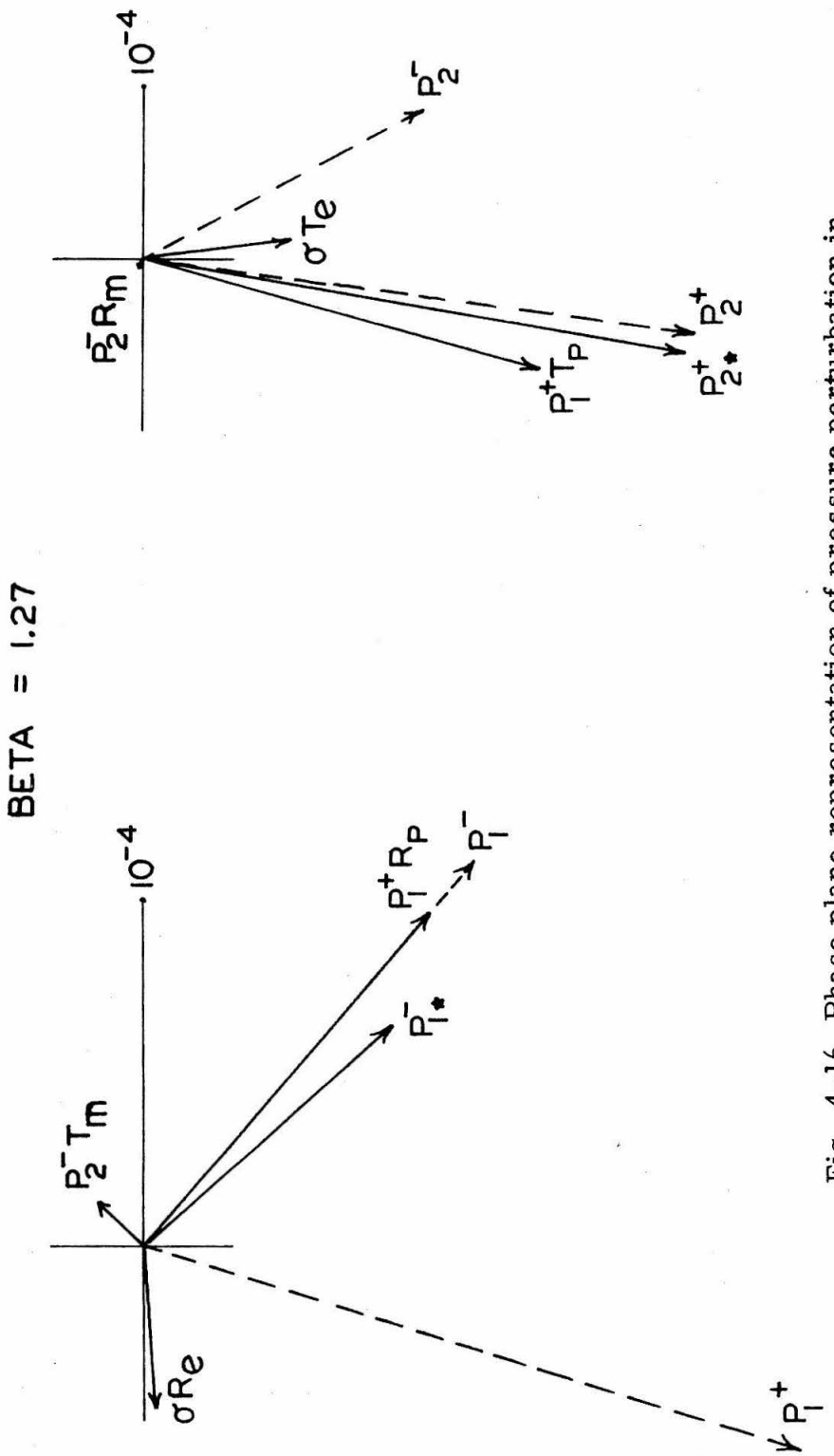

Fig. 4-16 Phase plane representation of pressure perturbation in constant area ducts, for experiment with higher fundamental frequency. (See Fig. 4-13 for explanation of symbols).

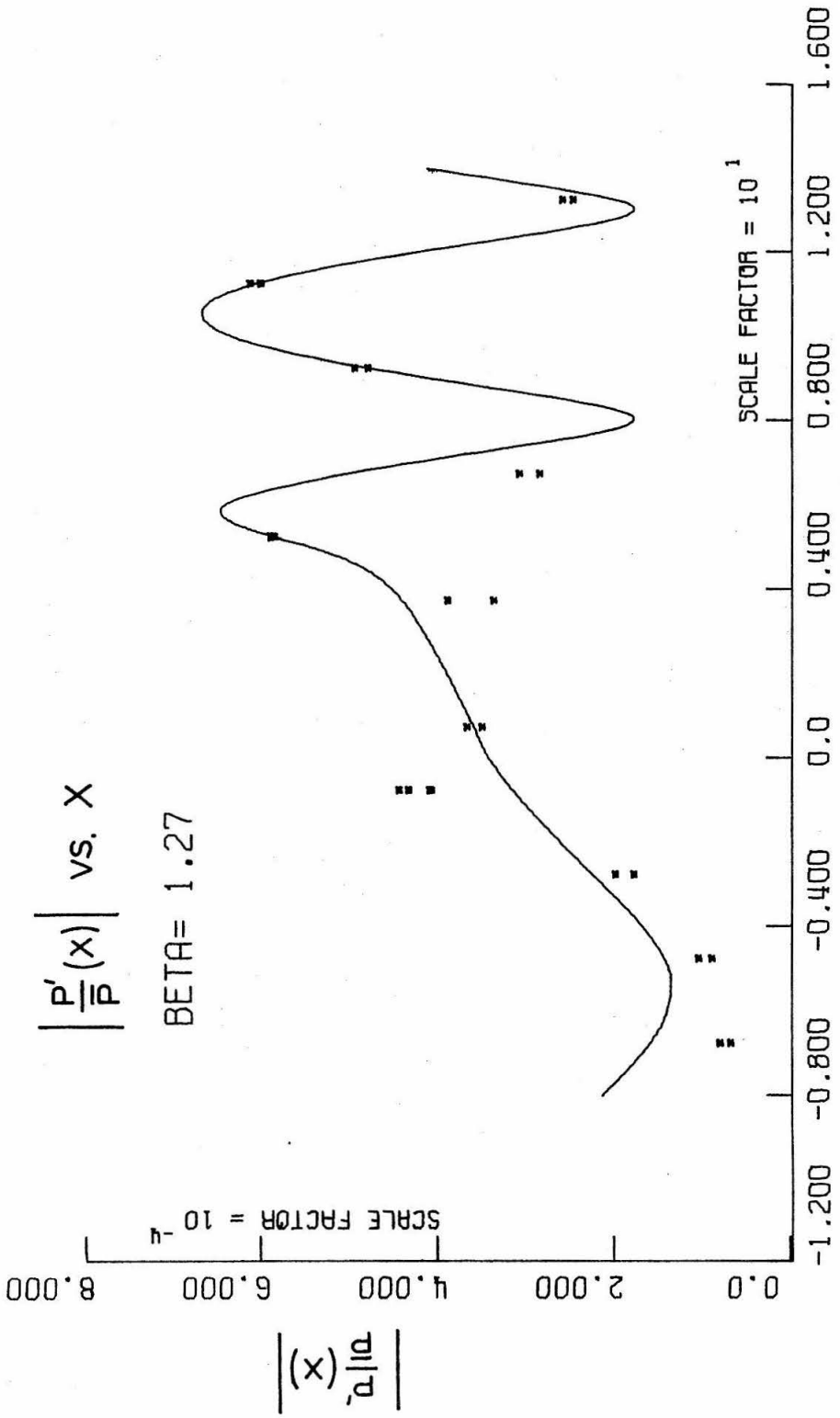

Fig. 4-17 Magnitude of pressure perturbation field in the tunnel for the "higher" frequency experiment.

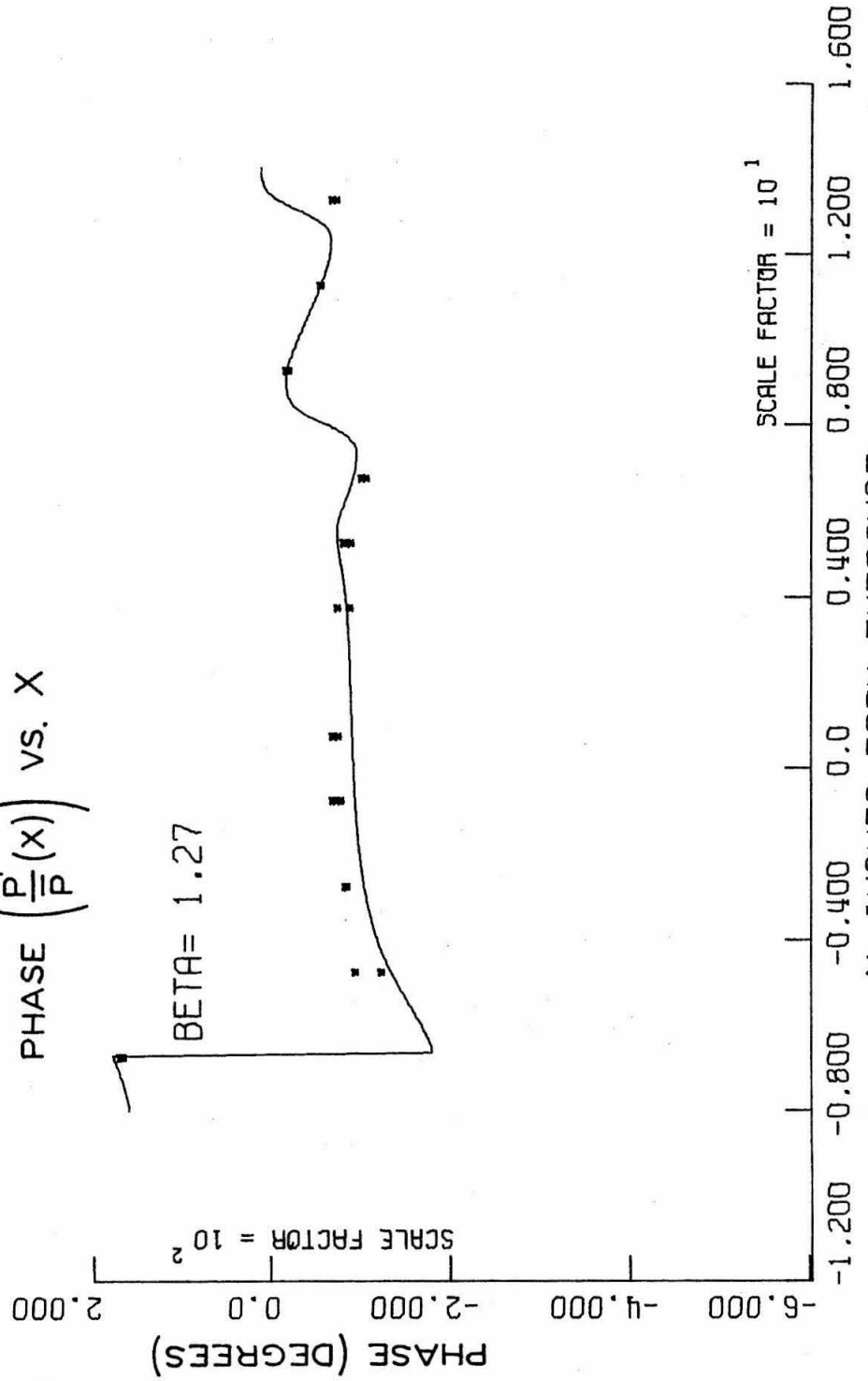

Fig. 4-18 Phase of pressure perturbation field in the tunnel for the "higher" frequency experiment.

REFERENCES FOR CHAPTER IV

1. Schlichting, H. Boundary Layer Theory, McGraw-Hill Book Co., New York (1968), p. 599.

2. Bull, M. "Wall Pressure Fluctuations Associated with Subsonic Turbulent Boundary Layer Flow," J. Fluid Mech., V. 28, 4 (1967), 719-754.

3. Schwartz, M. Information Transmission Modulation and Noise, McGraw-Hill Book Co., New York (1959).

4. Cooley, J., Lewis, P. and Welch, P. "Application of the Fast Fourier Transform to Computation of Fourier Integrals, Fourier Series and Convolution Integrals," IEEE Trans. on Audio and Electroacoustics, V. AU-15, 2 (June 1967).

5. Cooley, J., Lewis, P. and Welch, P. "The Fast Fourier Transform and Its Applications," IEEE Trans. on Education, V. 12, 1 (March 1969).

6. Pridmore-Brown, D. "Sound Propagation in Fluid Flowing through an Attenuating Duct," J. Fluid Mech., V. 4, 4 (1958), 393-406.

7. Hersh, A. and Catton, I. "Effect of Shear Flow on Sound Propagation in Rectangular Ducts," J. Acoust. Soc. Am., V. 55, 1 (1971), 992-1003.

8. Cooley, J., Lewis, P. and Welch, P. "The Fast Fourier Transform Algorithm: Programming Considerations in the Calculation of Sine, Cosine and Laplace Transforms," J. Sound Vib., V. 12, 3 (1970), 315-337.

V. EXPERIMENTS CONCERNING THE RESPONSE OF NOZZLE FLOWS TO TWO-DIMENSIONAL DISTURBANCES

5.1 Introduction

The analysis of Chapter II and the experiment presented in Chapter IV treat the one-dimensional interaction of pressure and entropy waves for subsonic nozzles. A similar treatment of supersonic nozzles was covered in references 6 and 8 of Chapter II. An obvious question arises, especially after considering the physical application. The pressure and entropy disturbances produced by the combustion process in the turbojet engine do not necessarily appear as one-dimensional waves interacting with the mean flow. This is especially true for the entropy disturbances, since they convect with the mean flow and may retain their general shape while passing through the engine. It is easy to imagine entropy spots, convecting from the burner through the turbine or nozzle, of small enough size to appear as three-dimensional disturbances. On the other hand, pressure waves of low enough frequency will tend to equilibrate (only plane modes propagate) so as to appear more "one-dimensional" to the mean flow.

It is our aim in this chapter to investigate the response of nozzles to disturbances which are not one-dimensional in nature. The nozzles to be investigated are the ones used in the experiment described in Chapter IV and a blowdown tunnel (which is choked) used in the experiments described by reference 8 of Chapter II. The pulse heater, as described in Chapter IV, will be used in the "dual" mode,

whereby the heat addition can be varied across the duct cross section. This cross-sectional variation is created by adding heat to the top third or to the bottom third of the flow cross section 180° out of phase.

An analysis (of periodic heat addition in a duct) will be described whereby the output of the pulse heater, in terms of entropy and pressure disturbances, can be found. The experiments consist of several frequencies (of pulse heater operation) for the two nozzles. Pressure perturbations are measured (primarily on the nozzle axis) and the results explained in terms of the output of the pulse heater as described by the analysis.

5.2 Experimental Apparatus: The Two-Dimensional Pulse Heater

The experiments performed on the subsonic nozzle differ from those described in Chapter IV only by the manner in which the pulse heater is operated. The supersonic nozzle was quite similar to the subsonic nozzle except that the nitrogen flow was accelerated from $M = .20$ to $M = 1.38$ in an axial distance of about 11". The throat position was 7.5" from the inlet and the Mach number distribution was very nearly linear through the nozzle. The nozzle is described in some detail in reference 8 of Chapter II. The reduced frequency for this nozzle uses the throat length, $\ell = 7.50$" as the length scale.

Recall that the pulse heater, which occupies about 2" of axial distance, is located about 8" upstream of the nozzle inlet position, $X = O$, see Figures 4-1 and 4-3. The heater is actually composed of three identical independent heaters, each of which occupies a third

of the duct cross section (one inch wide, three inches high). For the experiments to be described here, the center heater is not used. The remaining heaters, one occupying the top third of the duct cross section, and the other occupying the bottom third of the duct cross section, are pulsed 180° out of phase. This means that a voltage is applied to the top heater for 1/2 cycle (of the fundamental frequency) and then the bottom heater is pulsed for the remaining 1/2 cycle.

The heaters were operated from independent SCR's (see Appendix F). By passing the current from one SCR through a bank of power resistors (external to the blowdown tunnel) in series with the pulse heater, some of the power could be dissipated external to the pulse heater. In this manner the top heater was allowed to dissipate some fraction, α , of the power dissipated by the bottom heater. That fraction usually took on the values $\alpha = 0, 1/4, 1/2, 1$. The power dissipated by the bottom heater was approximately one-third the power dissipated by the entire heater when operated in the one-dimensional mode as in the experiments described in Chapter IV. Since each heater is one-third the resistance of the whole (5.4/3 = 1.8 ohms), 100 volts was the pulsing voltage for the bottom heater as opposed to 300 volts for the one-dimensional mode.

The data acquisition technique is similar to that explained in Chapter IV, except that more ensemble averaging was used. Note that the pressure disturbances we create in this experiment will be small compared to those of the one-dimensional heater. For the case $\alpha = 0$ one might expect pressure disturbances about one-third those of the one-dimensional experiments. In this case, it would be

necessary to average 900 ensembles to achieve a final signal-to-noise ratio similar to the value achieved with 100 averaged ensembles for the one-dimensional experiments. With the present facilities this is an impractical amount of data to be recorded. Instead, 400 ensembles were averaged; each ensemble was 2 cycles in length. The results presented here represent final signal-to-noise ratio about $(4/9)^{1/2} = 2/3$ that for the results of the one-dimensional experiments.

5.3 Fluctuating Heat Addition in a Two-Dimensional Duct

In order to understand the results of the experiment it will be necessary to know what disturbances the pulse heater creates, which are to interact with the nozzle. To that end, we present an analysis of a time-varying heat addition in a constant-area two-dimensional duct. We assume a duct of infinite axial dimension, height $2b$ and we allow an arbitrary heat addition over the region $0 \leq x \leq \ell$. We

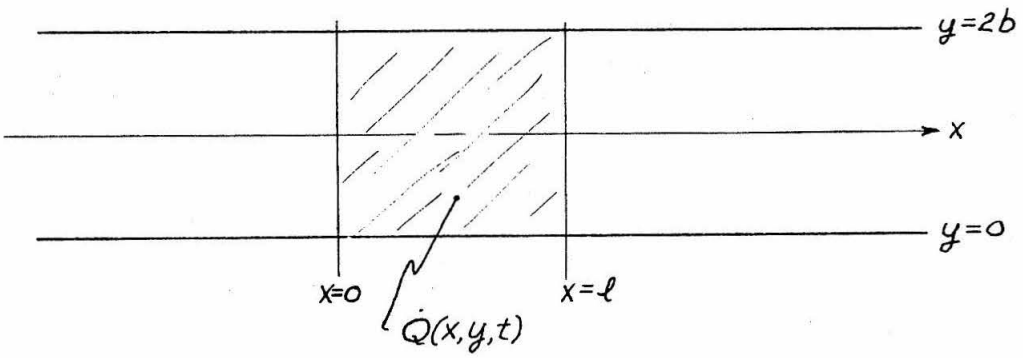

Diagram for the Analysis of Arbitrary Heat Addition in a Two-Dimensional Duct

neglect viscosity, thermal conductivity, and assume an ideal gas flows in the duct. The appropriate equations of continuity, axial momentum, vertical momentum, energy, and state are:

$$\frac{\partial \rho}{\partial t} + \frac{\partial}{\partial x}\rho u + \frac{\partial}{\partial y}\rho v = 0 \tag{5.1}$$

$$\rho\left(\frac{\partial}{\partial t} + u\frac{\partial}{\partial x} + v\frac{\partial}{\partial y}\right)u + \frac{\partial p}{\partial x} = 0 \tag{5.2}$$

$$\rho\left(\frac{\partial}{\partial t} + u\frac{\partial}{\partial x} + v\frac{\partial}{\partial y}\right)v + \frac{\partial p}{\partial y} = 0 \tag{5.3}$$

$$\rho C_v\left(\frac{\partial}{\partial t} + u\frac{\partial}{\partial x} + v\frac{\partial}{\partial y}\right)T + p\left(\frac{\partial u}{\partial x} + \frac{\partial v}{\partial y}\right) = Q(x,y,t) \tag{5.4}$$

$$p = \rho RT \tag{5.5}$$

The heat addition, $Q(x,y,t)$, is per unit volume. If the heat addition is small (compared to the flux of total enthalpy, for example), then we assume a solution which consists of the mean duct flow (constant) plus a small perturbation:

$$\begin{aligned} u(x,y,t) &= u_o + u'(x,y,t) \\ \rho(x,y,t) &= \rho_o + \rho'(x,y,t) \\ v(x,y,t) &= \quad v'(x,y,t) \\ p(x,y,t) &= p_o + p'(x,y,t) \\ T(x,y,t) &= T_o + T'(x,y,t) \end{aligned} \tag{5.6}$$

Inserting (5.6) into (5.1) - (5.5) and retaining terms linear in the perturbation quantities we find

$$\left(\frac{\partial}{\partial t} + u_o\frac{\partial}{\partial x}\right)\frac{\rho'}{\rho_o} + \frac{\partial u'}{\partial x} + \frac{\partial v'}{\partial y} = 0 \tag{5.7}$$

$$\left(\frac{\partial}{\partial t} + u_o\frac{\partial}{\partial x}\right)u' + \frac{\gamma p_o}{\rho_o}\frac{\partial}{\partial x}\frac{p'}{\gamma p_o} = 0 \tag{5.8}$$

$$\left(\frac{\partial}{\partial t} + U_o \frac{\partial}{\partial x}\right) v' + \frac{\gamma P_o}{\rho_o} \frac{\partial}{\partial y} \frac{P'}{\gamma P_o} = 0 \tag{5.9}$$

$$\left(\frac{\partial}{\partial t} + U_o \frac{\partial}{\partial x}\right)\left(\frac{P'}{\gamma P_o} - \frac{\rho'}{\rho_o}\right) = \frac{Q}{C_p T_o \rho_o} \equiv q(x,y,t) \tag{5.10}$$

which may be manipulated to find an expression for the pressure perturbation:

$$\left(\frac{\partial}{\partial t} + U_o \frac{\partial}{\partial x}\right)^2 \tilde{\mathcal{P}} - c^2\left(\frac{\partial^2}{\partial x^2} + \frac{\partial^2}{\partial y^2}\right)\tilde{\mathcal{P}} = \frac{\gamma P_o}{\rho_o} \tilde{F}(x,y,t) \tag{5.11}$$

where we define

$$\tilde{\mathcal{P}}(x,y,t) = \frac{P'}{\gamma P_o}$$

$$c^2 = \gamma P_o/\rho_o$$

$$M = U_o/c$$

$$\frac{\gamma P_o}{\rho_o} \tilde{F}(x,y,t) = \left(\frac{\partial}{\partial t} + U_o \frac{\partial}{\partial x}\right) q(x,y,t)$$

Since the surfaces $y = 0, 2b$ are flat, we must have $v'(x,0,t) = v'(x,2b,t) = 0$. Equation (5.9) then gives the boundary condition on the pressure :

$$\frac{\partial}{\partial y}\tilde{\mathcal{P}} = 0 \qquad y = 0, 2b \tag{5.12}$$

We also assume the radiation condition.

For periodic heat addition we let

$$\tilde{F}(x,y,t) = F(x,y)e^{i\omega t}$$

therefore

$$\tilde{\mathcal{P}}(x,y,t) = \mathcal{P}(x,y)e^{i\omega t}$$

and equation (5.11) becomes

$$\frac{1}{c^2}\left(-\omega^2+2i\omega u_o\frac{\partial}{\partial x}+u_o^2\frac{\partial^2}{\partial x^2}\right)p-\left(\frac{\partial^2}{\partial x^2}+\frac{\partial^2}{\partial y^2}\right)p=F(x,y) \tag{5.13}$$

If we solve the problem via the Green's function,

$$p(x,y)=\int_{-\infty}^{\infty}\int_{0}^{2b}G(x,y;\xi,\eta)F(\xi,\eta)\,d\eta\,d\xi$$

$$=\int_{0}^{\ell}\int_{0}^{2b}G(x,y;\xi,\eta)F(\xi,\eta)\,d\eta\,d\xi \tag{5.14}$$

(since $F(x,y)\equiv 0$, $\ell<x<0$), we see that this is identical to the problem which was solved in Section 3.4. Hence, the Green's function may be taken directly from (3.36), (3.37).

For the waves which propagate to $+\infty$, the attenuated waves are neglected and the Green's function simplifies:

$$G(x,y;\xi,\eta)=\sum_{n=0}^{N_1}A_n\cos\left(\frac{n\pi y}{2b}\right)\cos\left(\frac{n\pi\eta}{2b}\right)\exp\left\{i\frac{\omega}{c}(x-\xi)\left(\frac{M}{1-M^2}-\Omega_n\right)\right\}$$

Equation (5.14) gives for the pressure mode n :

$$p_n^{+}(x,y)\equiv p_n(x,y)\Big|_{x\to+\infty}=A_n\cos\left(n\pi\frac{y}{2b}\right)\exp\left\{i\frac{\omega}{c}x\left(\frac{M}{1-M^2}-\Omega_n\right)\right\}$$

$$\int_{0}^{\ell}\int_{0}^{2b}\cos\left(n\pi\frac{\eta}{2b}\right)\exp\left\{-i\frac{\omega}{c}\xi\left(\frac{M}{1-M^2}-\Omega_n\right)\right\}F(\xi,\eta)\,d\eta\,d\xi \tag{5.15}$$

$$0\le n\le N_1$$

For the waves which propagate to $-\infty$ the Green's function simplifies to:

$$G(x,y;\xi,\eta) =$$

$$\sum_{n=0}^{N} A_n \cos\left(n\pi\frac{y}{2b}\right)\cos\left(n\pi\frac{\eta}{2b}\right)\exp\left\{i\frac{\omega}{c}(x-\xi)\left(\frac{M}{1-M^2}+\Omega_n\right)\right\}$$

$$-\sum_{N_1+1}^{N} A_n \cos\left(n\pi\frac{y}{2b}\right)\cos\left(n\pi\frac{\eta}{2b}\right)\exp\left\{i\frac{\omega}{c}(x-\xi)\left(\frac{M}{1-M^2}-\Omega_n\right)\right\} \qquad (5.16)$$

The duct modes may be calculated from (5.14):

$$P_n^-(x,y) \equiv P_n(x,y)\Big|_{x\to-\infty} = A_n \cos\left(n\pi\frac{y}{2b}\right)\exp\left\{i\frac{\omega}{c}(x-\xi)\left(\frac{M}{1-M^2}\pm\Omega_n\right)\right\}$$

$$\int_0^{\ell}\int_0^{2b} \cos\left(n\pi\frac{\eta}{2b}\right)\exp\left\{-i\frac{\omega}{c}\xi\left(\frac{M}{1-M^2}\pm\Omega_n\right)\right\}F(\xi,\eta)\,d\eta\,d\xi \qquad (5.17)$$

$0 \le n \le N$
$N_1 < n \le N$

If the frequency is low enough such that

$$\omega < \omega_c \equiv \frac{\pi c}{2b}(1-M^2)^{1/2} \qquad (5.18)$$

then only the plane modes ($n=0$) will propagate, i.e., $N=0$. (The cutoff frequency, $f_c = \omega_c/2\pi$, for our duct is 2100 Hz.) In this case, the wave propagating to $+\infty$ becomes

$$P_o^+(x,y) = \frac{c}{4ib\omega}\exp\left(-i\frac{\omega}{c}\frac{x}{1+M}\right)\int_0^{\ell}\int_0^{2b}\exp\left(i\frac{\omega}{c}\frac{\xi}{1+M}\right)F(\xi,\eta)\,d\eta\,d\xi \qquad (5.19)$$

We would like to calculate P_o^+ for the heat input we expect from the pulse heater. The heat addition $Q(x,y)e^{i\omega t}$ will be constant for $0 \le x \le \ell$ and using the "α" notation to denote the

fraction of power dissipated by the top heater compared to the bottom heater, we get

$$2bWl\,Q(x,y) = \begin{cases} q_\omega & 0 \le y \le 2b/3 \\ 0 & 2b/3 < y < 4b/3 \\ -\alpha q_\omega & 4b/3 \le y \le 2b \end{cases} \tag{5.20}$$

Here, q_ω is the net heat addition component at frequency ω and the tunnel depth is W. The minus sign emphasizes that the heat addition to the lower third of the flow is 180° out of phase with the heat addition to the upper third of the flow. Then

$$e^{i\omega t} F(x,y) = \frac{1}{c^2}\left(\frac{\partial}{\partial t} + U_o \frac{\partial}{\partial x}\right) \frac{Q(x,y)}{C_p T_o \rho_o} e^{i\omega t}$$

$$= \begin{cases} \dfrac{i\omega/2bWl}{c^2 C_p T_o \rho_o}\, q_\omega & 0 \le y \le 2b/3 \\ 0 & 2b/3 < y < 4b/3 \\ \dfrac{-i\alpha\omega/2bWl}{c^2 C_p T_o \rho_o}\, q_\omega & 4b/3 \le y \le 2b \end{cases} \tag{5.21}$$

Inserting this value of F into (5.19) we find

$$p_o^+ = \left(\frac{1-\alpha}{3}\right)\left(\frac{1+M}{2}\right)\left(\frac{q_\omega}{C_p T_o \rho_o 2bWl\omega}\right)\left(1 - e^{i\frac{\omega}{c}\frac{l}{1+M}}\right)\left(i\, e^{-i\frac{\omega}{c}\frac{x}{1+M}}\right) \tag{5.23}$$

For the purely one-dimensional heat pulse, (5.20) would be replaced by

$$2blW\,Q(x,y) = q_\omega \qquad 0 \le y \le 2b \tag{5.24}$$

where the value of q_ω is unchanged. The result then is identical to (5.23) except the leading factor $(1-\alpha)/3$ is replaced by 1.0. It is clear that P_o^- must behave in a similar manner.

For the region $x>\ell$ we may re-write (5.10) in the form

$$\left(\frac{\partial}{\partial t}+u_o\frac{\partial}{\partial x}\right)s'(x,y,t)=0 \qquad (5.25)$$

Hence the entropy wave retains its shape as it convects towards the nozzle.

We summarize the above results for the experimental conditions of interest:

(i) The entropy wave produced by the pulse heater retains its shape as it convects towards the nozzle. This will, in general, be two-dimensional.

(ii) The plane waves produced by the pulse heater scale like $(1-\alpha)/3$ (where α is the ratio of power dissipated by the lower heater to that of the upper heater) of the plane waves produced by operating the heater in the one-dimensional mode.

5.4 Results of the Experiment and Discussion

Since the acoustic disturbances produced by the two-dimensional heater are only plane waves which scale like $(1-\alpha)/3$ compared to those produced by the one-dimensional heater, the pressure perturbation field through the complete tunnel resulting from these waves should scale like $(1-\alpha)/3$. We know how to treat the one-dimensional acoustic waves (see Chapters II and IV).

It only remains that we determine the response of the nozzle to the two-dimensional entropy waves. In the following experiments the heater was operated at a given frequency for values of α = 0, 1/4, 1/2 and 1. The pressure perturbation (at the fundamental frequency) was measured at several positions on the duct axis as well as one position approximately 1" above the axis at the position just upstream of the nozzle entrance (see Figure 4-1 for the subsonic nozzle). The purpose of this latter measurement was simply to detect any two-dimensional activity at that point, since the pressure recorded there should be identical to the pressure recorded on the duct axis (at the entrance location) for purely one-dimensional wave motion.

As a comparison, the results for the one-dimensional heat pulse experiment are also plotted. These data have been scaled such that the pressure on the (axis) inlet position is the same as the pressure at that position for the $\alpha=0$ experiment. Note that in the absence of entropy waves, this scaling value should be 1/3. Due to difficulties in precisely controlling the amplitude of the voltage supplied to the pulse heaters, and due to the effect of the two-dimensional entropy wave, this value varied by ± 10 per cent.

The results for the supersonic nozzle are plotted in Figures 5-1, 5-2. The off-axis measurement (near the inlet) is shown as the unattached point in all the graphs. For the case $\alpha=1$ we should have no pressure wave P_i^+ impinging upon the nozzle according to the analysis of Section 5.2. The results show very low values recorded for the pressure on the duct axis. (These values are actually the magnitude of the residual flow noise.) The off-axis measure-

ment, however, clearly shows a pressure disturbance. The entropy wave is completely asymmetric about the duct axis. This results in a pressure perturbation field which is completely asymmetric about the duct axis.

This implies a pressure node on the axis in the same sense that in a constant area duct, the odd (asymmetric) modes have a node on the duct axis. The value recorded off-axis confirms that there is a pressure disturbance in the duct. The higher frequency case (Figure 5-1) shows consistently increasing axial pressure perturbation as α decreases, indicating two things. The first is that a plane pressure wave, P_1^+, of scale $(1-\alpha)/3$ impinges upon the nozzle and increases in magnitude with decreasing α. The second is that the "increasing symmetry" of the entropy wave produces more symmetrical pressure perturbation fields and hence larger axial pressure measurements.

The results for the experiment performed at the lower frequency ($\omega \ell / a^* = .97$), shown in Figure 5-2, are similar; however, the two-dimensional effects are smaller. Note that with decreasing α, the data converge to the (scaled) one-dimensional results. In addition, the difference between the off-axis pressure and the on-axis pressure (at the inlet) is smaller for this experiment. These results imply that for a sufficiently long entropy spot (low frequency), the two-dimensionality of the spot may be neglected. The resulting pressure perturbation field will scale like the effective cross-sectional area of the duct that the entropy spot occupies. Note that in Figure 5-2 the pressure perturbation fields (for a given value of α) scale

like $1-\alpha$, in a crude way. It is expected that for decreasing frequency, this scaling will improve.

The results for the experiments performed in the subsonic nozzle are presented in Figures 5-3, 5-4, 5-5. It is to be expected that, for low enough frequency, the pressure perturbation fields (for each α) should again scale like $1-\alpha$. The dimensional frequency ω used in Figure 5-3 corresponds to that used in Figure 5-1. The dimensional frequency ω used in Figure 5-4 corresponds to that used in Figure 5-2. It was expected, since the scaling was effective in Figure 5-2, that it would be effective in Figure 5-4. It can be seen that this is not the case. The two-dimensional effects are as apparent in Figure 5-3 and in 5-4. This is especially obvious in the downstream constant-area duct, $x > 6.75''$, since only plane waves should propagate here. We knew that the plane waves due to the pressure disturbance, p_1^+ , created by the heater should scale properly. We do not know how the plane waves, created by the two-dimensional entropy wave, should scale. It is clear from the results in the downstream duct (Figures 5-3, 5-4) that these plane waves do not scale like $1-\alpha$.

The experiment was performed at a lower frequency ($f \approx$ 200 Hz) to verify that scaling would occur. These results are presented in Figure 5-5. The case $\alpha=0$ scales very closely to the one-dimensional results and the case $\alpha=\frac{1}{2}$ scales very closely to $1-\alpha=1/2$ of the one-dimensional results.

The results for the one-dimensional experiment (for the lowest frequency) are quite interesting, in themselves. In the down-

stream duct, the $P_1^+ T_P$ and the σT_e (see eq. (2.16)) components of P_2^+ apparently cancel, leaving near "silence." It is clear that the two-dimensional experiments must scale like $1-\alpha$ (for both pressure and entropy disturbance); otherwise, these experiments would not exhibit the cancellation in the downstream duct.

The conclusion remains the same as for the choked nozzle. For a sufficiently low frequency disturbance the two-dimensionality of the entropy spot may be neglected and the resultant pressure field will scale with the cross-sectional area occupied by the spot. It may be possible to analyze the problem by performing an expansion (in terms of frequency) for low frequency of the equations of motion. In this manner it may be possible to determine how small the frequency must be (and how the Mach number distribution affects that frequency limit) in order to neglect two-dimensional effects in the nozzle.

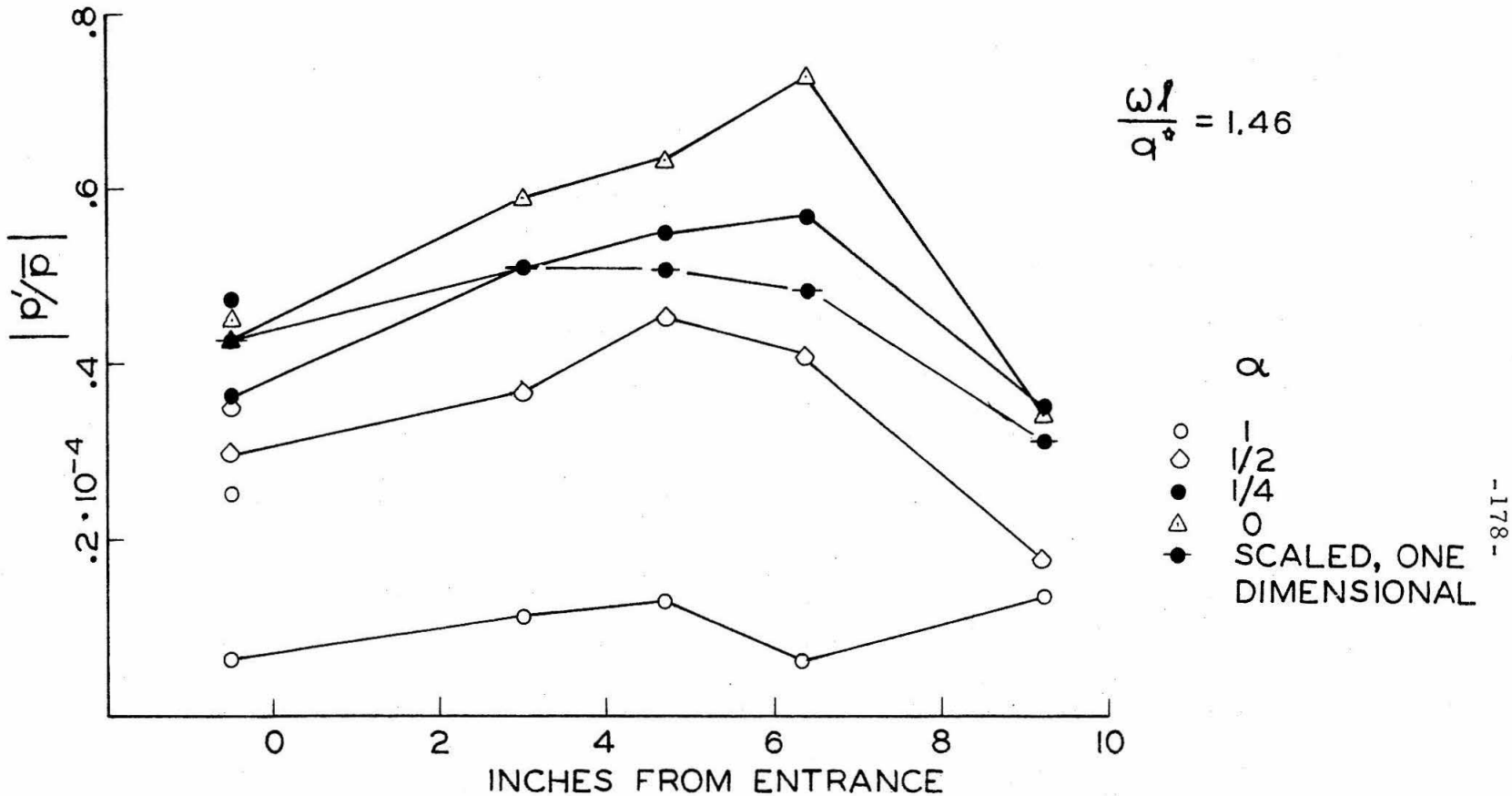

Fig. 5-1 Pressure perturbation amplitude through the supersonic nozzle for two-dimensional heater operation. Amount of power dissipated by lower heater is proportional to α. The nozzle throat is at 7.5" from entrance, dM/dx is constant.

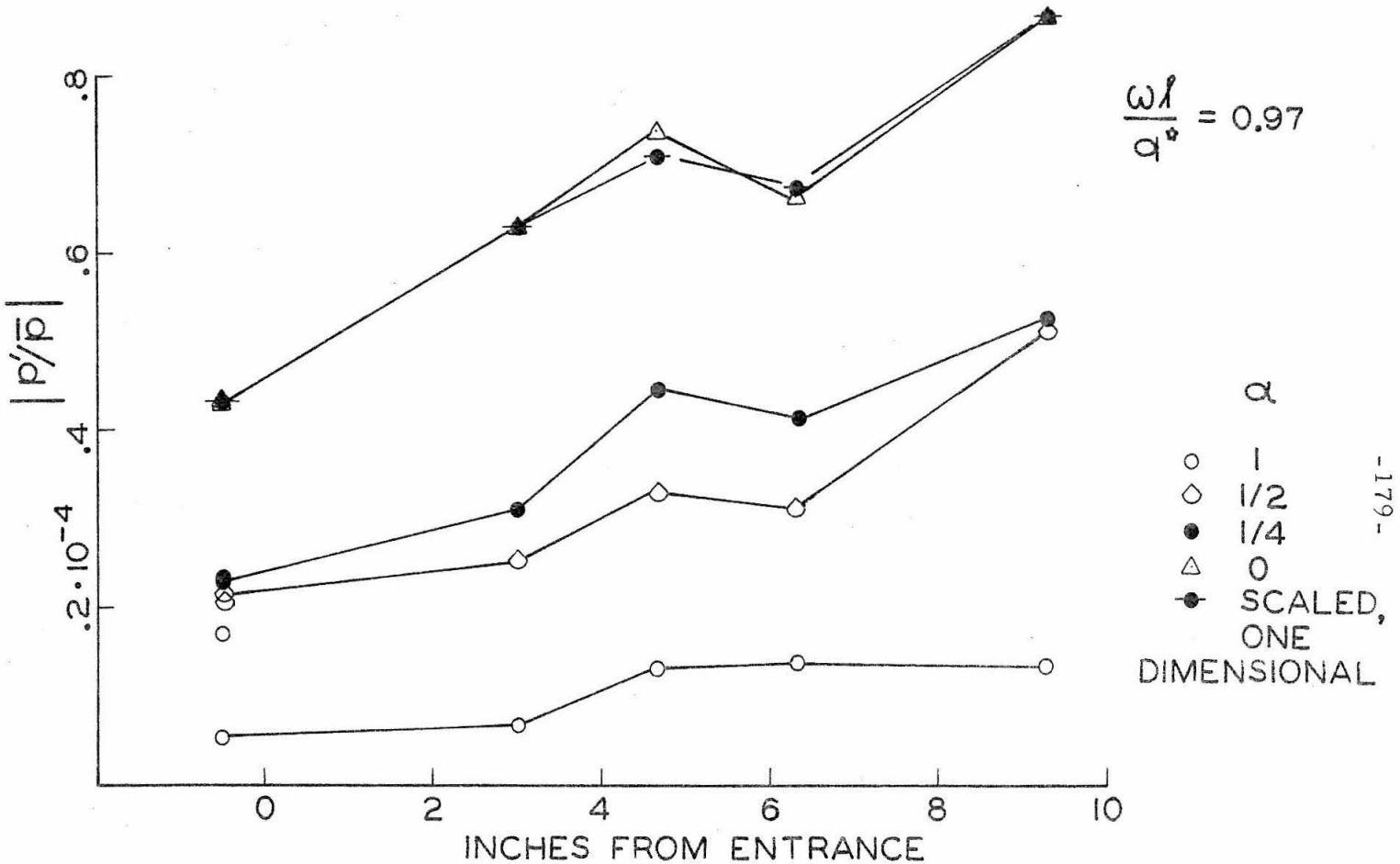

Fig. 5-2 Pressure perturbation amplitude through the supersonic nozzle for two-dimensional heater operation. Amount of power dissipated by lower heater is proportional to α. The nozzle throat is at 7.5" from entrance, dM/dx is constant.

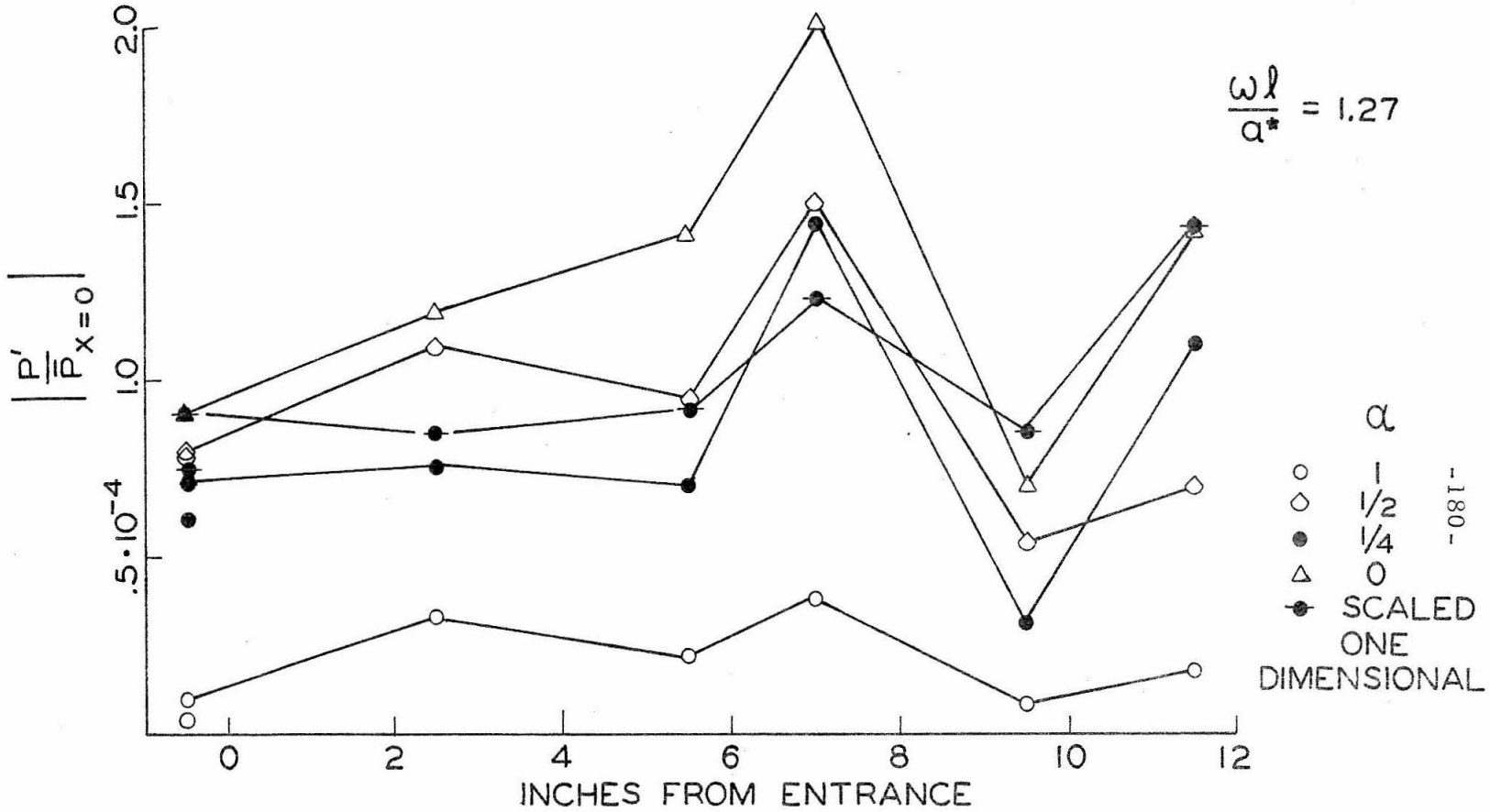

Fig. 5-3 Pressure perturbation amplitude through the subsonic nozzle for two-dimensional heater operation. Amount of power dissipated by lower heater is proportional to α.

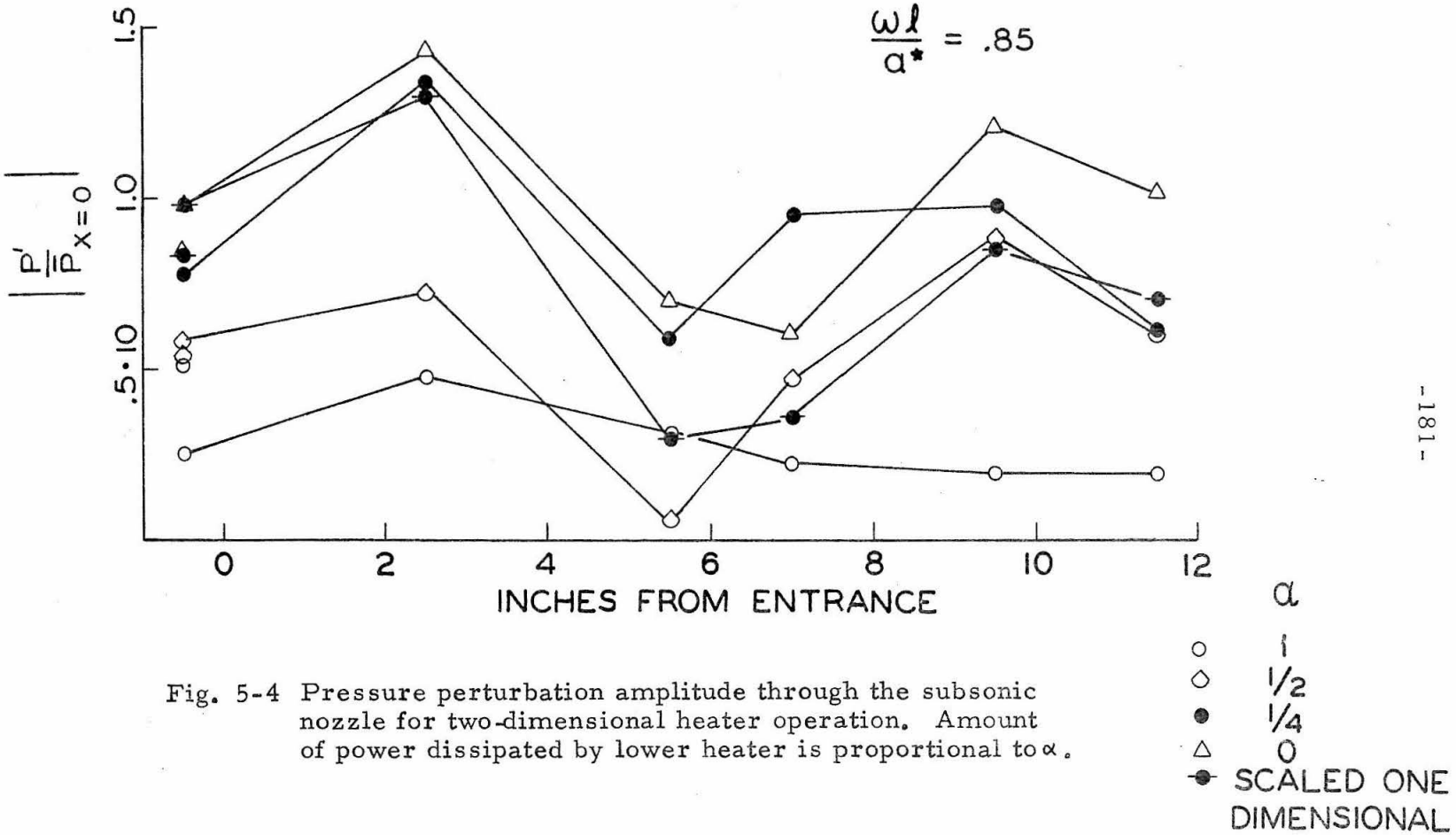

Fig. 5-4 Pressure perturbation amplitude through the subsonic nozzle for two-dimensional heater operation. Amount of power dissipated by lower heater is proportional to α.

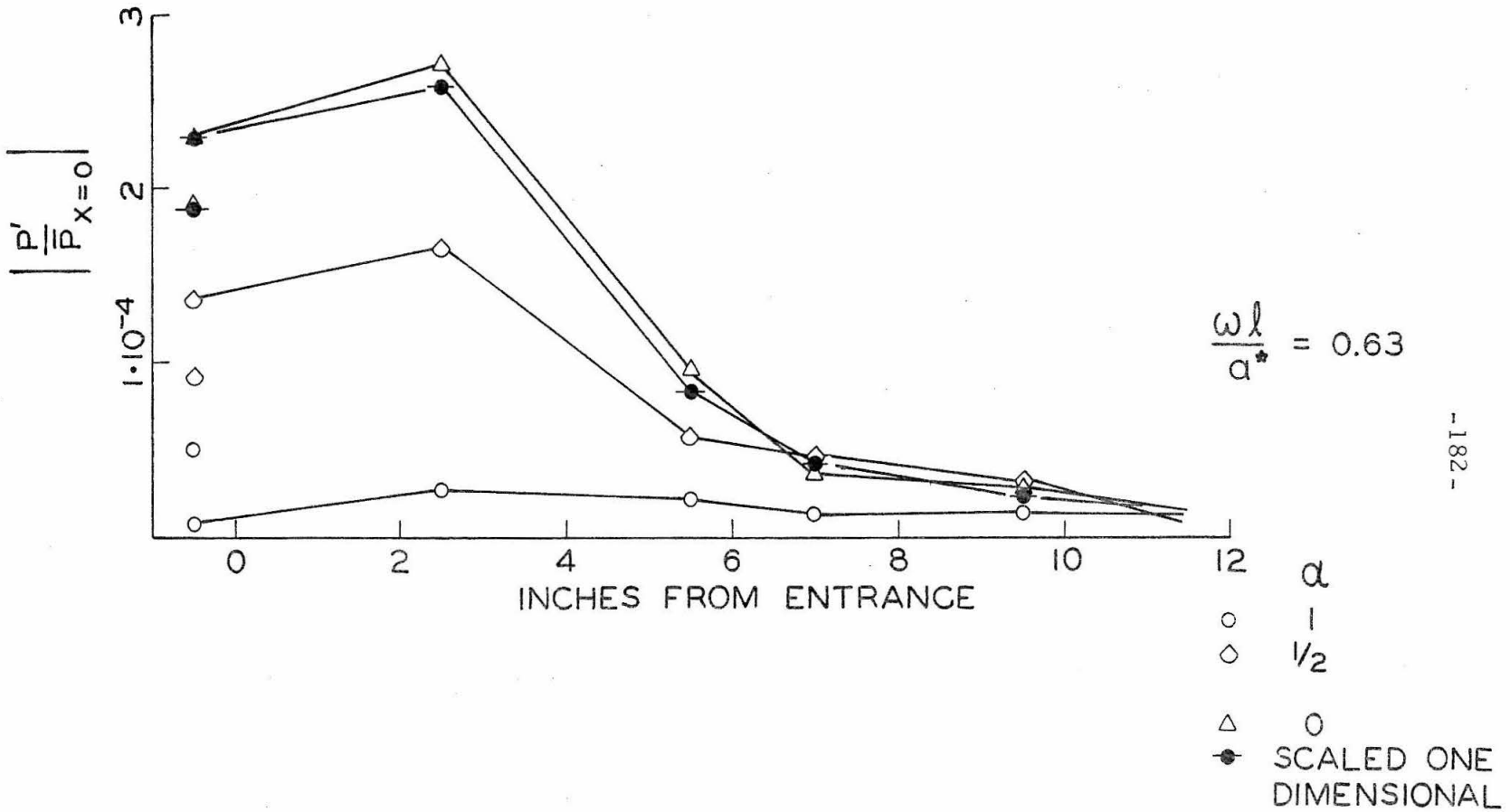

Fig. 5-5 Pressure perturbation amplitude through the subsonic nozzle for two-dimensional heater operation. Amount of power dissipated by lower heater is proportional to α.

APPENDIX A

First order steady solution

Starting with eqs. (3.24) and (3.25) we calculate

$$\frac{\partial \Phi}{\partial y}(\xi,0) = \frac{-U\pi\epsilon}{4a}\frac{1}{(2\pi)^{1/2}}\int_{-a}^{a}\left[2\sin\pi\frac{x}{a}+\sin 2\pi\frac{x}{a}\right]e^{-i\xi x}dx$$

which may be integrated and simplified to

$$\frac{\partial \Phi}{\partial y}(\xi,0) = \frac{Ui\pi\epsilon}{a^2}\left(\frac{\pi}{2}\right)^{1/2}\sin(a\xi)\left[\frac{1}{\left(\frac{\pi}{a}\right)^2-\xi^2}-\frac{1}{\left(\frac{2\pi}{a}\right)^2-\xi^2}\right] \tag{A1}$$

solving for $a(\xi)$ and $b(\xi)$ in eq. (3.26) and inserting into (3.27) we find that the solution for the velocity may be conveniently expressed as:

$$(1-M^2)^{1/2}u^{(1)}-iv^{(1)} = \frac{U\pi\epsilon}{2a^2}\int_{-\infty}^{\infty}\left[\frac{1}{\left(\frac{\pi}{a}\right)^2-\xi^2}-\frac{1}{\left(\frac{2\pi}{a}\right)^2-\xi^2}\right]$$

$$\frac{\sin a\xi}{\sinh((1-M^2)^{1/2}b\xi)}\exp\left[i\xi(x-i(1-M^2)^{1/2}(b-y))\right]d\xi \tag{A2}$$

If $|x|>a$ it is convenient to consider the integral

$$I_\ell(x,y) = \oint_\Gamma \frac{\sin a\zeta}{\left(\frac{\pi\ell}{a}\right)^2-\zeta^2}\,\frac{\exp[i\zeta(x-i(1-M^2)^{1/2}(b-y))]}{\sinh((1-M^2)^{1/2}b\zeta)}d\zeta \qquad \ell=1,2$$

where $Re\,\zeta=\xi$ and Γ is a contour along the ξ axis, closing with a semicircle. Denoting the principal value of the integral as PV we will have

$$(1-M^2)^{1/2}u^{(1)}-iv^{(1)} = \frac{U\pi\epsilon}{2a^2}\left\{PV(I_1(x,y))-PV(I_2(x,y))\right\} \tag{A3}$$

The poles at $\zeta=0,\pm\pi\ell/a$ do not contribute. If $x<-a$ we close the contour with a semicircle in the lower half plane ($Im\,\sigma<0$), as is clear from the exponential term in the integral. In this case

$$PV(I_\ell(x,y)) = -2\pi i \sum Res \tag{A4}$$

where Res are the residues from poles falling inside the contour.

In this case ($x<-a$) we must calculate residues of

$$\frac{\sin a\zeta}{\left(\frac{\pi\ell}{a}\right)^2-\zeta^2} \quad \frac{\exp[i\zeta(x+i((1-M^2)^{1/2}(y-b))]}{\sinh((1-M^2)^{1/2}b\zeta)} \tag{A5}$$

at $$\zeta = \frac{-in\pi}{(1-M^2)^{1/2}b} \qquad n=1,2\cdots$$

For each value of n this residue is

$$\frac{-i\sinh\left[\frac{n\pi a}{(1-M^2)^{1/2}b}\right]\exp\left(\frac{n\pi}{(1-M^2)^{1/2}b}(x+i(1-M^2)^{1/2}(y-b))\right)}{(-)^n(1-M^2)^{1/2}\,b\left[\left(\frac{\pi\ell}{a}\right)^2+\left(\frac{n\pi}{(1-M^2)^{1/2}b}\right)^2\right]}$$

Applying (A3) and (3.21) and separating real and imaginary parts we find

$$u^{(1)} = \frac{-U\pi^2\epsilon}{(1-M^2)ba^2}\sum_{n=1}^{\infty}\mathcal{P}_n \sinh\left[\frac{n\pi a}{(1-M^2)^{1/2}b}\right]\cos\left(n\pi\frac{y}{b}\right)\exp\left[\frac{n\pi x}{(1-M^2)^{1/2}b}\right]$$

$$v^{(1)} = \frac{U\pi^2\epsilon}{(1-M^2)^{1/2}ba^2}\sum_{n=1}^{\infty}\mathcal{P}_n \sinh\left[\frac{n\pi a}{(1-M^2)^{1/2}b}\right]\sin\left(n\pi\frac{y}{b}\right)\exp\left[\frac{n\pi x}{(1-M^2)^{1/2}b}\right] \tag{A6}$$

$$\frac{p^{(1)}}{\gamma P} = -M^2\frac{u^{(1)}}{U}$$

$x<-a$

$$\mathcal{P}_n \equiv \frac{1}{\left(\frac{\pi}{a}\right)^2+\left(\frac{n\pi}{(1-M^2)^{1/2}b}\right)^2} - \frac{1}{\left(\frac{2\pi}{a}\right)^2-\left(\frac{n\pi}{(1-M^2)^{1/2}b}\right)^2}$$

If $X>a$ we close the contour with a semicircle in the upper half plane. We will evaluate the residues of eq. (A5) at

$$\xi = \frac{in\pi}{(1-M^2)^{1/2}b}$$

applying eq. (A3) where the principal value is calculated from

$$PV(I_\ell(x,y)) = 2\pi i \sum Res$$

For each value of n the residue will be

$$\frac{i \sinh\left[\frac{n\pi a}{(1-M^2)^{1/2}\pi}\right] \exp\left[\frac{-n\pi}{(1-M^2)^{1/2}b}(x+i(1-M^2)(y-b))\right]}{(-)^n(1-M^2)^{1/2}b\left[\left(\frac{\pi\ell}{a}\right)^2+\left(\frac{n\pi}{(1-M^2)^{1/2}b}\right)^2\right]}$$

Applying (A3) and (3.21) and separating real and imaginary parts we find

$$u^{(1)} = \frac{-U\pi^2\epsilon}{b(1-M^2)a^2}\sum_{n=1}^{\infty} \rho_n \sinh\left[\frac{n\pi a}{(1-M^2)^{1/2}b}\right]\cos\left(n\pi\frac{y}{b}\right)\exp\left[\frac{-n\pi x}{(1-M^2)^{1/2}b}\right]$$

$$v^{(1)} = \frac{-U\pi^2\epsilon}{(1-M^2)^{1/2}ba^2}\sum_{n=1}^{\infty} \rho_n \sinh\left[\frac{n\pi a}{(1-M^2)^{1/2}b}\right]\sin\left(n\pi\frac{y}{b}\right)\exp\left[\frac{-n\pi x}{(1-M^2)^{1/2}b}\right]$$

$$\frac{p^{(1)}}{\gamma p} = -M^2\frac{u^{(1)}}{U}$$

$$x>a \qquad (A7)$$

If $-a<x<a$ we write

$$I_\ell(x,y) = \int_{-\infty}^{\infty} \frac{\sin a\xi}{\left(\frac{\pi\ell}{a}\right)^2-(\xi)^2}\,\frac{\exp[i\xi(x-i(1-M^2)(b-y))]}{\sinh((1-M^2)b\xi)}\,d\xi \qquad \ell=1,2$$

where the solution will be given by

$$(1-M^2)^{1/2}u^{(1)} - iv^{(1)} = \frac{U\pi\epsilon}{2a^2}\left[I_1(x,y) - I_2(x,y)\right] \tag{A8}$$

Now, we can let $I_\ell = \frac{1}{2i}(I_* - I_{**})$ where

$$I_* = \int_{-\infty}^{\infty} \frac{e^{ia\xi}}{\left(\frac{\pi\ell}{a}\right)^2 - \xi^2} \cdot \frac{\exp\left[i\xi(x - i(1-M^2)^{1/2}(b-y)\right]}{\sinh\left((1-M^2)^{1/2}b\xi\right)}\, d\xi$$

$$I_{**} \int_{-\infty}^{\infty} \frac{e^{-ia\xi}}{\left(\frac{\pi\ell}{a}\right)^2 - \xi^2} \cdot \frac{\exp\left[i\xi(x - i(1-M^2)^{1/2}(b-y))\right]}{\sinh\left((1-M^2)^{1/2}b\xi\right)}\, d\xi \tag{A9}$$

We consider I_{**} in the ζ plane ($Re\,\zeta = \xi$ again). We will close the contour in the lower half plane since $x - a < 0$. We must consider poles at $\zeta = \pm\pi\ell/a$, 0, and $\frac{-in\pi}{(1-M^2)^{1/2}b}$ all of which will contribute. The contribution to the principal value of the poles on the real axis may be calculated by indenting the contour around the poles below the real axis. In this manner the contribution from the pole at $\zeta = \frac{-\pi\ell}{a}$ is

$$\frac{-ia}{2\ell} \cdot \frac{\exp\left[-i\frac{\pi\ell}{a}((x-a) - i(1-M^2)^{1/2}(b-y))\right]}{\sinh\left(\pi\frac{\ell}{a}(1-M^2)^{1/2}b\right)}$$

and from $\zeta = \pi\ell/a$

$$\frac{-ia}{2\ell} \cdot \frac{\exp\left[i\frac{\pi\ell}{a}((x-a)) - i(1-M^2)^{1/2}(b-y))\right]}{\sinh\left(\pi\frac{\ell}{a}(1-M^2)^{1/2}b\right)}$$

and from $\zeta = 0$

$$\frac{i\pi}{(1-M^2)^{1/2}}\left(\frac{a}{\pi\ell}\right)^2$$

Now, calculating the residues from the poles at $\mathcal{S} = \frac{-in\pi}{(1-M^2)^{1/2}b}$ we find for each n

$$\frac{\exp\left[\frac{-n\pi a}{(1-M^2)^{1/2}b}\right]\exp\left[\frac{n\pi}{(1-M^2)^{1/2}b}\left(x-i\left((1-M^2)^{1/2}(b-y)\right)\right)\right]}{(-)^n(1-M^2)^{1/2}b\left[\left(\frac{\pi\ell}{a}\right)^2+\left(\frac{n\pi}{(1-M^2)^{1/2}b}\right)^2\right]}$$

for the residue. The principal value may be calculated by summing over n, multiplying by $-2\pi i$ and subtracting the contributions from the poles on the real axis.

In calculating I_* we close the contour in the upper half $\mathcal{S}$ plane since $x+a>0$. The contour will be indented above the poles on the real axis and in this way the contribution from the pole at $\mathcal{S}=-\pi\ell/a$ may be shown to be

$$\frac{ai}{2\ell}\;\frac{\exp\left[-i\pi\frac{\ell}{a}\left((x-a)-i(1-M^2)^{1/2}(b-y)\right)\right]}{\sinh\left[\frac{(1-M^2)^{1/2}b\pi\ell}{a}\right]}$$

and from $\mathcal{S}=\pi\ell/a$

$$\frac{ai}{2\ell}\;\frac{\exp\left[i\pi\frac{\ell}{a}\left((x-a)-i(1-M^2)(b-y)\right)\right]}{\sinh\left[\frac{(1-M^2)^{1/2}b\pi\ell}{a}\right]}$$

and from $\mathcal{S}=0$

$$\frac{-\pi i}{(1-M^2)^{1/2}b}\left(\frac{a}{\pi\ell}\right)^2$$

The residue of the poles $\mathcal{S}=\frac{in\pi}{(1-M^2)^{1/2}b}$ will be

$$\frac{\exp\left[\frac{-n\pi}{(1-M^2)^{1/2}b}\left((x+a)-i(1-M^2)(b-y)\right)\right]}{(-)^n(1-M^2)^{1/2}b\left[\left(\frac{\pi\ell}{a}\right)^2+\left(\frac{n\pi}{(1-M^2)^{1/2}b}\right)^2\right]}$$

The principal value may be calculated by summing over n, multiplying by $2\pi i$ and subtracting the contributions from the poles on the real axis.

The calculation of I_* , I_{**} then gives $I_1(x,y)$. Eq. (A8) will then give

$$u^{(1)} = \frac{U\pi\epsilon}{4a^2(1-M^2)^{1/2}} \left\{ \frac{3\pi}{2(1-M^2)^{1/2}b}\left(\frac{a}{\pi}\right)^2 \right.$$

$$+2a\left[\frac{\cos(\pi\frac{x}{a})\cosh(\frac{\pi}{a}(1-M^2)^{1/2}(b-y))}{\sinh(\frac{\pi}{a}(1-M^2)b)} + \frac{\cos(2\pi\frac{x}{a})\cosh(2\frac{\pi}{a}(1-M^2)^{1/2}(b-y))}{2\sinh(2\frac{\pi}{a}(1-M^2)^{1/2}b)}\right]$$

$$\left. + \frac{4\pi}{(1-M^2)^{1/2}b}\sum_{n=1}^{\infty} P_n \cosh\left[\frac{n\pi x}{(1-M^2)^{1/2}b}\right]\cos(n\pi\frac{y}{b})\exp\left[\frac{-n\pi a}{(1-M^2)^{1/2}b}\right] \right\}$$

$$v^{(1)} = \frac{-U\pi\epsilon}{4a^2}\left\{\right.$$

$$2a\left[\frac{\sin(\pi\frac{x}{a})\sinh(\frac{\pi}{a}(1-M^2)^{1/2}(b-y))}{\sinh(\frac{\pi}{a}(1-M^2)b)} + \frac{\sin(2\pi\frac{x}{a})\sinh(2\frac{\pi}{a}(1-M^2)^{1/2}(b-y))}{2\sinh(2\frac{\pi}{a}(1-M^2)^{1/2}b)}\right]$$

$$\left. + \frac{4\pi}{(1-M^2)^{1/2}b}\sum_{n=1}^{\infty} P_n \sinh\left[\frac{n\pi x}{(1-M^2)^{1/2}b}\right]\sin(n\pi\frac{y}{b})\exp\left[\frac{-n\pi a}{(1-M^2)^{1/2}}\right] \right\}$$

$$\frac{p^{(1)}}{\gamma p} = -M^2\frac{u^{(1)}}{U} \qquad -a<x<a \qquad \text{(A10)}$$

The complete solution is eqs. (A6), (A7), (A10).

APPENDIX B

Calculation of the Green's Function for the Second Order Inhomogenous Solution

We seek a solution of (3.30), (3.31) of the form of eq. (3.32). Since we expect a periodic solution, we write (3.30)

$$\left\{-\left(\frac{\omega}{c}\right)^2 + 2i\frac{M}{c}\omega\frac{\partial}{\partial x} + M^2\frac{\partial^2}{\partial x^2} - \frac{\partial^2}{\partial x^2} - \frac{\partial^2}{\partial y^2}\right\}\varphi = F(x,y) \qquad \text{(B1)}$$

or $\mathcal{L}\{\varphi\} = F(x,y)$ where $\mathcal{L}$ is the differential operator.

Now define $G_\epsilon(x,y;\xi,\eta)$ such that

$$\mathcal{L}\{G_\epsilon(x,y;\xi,\eta)\} = f_\epsilon(x,y;\xi,\eta) \qquad \text{(B2)}$$

where f_ϵ is a function which is zero outside the small square

$S_\epsilon : \xi-\epsilon < x < \xi+\epsilon,\ \eta-\epsilon < y < \eta+\epsilon$ and $\iint_{S_\epsilon} f_\epsilon\, dx\, dy = 1$.

or considering $S_{\epsilon'} : x-\epsilon < \xi < x+\xi,\ y-\epsilon < \eta < y+\epsilon$; $\iint_{S_{\epsilon'}} f_\epsilon\, d\xi\, d\eta = 1$.

Now define

$$\varphi_\epsilon(x,y) = \int_{-\infty}^{\infty}\int_{0}^{2b} G_\epsilon(x,y;\xi,\eta)\, F(\xi,\eta)\, d\xi\, d\eta$$

then

$$\mathcal{L}\{\varphi_\epsilon\} = \int_{-\infty}^{\infty}\int_{0}^{2b} f_\epsilon\, F(\xi,\eta)\, d\xi\, d\eta = \int_{\xi=x-\epsilon}^{x+\epsilon}\int_{\eta=y-\epsilon}^{y+\epsilon} f_\epsilon\, F(\xi,\eta)\, d\xi\, d\eta$$

If the forcing function in (B1) is continuous

$$\mathcal{L}\{\varphi_\epsilon\} \approx F(x,y)$$

and as $\epsilon \to 0$ we expect φ_ϵ to be the solution we seek if G_ϵ satisfies the boundary condition (3.31), and the radiation condition.

Outside the S_ϵ eq. (B2) gives

$$\left\{-\left(\frac{\omega}{c}\right)^2+2i\,\frac{M}{c}\omega\,\frac{\partial}{\partial x}+(M^2-1)\,\frac{\partial^2}{\partial x^2}-\frac{\partial^2}{\partial y^2}\right\}G(x,y;\xi,\eta)=0 \tag{B3}$$

where $\frac{\partial G}{\partial y}(y=0)=\frac{\partial G}{\partial y}(y=2b)=0$. Also G must satisfy the radiation condition. Solutions of (B3) which satisfy the boundary conditions on the duct top and bottom are like

$$\cos\left(n\pi\frac{y}{2b}\right)\exp\left[i\left(\frac{M}{1-M^2}\pm\left(\frac{1}{(1-M^2)^2}-\left(\frac{n\pi c}{2b\omega}\right)^2\frac{1}{1-M^2}\right)^{1/2}\right)\frac{\omega x}{c}\right] \tag{B4}$$

For shorthand we will write

$$\Omega_n=\left|\frac{1}{(1-M^2)^2}-\left(\frac{n\pi c}{2b\omega}\right)^2\frac{1}{1-M^2}\right|^{1/2} \tag{B5}$$

We note that if

$$\frac{n\pi c}{2b\omega}<(1-M^2)^{-1/2} \tag{B6}$$

the radical in (B4) is just Ω_n. If the inequality is reversed then the radical is $i\Omega_n$. We define N to be the largest integer n satisfying (B6). We also define N_1 to be the largest integer such that

$$\frac{N_1\pi c}{2b\omega}<1$$

Since $M<1$, $N_1\le N$ and for $n\le N_1$:

$$\frac{M}{1-M^2}<\Omega_n$$

and $N_1<n\le N$

$$\frac{M}{1-M^2}>\Omega_n$$

Choosing the (+) for the radical in (B4) we get waves propagating upstream if $n \le N$. Choosing the (-) for the radical we get waves propagating downstream if $n \le N_1$, and upstream if $N_1 < n \le N$. For n > N the waves attenuate if the proper sign on the radical is chosen. These allow us to write down the general homogeneous solution:

$x < \xi$

$$G(x,y;\xi,\eta) = \sum_{n=0}^{N} A_n \cos n\pi \frac{y}{2b} \exp\left[i\left(\frac{M}{1-M^2} + \Omega_n\right)\frac{\omega}{c}(x-\xi)\right] - \sum_{N_1+1}^{N} B_n \cos n\pi \frac{y}{2b} \exp\left[i\left(\frac{M}{1-M^2} - \Omega_n\right)\frac{\omega}{c}(x-\xi)\right] + \sum_{N+1}^{\infty} A_n \cos n\pi \frac{y}{2b} \exp\left[i\frac{M}{1-M^2}\frac{\omega}{c}(x-\xi)\right]\exp\left[\Omega_n \frac{\omega}{c}(x-\xi)\right] \qquad \text{(B7)}$$

$x > \xi$

$$G(x,y;\xi,\eta) = \sum_{N+1}^{\infty} C_n \cos n\pi \frac{y}{2b} \exp\left[i\frac{M}{1-M^2}\frac{\omega}{c}(x-\xi)\right]\exp\left[-\Omega_n \frac{\omega}{c}(x-\xi)\right] + \sum_{0}^{N_1} C_n \cos n\pi \frac{y}{2b} \exp\left[i\left(\frac{M}{1-M^2} - \Omega_n\right)\frac{\omega}{c}(x-\xi)\right] \qquad \text{(B8)}$$

Continuity of $\varphi(x,y)$ implies from (3.32)

$$G(x,y;\xi,\eta)\Big|_{x=\xi^-} = G(x,y;\xi,\eta)\Big|_{x=\xi^+}$$

from which we conclude

$$\begin{aligned} N+1 \le n < \infty \qquad & C_n = A_n \\ 0 \le n \le N_1 \qquad & C_n = A_n \\ N_1 < n \le N \qquad & B_n = A_n \end{aligned} \qquad \text{(B9)}$$

which will allow the elimination of B_n, C_n (in (B7), (B8)) in favor of A_n.

From (B2)

$$\lim_{\epsilon\to 0} \int_{x=\xi-\epsilon}^{\xi+\epsilon} \int_{y=\eta-\epsilon}^{\eta+\epsilon} \mathcal{L}\{G_\epsilon(x,y;\xi,\eta)dxdy = 1 \qquad \text{(B10)}$$

or $$\lim_{\epsilon\to 0} \int_{y=\eta-\epsilon}^{\eta+\epsilon} \int_{x=\xi-\epsilon}^{\xi+\epsilon} \left\{-\left(\frac{\omega}{c}\right)^2 + 2i\frac{M}{c}\omega\frac{\partial}{\partial x} + (M^2-1)\frac{\partial^2}{\partial x^2} - \frac{\partial^2}{\partial y^2}\right\} G\,dx\,dy = 1$$

Since G is continuous for $\xi-\epsilon < x < \xi+\epsilon$ we get

$$\lim_{\epsilon\to 0} \int_{y=\eta-\epsilon}^{\eta+\epsilon} \left\{ \frac{\partial G}{\partial x}\bigg|_{x=\xi-\epsilon}^{\xi+\epsilon} \right\} dy = \frac{-1}{1-M^2} \qquad \text{(B11)}$$

Therefore $\partial G/\partial x$ is not continuous across $x=\xi$, since if it were (B10) could not be satisfied as $\epsilon\to 0$. Inserting (B7), (B8), (B9) into (B11) we find

$$\lim_{\epsilon\to 0} \int_{\eta-\epsilon}^{\eta+\epsilon} \left\{ \sum_{n=0}^{N} A_n i\frac{\omega}{c}\Omega_n \cos\left(n\pi\frac{y}{2b}\right) + \sum_{N+1}^{\infty} A_n \frac{\omega}{c}\Omega_n \cos\left(n\pi\frac{y}{2b}\right)\right\} dy = \frac{-1/2}{1-M^2}$$

This equation implies that

$$\sum_{n=0}^{N} A_n i\frac{\omega}{c}\Omega_n \cos\left(n\pi\frac{y}{2b}\right) + \sum_{N+1}^{\infty} A_n \frac{\omega}{c}\Omega_n \cos\left(n\pi\frac{y}{2b}\right) = \frac{-1/2}{1-M^2}\delta(y-\eta) \qquad \text{(B12)}$$

else the equality could not be met as $\epsilon\to 0$.

Expanding the delta function in a cosine series:

$$\delta(y-\eta) = \frac{1}{2b} + \frac{1}{b}\sum_{n=1}^{\infty} \cos\left(n\pi\frac{y}{2b}\right)\cos\left(n\pi\frac{\eta}{2b}\right) \qquad 0 \le y \le 2b$$

we may equate coefficients in (B12) and find

$$A_o = \frac{c}{\omega b}\frac{1}{4i}$$

$$A_n = \frac{c}{\omega b}\frac{1}{2i}\left(1-\left(\frac{n\pi c}{2b\omega}\right)^2(1-M^2)\right)^{1/2}\cos\left(n\pi\frac{x}{2b}\right) \qquad 0<n\leq N$$

$$A_n = \frac{c}{\omega b}\frac{1}{2}\left(\left(\frac{n\pi c}{2b\omega}\right)^2(1-M^2)-1\right)^{1/2}\cos\left(n\pi\frac{x}{2b}\right) \qquad n>N$$

(B13)

which completes the calculation of the Green's function.

APPENDIX C

Forcing Function

The calculation of the forcing function to be used in (3.32) is described by (3.35). We give the results here. Let

$$b^* \equiv (1-M^2)^{1/2} b \qquad m \equiv \frac{M^2 \pi^2 \epsilon}{(1-M^2) b a^2} \tag{C1}$$

then:

$$\xi < -a \qquad \frac{-F(\xi,\eta)}{\sigma m} =$$

$$\sum_{n=1}^{\infty} \mathcal{P}_n \sinh\left(\frac{n\pi a}{b^*}\right) \exp\left(\frac{n\pi \xi}{b^*}\right) \exp\left[-ik_s(\xi \cos\nu_s + \eta \sin\nu_s)\right]$$

$$\left[\frac{n\pi}{b^*}\left(\frac{n\pi}{b^*} - ik_s\cos\nu_s\right)\cos\left(n\pi\frac{\eta}{b}\right) - \frac{n\pi}{b}\left(\frac{n\pi}{b}\cos\left(n\pi\frac{\eta}{b}\right) - ik_s \sin\nu_s \sin\left(n\pi\frac{\eta}{b}\right)\right)\right] \tag{C2}$$

$$\xi > a \qquad \frac{-F(\xi,\eta)}{\sigma m} =$$

$$-\sum_{n=1}^{\infty} \mathcal{P}_n \sinh\left(\frac{n\pi a}{b^*}\right) \exp\left(\frac{-n\pi \xi}{b^*}\right) \exp\left[-ik_s(\xi \cos\nu_s + \eta \sin\nu_s)\right]$$

$$\left[\frac{-n\pi}{b^*}\left(\frac{n\pi}{b^*} + ik_s\cos\nu_s\right)\cos\left(n\pi\frac{\eta}{b}\right) + \frac{n\pi}{b}\left(\frac{n\pi}{b}\cos\left(n\pi\frac{\eta}{b}\right) - ik_s \sin\nu_s \sin\left(n\pi\frac{\eta}{b}\right)\right)\right] \tag{C3}$$

$$-a < \xi < a \qquad \frac{F(\xi,\eta)}{\sigma m} = \exp\left[-ik_s(\xi\cos\nu_s + \eta\sin\nu_s)\right]\Bigg\{$$

$$-ik_s\cos\nu_s\left[\left(\frac{-b^*}{2}\right)\left(\frac{\sin\pi\frac{\xi}{a}\cosh\left(\frac{\pi}{a}\frac{b^*}{b}(b-\eta)\right)}{\sinh(\pi b^*/a)} + \frac{\sin 2\pi\frac{\xi}{a}\cosh\left(\frac{2\pi}{a}\frac{b^*}{b}(b-\eta)\right)}{\sinh(2\pi b^*/a)}\right.\right.$$

$$+\sum_{n=1}^{\infty} P_n \exp\left(\frac{-n\pi a}{b^*}\right)\frac{n\pi}{b^*}\sinh\left(\frac{n\pi\xi}{b^*}\right)\cos\left(n\pi\frac{\eta}{b}\right)\Bigg]$$

$$-\frac{b^*\pi}{2a}\left(\frac{\cos(\pi\frac{\xi}{a})\cosh\frac{\pi}{a}\frac{b^*}{b}(b-\eta)}{\sinh(\pi b^*/a)}+2\,\frac{\cos(2\pi\frac{\xi}{a})\cosh\frac{2\pi}{a}\frac{b^*}{b}(b-\eta)}{\sinh(2\pi b^*/a)}\right)$$

$$+\sum_{n=1}^{\infty} P_n \exp\left(\frac{-n\pi a}{b^*}\right)\left(\frac{n\pi}{b^*}\right)^2\cosh\left(\frac{n\pi\xi}{b^*}\right)\cos\left(n\pi\frac{\eta}{b}\right)$$

$$-(i+k_s\sin\nu_s)\Bigg[-\frac{b}{2}(1-M^2)\left(\frac{\cos(\pi\frac{\xi}{a})\sinh(\frac{\pi}{a}\frac{b^*}{b}(b-\eta))}{\sinh(\pi b^*/a)}+\frac{\cos(2\pi\frac{\xi}{a})\sinh(\frac{2\pi}{a}\frac{b^*}{b}(b-\eta))}{\sinh(2\pi b^*/a)}\right)$$

$$-\sum_{n=1}^{\infty} P_n \exp\left(\frac{-n\pi a}{b^*}\right)\cosh\left(\frac{n\pi\xi}{b^*}\right)\frac{n\pi}{b}\sinh\left(n\pi\frac{\eta}{b}\right)\Bigg]$$

$$+\frac{b}{2a}(1-M^2)^{3/2}\pi\left(\frac{\cos(\pi\frac{\xi}{a})\cosh(\frac{\pi}{a}\frac{b^*}{b}(b-\eta))}{\sinh\pi b^*/a}+2\,\frac{\cos(2\pi\frac{\xi}{a})\cosh(\frac{2\pi}{a}\frac{b^*}{b}(b-\eta))}{\sinh(2\pi b^*/a)}\right)$$

$$-\sum_{n=1}^{\infty} P_n \exp\left(\frac{-n\pi a}{b^*}\right)\cosh\left(\frac{n\pi\xi}{b^*}\right)\left(\frac{n\pi}{b}\right)^2\cos\left(n\pi\frac{\eta}{b}\right)\Bigg\} \qquad \text{(C4)}$$

We recall that ν_s is the angle between the axial direction and the normal to the entropy wavefront, and the P_n were defined by (3.28).

APPENDIX D

Second Order Homogeneous Solution

We give here the details of the inversion (3.53) leading to (3.54) and (3.55). We need

$$H(x)=\frac{1}{(2\pi)^{1/2}}\int_{-\infty}^{\infty}\frac{\sinh(y\,g(\xi))}{\sinh(2b\,g(\xi))}\,e^{-i\xi x}\,d\xi$$

$$G(x)=\frac{1}{(2\pi)^{1/2}}\int_{-\infty}^{\infty}\frac{\sinh((2b-y)g(\xi))}{\sinh(2b\,g(\xi))}\,e^{-i\xi x}\,d\xi \qquad \text{(D1)}$$

Consider the contour integral in complex $\sigma=\xi+i\eta$ space:

$$I=\oint\frac{\sinh(y\,g(\sigma))}{\sinh(2b\,g(\sigma))}\,e^{-i\sigma x}\,d\sigma \qquad \text{(D2)}$$

The function in the contour integral will have poles at σ_n where

$$g(\sigma_n)=\frac{in\pi}{2b} \qquad n=\pm1,\pm2\cdots$$

$$g^2(\sigma_n)=-\left(\frac{n\pi}{2b}\right)^2=\frac{\omega}{c}\left(2\sigma_n M-\frac{\omega}{c}\right)+(1-M^2)\sigma_n^2$$

from (3.47).

Solving for

$$\sigma_n=-\frac{\omega}{c}\frac{M}{1-M^2}\pm\frac{1}{1-M^2}\left(\left(\frac{\omega}{c}\right)^2-(1-M^2)\left(\frac{n\pi}{2b}\right)^2\right)^{1/2} \qquad \text{(D3)}$$

The following diagram shows the position of poles

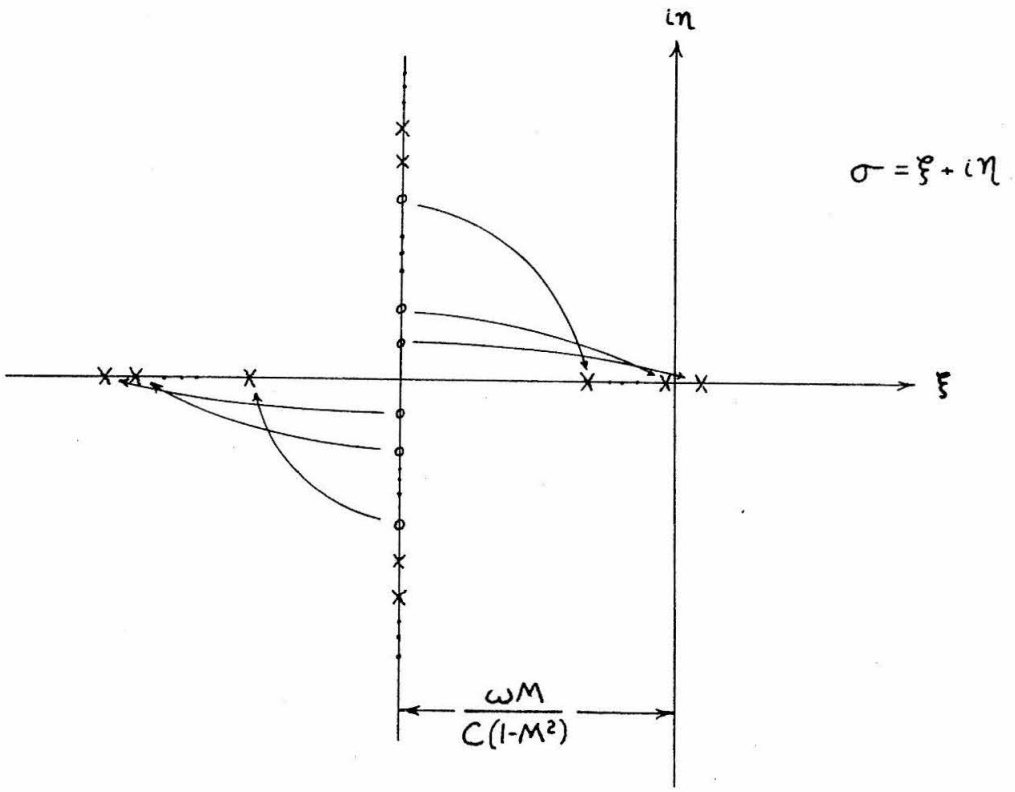

Location of poles as per equation (D3)

In this diagram the x represents a pole. For ω below a certain minimum value, all poles will lie off the ξ axis. As ω increases all the poles will move towards the ξ axis until the pair closest to the ξ axis meet on it and with increasing ω, move outwards along the ξ axis. The small circles represent poles which have moved, as shown by the arrows, to a position on the ξ axis. The poles on $-\xi = \omega M/(C(1-M^2))$ represent attenuating (or growing) waves, those on the ξ axis represent propagating waves.

We choose a contour (for (D2)) on the entire ξ axis and close with a semicircle either above or below the ξ axis. The

contour will be indented around the poles on the ξ axis. Due to the exponential term in (D2) we take the lower contour (and indent below the real poles) if x is positive. If x is negative we take the upper contour and indent above the real poles. The contribution to the principal value of the integral from the portion of the contour indented around the real poles may be calculated. The contribution from the poles lying off of the ξ axis will be $2\pi i$ x sum of residues of these poles if they lie above ξ axis and the negative of this if they lie below the ξ axis. From (D3), the poles will lie on the ξ axis if $n \leq N$ where N is the largest integer such that

$$\left(\frac{\omega}{c}\right)^2 > (1-M^2)\left(\frac{N\pi}{2b}\right)^2$$

The summation in (3.54) and (3.55) from $1 \leq n \leq N$ represents the contribution from the real poles. The summation from $N < n$ represents the contribution from the poles lying off the ξ axis.

APPENDIX E

Integrals Represented as $I_{\alpha \ell m}$, Etc.

We have represented in (3.78), (3.81) and (3.82) a number of integrals which resulted from calculation of (3.32). The first index is used to identify the integral. The index m indicates the acoustic mode number and the limits are specified by the equation it is used in, (3.78) for example. The index n results from the series representation of the wall deflection and has limits from 1 to ∞. The index ℓ is an integer, either 1 or 2.

We define the quantity $\mathcal{M}_m^+$ or $\mathcal{M}_m^-$

$$\mathcal{M}_m^{\pm} = \frac{1}{M(1-M^2)} \pm \left(\frac{1}{(1-M^2)^2} - \left(\frac{m\pi}{2\beta\delta} \right)^2 \frac{1}{1-M^2} \right)^{1/2} \qquad 0 \le m \le N$$

We assume that $\beta \mathcal{M}_m^{\pm} \neq \pi\ell \quad \ell = 1,2$ and proceed to define the quantities.

$$\begin{pmatrix} \frac{I_{a\ell m}}{a} \\ \\ \frac{I_{a'\ell m}}{a} \end{pmatrix} = \frac{i(-)^{\ell} \sin\left[\beta M_m^{\mp}\right] 2\pi\ell}{(\pi\ell)^2 - (\beta M_m^{\mp})^2} \qquad (E1)$$

$$\begin{pmatrix} \frac{I_{b\ell m}}{a} \\ \\ \frac{I_{b'\ell m}}{a} \end{pmatrix} = \frac{-2(-)^{\ell} \sin\left[\beta M_m^{\mp}\right] (\beta M_m^{\mp})}{(\pi\ell)^2 - (\beta M_m^{\mp})^2} \qquad (E2)$$

$$\begin{pmatrix} \frac{I_{cnm}}{a} \\ \\ \frac{I_{c'nm}}{a} \end{pmatrix} = 2i\left\{\sinh\left[\frac{n\pi}{\delta(1-M^2)^{1/2}}\right]\cos\left[\beta M_m^{\mp}\right](\beta M_m^{\mp}) - \frac{n\pi}{\delta(1-M^2)^{1/2}}\cosh\left[\frac{n\pi}{\delta(1-M^2)^{1/2}}\right]\sin\left[\beta M_m^{\mp}\right]\right\}$$

$$\div \left\{\left[\frac{n\pi}{\delta(1-M^2)^{1/2}}\right]^2 + (\beta M_m^{\mp})^2\right\} \qquad (E3)$$

$$\begin{pmatrix} \frac{I_{dnm}}{a} \\ \\ \frac{I_{d'nm}}{a} \end{pmatrix} = 2\left\{\left(\frac{n\pi}{\delta(1-M^2)^{1/2}}\right)\sinh\left(\frac{n\pi}{\delta(1-M^2)^{1/2}}\right)\cos\left[\beta M_m^{\mp}\right] + (\beta M_m^{\mp})\cosh\left[\frac{n\pi}{\delta(1-M^2)^{1/2}}\right]\sin\left[\beta M_m^{\mp}\right]\right\}$$

$$\div \left\{\left[\frac{n\pi}{\delta(1-M^2)^{1/2}}\right]^2 + (\beta M_m^{\mp})^2\right\} \qquad (E4)$$

$$\left(\frac{I_{eml}}{a}\right) =$$

$$(-)^m \left\{ \frac{i\beta}{M} \tan(\nu_s) \cosh(\pi l \delta (1-M^2)^{1/2}) \left[\exp(-2i \tfrac{\beta\delta}{M} \tan\nu_s) - (-)^m \right] \right.$$

$$\left[\left(\frac{\beta}{M} \tan\nu_s\right)^2 + (\pi l)^2 (1-M^2) - \left(\frac{m\pi}{2\delta}\right)^2 \right] + \sinh\left[\pi l \delta (1-M^2)^{\frac{1}{2}}\right]$$

$$\left[\exp\left(-2i \tfrac{\beta\delta}{M} \tan\nu_s\right) + (-)^m \right] \left[\pi l (1-M^2)^{\frac{1}{2}} \left(\left(\tfrac{\beta}{M} \tan\nu_s\right)^2 + \pi^2 l^2 (1-M^2) \right.\right.$$

$$\left.\left. + \left(\frac{m\pi}{2\delta}\right)^2 \right) \right] \Bigg\} \div \left\{ \left(\frac{\beta}{M} \tan\nu_s\right)^4 + 2\left(\frac{\beta}{M} \tan\nu_s\right)^2 \left[(\pi l)^2 (1-M^2) - \left(\frac{m\pi}{2\delta}\right)^2 \right] \right.$$

$$\left. + \left[(\pi l)^2 (1-M^2) + \left(\frac{m\pi}{2\delta}\right)^2 \right]^2 \right\} \qquad (E5)$$

$$\left(\frac{I_{hml}}{a}\right) = -(-)^m \left\{ \cosh(\pi l \delta (1-M^2)^{1/2}) \left[\exp(-2i \tfrac{\beta\delta}{M} \tan\nu_s) - (-)^m \right] \right.$$

$$\left[\pi l (1-M^2)^{\frac{1}{2}} \left(\left(\tfrac{\beta}{M} \tan\nu_s\right)^2 + (\pi l)^2 (1-M^2) + \left(\frac{m\pi}{2\delta}\right)^2 \right) \right]$$

$$+ i\tfrac{\beta}{M} \tan(\nu_s) \sinh(\pi l \delta (1-M^2)^{1/2}) \left[\exp\left(-2i\beta \tfrac{\delta}{M} \tan\nu_s\right) + (-)^m \right]$$

$$\left[\left(\tfrac{\beta}{M} \tan\nu_s\right)^2 + (\pi l)^2 (1-M^2) - \left(\frac{m\pi}{2\delta}\right)^2 \right] \div \left\{ \left(\tfrac{\beta}{M} \tan\nu_s\right)^4 \right.$$

$$+ 2\left(\frac{\beta}{M}\tan\nu_s\right)^2\left[(\pi\ell)^2(1-M^2)-\left(\frac{m\pi}{2\delta}\right)^2\right]+\left[(\pi\ell)^2(1-M^2)+\left(\frac{m\pi}{2\delta}\right)^2\right]^2\Bigg\}$$

(E6)

$$\left(\frac{I_{fmn}}{a}\right) = 2\delta\int_0^{'}\cos(m\pi\eta)\cos(2n\pi\eta)\,e^{-(i2\frac{\beta\delta}{M}\tan\nu_s\,\eta)}\,d\eta =$$

$$i\left[1-(-)^m\exp\left(-2i\beta\frac{\delta}{M}\tan\nu_s\right)\right]\left[\delta^2\frac{\beta}{M}\tan\nu_s\right]\left[\pi^2\left(n^2+\left(\frac{m}{2}\right)^2\right)\right.$$

$$\left.-\left(\frac{\beta\delta}{M}\tan\nu_s\right)^2\right]$$

$$\div\left\{\left[(\pi(n+\tfrac{1}{2}m))^2-\left(\frac{\beta\delta}{M}\tan\nu_s\right)^2\right]\left[(\pi(n-\tfrac{m}{2}))^2-\left(\frac{\beta\delta}{M}\tan\nu_s\right)^2\right]\right\}$$

$$n\neq\pm\left(\frac{m}{2}\pm\frac{\beta\delta}{M\pi}\tan\nu_s\right)$$

(E7)

$$\left(\frac{I_{gmn}}{a}\right) = 2\delta\int_0^{'}\cos(m\pi\eta)\sin(2n\pi\eta)\,e^{-(i2\frac{\beta\delta}{M}\tan\nu_s\,\eta)}\,d\eta =$$

$$(n\pi\delta)\left[1-(-)^m\exp\left(-2i\beta\frac{\delta}{M}\tan\nu_s\right)\right]\left[\pi^2\left(n^2-\left(\frac{m}{2}\right)^2\right)-\left(\frac{\beta\delta}{M}\tan\nu_s\right)^2\right]$$

$$\div\left\{\left[(\pi(n+\tfrac{1}{2}m))^2-\left(\frac{\beta\delta}{M}\tan\nu_s\right)^2\right]\left[(\pi(n-\tfrac{m}{2}))^2-\left(\frac{\beta\delta}{M}\tan\nu_s\right)^2\right]\right\}$$

$$n\neq\pm\left(\frac{m}{2}\pm\frac{\beta\delta}{M\pi}\tan\nu_s\right)$$

(E8)

APPENDIX F

Description of Electrical Circuits

This section discusses the function of all electrical equipment associated with creating the heater pulses and controlling data acquisition which are represented in Fig. 4-4. The main dc power supply has been discussed in Ref. 8 of Chapter 2 and will simply be described here as a source of dc power. This source could supply up to 100 amps at up to 300 volts.

(i) The SCR (Silicon Controlled Rectifier) Commutation Circuit

The SCR commutation circuit is shown in Fig. F-1. This circuit was designed to commutate either between a dummy load and a main load (one-dimensional heat pulse "single mode") or a dummy load and two main loads (to produce a heat pulse which was not uniform over the cross section--see Chapter 5). The dummy load, R_D was typically 65 Ω. This would be varied slightly with operating frequency in order to give proper commutation and duty cycle. The sole purpose of this dummy load/SCR is to cause commutation, i.e., turn off the main SCR. In the single mode of operation SW2 is left open. SW1 is closed and pulses are supplied to the gate of SCR-1 and SCR-D as shown below.

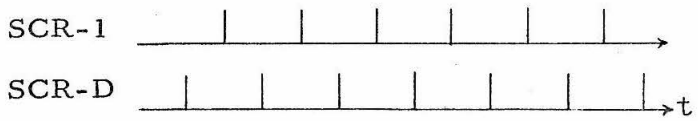

These pulses arrive at the gate at the chosen fundamental frequency, i.e.,200, 250, 300, 400 Hz. Note that the pulses are spaced evenly. This allows the dummy SCR to turn off the main SCR after one-half cycle.

In the dual mode all three SCR's are operational. SW1 and SW2 are closed and pulses are supplied to the gates as shown below

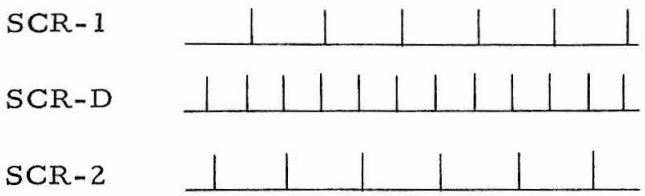

Pulses arrive at gate of SCR-1 and SCR-2 at the chosen fundamental frequency and are out of phase. Note that pulses arrive at the gate of the dummy SCR at twice the fundamental frequency and slightly before a pulse arrives at one of the main SCR's. This allows the main SCR (supposed to be conducting) to be turned off just before the other main SCR received its gate pulse. The dummy SCR was normally needed only to start commutation, after that pulses were not sent to its gate. This allowed an extremely sharp square wave to be pulsed across the heaters.

The voltage from across the anodes of the main SCR's was usually monitored during experiments (for single mode the voltage from anode to ground was observed) and is shown below

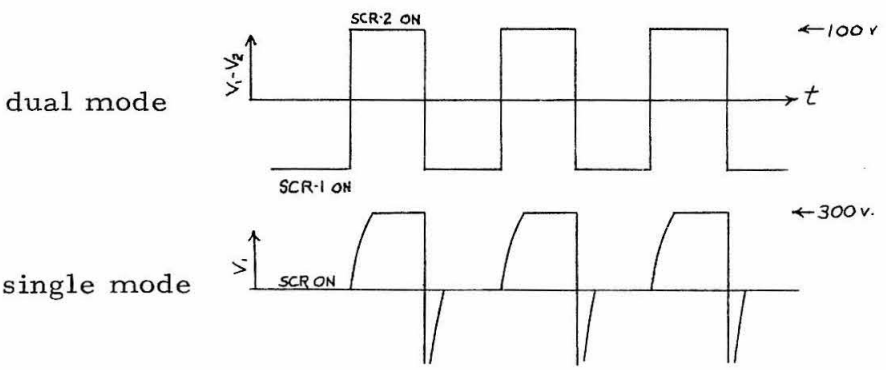

Typical SCR Output Waveform

The SCR's are General Electric type 154D. The RC circuit shown across the two main SCR's is called a snubber circuit and limits the rate of rise of voltage across the SCR to a value such that the SCR will not turn on spuriously.

(ii) Pulse Amplifier

Each SCR gate is supplied 20 volt, 1 amp pulses from one of three pulse amplifiers. The circuit is shown in Fig. F-2. The amplifier receives a pulse from the logic section through an optical isolator. The purpose of this is to isolate the clock, logic and data controller ground from the SCR commutation circuit. The commutation of the SCR's causes a large amount of electrical ground noise which must not reach the logic.

The pulse then triggers a UJT which is followed by a four transistor amplifier which gives the necessary current drive. The UJT is used because it allows an extremely fast pulse to be supplied to the SCR gate. This allows commutation at current levels near the rated capacity of the SCR (~100a.). Typical (unloaded) rise times for this amplifier were approximately 20 ns.

(iii) Pulse generator logic

The function of the logic is to deliver to the pulse amplifiers (through the ground isolators) pulses of the proper frequency and phase so as to give desired heater operation. The logic receives a TTL square wave (from the time clock) of the fundamental frequency for single mode operation and at twice the fundamental frequency for dual mode operation from the clock circuit (frequency reference). The circuit diagram is Fig. F-3.

The operation in the single mode is straightforward. The timer (NE555) effectively "shortens" the TTL pulse width from the clock. The falling edge of this pulse triggers the one shot (SN74121), which in turn sends a pulse to the dummy load pulse amplifier. The rising edge (after inversion) triggers another one shot which provides a pulse to the main pulse amplifier. The "delay" control on the timer may be adjusted to determine the relative phase of these two signals.

In the dual mode the dummy signal is the same, except that its frequency is twice the fundamental frequency. The rising edge of the timer operating at twice the fundamental frequency drives a flip flop (SN7470) the output of which is now at the fundamental frequency. This output and its complement drive one shots which in turn drive the main pulse amplifiers out of phase of the fundamental frequency. The delay control now determines the time lapse after the dummy SCR is pulsed until the main SCR is pulsed (turns on). The delay may be adjusted (during operation) to a minimum or may be set at a large value ($\sim 60\mu s$) and the dummy SCR simply shut off after commutation begins.

(iv) The Frequency Reference and Clock (Fig. F-4)

A 1.0 MHz crystal oscillator provides a time base for the entire experiment. The clock allows the choice of four fundamental frequencies and are given below with approximate values used as aliases:

True Frequency	Alias
195.3125 Hz	"200"
260.4166 Hz	"250"
312.500 Hz	"300"
390.625 Hz	"400"

The clock generates two TTL signals. The first operates the A/D clock and is of such a frequency that the A/D multiplexes each channel at 32 (or 16 if desired) times the fundamental frequency. The second signal is sent to the pulse generator and will be of the fundamental frequency (for single mode) or twice that (for dual mode).

(v) Data Controller

The data controller, Fig. F-5 , was designed to determine when the A/D converter should accept data and when it should not. The length of time during which data acquisition is enabled determines the ensemble length. This ensemble of data would be the correct length in time to allow exactly 2^M (M = 0, 1, 2, 3, or 4) cycles of the fundamental frequency to pass. After one ensemble has been acquired the controller disables the A/D converter. During this period (called delay) the data, which has geen digitized, is added to the previous ensemble of data or it is written on the disk, whichever is preferred. The delay was calibrated (in a manner to be described) so that as soon as the adding process was complete or as soon as the program began writing data on the disk the A/D converter could resume data acquisition in phase with the main heater pulse.

The actual logic is a synchronous sequential circuit. It is synchronous with the fundamental frequency. The term sequential refers to the fact that the logic passes sequentially through several states as shown below with a description of each state.

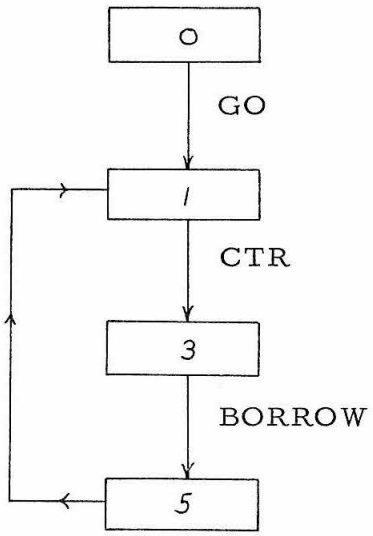

State 0: Set binary counter to zero, load count down scalers.
Wait for GO signal.

State 1: Set data enable true (allow data acquisition).
Count cycles of fundamental frequency on binary counters.
Set CTR true when correct number of cycles have been acquired.

State 3: Set data enable false (discontinue data acquisition).
Start count down scalers.
Set BORROW true when scalers set to zero.

State 5: Clear binary counters.
Reload countdown scalers.
(go to State 1).

The J-K flip-flops (see Fig. F-5) determine the state of the controller. The 4 line to 10 line decoder converts the state code to decimal for display purposes. When the decoder goes into State 1 the binary counters are enabled and count the pulses arriving on the input (fundamental frequency supplied by pulse generator logic) until the proper number of cycles has been counted. The controller then goes into State 3 when the count down scalers are enabled. They also count input pulses, but start at a preset value (set before beginning an experiment) and count down to zero. When the scalers read zero (indicating that the desired time delay has occurred), the counters are cleared, the scalers are reloaded and we return to State 1 to take in more data.

Note that if the delay were set too short, then as soon as the computer finished averaging the latest ensemble, we would resume data acquisition without regard to heater pulse phase. Since the data enable signal is synchronous, the time at which we resume data acquisition will occur (at least) in the middle of the next data enable state (State 1). When we go into State 3 the computer will not have received enough data (it expects exactly 1 ensemble) and will wait until the next State 1. Hence, 2 ensembles have passed, while the computer has only been satisfied once. This fact was used to calibrate the delay. The delay was decreased until more ensembles had been passed than expected. This meant that the delay was too short. The delay was increased slightly until the expected number of ensembles had passed. Hence, the minimum amount of time (when the data was not being acquired) was wasted in an experiment.

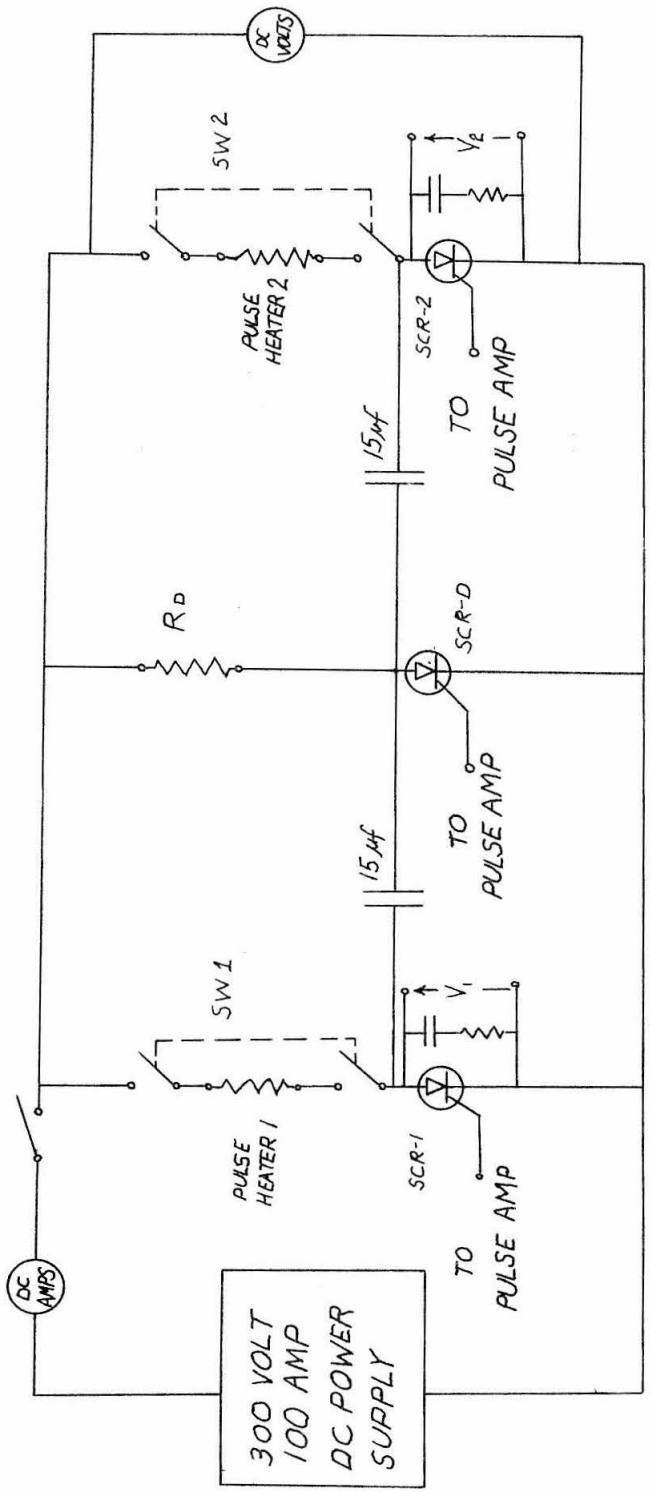

Figure F-1.

SCR COMMUTATION CIRCUIT

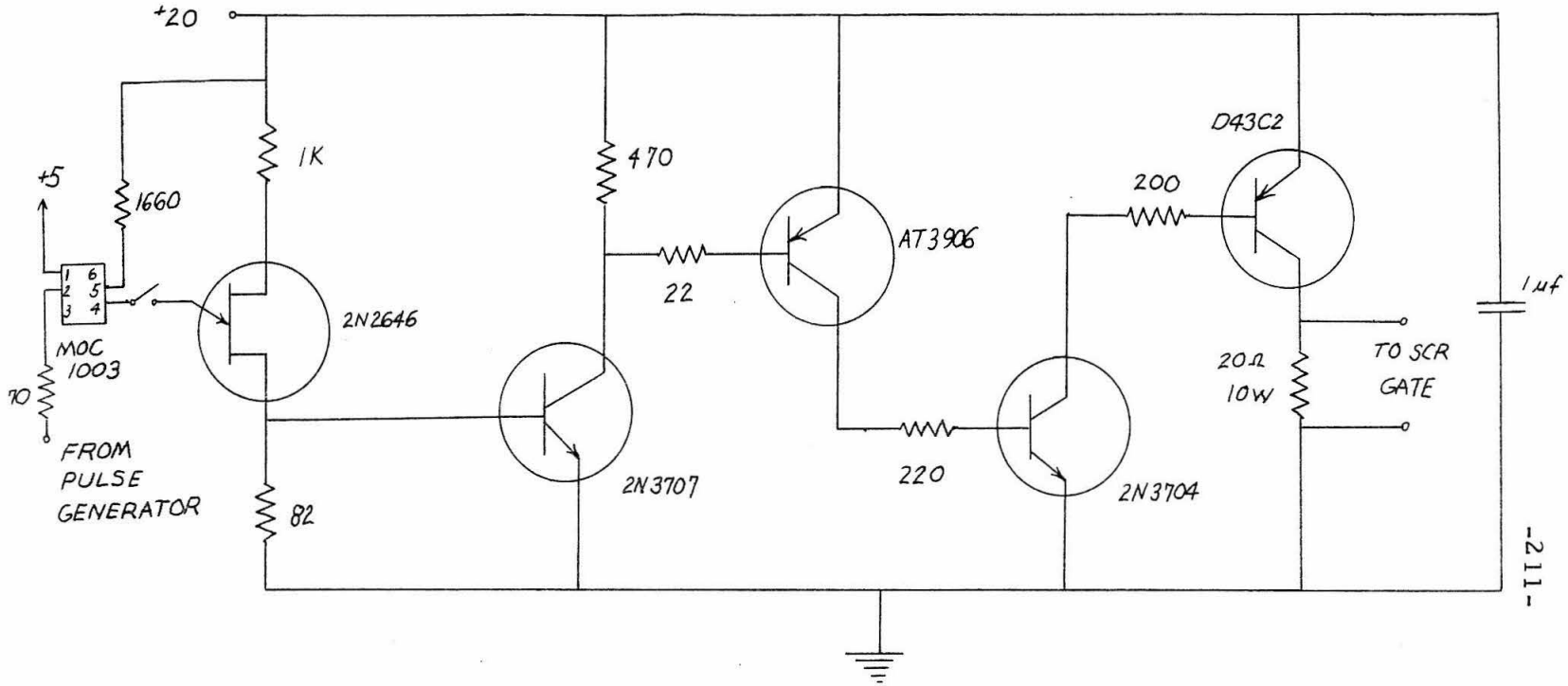

Figure F-2.

GATE PULSE AMPLIFIER

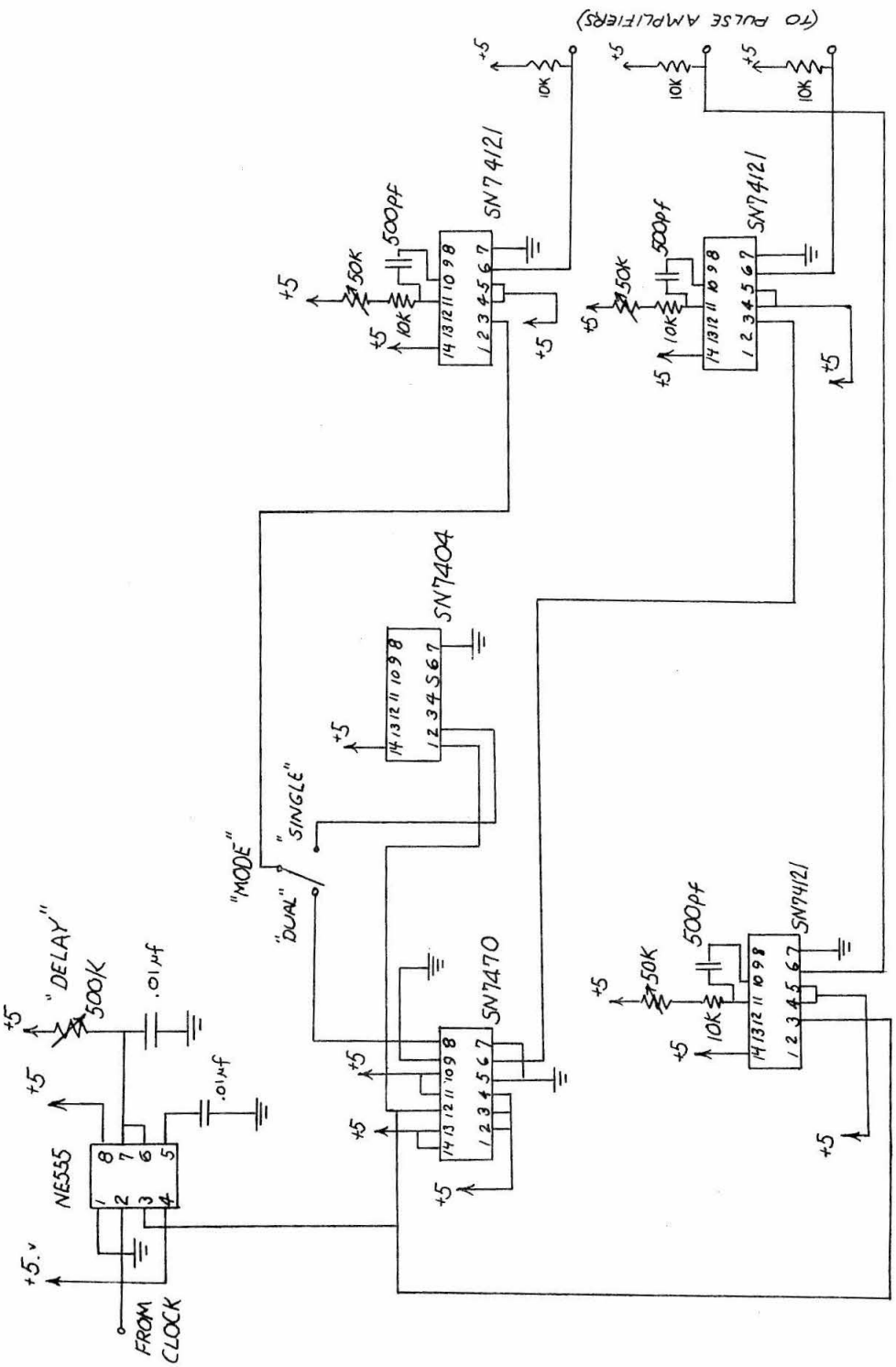
PULSE GENERATOR
(TO PULSE AMPLIFIERS)
"DELAY"
500K
.01μf
NE555
FROM CLOCK
+5.V
"MODE"
"SINGLE"
"DUAL"
SN7404
SN7470
SN74121
50K
500pf
10K

Figure F-3.

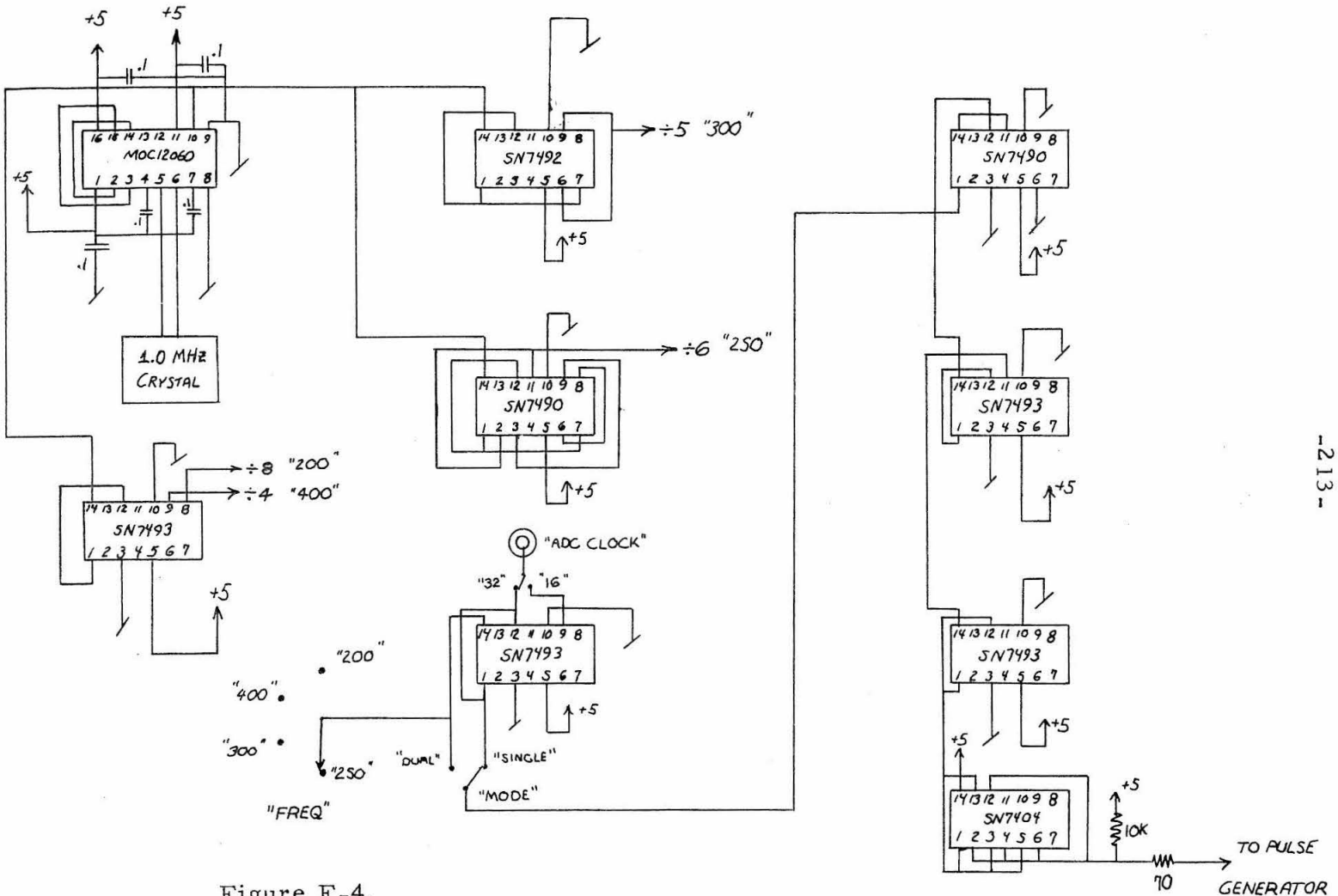

Figure F-4.

FREQUENCY REFERENCE

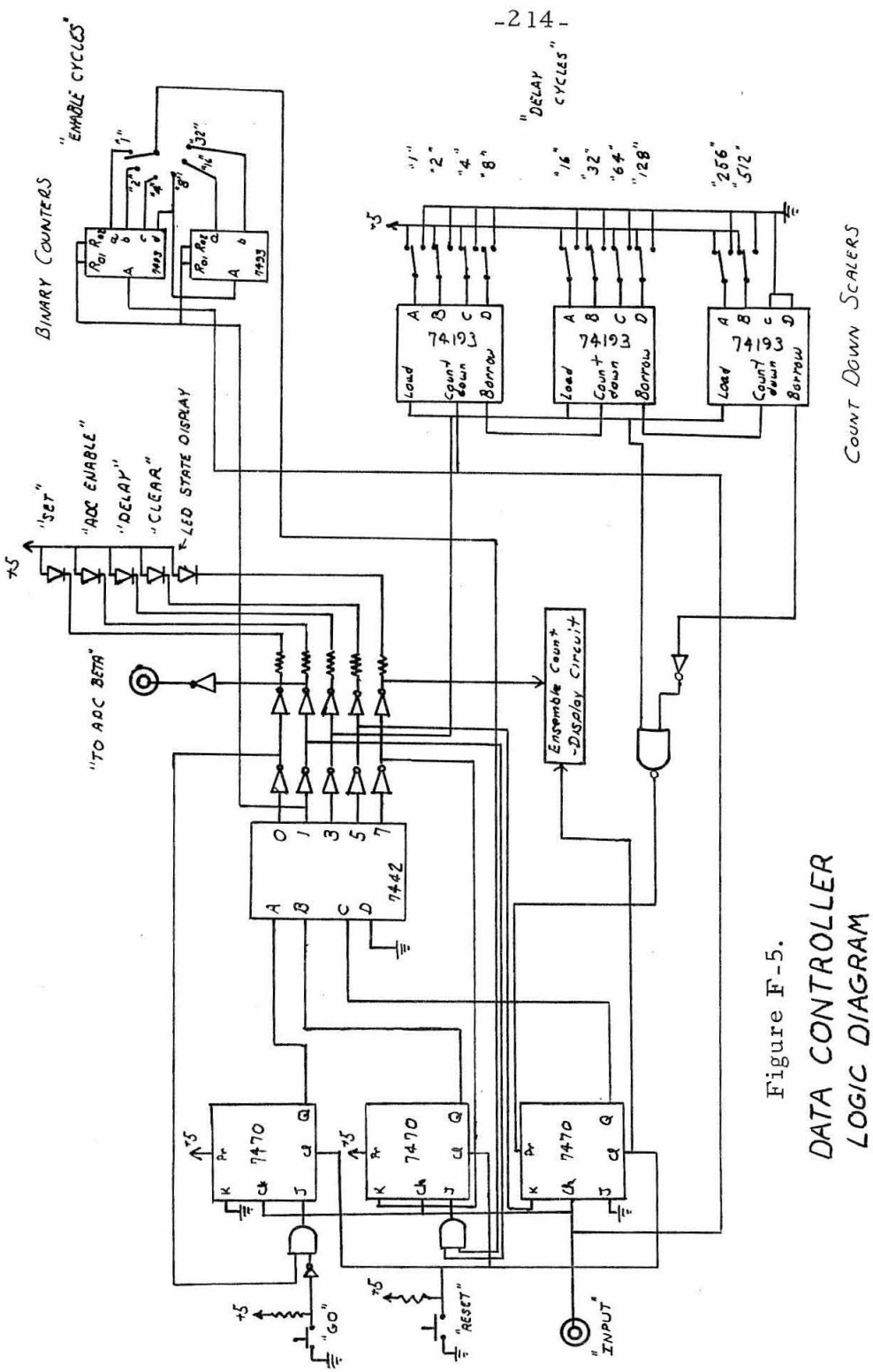

Figure F-5.

DATA CONTROLLER
LOGIC DIAGRAM

APPENDIX G

Notation for Chapter II

x	dimensionless axial position in duct
ℓ	nozzle length
M_1	inlet Mach number
M_2	exit Mach number
Z_1	velocity perturbation normalized by local mean velocity
Z_2	pressure perturbation normalized by local mean pressure $\times \gamma$
Z_3	entropy perturbation normalized by C_p
U	local mean velocity normalized by a^*
β	reduced frequency $= \omega\ell/a^*$ for Sections 2.2, 2.3 $= \omega\ell/(\bar{u}_2 - \bar{u}_1)$ elsewhere
$C_{1\pm}$	dimensionless wave numbers in upstream duct
$C_{2\pm}$	dimensionless wave numbers in downstream duct
P_1^+	acoustic wave upstream of nozzle propagating downstream
P_1^-	acoustic wave upstream of nozzle propagating upstream
P_2^+	acoustic wave downstream of nozzle propagating downstream
P_2^-	acoustic wave downstream of nozzle propagating upstream
T_p	P_2^+/P_1^+
R_p	P_1^-/P_1^+
T_m	P_1^-/P_2^-
R_m	P_2^+/P_2^-
T_e	P_2^+/σ
R_e	P_1^-/σ
σ	value of Z_3 at nozzle inlet

ζ, ζ_i, ζ_e	independent variable used in high-frequency analysis (and the value at inlet and exit) denoting axial position
P	Z_2 as used in high-frequency analysis
U	Z_1 as used in high-frequency analysis
η	$i\beta$
$Z_{oe}, Z_{1e}, \Delta\phi_{\pm}$	functions of M_1, M_2
T	indicates T_p or T_m
R	indicates R_p or R_m

Subscripts

e	indicates entropy disturbance
p	indicates P_1^+ disturbance
m	indicates P_2^- disturbance
∞	high-frequency value
o	low-frequency (quasi-steady) value